Extreme Waves, Overtopping and Flooding at Sea Defences

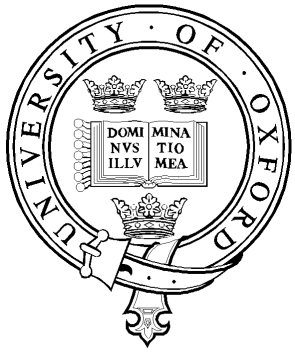

Alison Hunt
St Edmund Hall
Michaelmas Term, 2003

A thesis submitted in partial fulfilment for the degree of Doctor of Philosophy at the University of Oxford.

Department of Engineering Science
University of Oxford
Parks Road
Oxford OX1 3PJ

Abstract

This thesis describes experiments that were carried out using focused wave groups in the UK Coastal Research Facility (UKCRF). Considerable effort was put into calibrating the UKCRF to determine the relationship between the input signals sent to the paddles and the waves generated in the facility. Focused wave groups of various sizes and phases, based on NewWave theory were generated, and measurements were made of the resulting surface elevation data, water particle kinematics, wave runup and overtopping volumes. NewWave theory models the profile of extreme waves in a Gaussian (random) sea. The thesis describes the first time this model has been applied in the context of coastal wave transformation.

A method for the separation of the underlying harmonic structure of a focused wave group is described and results presented. This technique has been used in relatively deep water but is shown to work successfully in the coastal zone until wave overturning. A method has been devised to provide a theoretical Stokes-like expansion of the free and bound waves to model the surface elevation and water particle kinematics of the focused wave groups. Satisfactory agreement is achieved between the theoretical predictions of UKCRF measurements. Suggestions are made for an improved model.

The underlying harmonic structure of the focused wave groups is presented as stacked time histories that give insight into the wave transformation process from deep to shallow water. Particular attention is paid to the low frequency wave generated as the wave group interacts with the beach. This is compared to the low frequency wave that is generated by a solitary wave in the UKCRF.

Runup and overtopping measurements are in reasonable agreement with predictions based on certain empirical formulae, but not others. These comparisons are useful in identifying those formulae able to predict runup and overtopping of extreme waves in the coastal zone.

Acknowledgments

I would like to thank the Engineering and Physical Sciences Research Council for the funding that enabled this research to be undertaken: the Oxford grant GR/N22595 (Extreme waves, overtopping and flooding at sea defences), the linked UMIST grant GR/N21741 and an LDA equipment grant to Oxford GR/R05369.

I am glad to have the opportunity to thank my supervisors Dr. Paul Taylor and Professor Alistair Borthwick. They have been tremendously supportive of the research, my endeavours to write a second doctoral thesis and my career development. I would also like to acknowledge the supervision and encouragement of Professor Peter Stansby at UMIST and the support and camaraderie of my co-worker on the experimental phase of the project, Dr. Tong Feng, also of UMIST.

I would like to thank Dr. James Sutherland, manager of the UK Coastal Research Facility (UKCRF), for his support during my period of time at HR Wallingford, Tom Stevenson who provided cheerful technical assistance in the UKCRF and Dr. Alan Brewer for his technical expertise and willingness to provide assistance at short notice. Alan died in 2002 and I know that he will be greatly missed by all who knew him and worked with him.

Returning to the Engineering Science Department at Oxford, my fellow graduate students and research assistants have been a tremendous source of academic encouragement. I would like to particularly thank Dr. Jun Zang for her friendship and forbearance. I wish her well in her academic career in Oxford.

On a personal level I would like to thank my family for their support during this period of research: for bearing with me being a student just a little longer, and providing pleasurable distraction. Most importantly I want to acknowledge Him who gave me the grace to carry out this work: “Now to the King eternal, immortal, invisible, the only God, be honour and glory for ever and ever.” Romans 16:27 NIV

Contents

1 Introduction and literature review **8**

1.1 Climate change and flooding 8

1.2 A design wave for coastal engineering 9

1.3 Introduction to focused wave groups 10

1.3.1 Previous use of focused wave groups 10

1.3.2 Nonlinearities of focused wave groups 11

1.4 Wave interactions with beaches and coastal structures 12

1.4.1 Wave breaking 12

1.4.2 Wave runup 15

1.4.3 Wave overtopping of coastal structures 18

1.5 Aims and Objectives 24

1.5.1 Specific Objectives 24

2 Test Cases **25**

2.1 Focused wave groups 25

2.2 Embedded wave groups 30

2.3 Solitary wave 31

3 Theoretical background **34**

3.1 Focused wave concept 34

3.1.1 Unidirectional waves 34

3.1.2 Oblique unidirectional focused waves 35

3.1.3 Spread sea focused waves 35

3.2 NewWave concept 36

3.3 Mathematical basis . . . 36
3.3.1 Stokes wave . . . 36
3.3.2 Isolation of harmonics . . . 39
3.3.3 Parasitic free waves . . . 40
3.4 Separation of harmonics example . . . 42
3.4.1 Time series and amplitude spectra . . . 42

4 Experimental Arrangement 54
4.1 U.K. Coastal Research Facility (UKCRF) . . . 54
4.1.1 Wave basin . . . 54
4.1.2 Paddles . . . 55
4.1.3 Wave gauges . . . 57
4.1.4 Paddle control . . . 58
4.2 Calibration of the UKCRF . . . 59
4.2.1 Outline of calibration procedure . . . 59
4.2.2 Calibration results . . . 62
4.3 Instrumentation for test measurements . . . 73
4.3.1 Wave gauge array . . . 74
4.3.2 Laser Doppler Anemometer (LDA) measurements . . . 76
4.3.3 Acoustic Doppler Velocimeter (ADV) measurements . . . 78
4.3.4 Sea wall . . . 79
4.3.5 Image Recording . . . 81

5 Visualisation of focused wave group dynamics and harmonic structure 84
5.1 Focused wave group interacting with a plane beach . . . 84
5.1.1 Crest focused time series . . . 85
5.1.2 Trough focused time series . . . 87
5.1.3 Addition plots . . . 87
5.1.4 Subtraction plots . . . 91
5.1.5 Low frequency waves . . . 94
5.1.6 Conclusions . . . 111
5.2 Focused wave group interacting with a sea wall . . . 112

5.2.1 Sea wall structure . . . 112
5.2.2 Gauge placement for sea wall experiments . . . 112
5.2.3 Crest and trough focus time series . . . 113
5.2.4 Addition time series . . . 113
5.2.5 Subtraction times series . . . 120
5.2.6 Longshore variation of low frequency wave . . . 120
5.2.7 Conclusions . . . 123
5.3 Solitary wave interacting with plane beach . . . 124
5.3.1 Low frequency waves generated by a solitary wave . . . 124
5.4 Embedded focused waves interacting with a plane beach . . . 126
5.4.1 Generation of embedded wave groups . . . 126
5.4.2 Removal of background regular waves . . . 130
5.4.3 LFW of embedded group compared with LFW of lone focused wave group . . . 134
5.4.4 Conclusions . . . 138
5.5 Chapter Conclusions . . . 139

6 Extreme waves in the surf zone 140

6.1 Extreme wave breaking in the surf zone . . . 140
6.1.1 Experimental setup . . . 141
6.1.2 Height and position of wave breaking . . . 142
6.1.3 Frequency shifts . . . 147
6.1.4 Wave group energy . . . 149
6.1.5 Conclusions . . . 154
6.2 Runup on plane beach . . . 154
6.2.1 Experimental procedure . . . 155
6.2.2 Effect of low frequency error wave on runup . . . 156
6.2.3 Relationship between wave height and runup . . . 158
6.2.4 Parametric study of extreme wave runup . . . 161
6.2.5 Correlation of runup with low frequency wave . . . 169
6.2.6 Comparison with other wave runup investigations . . . 170

6.2.7 Conclusions . . . 175
6.3 Overtopping of a sea wall . . . 175
6.3.1 Experimental procedure . . . 176
6.3.2 Effect of low frequency error wave on overtopping . . . 179
6.3.3 Relationship between wave height and overtopping . . . 181
6.3.4 Effect of obliqueness and multi-directionality . . . 182
6.3.5 Relationship between overtopping and runup . . . 182
6.3.6 Comparison with other overtopping investigations . . . 184
6.3.7 Comparison of measured overtopping volumes with present permissible rates . . . 191
6.3.8 Influence of wind on overtopping . . . 194
6.3.9 Conclusions . . . 196

7 Kinematics 197

7.1 Background . . . 197
7.2 Experimental procedures . . . 197
7.3 Kinematics of single focused wave group at the toe of the beach . . . 199
7.3.1 Normally incident wave group . . . 199
7.3.2 Oblique incidence wave group . . . 206
7.4 Kinematics of repeated focused wave groups at beach toe . . . 208
7.4.1 Normally incident repeated wave group . . . 209
7.4.2 Oblique incidence repeated wave group . . . 211
7.5 Kinematics of repeated focused group in the outer surf zone . . . 215
7.5.1 Normally incident repeated wave group . . . 217
7.5.2 Oblique incidence repeated wave group . . . 220
7.6 Kinematics of repeated focused group in inner surf zone . . . 224
7.6.1 Normally incident repeated wave group . . . 228
7.6.2 Oblique incidence repeated wave group . . . 229
7.7 Conclusions . . . 231

8 Conclusions and Recommendations 234

8.1 Conclusions . . . 234

8.2 Recommendations 236

A Experiments undertaken **238**

A.1 Unidirectional wave groups 238

A.2 Spread sea wave groups 239

A.3 Embedded unidirectional focused wave groups 240

B Second order shallow water coefficients **241**

C Selected wave gauge locations **242**

Nomenclature

		Units
A	Measured wave amplitude	m
A_0	Input wave amplitude	m
A_O	Owen's constant	
B_O	Owen's constant	
α	Angle of beach slope	radians
α_S	SPM overtopping coefficient	
β	Angle of sea wall	radians
c	Overtopping reduction factor parameter (VdM & Janssen 1995)	
C	Overtopping reduction factor parameter (Owen 1980)	
d	Water depth	m
h	Height of sea wall crest above toe of sea wall	m
h_m	Height of SWL above toe of sea wall	m
H_s	Significant wave height	m
N	Number of waves	
N_{ow}	Number of overtopping waves	
Q	Mean overtopping discharge per unit length (p.u.l.) of sea wall	$m^3/s/m$
Q_m	Mean overtopping discharge p.u.l. of sea wall at model scale	$m^3/s/m$
Q_p	Mean overtopping discharge p.u.l. of sea wall at prototype scale	$m^3/s/m$
Q_S	Overtopping discharge p.u.l. of sea wall	$m^3/s/m$
Q_O^*	Owen's dimensionless overtopping discharge	
Q_V^*	Van der Meer's dimensionless overtopping discharge	
Q_S^*	SPM overtopping coefficient	

		Units
Q	Mean overtopping discharge per unit length (p.u.l.) of sea wall	$m^3/s/m$
Q_m	Mean overtopping discharge p.u.l. of sea wall at model scale	$m^3/s/m$
Q_p	Mean overtopping discharge p.u.l. of sea wall at prototype scale	$m^3/s/m$
Q_S	Overtopping discharge p.u.l. of sea wall	$m^3/s/m$
Q_O^*	Owen's dimensionless overtopping discharge	
Q_V^*	Van der Meer's dimensionless overtopping discharge	
Q_S^*	SPM overtopping coefficient	
R	Wave runup	m
R_O^*	Owen's dimensionless wave runup	
R_c	Sea wall crest freeboard	m
T_m	Mean wave period	s
x_f	Wave group focus location	m
ψ	Wave group phase	degrees
θ_0	Angle of incidence of wavefront	degrees
θ_s	Degree of wavefront spread	degrees
ξ_0	Surf similarity parameter or Irribarren number	

Chapter 1

Introduction and literature review

1.1 Climate change and flooding

oastal flooding occurs as a result of high tides, storm surges and wind-induced waves. It is therefore of vital importance to be able to predict the behaviour and impact of those waves with the potential to cause damage to the coastal environment.

During the 20th century global mean sea levels rose by 1 to 2 mm/yr. This compares with only 0.1 to 0.2 mm/yr over the last 3,000 years (obtained using geological data). The relatively large sea level rise of modern times can be seen in the water levels around the UK, recorded in the Permanent Service for Mean Sea Level (PSMSL) at the Proudman Oceanographic Laboratory. For example, since 1916 there has been a 1.64 mm/yr rise in sea level at Newlyn in Cornwall, since 1858 a 1.38 mm/yr rise in Liverpool (Gladstone Docks), and since 1896 a 1.85 mm/yr rise in Sheerness in Kent. There is growing evidence to suggest that sea-levels will continue to rise.

A report by Cotton (1999) for the UK Environment Agency, JERICHO project, states that there is high confidence that there will be a rise in the UK mean sea level of up to[1] 72 cm by 2050. The worst case scenario for the east coast of the UK is actually worse than this, since the figure of 72 cm does not take into account predicted vertical land movements in the UK. These are published by Shennan (1989) and for 2050 predict that East Anglia will sink

[1] This is based upon the highest predicted increases of CO_2 of 1% per year. A medium-high CO_2 prediction (based upon pre-industrial CO_2 doubling by 2050 and 1961-90 levels doubling by 2080) suggest a UK mean sea level rise of only 26 cm.

by 9 cm, though at the other extreme Western Scotland will rise by 11 cm.

Prediction of wave heights is fraught with difficulty: in fact the latest report from the UK Climate Impacts Programme (Hulme et al. 2002) does not include any wave height predictions. Hulme et al. (2002) suggest that changes in offshore wave climate and wind direction are not well quantified. This is because predictive models of wave height rely on climatic variables such as wind speed. There is low confidence in climatic variability predictions and so wave height estimates must be viewed with some scepticism. The European WASA (Waves and Storms in the Atlantic) programme, published by the WASA Group (1998) concluded that, although any projected changes lie within the natural range of variability, mean and extreme waves in the North Sea may increase slightly, by 10-20%. Sutherland and Wolf (2002) predict that by 2075 extreme wave heights will be within 5% of the present day values and that changes in the mean annual offshore wave angles will be within 5°. Changes to wave direction would be important since they may lead to greater exposure to offshore waves.

Even if there is little confidence in increased wave heights, the catalogue of evidence for a continued increase in mean sea level means that there is certain to be extra energy in the form of extreme waves which could breach present day coastal defences more frequently.

1.2 A design wave for coastal engineering

Coastal engineers currently use either regular waves or long duration random wave simulations to investigate over-topping of coastal structures. Regular waves do not provide a realistic event, either in terms of shape or regularity. Random waves have the drawback that in order to generate a realistic extreme event the time simulation must be very long indeed. Therefore, a new design wave is required: one that is better representative of waves in realistic sea states and hence useful to coastal engineers in planning the protection of our coastlines. One strong candidate is a focused wave group - a large *transient* wave. A focused wave group is a generic description of a wave that is composed of a number of individual wave trains that come into phase at a particular time and place to produce a large event. Small changes to the focused wave group will affect the surface set-up and wave height causing different effects on coastal flooding. Therefore it is imperative that the focused group has the realistic shape

of a large wave. These requisites are found in the NewWave, a design wave methodology that has recently been taken up by the offshore industry. Tromans et al. (1991) introduced the concept of NewWave for deepwater applications. Tromans et al. (1991) proposed that for large crests, the most probable value of the surface elevation, around the crest, is the product of the crest elevation and the autocorrelation function of the ocean surface elevation. Importantly, this implies that the *shape* of the wave is related to the underlying sea-state. The underlying theory was first developed by Lindgren (1970) who carried out mathematical analysis on normal processes near a local maximum. The theory was also independently formulated by Boccotti (1983), who produced new statistical results of wind waves, mostly looking at wave periods. Jonathan & Taylor (1995) have since validated the NewWave theory against North Sea winter storm data.

1.3 Introduction to focused wave groups

1.3.1 Previous use of focused wave groups

Focused wave groups have been utilised in laboratory basins as a convenient way to investigate large transient waves under controlled conditions. Rapp and Melville (1990) used focused wave groups to generate large breaking waves in order to investigate breaking criteria and energy fluxes.

Focused wave groups can be generated using different techniques. Longuet-Higgins (1974) produced a wave focused group by introducing a continuous modulation of the driving frequency sent to the paddle. Rapp and Melville (1990) used linear theory to determine the appropriate phasing of the individual wave trains. Baldock et al. (1996) also used this method, though aware of its shortcomings due to nonlinear interactions (see discussion of 1.3.2).

Laboratory-based experimental work undertaken by Barnes (1996) studied the interaction of wave groups with beaches in an attempt to understand the resulting low frequency waves. In contrast to the work of Rapp and Melville (1990) and Baldock et al. (1996), Barnes (1996) generated wave groups by superimposing a number of solitary waves onto a trough with a sine wave shape (to balance the mass flux of the solitary waves).

1.3.2 Nonlinearities of focused wave groups

Investigations have been carried out into why the *size* of the focused wave group is greater than the sum of the individual amplitudes of the components used to create the focused event. A body being more than the sum of its parts has many analogies in the wider world, but the underlying reason for *this* particular phenomenon is due to interactions between the individual wave trains. Longuet-Higgins and Stewart (1960) first identified so-called wave-wave interactions in a paper that described mathematically the existence of additional[2] higher order harmonics due to the interaction of two waves of considerably different frequencies. Longuet-Higgins and Stewart (1960) calculated the changes in wavelength and amplitude of a shorter wave train that was superposed on and interacted with a much longer wave. They also introduced the concept of radiation stress of the waves. A substantial investigation was undertaken by Baldock et al. (1996) into nonlinear interactions of unidirectional[3] focused wave groups. Baldock et al. (1996) found that the level of nonlinearities increases with increasing input amplitude and decreases with increasing bandwidth. For their largest wave, Baldock et al. (1996) found that the maximum crest elevations were 40% higher than predicted by linear theory, and 30% larger than *second* order theory.

Nonlinearities affect not only the size of the focused wave group, but the point in time and space at which the group comes into focus. Longuet-Higgins (1974) was the first to discover a shift in the expected focus location. The shift was also noted by Rapp and Melville (1990). The phenomenon was investigated by Baldock et al. (1996) who discovered that there was a permanent change in the relative phase of the free waves even though most of the nonlinear interactions were fully reversible. Baldock et al. (1996) suggest that this explains the downstream shifting of the focus location.

As mentioned earlier, Baldock et al. (1996) found that the maximum crest elevations of large focused wave groups were in poor agreement with second order theory. This led to further investigations being carried out by Johannessen and Swan (2001) with a spread sea to investigate the effects of directionality on nonlinearities. The significant finding was that nonlinearities *decrease* with *increasing* directionality; i.e. the greatest angular distribution of waves gives the best agreement with second order theory. Johannessen and Swan (2001)

[2] Higher order harmonics of *regular* waves had been identified by Stokes in 1847.

[3] The term uni-directional means a long-crested wave that produces a line focus.

also found that wave groups equally close to their breaking limit produce an evolution that is independent of the directional spread. This finding indicates why there has been better agreement between field data and second order theory than between unidirectional laboratory flume data and theory. Jonathan et al. (1994) carried out analysis on field data using storm waves in the northern North Sea. They found that there was reasonable agreement between the data and second order theory.

As a focused wave group comes into focus and subsequently disperses there are significant transfers of energy to other harmonics, leading to large increases in local energy density. Baldock et al. (1996), in their laboratory study of unidirectional focused wave groups, produce power spectra derived from surface elevation time histories at various positions relative to the focus location. The spectra show a transfer of energy from initial input range to higher frequencies when the wave is at or near focus. Baldock et al. (1996) state that this transfer of energy (which provides a large increase in the local energy density) is consistent with the considerable increase in local surface elevation. They noted that the energy changes were reversible if no wave breaking occurred. These results are consistent with the numerical simulations of Gibbs (2003).

Peregrine et al. (1988) examined the theoretical and experimental focusing of water waves for multidirectional wave fronts. Their theoretical approach uses the nonlinear Schrödinger equation - a weakly nonlinear wave modulation theory (used in an earlier analysis by Peregrine (1983)). Peregrine et al. (1988) found that the theory gave satisfactory agreement with experimental results, even close to breaking. The numerical and experimental results indicated the importance of linear diffraction in wave focusing at a point.

1.4 Wave interactions with beaches and coastal structures

1.4.1 Wave breaking

In shallow water the commencement of large scale wave breaking heralds the beginning of the surf zone - that dynamic region of the sea which is responsible for much of the transport of sediment and rapidly changing bathymetry. Wave breaking has been investigated extensively since the process sheds light on nearshore current generation, longshore bar formation as well as forces on man-made coastal structures such as seawalls and groynes.

In deep water, the greatest influence on waves comes from above - from the wind. As waves move into shallow water their wave lengths decrease and their heights increase. This leads to a steepening of the wave until the wave breaks. After breaking the wave will continue to travel up the beach as a bore of water.

The limiting steepness of the wave is related to the relative depth (wave height to water depth ratio) and the beach slope. One parameter of crucial importance is the *breaker depth* index. This is simply the ratio of wave height to still water depth at the position of breaking. Initial studies to determine the breaker depth index were carried out by McCowan (1891) who investigated the theoretical behaviour of solitary waves. He proposed a breaker index of 0.78, which is still used as a rule of thumb. Later, the breaker index of laboratory-generated regular waves was examined by Weggel (1972) who proposed a formula that must be solved iteratively and is dependent upon beach slope. For a flat bottom the breaker index tends to the same value as given by McCowan (1891), but at the other extreme for a (theoretical) vertical slope a standing wave would be generated and the index is double the value, at 1.56.

Regular waves have no height variation in time and should always break at the same position. However, irregular waves being a succession of waves of varying heights should break at different locations which may or may not be determined from the breaker index. Svendsen & Veeramony (2001) investigated wave breaking in wave groups, particularly the position at which the waves break and how the grouping of the waves changes as it travels through the surf zone. Svendsen & Veeramony (2001) used groups of cnoidal waves with different groupiness factors. They found that the location of the start of breaking of an individual wave in the group was affected by the groupiness of the waves i.e., it was not determined simply by the individual wave height and depth. They also found that the wave height to depth ratio at breaking had a wider variation for individual waves in the group than for regular waves, and that groupiness was conserved inside the surf zone. The maximum wave height to depth ratio (breaker depth index) that they found was 2.

Ting (2002) also investigated breaking for wave groups generated using a narrow-banded spectrum. He found that the wave height to water depth approached a constant value inside the surf zone, and that the shape of the spectrum affected the temporal and spatial variability of wave breaking. A narrow-banded spectrum produced a wide surf zone dominated by spilling breakers, whereas a broad-banded spectrum produced a relatively narrow surf zone dominated

by plunging breakers (Ting 2001). Ting (2001) also noted that the position of wave breaking may have been unduly influenced by spurious long waves in the basin.

Seyama and Kimura (1988) carried out a study on unidirectional random waves and found that the ratio of wave height to water depth at breaking was 30% less than for regular waves.

The generation of a varying break point which occurs as a result of irregular wave breaking is one theory for the generation of 'surf beat', the low frequency, infragravity wave that accompanies short wave oscillations. This phenomenon was first identified in the field by Munk (1949) and then corroborated by Tucker (1950) also in a series of field measurements. They observed that long, low frequency waves had a positive correlation with wave breaking. Recently Baldock et al. (2000) investigated the laboratory generation of surf beat using bichromatic wave groups[4]. There has been some debate as to what mechanisms underlie surf beat. Longuet-Higgins and Stewart (1962; 1964) suggested that surf beat arises due to the release of low frequency waves at breaking and their subsequent reflection at the shoreline. However, this theory has been replaced by *time-varying breakpoint* generation. Incident wave groupiness produces a time-varying breakpoint position, which in turn radiates long waves that travel both shoreward and seaward. The interaction of the shoreward and seaward waves then produces the surf beat. Baldock et al. (2000) provide evidence for this theory, from extensive laboratory investigations. Their findings that the surf beat is linearly dependent on short wave amplitude and dependent on the normalised surf zone width are in agreement with time-varying breakpoint theory.

Surf beat or low frequency waves (LFW) have also been studied by Barnes (1996). He was able to generate a LFW as a result of wave group interactions with a beach, in a laboratory. He found that the generation point was at the shoreline, in the swash zone. Also when the individual waves that comprised the group were closely spaced the only reflection was a single long wave, in contrast to the case where individual waves are spaced far apart, and there is a reflection of each individual wave of the group. In addition he found that the size of the reflected wave was dependent on the slope of the beach, being greater for steeper slopes, as one would expect. Barnes (1996) also generated a solitary wave and found that the resulting LFW was similar in form and timing to that produced by the wave groups.

[4] i.e. linear wave components at two frequencies.

1.4.2 Wave runup

Wave runup is defined variously as either the sum of the vertical wave setup and swash motions by oceanographers, or the maximum extent of vertical elevation of water level by coastal engineers; in each case on the solid boundary of the fluid domain. These two definitions are in fact one and the same thing.

There are two distinct classes of runup: (a) runup on a beach and (b) runup on a coastal structure. There is a fundamental difference in the way that they have been investigated and the motivation for so doing.

Wave runup on a beach

As already mentioned, researchers concerned with the beach environment define wave runup as the sum of wave set-up and swash oscillations. Wave set-up is the elevation of the water level shoreward of the breaker line associated with changes in the momentum flux due to wave shoaling and breaking[5]. Bowen et al. (1968) carried out the first investigations into wave set-up (and set-down). Researchers have since carried out field studies of set-up (Guza & Thornton 1981; Holman & Sallenger 1985; and Nielsen, 1988). The swash oscillations that compose runup are themselves composed of incoming wave bores from individual broken waves and much lower frequency, so-called infragravity, waves. The discovery that swash has two components that could be separated by spectral analysis was first made by Guza and Thornton (1982).

The relative importance of the two types of swash oscillations depends a great deal on the beach slope and the nature of the incoming wavefield. The Iribarren number or surf similarity parameter, ξ_o, (Battjes 1974) is a very useful parameter that is proportional to the beach slope and incorporates information on the offshore wave conditions. It is given by

$$\xi_o = \frac{\tan\alpha}{\sqrt{H_o/L_o}} \tag{1.1}$$

where α is the beach slope, H_o is the offshore wave height and L_o is the offshore wavelength.

For a steep slope with a high Iribarren number the incoming bores dominate, though infragravity waves still exist (Kobayashi et al. 1990). Both components are dependent upon

[5] There is a related, but smaller set-down that occurs seaward of the breaker line.

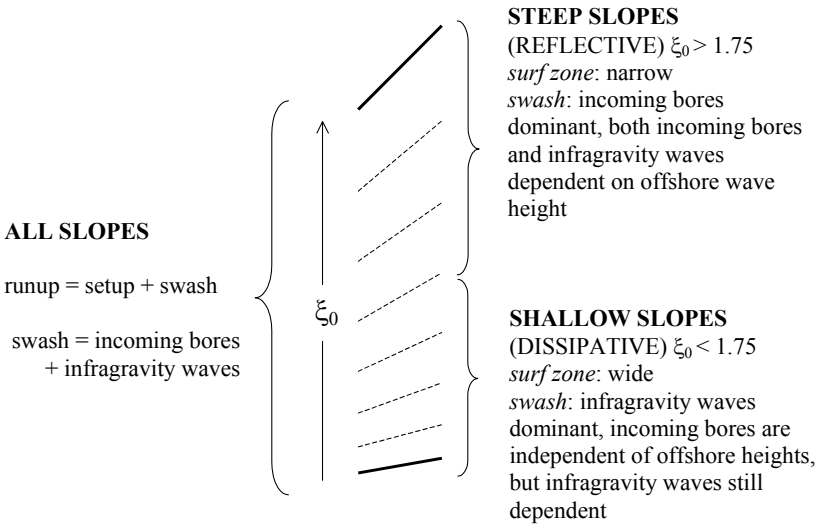

Figure 1.1: Effect of slope on wave characteristics.

the offshore wave conditions i.e., the larger the offshore wave height the greater the incoming bore and infragravity wave. This class of beach is called *reflective*. For a gentle slope with a low Iribarren number, the infragravity waves dominate and only these waves have a dependence on the offshore wave conditions. This type of beach is known as *dissipative*. A dissipative beach removes energy through bed friction. This effect on runup of increasing Iribarren number is shown schematically in Figure 1.1.

Guza and Thornton (1982) found that the amplitude of the swash due to incoming bores was not directly dependent on offshore conditions, whereas there was a clear correlation between swash from infragravity waves and offshore wave height. This lack of dependence of incoming bore on offshore conditions can be explained with a simple example. For a gentle slope the surf zone is very wide. If the offshore wave height doubles then waves will break in water twice the depth and much further from the previous shore-line, reducing the proportion of the extra energy of the bore reaching the shore.

Remarkably little research has been carried out to determine empirical formulae for beach runup. Nearshore oceanographers have determined relationships for swash oscillations, i.e. runup with respect to set-down rather than the SWL. Holman and Sallenger (1985) carried out field experiments to determine an empirical relationship for the significant swash height. Holman (1986) analysed the data further to produce an empirical relationship for wave runup

that included a simple expression to determine set-up.

For gentle slopes, wave runup is smaller and since set-up is independent of slope, set-up must be larger in proportion to swash. Therefore there are only small swash motions on dissipative beaches (Kobayashi et al. 1989). Conversely, on reflective beaches swash oscillations are greater than wave set-up (Battjes 1974). It should be noted though there are no infragravity waves associated with regular waves because there are no long bound waves or surf zone oscillations to generate them.

Infragravity waves can become trapped in the surf zone when the incoming low frequency wave approaches the coast at an angle. The wave that is reflected from the beach is refracted as it moves into deeper water and will turn the wave towards the shore again. These waves are also called *edge* waves. They have been investigated in the field by Holman and Bowen (1979) and Oltman-Shay & Guza (1987) amongst others. One of the beaches that Oltman-Shay & Guza (1987) studied showed a considerable contribution to beach runup from edge waves.

Wave runup on a coastal structure

Determination of runup is of critical importance in the design of sea defence structures. If wave runup is greater than the crest of a sea wall, overtopping will occur, with potentially grave consequences for people and property on the landward side. Coastal engineers currently base their designs upon regular or irregular wave runup theories. Each approach uses empirical formulae from laboratory hydraulic tests.

Coastal structures generally, though not exclusively, have steeply sloping faces. Wave runup on a coastal structure depends on many parameters including angle of slope, wave height, depth of water at toe of structure, slope roughness and permeability. Early attempts to produce empirical formulae were limited to smooth slopes in deep water in order to reduce the number of parameters to investigate. Hunt (1959) proposed a simple formula for runup of regular waves that was synthesized further by Battjes (1974) by the use of the Iribarren number. This formula has also been used for beach runup but was determined for regular waves in laboratory conditions.

For steeply sloping faces the structure is highly reflective. This means that incoming bores will be dominant over low frequency waves and the bores are very dependent on offshore

conditions. Since wave setup is independent of slope, swash oscillations will be greater than setup. There will also be a narrow surf zone on the slope.

There have been relatively few laboratory investigations into irregular wave runup on gentle slopes. One investigation of note is that of Mase (1989) who investigated wave runup on four different slopes ranging from 1:5 to 1:30. The value of the Iribarren number ranged from around 0.5 to just under 3, i.e. covering both dissipative and reflective slopes. Mase proposed several formulae for different statistical likelihoods of runup: maximum[6], 2% exceedance, 10% exceedance, highest one-third and the mean value. Mase (1989) notes that there is some discrepancy between these formulations, and those provided by Holman (1986) for beach runup. Mase suggests that the difference is due to permeability and roughness.

1.4.3 Wave overtopping of coastal structures

Laboratory based experiments on overtopping rates and runup of regular waves were undertaken by Saville & Caldwell (1953) and Saville (1955)), followed by larger model tests by Saville (1958) on Lake Okeechobee. Later, whilst working on the related phenomenon of runup, Saville (1962) proposed that regular wave theories could be extended to apply to individual irregular waves. This was termed the "hypothesis of equivalency". This hypothesis was substantiated to some extent by the work of Tsurata & Goda (1968) (and also Van Oorschot & D'Angremond 1968; Battjes 1971; and Gunbak & Bruun 1979). Tsuruta and Goda (1968) generated both regular and irregular wave trains, and measured mean and individual overtopping discharges. They compared overtopping volumes of regular waves with irregular waves that had the same significant wave heights. They found that the mean overtopping discharge of irregular waves was smaller than those of regular waves, but it increased with decreasing wave height i.e. for small waves there is good agreement, but for big waves irregular mean overtopping discharge is smaller than for regular waves. However, Tsuruta and Goda (1968) found that the individual overtopping discharge of irregular waves is very similar to that of regular waves. They found a little scatter in the data due to interference of preceding waves and difficulty in measuring individual overtopped volumes.

[6]The word maximum is a misnomer since it is impossible to predict what the absolute maximum would be since the tail of the Rayleigh probability distribution for the size of waves is unbounded: as the size of the wave increases, the probability of occurence simply reduces towards zero.

The problem with the "hypothesis of equivalency" is that it neglects the interactions between the waves i.e., wave groupiness. An alternative approach was to assume that runup has a Rayleigh distribution (Ahrens 1977; Battjes 1971; and Losada & Gimenez-Curto, 1981). This method is simple but obviously omits much important physics (Kobayashi & Raichle, 1994).

The complications of irregular waves were put to one side when Weggel (1976) proposed an empirical formulation for overtopping of regular waves. Weggel (1976) built on the work of Saville & Caldwell (1953) and Saville (1955)) but provided a non-dimensional formulation. He also investigated the effect of scale on overtopping, and found that for smaller model scales there was a more rapid drop-off of the overtopping rate with increasing structure height. However, there have been contradictory findings on the effects of scale: on one hand Weggel (1976) concludes that "the primary influence of scale on the overtopping of smooth sloped structures is through scale effects manifest in the runup phenomena"; Jensen & Juhl (1987) found that the Reynolds number was of importance as it determines the turbulence level in the wave up-rush; and Kobayashi & Raichle (1994), in providing a numerical model of overtopping, state that the numerical model needs to be evaluated with large scale test results as one of the coefficients used in the empirical formulae is "likely to be influenced by scale effects". These views contradict the rather more optimistic view of Franco & Franco (1999) who state that "scale effects were found to be negligible when comparing test results at small and large scales".

Numerical investigations were made by Jervis & Peregrine (1996) into scale effects on wave overtopping. They included the effects of surface tension in their numerical model and found that errors in scaling experimental overtopping results to prototype scale were larger than expected. They also found that runup values were affected by surface tension.

One of the influences of overtopping that obviously does not scale, because of surface tension, is 'breaker spray'. Overtopping of spray occurs when the turbulent wave front travels up the coastal structure and causes water to be thrown into the air. This water is then blown over the structure by wind. It is difficult to model this phenomenon in the laboratory because of the scale effect, but Jensen & Juhl (1987) state that when wave runup is large it is 'green water' that passes the crest of the structure which is less susceptible to transport by wind. This is confirmed by Franco & Franco (1999) who found that "additional breaker-

spray transport due to wind is found to be negligibly small in comparison with representative overtopping".

The Shore Protection Manual (1984) of the US Army Corps of Engineers adopted the regular wave based empirical formulation of Weggel (1976) to predict overtopping rates. It provided an extension to the regular wave formulation by assuming that overtopping could be described by a Rayleigh distribution, as proposed by Ahrens (1977).

During the same period of time that the Shore Protection Manual (1984) was suggesting that overtopping rates should be based upon regular wave theory, extensive laboratory overtopping experiments using irregular waves were being carried out in the UK. The outcome of these experiments was the seminal report by Owen (1980), which proposed proposing empirical design formulae based upon irregular waves. This approach has been adopted by the UK coastal engineering community.

Following greater access to wave basins with the capability to generate irregular waves, many empirical formulations based upon irregular waves have been derived (see e.g. Van der Meer, 1994; Van der Meer, 1987 and 1988; Van der Meer & Stam, 1992; De Waal & Van der Meer, 1992; Van der Meer & Janssen, 1995; Seelig & Ahrens, 1995; and Davidson et al., 1996). Since these formulations are based upon somewhat more realistic conditions of irregular waves, they should provide more accurate predictions.

Historically, most of the overtopping research has focused on a *mean* overtopping rate. It is relatively straightforward to run an experiment for a period of time, collecting all the overtopped water and then calculating the mean overtopping volume per unit width of structure. It is more difficult to measure the overtopped volume of each individual wave. Tsurata and Goda (1968) measured the overtopping volumes of individual waves using a bucket and connected to a movable carriage via a load cell. The weight of the bucket was continuously recorded enabling the volume of individual waves to be determined. The number of overtopping waves may also be determined from the record. Variations on this technique are still being used today. Su et al. (1992) proposed a Weibull distribution for the exceedance probability distribution of each overtopping volume. Based upon the Weibull distribution, Van der Meer & Janssen (1995) and Franco & Franco (1999) provide a method for calculating the 'maximum' overtopping volume. This value is perhaps more useful for safety purposes than a mean value (Allsop, 1994; HR Wallingford report W178, 1999; and Franco & Franco,

1999).

It is not in fact possible to build a seawall structure that can guarantee a zero overtopping rate since it is not possible to predict the size of the maximum wave that will overtop, although the statistical likelihood of an extremely large wave will be very small. Most coastal structures are built to permit a certain level of overtopping. There have been several investigations into permissible rates of overtopping which can be broken down into tolerable limits for structural safety and those for the safety of pedestrians, cars and buildings beyond the structure. Goda & Tsuruta (1968) approach the subject from the point of view of the size of the size of pumping stations that would be required to prevent the accumulation of water. Goda (1985) summarises findings for both coastal dykes and revetments and also for the safety of people and cars travelling at speed. The permissible overtopping for safety considerations referred to in Goda (1985) all come from publications in Japanese. An extensive field study was carried out by Fukuda et al. (1974). They employed the skills of several harbour engineers who viewed video footage of overtopping waves whose overtopping rates were measured. The engineers were asked to comment on the extent to which the waves would affect a person, a car and a house. These are obviously subjective findings but they are accepted by coastal engineers and appear in the guidance of Owen (1980). More recently, laboratory experiments have been carried out on model cars and people (Franco et al. 1994). The findings suggest that the permissible limits should be increased. However, as Allsop (1994) points out, this study does not take into account the shock of a person being engulfed in cold water. No international guidelines exist on this important subject.

There have been several recent investigations into the effect of wave obliquity and multi-directionality on overtopping rates, which provide a more complete picture of real seas. De Waal & Van der Meer (1992) carried out experiments on smooth slopes and found that for increasing angles of attack, the overtopping rates[7] of both long and short-crested seas were reduced, more so for short-crested seas. There were a few data points in the long-crested experiments that suggested an increase in the overtopping rate, but the overall trend was for a reduction in the rate. De Waal & Van der Meer (1992) noted that for normally incident waves there was no reduction in overtopping rates for short-crested seas in comparison to

[7] It would appear that the experiments to determine reduction factors for overtopping rates actually measured runup, and overtopping trends deduced from these.

long-crested seas. Also, overtopping rates remained the same regardless of the spreading angle of the multidirectional seas. Juhl & Sloth (1994) carried out laboratory investigations on oblique long-crested waves overtopping rubble mound breakwaters. They found a much greater decrease in the overtopping rates for increasing angles of attack, because of the increased friction and porosity of the structure. Juhl & Sloth (1994) also found that the level of reduction due to obliquity was dependent on the structure's freeboard. Franco & Franco (1999) carried out extensive investigations into the overtopping of several types of vertical structures. For plain vertical walls they found that there was a reduction in overtopping rate with long-crested seas, but not as great as for simple slopes (De Waal & Van der Meer, 1992) or rubble mound breakwaters (Juhl & Sloth, 1994). With short-crested seas Franco & Franco (1999) found that there was a slight increase for small angles of attack, but a reduction thereafter. This slight increase for small angles of attack is also reported by Owen (1980), but for the case of long-crested seas. However, the HR Wallingford report W178 (1999), which provides an update of the Owen (1980) report, suggests that a reduction of overtopping is most likely for all oblique angles, despite a few data points that indicated an increase. Franco & Franco (1999) found that, in contrast to De Waal & Van der Meer (1992), for normally incident waves hitting vertical walls short-crested seas produce less overtopping than long-crested seas. Franco & Franco (1999) also found that the percentage of overtopping waves reduced almost linearly with increasing angle of incidence. The probability of the wave overtopping decreased more slowly than the overtopping rate with the effect that the total overtopping water volume is distributed over a larger number of smaller events. This is obviously preferable to having a smaller number of larger events.

Overtopping research has primarily focused upon regular and irregular waves. However, since the work of Kobayashi and Karjadi (1994) to introduce a representative solitary wave period and associated surf similarity parameter, it is possible to compare the overtopping of solitary waves with regular and irregular waves.

There has recently been some work to consolidate and improve upon some of the accepted of overtopping prediction methods. The Shore Protection Manual (1984) method has been revisited by Hu and McCauley (1997) in a bid to improve the accuracy of the overtopping rates. As previously mentioned, the Shore Protection Manual (1984) uses the work of Ahrens (1977). One of the assumptions made by Ahrens (1977) was that one of the empirical co-

efficients remained unchanged from regular to irregular waves. Hu and McCauley (1997) do not make this assumption and provide a new expected estimate of overtopping that comes closer to values predicted by Van der Meer & Janssen (1995). The work of Owen (1980) has been incorporated into an updated report by HR Wallingford (1999). The report provides more extensive design guidance for many different structure types, includes the effects of wave front obliquity and multidirectionality, and also enables the prediction of numbers of overtopping waves and individual overtopping volumes. Hedges & Reis (1998) carried out regression analysis on Owen's original data and have found that the new (H&R) model predicts lower seawall crest elevations than the Owen model, with potential associated cost savings.

There have been attempts to compare results predicted by the different empirical formulae and numerical and experimental results. Kobayashi & Raichle (1994) compared results from laboratory overtopping experiments of revetments with results predicted by the Shore Protection Manual (1984). They found that the Shore Protection Manual (1984) under-predicted the average overtopping rate and over-predicted the overtopping probability. Dodd (1998) compared his numerical model overtopping results with laboratory data and predictions by the Owen (1980) formulae. He found that the numerical model predicted overtopping with much greater accuracy and concluded that the Owen (1980) formulae are poor at predicting large overtopping rates. A numerical model based on shallow-water equations (Shen & Meyer, 1963) has recently been used by Peregrine & Williams (2001) to evaluate the overtopping flow and total volume for one swash event.

Finally, a note on the accuracy of the empirical formulae. For all the experiments that have been undertaken both in the laboratory and in the field there is a rather depressing lack of confidence in the ability to make accurate predictions of the overtopping rates. Douglass (1985) states that overtopping rates will be at best within a factor of three of the real values. Even fifteen years later, the HR Wallingford report (1999) warns that the empirical formulae most trusted by the UK coastal community are "accurate only to within one order of magnitude". Goda (1985) suggests probable ranges of variation of estimated rates of overtopping to the true value, for different structures. The least certainty is for high overtopping rates of block mound seawalls where the range varies between 0.05 and 10 times. This inaccuracy stems from the nature of the logarithmic design curves. Goda (1985) concludes that, as a result of the inability to accurately predict overtopping rates, the most appropriate use of

the empirical formulae may be in the design of structures for laboratory hydraulic tests prior to full-scale construction.

1.5 Aims and Objectives

The overall aim of this research is to provide a body of evidence by which to examine the suitability of NewWave as a design wave in the coastal zone.

1.5.1 Specific Objectives

1. To provide information to coastal engineers on the use of NewWave focused groups for the estimation of coastal structure runup and overtopping calculations compared with current empirical formulae based upon either regular or irregular waves.

2. To provide a database of focused wave group transformations up a beach with and without a sea wall, for interpretation and modelling purposes.

3. To identify the harmonic structure of a focused wave group.

4. To present focused wave group transformation data qualitatively as stacked time histories in order to give insight into the physical processes, and to make quantitative comparisons of the data against theory.

5. To investigate the generation of low frequency waves caused by the interaction of focused wave groups (both unidirectional and spread directionally) with a plane beach.

6. To provide kinematics data for the water particle velocities in NewWave at the focus location and in shallow water depths.

Chapter 2

Test Cases

Forty-four different wave cases were generated and measured in the U.K. Coastal Research Facility. These fell within the following wave categories: focused wave groups, regular waves, embedded wave groups and a solitary wave.

2.1 Focused wave groups

Within the focused wave group category are several further distinctions as shown in Figure 2.1.

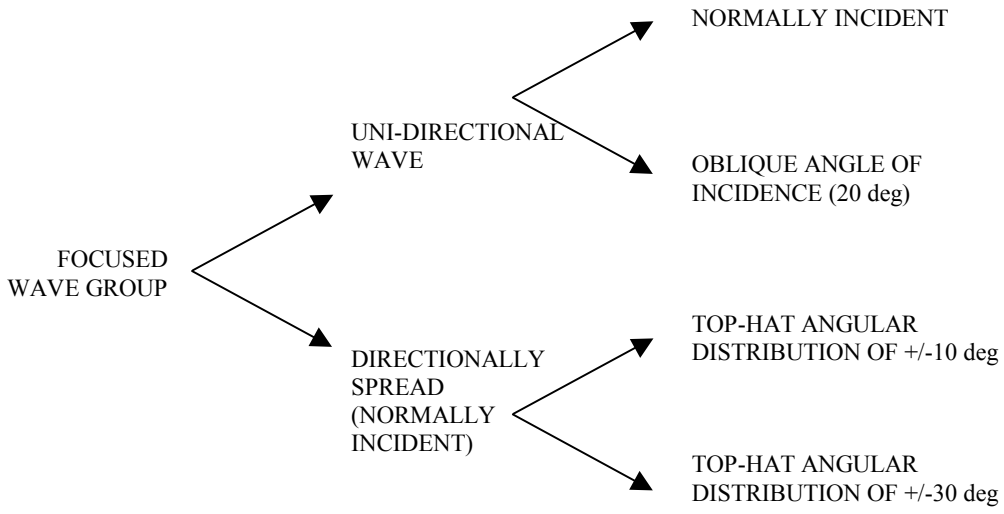

Figure 2.1: Focused wave group categories.

The primary distinction is whether the waves are long or short-crested, i.e. unidirectional

or spread sea. The long-crested waves are subdivided into normally incident and oblique; the short-crested waves have two different ranges of angular distribution - either -10° to +10° or -30° to +30°. For each of the final four categories on the right hand side of Figure 2.1 there are eight associated wave groups: three different focus locations - the toe of the beach, a quarter way up the beach and halfway up the beach, and a fourth wave that is again focused at the toe of the beach but is half the size of the large wave. The other four waves are inverted versions of the original waves.

In generating the focused wave groups for the experimental tests there were three obvious options for the underlying frequency spectrum: top hat spectrum, JONSWAP spectrum or Pierson-Moskowitz (P.M.) spectrum. A top hat spectrum is one in which all the wave component amplitudes are identical. The advantage of the top hat spectrum is that there was already considerable wave generation data available from the calibration phase (which used the top hat spectrum). However, it is not representative of real sea-states.

JONSWAP and P.M. spectra have the forms shown in Eqns (2.1) and (2.2), respectively.

$$S(f) = (f_p/f)^5 \exp^{-\frac{5}{4}(f_p/f)^4} \tag{2.1}$$

$$S(f) = (f_p/f)^5 \exp^{-\frac{5}{4}(f_p/f)^4} \gamma^{\exp^{\frac{-(f-f_p)^2}{2\sigma^2 f_p^2}}} \tag{2.2}$$

where the peak frequency, $f_p = 0.4639$ Hz for these experiments, and the JONSWAP parameters $\sigma = 0.07$ for $f < f_p$ and 0.09 for $f > f_p$ and $\gamma = 3.3$ are selected to be the values commonly used for offshore engineering design. Figure 2.2 shows the top hat, JONSWAP and P.M. spectra for a 100 mm amplitude wave group. Figure 2.3 shows the amplitude spectra corresponding to the signals sent to the paddles which are modified by the paddle transfer functions. The modified spectra are roughly the same shape as their theoretical counterparts, though at lower frequencies they are up to 60% larger.

Figure 2.4 shows the linear predicted surface elevation of a normally incident 100 mm amplitude unidirectional focused wave group generated using the three spectral forms. It can be seen that whilst all the spectra lead to a central 100 mm crest there is great variation in the size of the other crests and troughs. The JONSWAP spectrum produces a wave group with very smooth undulations of considerable size when compared to the groups based upon either a top hat or P.M. spectrum. However, this is only half the story. Figure 2.5 shows

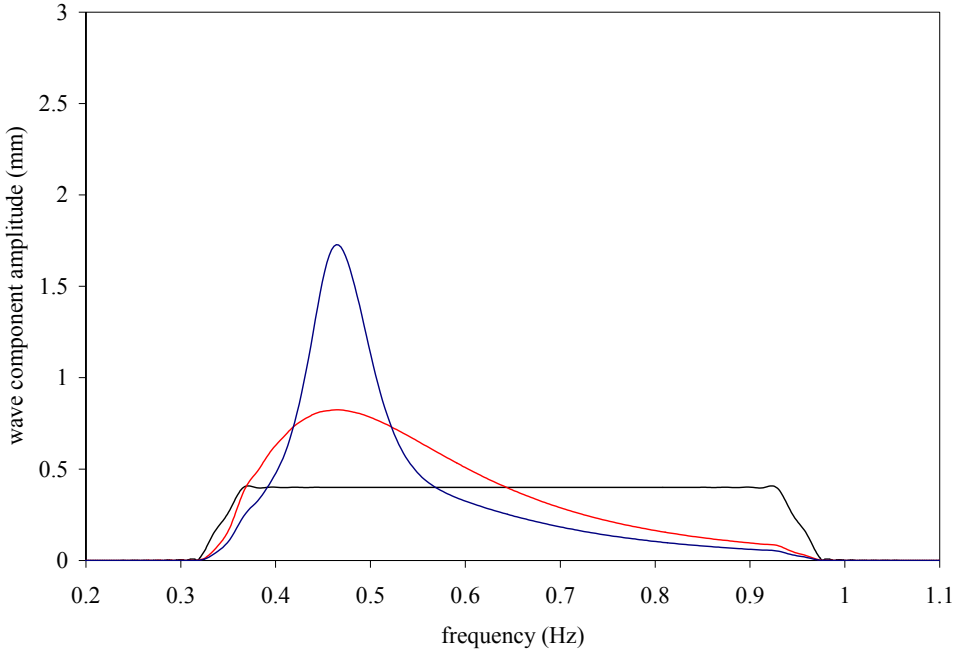

Figure 2.2: Amplitude spectra of 100 mm amplitude focused wave group: — (black), top-hat; — (blue), JONSWAP; — (red), Pierson-Moskowitz.

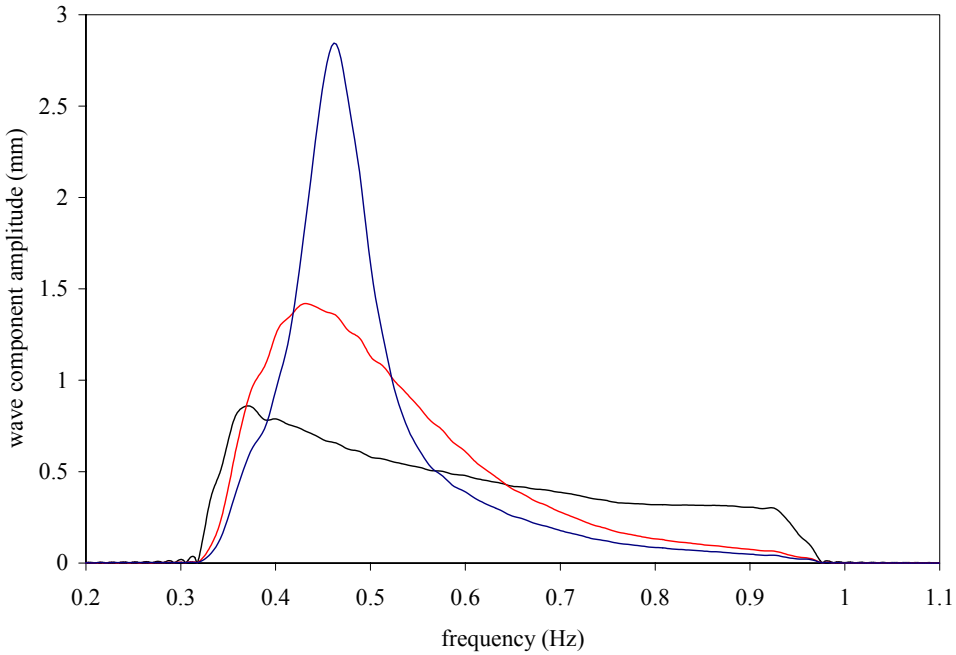

Figure 2.3: Amplitude spectra of paddle signals required to generate a 100 mm amplitude focused wave group: — (black), top-hat; — (blue), JONSWAP; — (red), Pierson-Moskowitz.

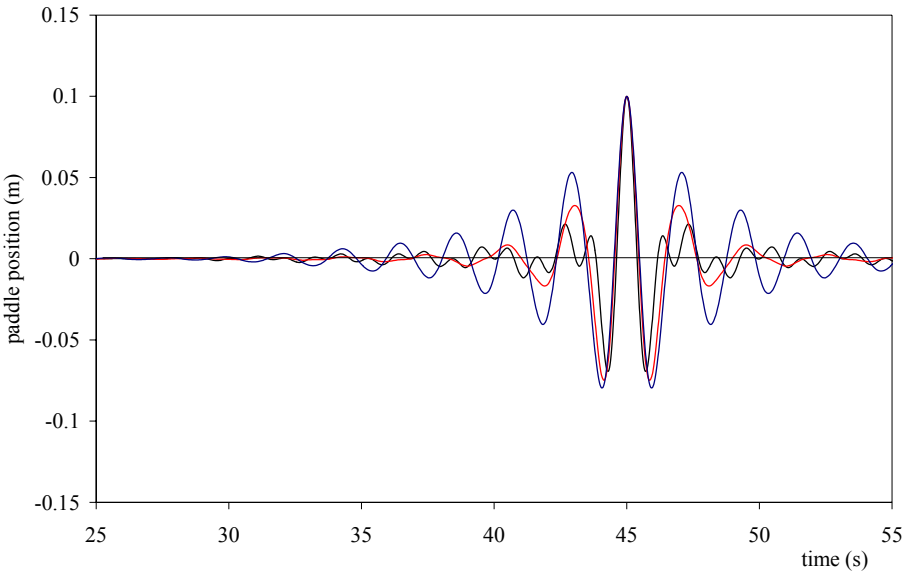

Figure 2.4: Surface elevation time history of a 100 mm amplitude focused wave group obtained using different spectra: — (black), top-hat; — (blue), JONSWAP; — (red), Pierson-Moskowitz.

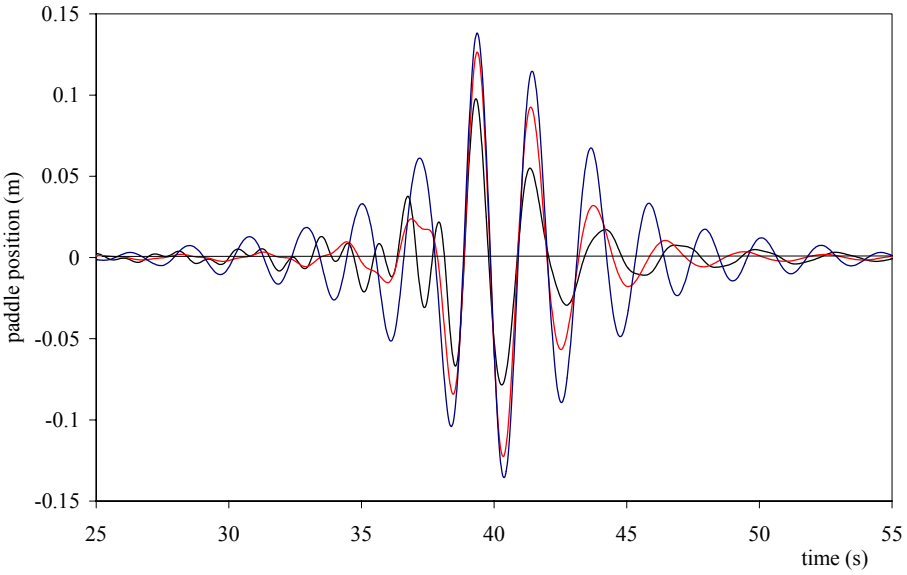

Figure 2.5: Time history of paddle positions required to generate a 100 mm amplitude focused wave group using different spectra: — (black), top-hat; — (blue), JONSWAP; — (red), Pierson-Moskowitz.

the paddle motions necessary to produce the 100 mm waves (with paddle transfer functions incorporated).

The time history of paddle displacements illustrates very clearly which spectrum places greatest demand on the paddles. This is of crucial practical significance, because the paddles appeared to work less well when larger waves were demanded. The broadest spectrum, the top hat, requires the smallest paddle excursions. However, this spectrum is ruled out because it is not a realistic model for natural sea waves. Of the two remaining spectra, the P.M. spectrum was quantifiably better in terms of paddle amplitudes. It was on the basis of these findings that all the focused wave groups generated in this experimental work used an underlying P.M. spectrum.

Since large over-topping was desired, the focused wave groups were designed to be as large as possible before either the wave broke or the paddle amplifiers tripped.[1] The maximum input amplitude is 114 mm for a wave focusing at the toe. Due to non-linear effects, this corresponded to a measured crest of 142.5 mm and trough of 67.7 mm (i.e. a wave height of 210.2 mm) for a unidirectional wave group. This maximum input amplitude of 114 mm was also chosen for the wave focusing at 3/4 depth, but not for the half depth wave, as it broke in the focal depth. The largest input amplitude for half depth (i.e. 250 mm water) was 90 mm, corresponding to a crest of 134 mm, a trough of 54 mm with an overall wave height of 188 mm. The small focused wave had an input amplitude of 57 mm corresponding to a measured crest of 66 mm, a trough of 40 mm and an overall wave height of 106 mm. These input values are summarised in Table 2.1.

Table 2.1: Input amplitudes of focused wave groups.

focus location	η_{in}**(mm)**
toe	114
3/4 depth	114
1/2 depth	90
toe	57

The above wave input amplitudes were used for the normally incident, oblique and spread

[1] This was a tedious problem caused by excessive paddle accelerations, and necessitated time-consuming re-booting of the paddle control system.

sea waves. Additionally, the inverted wave groups had the negative of these values i.e., rather than focused to produce a tall crest, the phase of each component is shifted by 180° to produce a deep trough.

2.2 Embedded wave groups

Due to time constraints it was not possible to generate the length of random wave signals that would be needed to produce meaningful data containing a representative extreme wave. Therefore 'pseudo-random' or embedded wave groups were generated that consisted of a regular wave train with a NewWave embedded in it. This was done because the interaction of a large wave with a structure may depend not only on the details of the large wave but also on the state of the local flow field as the large wave arrives. The use of a regular wave background may crudely provide an estimate of the 'memory' effect of the system state as the large wave arrives. For a regular wave, the standard deviation, σ, is given by $\sigma = A/\sqrt{2}$. For NewWave at a 1 in 1000 wave (typically 3 hour) the linear crest $A_{NW} \simeq 4\sigma = H_s$, therefore the regular wave amplitude was chosen to be $A = \sqrt{2}\sigma = \sqrt{2}H_s/4 = 40.3$ mm. A focused wave group of amplitude 114mm was superimposed on this regular wave train. The zero-crossing frequency may be obtained from the following expression

$$\omega_z^2 = \frac{\int S(\omega)\ \omega^2\ d\omega}{\int S(\omega)\ d\omega} \tag{2.3}$$

where ω is wave frequency (radians) and ω_n is the zero-crossing wave frequency (radians). For the P.M. spectrum used in this thesis this gives a zero-crossing wave *period* of 1.747 sec. Incidentally the peak period of the P.M. spectrum is 2.16 sec, giving a ratio of these two periods of 0.8, which is also the approximate value of the ratio of zero crossing period to peak period in a random sea.

Four different embedded waves were generated: NewWave crest coincident with regular wave crest, NewWave crest coincident with regular wave trough and these two sequences inverted. The process of embedding a focused wave group in another wave train followed the method used by Taylor et al. (1997).

1. η' =regular wave - (regular wave amplitude×Unit NewWave)
2. $\eta'' = \eta'$+ NewWave amplitude×Unit NewWave

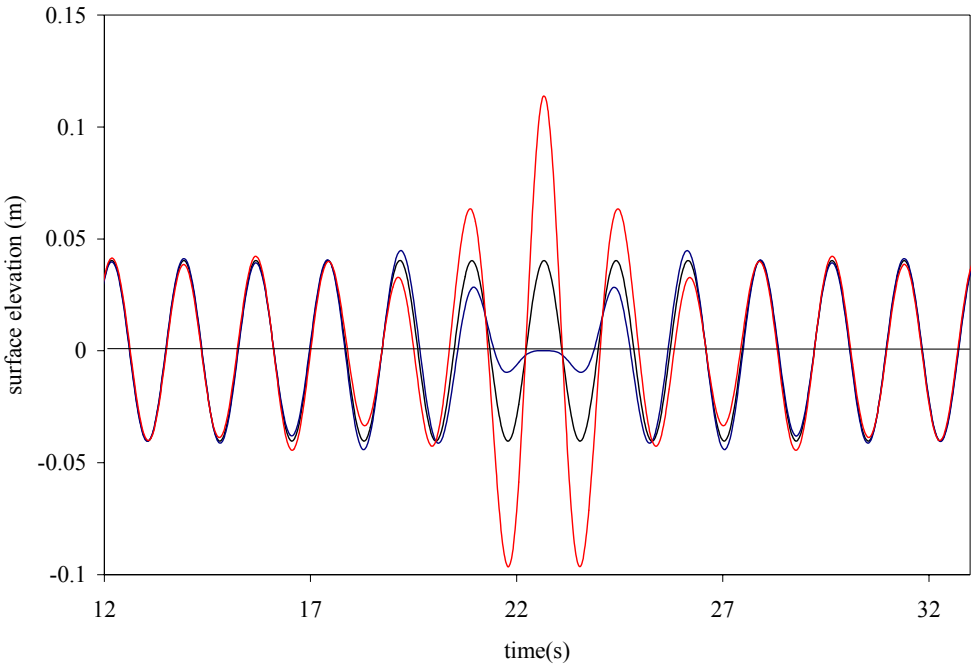

Figure 2.6: Superposition of NewWave onto a regular wave to produce an embedded wave group: — (black), regular wave; — (blue), regular wave minus unit NewWave; — (red), resultant embedded NewWave.

Figure 2.6 shows the surface elevations of the original regular wave and the intermediate and final wave.

2.3 Solitary wave

A 100 mm solitary wave was generated. The maximum size was limited by the paddle acceleration rather than water depth. The paddle signal time history required to generate a solitary wave is given by Hughes (1993), and is as follows. For a piston-type paddle, the surface elevation of a solitary wave at the paddle is given by

$$\eta(x,t) = H\ Sech^2(\kappa(Ct - X_0)) \tag{2.4}$$

in which

$$\kappa = \sqrt{\frac{3H}{4h^3}} \tag{2.5}$$

where H is the wave height and h is the still water depth; C is wave celerity given by

$$C = \sqrt{g(h+H)} \tag{2.6}$$

where g is the acceleration due to gravity; t is time and X_o is the paddle displacement.

The extremes of the paddle displacement are

$$X_o(\pm\infty) = \pm\frac{H}{\kappa h} \tag{2.7}$$

The iterative equation for paddle displacement is

$$X_o^{(i+1)} = X_o^{(i)} - \frac{\left[X_o^{(i)} - \frac{H}{\kappa h}\tanh\kappa(Ct - X_o^{(i)})\right]}{\left[1 + \frac{H}{h}\sec h^2\kappa(Ct - X_o^{(i)})\right]} \tag{2.8}$$

At t=0, Eqn. (2.8) can be solved to yield an initial paddle position of

$$X_o(0) = -\sqrt{\frac{4Hh}{3}} \tag{2.9}$$

The final paddle position is given by

$$X_o(t_f) = +\sqrt{\frac{4Hh}{3}} \tag{2.10}$$

Figure 2.7 shows the paddle displacement time series required to generate a solitary wave of 100 mm amplitude. Firstly, it is necessary to move the paddle from its resting position at $X_o = 0$. The paddle is brought back to the initial position given by Eqn. (2.9). A hyperbolic tangent function is chosen for this paddle motion to minimise basin disturbances. For the same reason, there is a settling period of 100 sec following the paddle movement. The paddle is then pushed rapidly forward using displacement values obtained by solving Eqn. (2.8). After the solitary wave is generated the paddle is brought back to its resting position. These four time periods are illustrated on Figure 2.7 (a), while Figure 2.7 (b) shows greater resolution of the solitary wave generation phase. Due to the length of the paddle signal[2] and the slow variations of the paddle motions, the solitary wave had a paddle update period of 0.05 sec (compared with an update period of 0.01 sec for all the other waves).

[2]Long paddle signals occupy more disk space and take longer to generate.

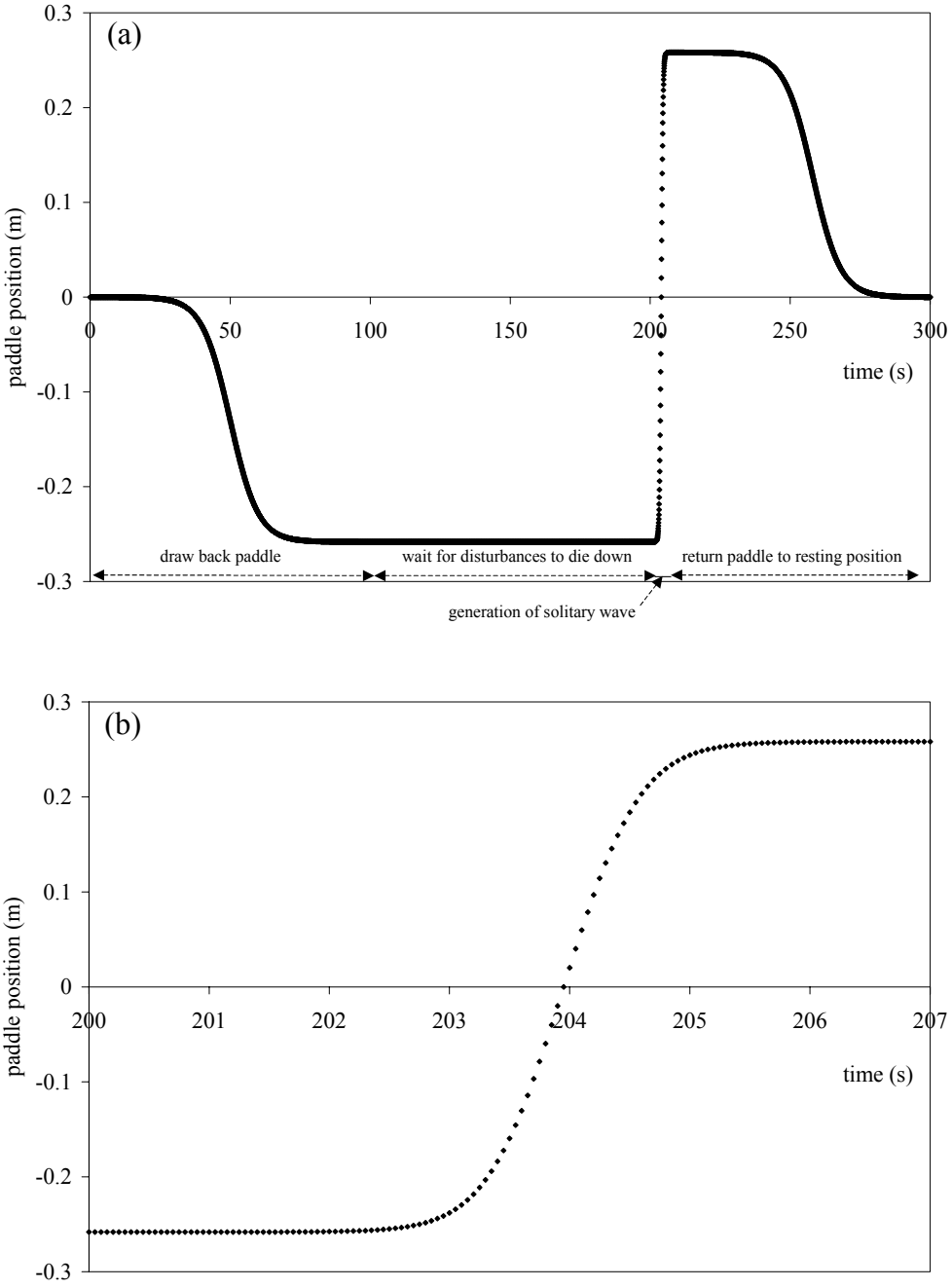

Figure 2.7: Paddle time histories required to generate a 100 mm solitary wave. (a) Entire paddle time series showing paddle moving back from equilibrium, settling for 100 sec, pushing forward and finally moving back. (b) Detail of solitary wave generation.

Chapter 3

Theoretical background

3.1 Focused wave concept

3.1.1 Unidirectional waves

A focused wave is composed of a number of individual wave components that come into phase at a point in time and space. The surface elevation of a focused wave group, based upon linear theory, is given by the following expression

$$\eta(x,t) = \sum_{n=0}^{N} a_n \cos(k_n x - \omega_n t + \phi_n) \tag{3.1}$$

where N is the number of wave components, a_n is the wave amplitude, k_n is the wave number, ω_n is the frequency and ϕ_n is the phase angle of the nth component. In order to generate a focused wave group in the laboratory it is necessary to specify the amplitudes, frequency and phase of the individual wave components that will give a maximum surface elevation at the required focus time and location. The wave number component values are calculated according to the linear dispersion equation

$$\omega_n^2 = g k_n \tanh(k_n d) \tag{3.2}$$

where g is the acceleration due to gravity and d is the water depth. This equation was solved iteratively using the Newton-Raphson method.

Eqn. (3.1) gives the surface elevation, but what is actually required is the paddle position which has a $\pi/2$ phase shift compared with the surface elevation. Therefore, the cosine of

Eqn. (3.1) becomes a minus sine. Also Eqn. (3.1) will need to be evaluated at the paddle position.[1]

The definition of a focus point for the wave system defined by Eqn. (3.1) is that there is a combination of position, time and phase such that all (or most) of the crests of the individual wave components coincide at a point. As the wave group moves away from this focus point, both forwards and backwards in time, the energy becomes distributed over an increasingly large region of water and the surface elevations within this region reduce accordingly.

3.1.2 Oblique unidirectional focused waves

For waves generated at an oblique angle to the paddles, the surface elevation is given by

$$\eta(x,t) = \sum_n a_n \cos(k_n(x\cos\theta + y\sin\theta) - \omega_n t + \phi_n) \tag{3.3}$$

where θ is the generation angle, relative to the x-axis. There are practical limitations to the maximum (and minimum) values of θ that may be chosen for experimental work, governed by the generation of spurious waves from the paddles as discussed by McIver (2001). For a wave period of 0.8 sec in the UKCRF the maximum angle is approximately $\theta = \pm 30°$.

3.1.3 Spread sea focused waves

The representation of a spread sea focused wave group is slightly more complicated. Now it is necessary to allow the value of θ to vary, and to introduce a spreading factor, $b(\theta)$. The relationship is given by

$$\eta(x,t) = \sum_{n=0}^{N} a_n \sum_{m=0}^{M} b_m \cos(k_n(x\cos\theta_m + y\sin\theta_m) - \omega_n t + \phi_n) \tag{3.4}$$

where M is the number of spreading angles and θ_m is the angle of the mth component.

A number of different spreading functions are commonly used. These include Gaussian or wrapped-normal,

$$b(\theta) = \frac{1}{\sqrt{2\pi}\sigma_\theta} \exp^{-\frac{\frac{1}{2}(\theta-\theta_p)^2}{\sigma_\theta^2}} \tag{3.5}$$

[1] This is a simplistic approach since in reality the displacement of the water surface will be modified by depth terms since the water is effectively shallow. Therefore the wave paddles will need to be calibrated. This calibration procedure is explained in Chapter 4.2.

where σ_θ is the variance of the angular distribution and θ_p is the mean wave direction; Cosine-squared,

$$b(\theta) = \begin{cases} \frac{2}{\pi}\cos^2\theta & for \ |\theta| \leq \frac{\pi}{2} \\ 0 & for \ |\theta| > \frac{\pi}{2} \end{cases} \tag{3.6}$$

and Top hat,

$$b(\theta) = c \tag{3.7}$$

where c is a constant.

For all these distributions it is required that

$$\sum_{m=0}^{M} b_m = 1 \tag{3.8}$$

3.2 NewWave concept

NewWave theory demonstrates that in the region of the largest wave crest, the averaged shape of an extreme wave has a profile matching the autocorrelation function of the underlying sea spectrum. The amplitude is given by the statistics of the Rayleigh distribution for the largest wave in N waves. The wave component amplitudes necessary to generate NewWave are given by

$$a_n = A_N S_n(\omega)\Delta\omega_n / \sum_n S_n(\omega)\Delta\omega_n \tag{3.9}$$

where $S_n(\omega)$ is the discretised energy spectrum, $\Delta\omega_n$ is the frequency increment and $A_N = \sqrt{2m_0(\ln(N))}$ where N is the number of waves and m_0 is the first moment of the underlying energy spectrum calculated according to the following expression

$$m_0 = \int_0^\infty S(\omega)d\omega \tag{3.10}$$

3.3 Mathematical basis

3.3.1 Stokes wave

This section briefly summarises the Stokes wave expansions for regular and irregular waves that are used in the analysis of the focused wave group.

Regular waves

Real waves of finite amplitude are not sinusoidal, but have crests that are taller and narrower than the troughs. Real waves can be described by a perturbation expansion, where each additional term provides a correction to the theoretical model. However, the formulation of additional terms is a non-trivial exercise. Fenton's (1990) recent formulation of the Fourier series has superseded the historical perturbation expansions and is relatively simple to apply. The Stokes expansion result up to fifth order given by Fenton (1990), for a regular wave is

$$\eta(x,t) = \frac{1}{k}\sum_{i=1}^{5}\epsilon^i \sum_{j=1}^{i} B_{ij}\cos j(kx-\omega t) \tag{3.11}$$

where η is the free surface elevation above the still water level, x is the horizontal cross-shore distance in the direction of propagation, t is time, k is the wave number, ω is the wave frequency, $\epsilon = ka$ where a is wave amplitude, and B_{ij} are coefficients given by Fenton (1990).

The B_{ij} terms are functions of water depth. For *deep water,* up to third order, $B_{11} = 1$, $B_{22} = 1/2$ and $B_{33} = 3/8$ and the free surface elevation has the form

$$\eta(x,t) = a\cos(\omega t - kx) + \frac{1}{2}a^2 k\cos 2(\omega t - kx) + \frac{3}{8}a^3k^2\cos 3(\omega t - kx) \tag{3.12}$$

The first term in the expansion is the linear term - a simple sinusoidal wave. The frequency and wave number of this term obey the linear dispersion relation, given by

$$\omega^2 = kd\tanh(kd) \tag{3.13}$$

where d is the water depth. The second term in Eqn. (3.12) is the second order correction. It has a frequency that is double that of the linear term. The frequency (2ω) and wave number $(2k)$ pair of this term do *not* obey the dispersion relation. This wave travels at the same speed as the linear term and is described as a *bound* wave, in contrast to the linear term which is called a *free* wave. The final term in the expansion is the third order correction. The frequency is now three times that of the linear wave. Like the second order term it is a *bound* wave that travels with the linear wave, and it also has a frequency and wave number combination that do not satisfy the linear dispersion relation.

For *finite water depth*, the coefficients B_{ij} are much more complicated. To *second* order, the expansion[2] has $B_{11} = 1$ and $B_{22} = \coth kh(1+2S)/(2(1-S))$, where S =sech$(2kh)$,

[2]It would be possible to provide the *third* order expansion to be consistent with Eqn. (3.12), but the term is very complicated and it is not required for the following analysis.

leading to

$$\eta(x,t) = a\cos\psi + \frac{a^2k}{4}\frac{\cosh(kh)}{\sinh^3(kh)}\left(2+\cosh(2kh)\right)\cos 2\psi \tag{3.14}$$

where $\psi = \omega t - kx$. As for Eqn. (3.12), the first term is the linear, free wave. The second term has a more complicated coefficient, but is still a second order correction to the linear wave. It is a bound wave of double the linear wave frequency.

Combination of regular wave trains

Linear theory gives a surface elevation of

$$\eta(x,t) = \sum_{n=1}^{N} a_n \cos\psi_n \tag{3.15}$$

where N is the number of waves. For two waves

$$\eta(x,t) = a_1\cos\psi_1 + a_2\cos\psi_2 \tag{3.16}$$

A second order Stokes expansion, for *deep water* is given by Baldock (1995)[3]

$$\eta(x,t) = \sum_{n=1}^{N}\eta_{(n)} + \sum_{n=1}^{N}\sum_{m=n+1}^{N}\eta_{(n,m)} \tag{3.17}$$

where $\eta_{(n)}$ is the second-order Stokes solution for the nth wave component and $\eta_{(n,m)}$ is the second-order interaction between the nth and mth components of the wave group. For the simplest case of two waves in *deep water*

$$\begin{aligned}
\eta(x,t) &= \sum_{n=1}^{2}\eta_{(n)} + \sum_{n=1}^{2}\sum_{m=n+1}^{2}\eta_{(n,m)} && (3.18)\\
&= \eta_{(1)} + \eta_{(2)} + \eta_{(1,2)} \\
&= a_1\cos\left(\omega_1 t - k_1 x\right) + \frac{1}{2}a_1^2 k_1 \cos 2\left(\omega_1 t - k_1 x\right) \\
&\quad + a_2\cos\left(\omega_2 t - k_2 x\right) + \frac{1}{2}a_2^2 k_2 \cos 2\left(\omega_2 t - k_2 x\right) \\
&\quad + \frac{1}{2}a_1 a_2\left(k_1+k_2\right)\cos\left(\left(\omega_1+\omega_2\right)t - \left(k_1+k_2\right)x\right) \\
&\quad - \frac{1}{2}a_1 a_2\left(k_1-k_2\right)\cos\left(\left(\omega_1-\omega_2\right)t - \left(k_1-k_2\right)x\right) && (3.19)
\end{aligned}$$

The individual terms can be described as follows:

$a_1\cos\cos\left(\omega_1 t - k_1 x\right) + a_2\cos\left(\omega_2 t - k_2 x\right)$ are free waves which provide the linear contribution, each satisfying the dispersion relation;

[3] This draws upon much earlier work by Longuet-Higgins and Stewart (1960).

$\frac{1}{2}a_1^2 k_1 \cos 2\left(\omega_1 t - k_1 x\right) + \frac{1}{2}a_2^2 k_2 \cos 2\left(\omega_2 t - k_2 x\right)$ give a second order contribution for each individual wave (these are bound waves that have double the frequency of the respective linear terms and do not satisfy the dispersion relation);

$\frac{1}{2}a_1 a_2 \left(k_1 + k_2\right) \cos((\omega_1 + \omega_2)\, t - (k_1 + k_2)\, x)$ is an additional *high* frequency second order harmonic describing wave-wave interactions, and is a bound wave, not satisfying the dispersion relation; and

$\frac{1}{2}a_1 a_2 \left(k_1 - k_2\right) \cos\left((\omega_1 - \omega_2)\, t - (k_1 - k_2)\, x\right)$ is an additional *low* frequency second order harmonic describing wave-wave interactions, and is also a bound wave not satisfying the dispersion relation.

The more complicated version of second order Stokes expansion for the case of two waves in water of *finite depth* is

$$\begin{aligned}
\eta(x,t) &= \sum_{n=1}^{2} \eta_{(n)} + \sum_{n=1}^{2} \sum_{m=n+1}^{2} \eta_{(n,m)} \\
&= \eta_{(1)} + \eta_{(2)} + \eta_{(1,2)} \\
&= a_1 \cos\psi_1 + \frac{a_1^2 k_1}{4} \frac{\cosh(k_1 h)}{\sinh^3(k_1 h)} \left(2 + \cosh(2k_1 h)\right) \cos 2\psi_1 \\
&\quad + a_2 \cos\psi_2 + \frac{a_2^2 k_2}{4} \frac{\cosh(k_2 h)}{\sinh^3(k_2 h)} \left(2 + \cosh(2k_2 h)\right) \cos 2\psi_2 \\
&\quad + \frac{a_1 a_2}{2g} \left[C \cos\left(\psi_1 - \psi_2\right) - D \cos\left(\psi_1 + \psi_2\right)\right]
\end{aligned} \tag{3.20}$$

where C and D are coefficients given in Appendix B. The terms of Eqn. (3.20) make similar contributions as for the deep water case of Eqn. (3.18).

3.3.2 Isolation of harmonics

By the judicious addition and subtraction of the original wave group and its inverted form (i.e. all linear wave component amplitudes are negative) it is possible to isolate the harmonics that comprise the nonlinear group. This enables the investigation of a variety of phenomena.

Consider a wave 'group' consisting of two individual wave components. The appropriate free surface elevation equation for deep water (Eqn. (3.18)) is duplicated below

$$\begin{aligned}
\eta_c &= a_1 \cos\psi_1 + \frac{1}{2}a_1^2 k_1 \cos\left(2\psi_1\right) \\
&\quad + a_2 \cos\psi_2 + \frac{1}{2}a_2^2 k_2 \cos\left(2\psi_2\right) \\
&\quad + \frac{1}{2}\left(a_1 a_2 \left[\left(k_1 + k_2\right) \cos\left(\psi_1 + \psi_2\right) - \left(k_1 - k_2\right) \cos\left(\psi_1 - \psi_2\right)\right]\right)
\end{aligned} \tag{3.21}$$

Here, the subscript c indicates crest focus.

If the same two waves are used again, but are inverted, i.e. a trough focus, the following surface elevation is obtained

$$\begin{aligned}\eta_t &= -a_1\cos\psi_1 + \frac{1}{2}a_1^2k_1\cos(2\psi_1) \\ &\quad -a_2\cos\psi_2 + \frac{1}{2}a_2^2k_2\cos(2\psi_2) \\ &\quad +\frac{1}{2}\left(a_1a_2\left[(k_1+k_2)\cos(\psi_1+\psi_2) - (k_1-k_2)\cos(\psi_1-\psi_2)\right]\right)\end{aligned} \tag{3.22}$$

The subscript t indicates trough focus.

Notice that the linear contributions are inverted, but the second order terms are not, since the amplitude terms are products of pairs of linear terms and any sign changes of the linear terms are lost. Two mathematical combinations of the wave groups are useful

$$\begin{aligned}\eta_{addn} &= (\eta_c+\eta_t)/2 \\ &= \frac{1}{2}a_1^2k_1\cos(2\psi_1) + \frac{1}{2}a_2^2k_2\cos(2\psi_2) \\ &\quad +\frac{1}{2}\left(a_1a_2\left[(k_1+k_2)\cos(\psi_1+\psi_2) - (k_1-k_2)\cos(\psi_1-\psi_2)\right]\right)\end{aligned} \tag{3.23}$$

$$\begin{aligned}\eta_{subn} &= (\eta_c-\eta_t)/2 \\ &= a_1\cos\psi_1 + a_2\cos\psi_2\end{aligned} \tag{3.24}$$

It is evident that the addition terms contain only second order harmonics, whilst the subtraction terms contain the linear contributions. Actually, this can be extended for higher orders so that '*addition' terms contain all even harmonics* and *'subtraction' terms contain odd harmonics*. This result is elegant in its simplicity but is very powerful. It is one motivation behind generating focused wave groups and corresponding inverted groups. The method allows complete extraction of components with no noise/band overlaps. It should be noted that it is vital to produce wave groups in a well calibrated facility so that the accuracy of the phase inversion is assured.

3.3.3 Parasitic free waves

When waves are generated at the paddles, all but the very smallest will contain nonlinearities. However, the paddle positions sent to the paddles were based upon linear theory, with no

higher order corrections. Therefore, at the paddle, an instantaneous compensation occurred between the actual non-linear wave generated and the desired linear wave, in the form of extra components. These components produce a 'free' wave. The term 'free' indicates that these waves are not bound to the wave group and their motion in the basin is governed by linear dispersion. Since free waves are generally not desirable they are often termed 'parasitic' or 'error' waves. The largest error waves that are generated have the same second order high and low frequencies as the second order bound Stokes terms, but different wave numbers.

Table 3.1: Pairs of bound and parasitic waves due to linear paddle signals.

Bound waves	Parasitic free waves
$+\frac{1}{2}a_1^2 k_1 \cos 2\left(\omega_1 t - k_1 x\right)$	$-\frac{1}{2}a_1^2 k_1 \cos 2\left(\omega_1 t - k_1' x\right)$
$+\frac{1}{2}a_2^2 k_2 \cos 2\left(\omega_2 t - k_2 x\right)$	$-\frac{1}{2}a_2^2 k_2 \cos 2\left(\omega_2 t - k_2' x\right)$
$+\frac{1}{2}a_1 a_2 \left(k_1 + k_2\right) \cos((\omega_1 + \omega_2)\, t - (k_1 + k_2)\, x)$	$-\frac{1}{2}a_1 a_2 \left(k_1 + k_2\right) \cos((\omega_1 + \omega_2)\, t - k_{12}' x)$
$-\frac{1}{2}a_1 a_2 \left(k_1 - k_2\right) \cos\left((\omega_1 - \omega_2)\, t - (k_1 - k_2)\, x\right)$	$+\frac{1}{2}a_1 a_2 \left(k_1 - k_2\right) \cos\left((\omega_1 - \omega_2)\, t - k_{12}'' x\right)$

The wave numbers k_{12}' and k_{12}'' can be obtained using linear dispersion. These pairs of waves cancel each other out at the paddle, but nowhere else in the basin, where they will travel at different speeds to their respective bound wave originator.

The first three parasitic waves in Table 3.1 are high frequency terms that travel more slowly than the linear free wave. The action of these waves will therefore not interfere with the transformation of the focused group. However, the fourth parasitic wave in Table 3.1 is a low frequency wave that travels faster than the linear term and will therefore need to be taken account of when analysing the results. The low frequency bound wave is called the set-down term as it describes the lowering of the water surface under the wave group. The corresponding parasitic wave is of opposite sign and is therefore an elevation of the water surface. Since this wave travels faster than the main group it will be evident as a hump of water leading the wave group.

The parasitic waves are insensitive to the phase of the focused wave since they are a second order phenomenon, e.g. a trough focus wave with the same amplitude but opposite sign of input amplitude to a crest focus wave will still have a leading hump due to the low frequency parasitic wave.

Of course parasitic waves accompany all bound waves that are generated at the paddle, including the higher order harmonics. Since the magnitude of the bound waves reduce substantially for each correction term, so too will the parasitic wave, therefore it is of reduced significance at higher orders.

It is possible, but of little benefit, to produce similar pairings of bound and parasitic waves for shallow water. They will be qualitatively identical to those of Table 3.1, but with more complicated coefficients.

Parasitic waves affect the isolation of harmonics that was demonstrated for deep water in Section 3.3.2. It was noted that η_{addn} contained *even* harmonics. This will include all four *even*[4] parasitic terms shown above. The η_{subn} terms contain *odd* harmonics, i.e. the largest parasitic wave will be of third order.

Although the details of what occurs at the paddles is actually more complicated than this discussion suggests, due to local evanescent components close to the paddle, these do not propagate across the basin to the beach. Thus, the evanescent modes need not be considered further.

3.4 Separation of harmonics example

3.4.1 Time series and amplitude spectra

Figures 3.1 and 3.2 show the surface elevations and corresponding amplitude spectra[5] at four positions in the basin, for wave group 1 (WG1) and wave group 5 (WG5), which are respectively the crest focused and trough focused groups with an input amplitude of 114 mm and a focus location at the toe of the beach. More details of these groups are given in Appendix A. Figure 3.3 shows the locations of these four measurement gauges.

Looking first at the surface elevation time histories, on the left of Figure 3.1, the crest focused wave is clearly visible. At the focus location, B, the wave is clearly focused, i.e. the

[4] The analysis of parasitic waves has been carried out to second order, but it could be extended to include higher harmonics.

[5] Amplitude spectra are deduced from the surface elevation time histories using a Fourier transform

$$X(k) = \sum_{n=1}^{N} x(n) e^{(-2j\pi(k-1)(n-1)/N)}, 1 \leq k \leq N$$

where x is the input data of length N.

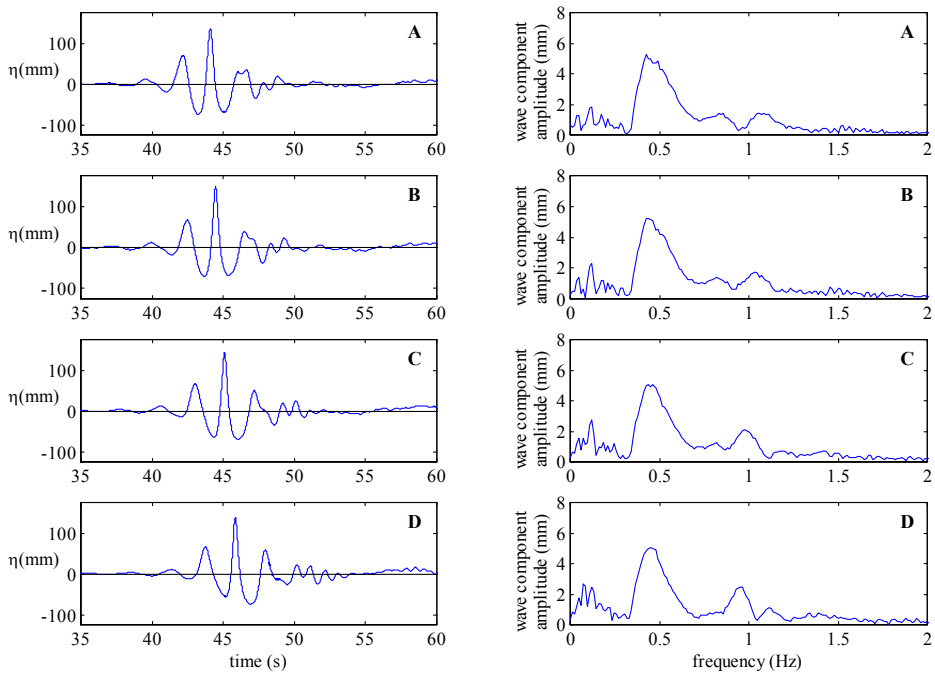

Figure 3.1: Surface elevation time histories and amplitude spectra of a crest focused wave group, at locations A, B, C and D in the basin.

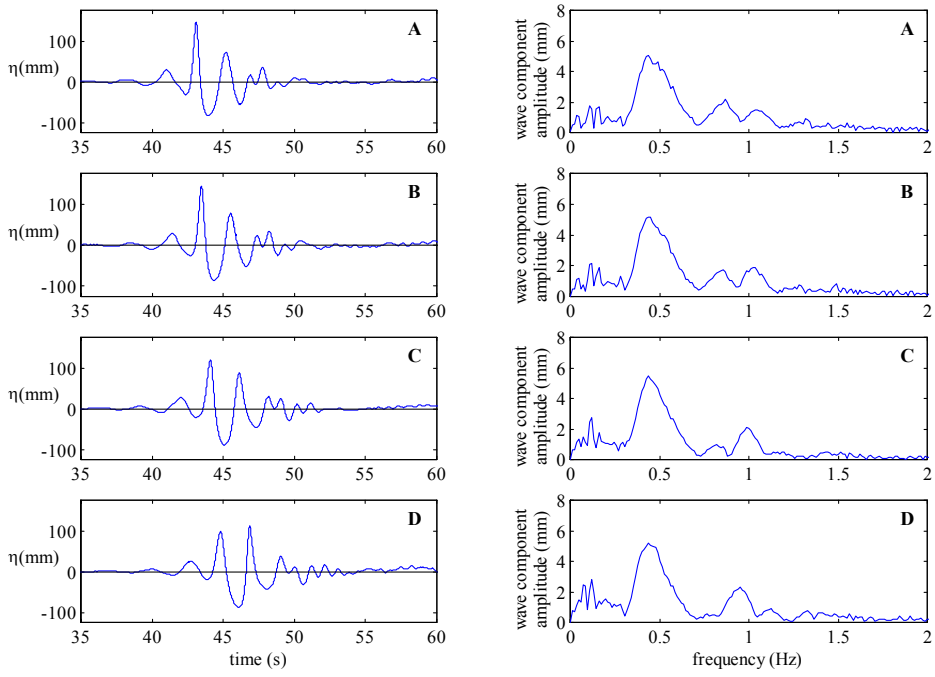

Figure 3.2: Surface elevation time histories and amplitude spectra of a trough focused wave group, at locations A, B, C and D in the basin.

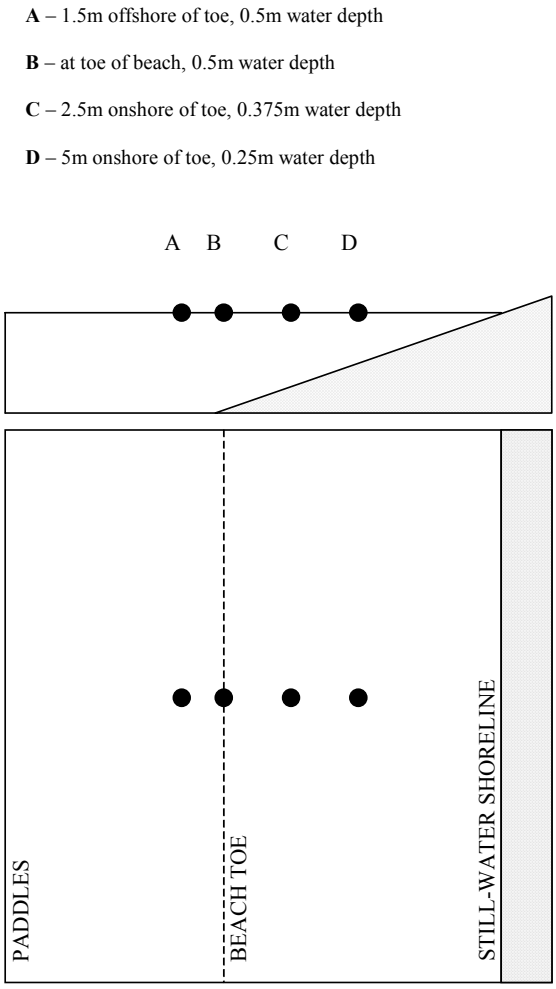

Figure 3.3: Location of four key measurement positions.

size of the troughs either side of the central crest are the same amplitude. Location A, which is 1.5 m offshore of the toe of the beach shows the wave nearly in focus, but with the trough to the left of the central crest slightly larger than the trough to the right. At locations C and D the trough to the right of the central crest becomes larger than the trough on the left hand side. The crests of the waves become increasingly steep in shallow water. This is particularly noticeable at location D, where the rise of the wave crest that peaks at about 46 secs is nearly vertical. This wave has a height of nearly 200 mm in a water depth of about 250 mm and is evidently very close to breaking. There is evidence at all four locations of high frequency waves following the wave group and also signs of a low frequency wave to the right of the group[6].

[6]The low frequency wave evident in these plots is actually a reflected wave and not part of the original

The amplitude spectra in Figure 3.1 each contain a significant peak centred at about 0.5 Hz. This is the peak of the linear group input. The size of the peak reduces slightly as the wave travels into shallower water. There are other peaks at around half the linear peak frequency and double the peak frequency. The size of these nonlinear peaks increase in shallow water[7].

Figure 3.2 shows time histories and amplitude spectra for trough focused wave groups and has very similar characteristics to those seen in Figure 3.1. One point of note though is that the wave group at the focus location does not look particularly well focused, i.e. the *crests* either side of the central trough are not the same amplitude as each other. The reason for this is that although the crest focused wave of Figure 3.1 looks well focused at location B, it is actually distorted by the low frequency error wave. The trough focused wave is generated using the inverted paddle signals of the crest focused wave which will therefore have a focus location that is some way off where it should be.

Figures 3.4 and 3.5 show the result of carrying out the addition and subtraction operations, detailed in Section 3.3.2.

There are several points to note:

- The amplitude spectra of the composite 'addition' signal of Figure 3.4 have one low frequency peak at about 0.2 Hz and then more peaks at around 1 Hz. There are possibly two peaks at this higher frequency, which vary in size according to water depth (and hence proximity to focus). These spectra should contain only even harmonics.

- The 'subtraction' amplitude spectra of Figure 3.5 are dominated by the linear group which has a peak at around 0.5 Hz. There is evidence of a third order harmonic at around 1.5 Hz. There is also a small low frequency peak at around 0.2 Hz. These are the odd harmonics.

- The shape of the 'subtraction' wave group begins to degrade beyond position C at 0.375 m. It can be seen that the second trough which occurs at 47 sec becomes *spiky*. This effect is even worse at position D in 0.25 m depth of water. The reason for this is that

group.

[7] The decrease in the size of the linear peak does not balance the increase in size at other frequencies because (i). the time signals that these amplitude spectra are derived from also include reflections from the beach at later times and (ii). energy is conserved, not wave component amplitude.

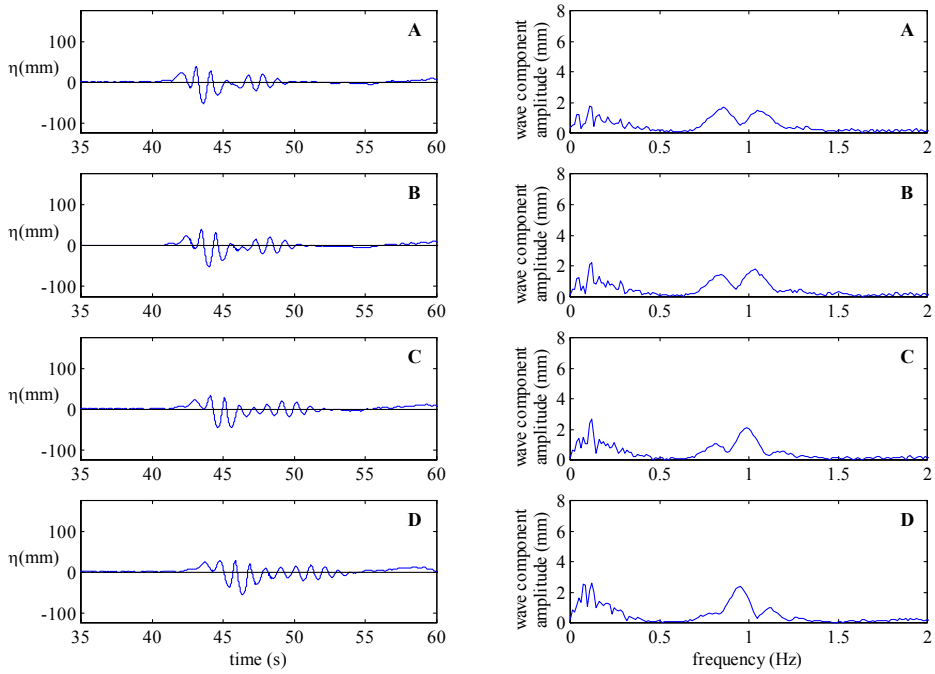

Figure 3.4: Surface elevation time histories and amplitude spectra of 'addition' terms, at locations A, B, C and D in the basin.

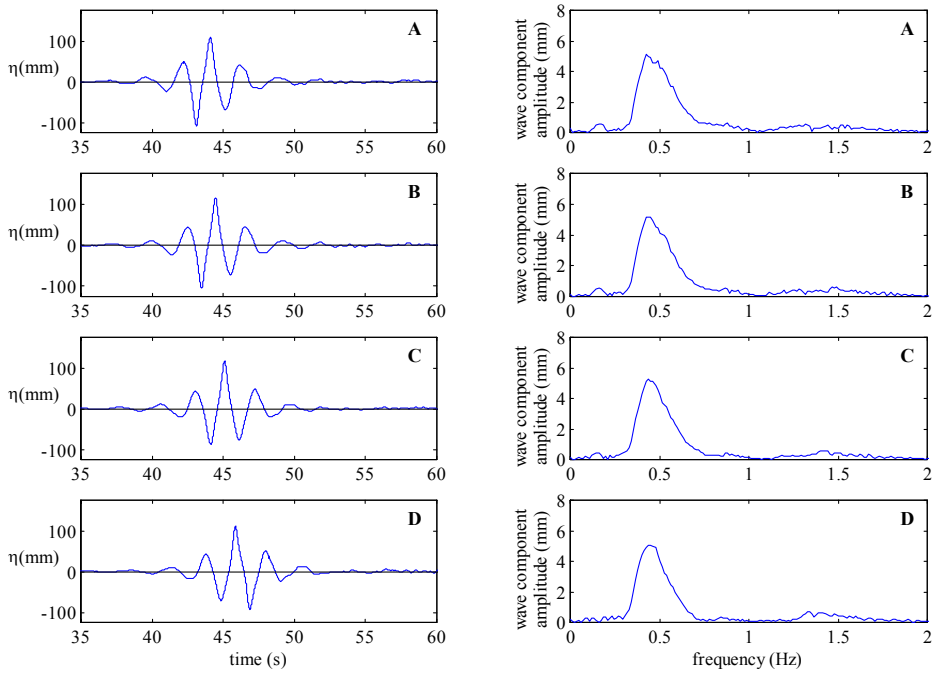

Figure 3.5: Surface elevation time histories and amplitude spectra of 'subtraction' terms, at locations A, B, C and D in the basin.

the crests and troughs begin to behave differently: crests move faster then troughs in very shallow water, so the addition and subtraction of original and inverted groups no longer produces a meaningful wave form. However, this loss of alignment in very shallow water does not matter for the release of low frequency waves which are of considerable importance. The loss of alignment is a sign of triad interactions where energy is lost from the linear group to bound harmonics.

- It can be seen from the 'subtraction' spectra that the relative sizes of the 1st order (linear) peak at 0.5 Hz and the 3rd order peak at around 1.5 Hz change slightly as the wave group moves into shallow water. It would seem that the linear group gives up energy to higher order harmonics.

Evidence for bound and parasitic waves can be obtained by filtering the time signal for either low frequency or high frequency information. In practice this is achieved by choosing a cut-off point in the amplitude spectrum. For example, the amplitude spectrum of Figure 3.4 which shows addition terms (even harmonics) has a reduction in size down to zero at 0.5 Hz, at each of the four gauge positions. This therefore makes a convenient cut-off point. The peak of the linear spectrum is at 0.464 Hz, therefore, the second order low frequency terms would be expected at around 0.23 Hz, and second order high frequency terms at around 0.92 Hz, i.e. a safe distance from the cut-off point. An inverse Fourier Transform is carried out on the truncated amplitude spectra to regenerate the filtered time series. Figures 3.6 and 3.7 are obtained from 0.5 Hz low-pass and high-pass filtered 'addition' terms, respectively.

It is evident particularly from the surface elevation plot closest to the paddle in Figure 3.7 that there are two distinct wave groups. The group that peaks at around 48 sec is the error wave which travels more slowly than the main wave group. It is responsible for the wiggles following the crest focus and trough focus in Figures 3.1 and 3.2. Since the wave travels more slowly than the bound high frequency second order harmonics of the main group it does not interfere with the focusing event. However, looking now at the low frequency wave in Figure 3.6 it can be seen that the error wave *precedes* the bound wave (the low frequency bound wave is the trough-like set-down term).

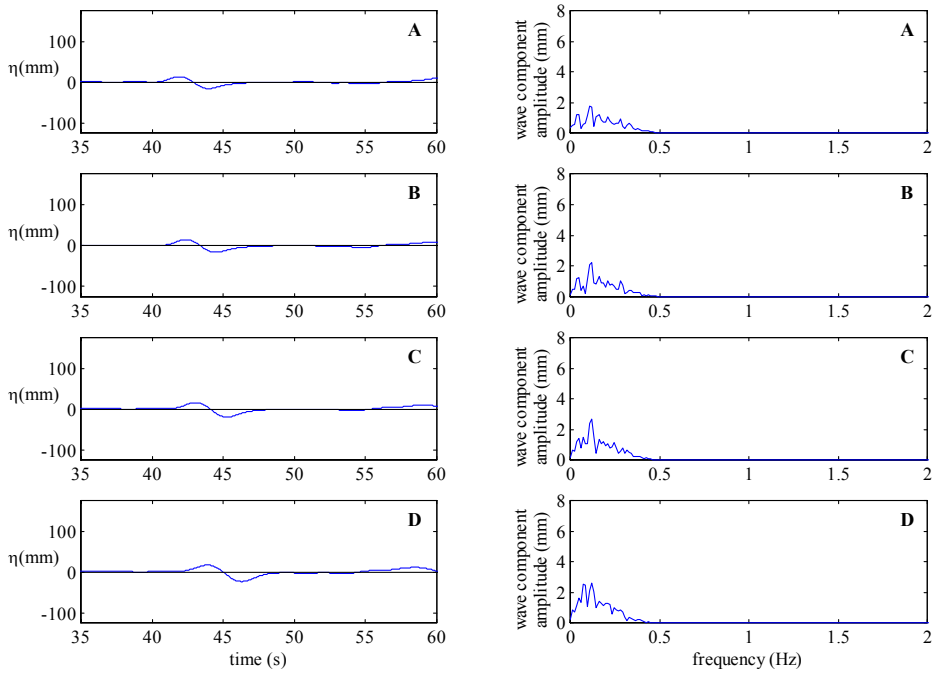

Figure 3.6: Surface elevation time histories and amplitude spectra of 'addition' terms low frequency band-pass filtered at 0.5 Hz, measured at locations A, B, C and D in the basin.

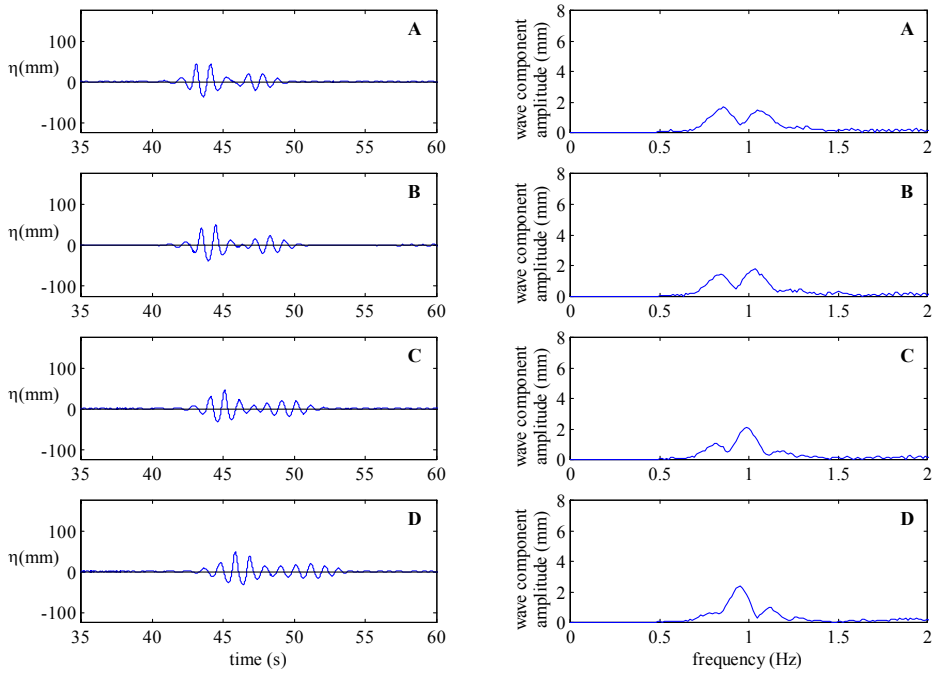

Figure 3.7: Surface elevation time histories and amplitude spectra of 'addition' terms high frequency band-pass filtered at 0.5 Hz, measured at locations A, B, C and D in the basin.

Stokes-like expansion and bound wave structure

It may be possible to compare harmonics obtained by manipulation of the experimental data, with those predicted using a Stokes-like expansion. The harmonics are deduced by carrying out simple addition and subtraction calculations outlined in the previous section, along with some filtering of the frequency spectrum. A Stokes like expansion is proposed as follows.

A wave group is an irregular record that can be described thus

$$\eta_L(x,t) = \sum_n a_n \cos(k_n x - \omega_n t + \phi_n) \tag{3.25}$$

where the subscript L denotes a *linear* signal and ϕ_n a phase angle. The action of a Hilbert transform on the wave group produces the following expression

$$\eta_{LH}(x,t) = \sum_n a_n \sin(k_n x - \omega_n t + \phi_n) \tag{3.26}$$

i.e. the Hilbert transformed wave group is phase shifted by 90° and contains the same amplitudes, as the non-transformed group. The envelope of the wave group can be defined in terms of the original group and its Hilbert transform thus

$$E = \sqrt{\eta_L^2 + \eta_{LH}^2} = A(t) \tag{3.27}$$

Assume

$$\eta_L(x,t) = \sum_n a_n \cos(k_n x - \omega_n t + \phi_n) = A(t)\cos(\overline{k}x - \overline{\omega}t + \phi_n) \tag{3.28}$$

and

$$\eta_{LH}(x,t) = \sum_n a_n \sin(k_n x - \omega_n t + \phi_n) = A(t)\sin(\overline{k}x - \overline{\omega}t + \phi_n) \tag{3.29}$$

where $\overline{k}$ is the average wave number and $\overline{\omega}$ the average wave frequency, based upon the linearized spectrum.

This Stokes like expansion treats the wave system as locally regular, whereas the general second order expansion does not. Therefore it is an *approximation.*

Second Order term, $\eta_{(2)}$ A second order Stokes-like correction based upon the Stokes expansion of Eqn. (3.11) is

$$\begin{aligned} A(t)^2 \cos 2(\overline{k}x - \overline{\omega}t + \phi_n) &= A(t)^2 \left[\cos^2(\overline{k}x - \overline{\omega}t + \phi_n) - \sin^2(\overline{k}x - \overline{\omega}t + \phi_n)\right] \\ &= \eta_L^2 - \eta_{LH}^2 \end{aligned}$$

Therefore the second order term is:

$$\eta_{(2)} \simeq B_{22}\overline{k}(\eta_L^2 - \eta_{LH}^2) \tag{3.30}$$

This description is applicable to the first three second order bound waves listed in Table 3.1.

A method for incorporating a low frequency, set-down term in a similar manner is still under investigation.

Reproduction of error waves from linear signal

It is possible to use the linearised signal to generate estimates for the second order sum bound wave and error waves as follows.

Calculation of second order bound waves:

(i). Carry out 'difference' procedure.

(ii). Remove high and low frequency part of spectrum leaving only input frequency range.

(iii). Calculate amplitude (a_n) and phase (ψ_n) components from the linearised spectrum.

(iv). Use a_n and ψ_n to calculate the linear signal, η_L, at the toe using Eqn. (3.25).

(v). Use a_n and ψ_n to calculate the Hilbert transform of the linear signal, η_{LH}, at the toe using Eqn. (3.26).

(vi). Use η_L and η_{LH} in Eqn. (3.30) to estimate the bound wave at the toe of the beach.

Calculation of second order parasitic waves:

Steps (i) to (iii) as before.

(iv). Use a_n and ψ_n to calculate the *negative* of the linear signal, $-\eta_L$, at the *paddle* using Eqn. (3.25) with a minus sign.

(v). Use a_n and ψ_n to calculate the *negative* Hilbert transform of the linear signal, $-\eta_{LH}$, at the *paddle* using Eqn. (3.26) with a minus sign.

(vi). Use $-\eta_L$ and $-\eta_{LH}$ in Eqn. (3.30) to calculate the error wave at the paddle.

(vii). Calculate amplitude (a_n) and phase (ψ_n) components from the spectrum of the error wave at the paddle.

(viii). Use a_n and ψ_n to calculate the error wave at the paddle using Eqn. (3.25) and then use linear dispersion to allow these waves to move to the toe.

Figures 3.8 and 3.9 show the results of this procedure, both in the time and frequency domain. It can be seen that there is very good agreement between the experimental results

and the results obtained using the Stokes-like expansion for both the locally bound waves and the error wave system over a frequency range covering both the linear and second-order sum terms.

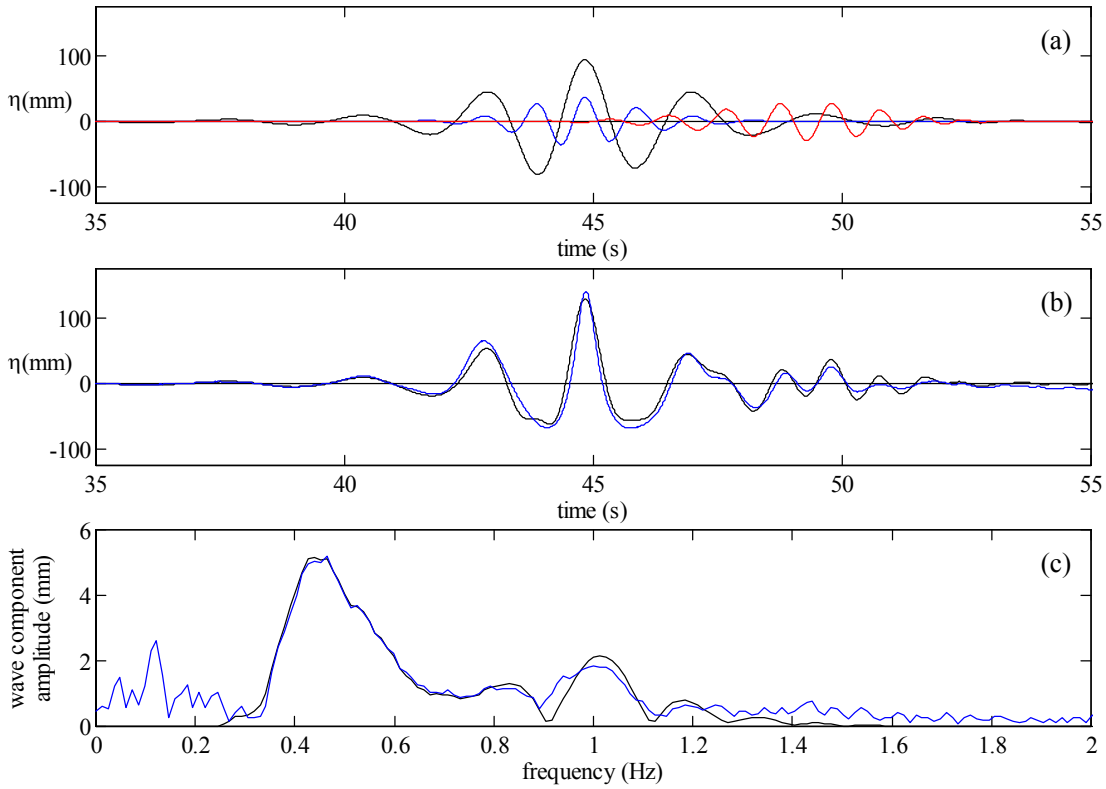

Figure 3.8: Crest focused wave group (a) time series of individual components: (black) —, linearised signal obtained from low band-pass filtered 'subtraction' time series; (blue) - - -, theoretically derived local B22 correction; and (red) $\cdots$, theoretically derived high frequency paddle error wave (b) comparison of experimental and theoretical time series: (black) —, experimental data; (blue) - - -, sum of the three theoretically derived components (c) comparison of experimental and theoretical amplitude spectra: (black) —, experimental data; (blue) - - -, sum of the three theoretically derived components.

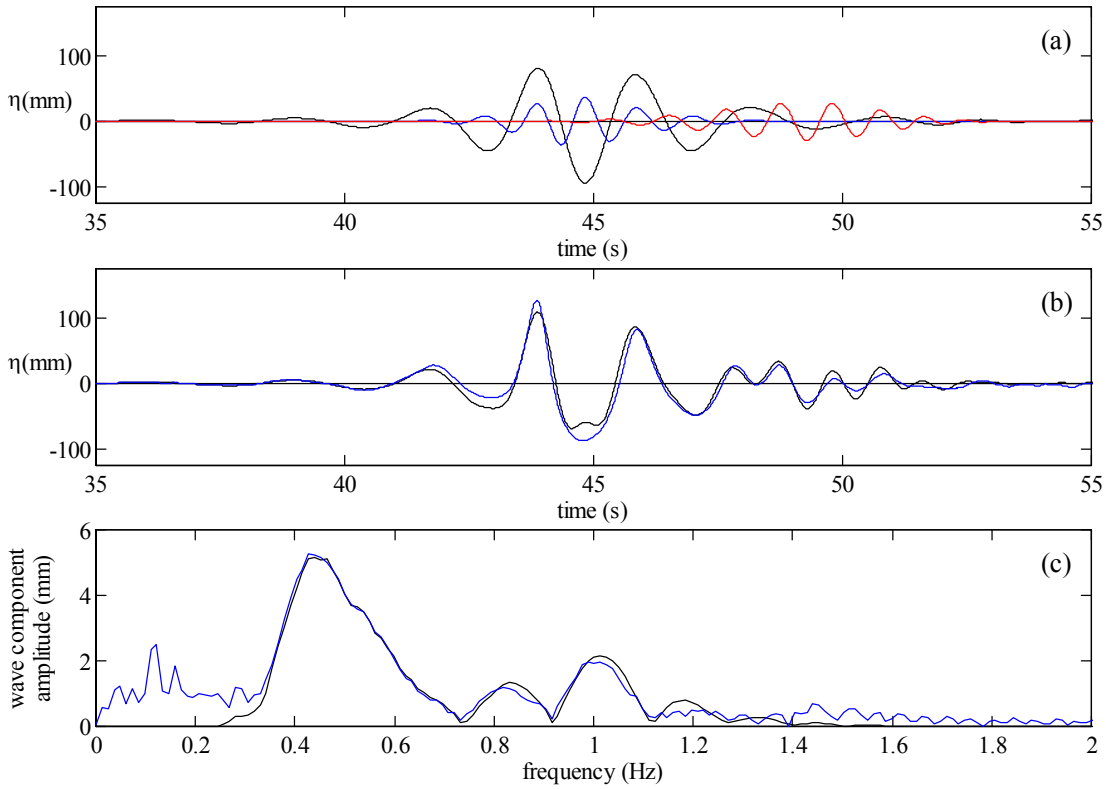

Figure 3.9: Trough focused wave group (a) time series of individual components: (black) —, linearised signal obtained from low band-pass filtered 'subtraction' time series; (blue) - - -, theoretically derived local B22 correction; and (red) $\cdots$, theoretically derived high frequency paddle error wave (b) comparison of experimental and theoretical time series: (black) —, experimental data; (blue) - - -, sum of the three theoretically derived components (c) comparison of experimental and theoretical amplitude spectra: (black) —, experimental data; (blue) - - -, sum of the three theoretically derived components.

Chapter 4

Experimental Arrangement

4.1 U.K. Coastal Research Facility (UKCRF)

The U.K. Coastal Research Facility (UKCRF) was constructed in 1994 at HR Wallingford in Oxfordshire. It was designed to facilitate fundamental and applied coastal research, and is co-owned by HR Wallingford and the Engineering and Physical Sciences Research Council (EPSRC). The UKCRF is equipped with the capability to generate both waves *and* currents, though for this research programme it was only necessary to use the wave-making capabilities.

4.1.1 Wave basin

The internal dimensions of the wave basin measure 36 m by 20 m. Figure 4.1 is a schematic diagram of the facility, additionally showing placement of wave gauges for the calibration phase of the work.

The wave basin has a concrete floor which provides a flat base for any necessary additional bathymetry. In order to investigate the evolution of waves onto a plane beach, a 1:20 beach was installed. The beach was constructed from a base of sand with a cement skim. The toe of the beach started about 8 m from the front face of the wave-makers.

The water depth of the basin can be varied between 0.3 m and 0.8 m. To allow for run-up of the waves on the beach the depth for the present tests was chosen to be 0.5m. There was a little leakage of water into the basin through defective valves and more significant leakage out, due to seepage through the floor. The water level generally fell about 3 mm over a 24 hour period and was readjusted every morning.

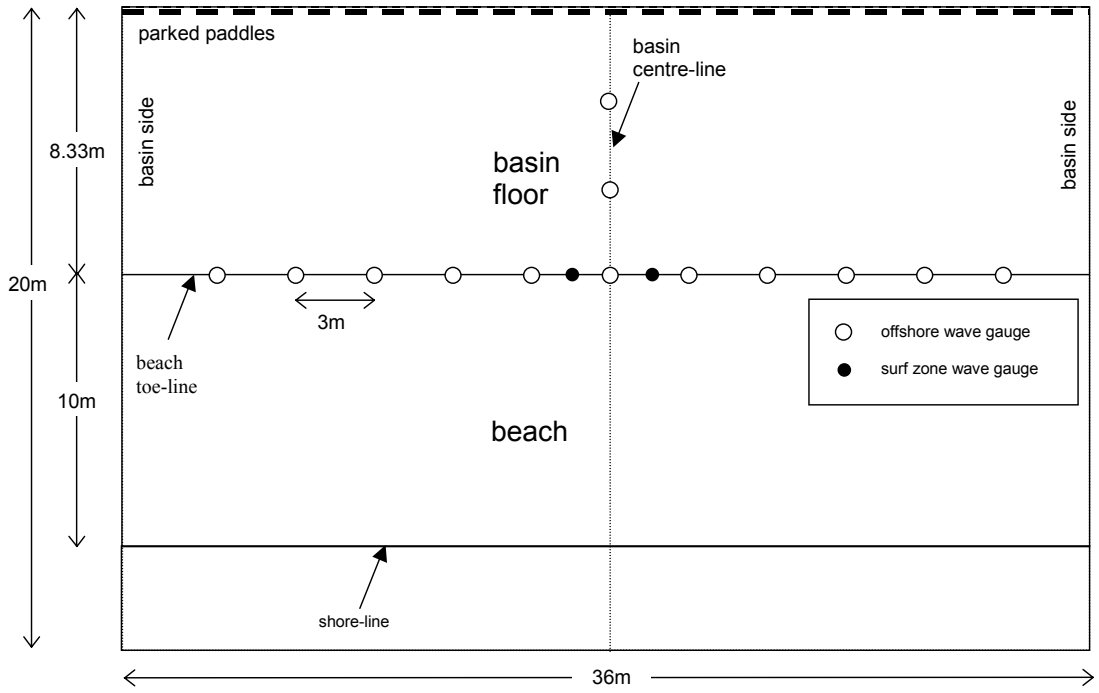

Figure 4.1: Schematic diagram of the UKCRF showing dimensions and layout of wave gauges for calibration phase.

Along the side of the facility, lateral walls consisted of sheets of marine plywood which ran from the basin floor to approximately 50cm above SWL. The flat sides are fully reflective and correspond to simple boundary conditions, useful for numerical modelling.

4.1.2 Paddles

The UKCRF has a multi-element wave-maker, comprising 72 independently operated piston-type paddles (shown in Figure 4.2). Each paddle stands around 1.5 m high and is 0.5 m wide. On the front face of each paddle is a wave gauge to provide information for an active absorption system and two vertical baffles to reduce fluid flow laterally over the face. It is possible to operate the paddles in absorption mode, but results from other research recently carried out in the UKCRF by McIver (2001) suggest that this degrades the quality of the generated waves. Therefore the paddles were operated in *non-absorption* mode.

Prior to operation of the paddles it is necessary to 'park' the paddles. This is an automated process whereby each paddle is given a position offset relative to its position at power-down. These positions are stored in a file and can be adjusted if necessary. Before the basin was

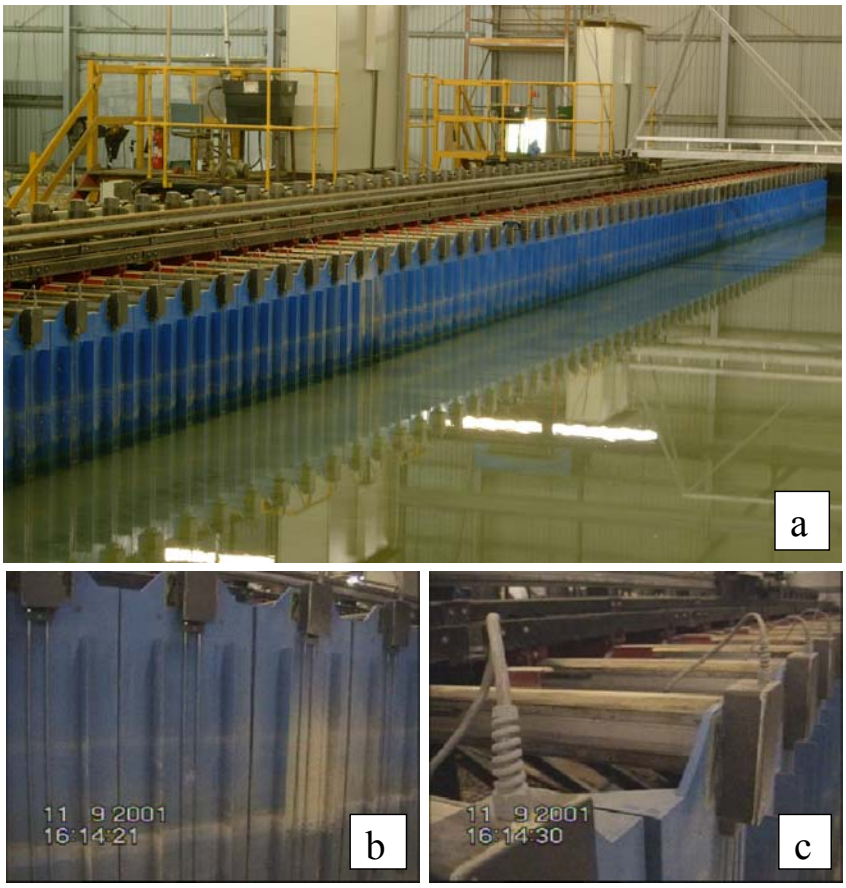

Figure 4.2: Piston-type paddles in the UKCRF. (a) Parked paddles in water depth of 0.5 m. (b) Vertical skew of Paddle 22, in dry basin. (c) Closer shot of Paddle 22.

filled with water, and after parking had taken place, a visual examination of the paddles gave cause for concern due to poor alignment of the front faces of the paddles. These varied by as much as 42 mm between the furthest forward and furthest backward paddles. It was therefore necessary to produce a new paddle position offset file. The procedure for generating new paddle offsets was as follows:

1. The paddles at either side of the basin were positioned equidistant from the instrument bridge rail at the back of the basin.

2. The position offset of each of the paddles relative to the end two paddles was measured at a height of 250 mm, relative to the basin floor (see later comment on paddle skew).

3. Corrections were made to the parking positions of the paddles via the position parking file.

The end result of this process was the reduction of the alignment error to less than 10 mm over all 72 paddles.

A complication of the initial positioning of the paddles was that the front face of ten of the paddles exhibited some degree of vertical skew i.e. the paddles were aligned with their neighbours at a height of 250 mm, but not higher or lower. Figures 4.2 (b) and (c) shows the case of paddle 22 where the offset at the top of the paddle was around 20 mm. The effect of paddle skew was minimised by determining paddle position offsets at the half water depth.

4.1.3 Wave gauges

The instrumentation of the UKCRF includes a number of conductance-type offshore and surf zone wave gauges. The advantage of the offshore wave gauges is that they can be remotely operated, enabling much faster and potentially more accurate calibration of the gauges. However the surface piercing wires of the offshore gauges were much thicker and spaced further apart than the smaller surf zone gauges. Results from both types of gauges were investigated to assess whether the offshore gauges were less accurate. The investigation used small waves (< 25 mm input amplitude) generated at three different angles - normally incident, $+10^\circ$ and $+20^\circ$. The surface elevation time history of a small wave gauge and its neighbouring large gauge were compared, after being corrected for phase differences for the oblique waves. The sizes of the troughs were very similar i.e. well within 1 mm, but there was a quantifiable difference in the size of the crests. Figure 4.3 shows the difference between the crest sizes measured using the large and small wave gauges. The large wave gauges consistently read higher values than the small wave gauges. There appears to be a trend of increasing deviation in the measurements for larger waves and larger angles of incidence. However, it should be borne in mind that all of the results except one fall within a 2 mm range, which is within the margin of error of the difference results[1]. In conclusion the large gauges *do* appear to have a greater degree of inaccuracy when compared to the small gauges but not enough to warrant not using them. As a concession two small gauges were included in the line of gauges where the most critical measurements were needed (as illustrated in Figure 4.1).

Figure 4.1 shows the arrangement of the gauges in the basin for the calibration phase.

[1] The measurement error of small wave gauges is approximately $\pm$1mm.

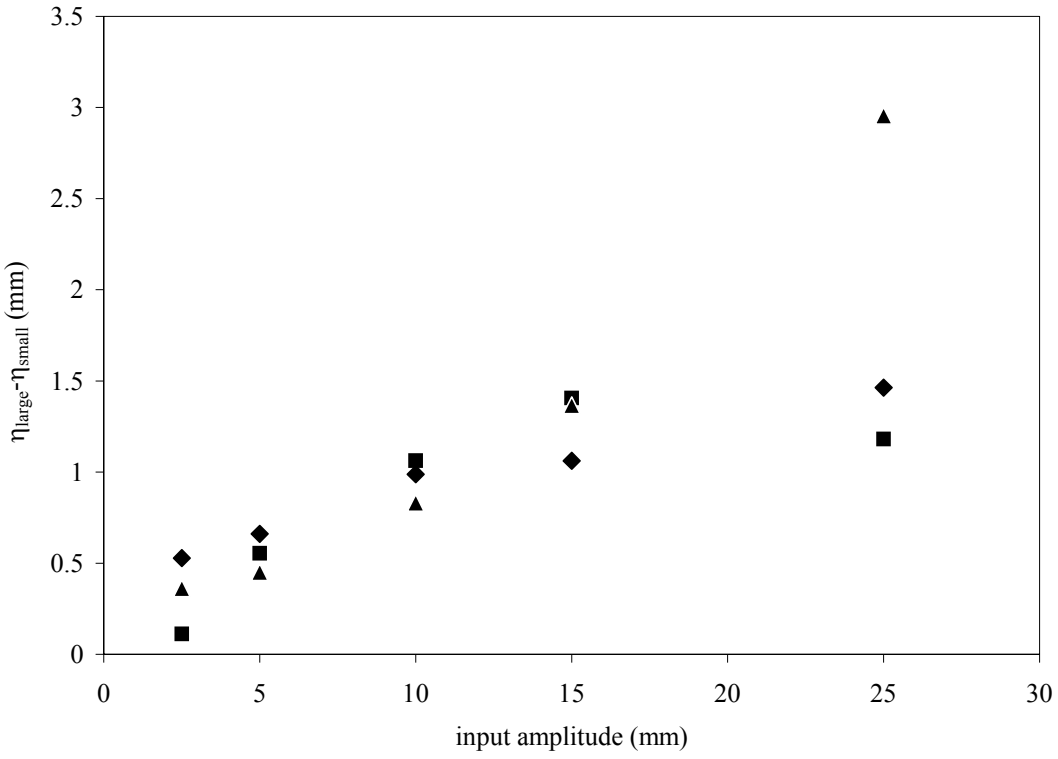

Figure 4.3: Difference in measured crest elevations from large and small gauges at three angles: ♦, normally incident; ■, +10°; and ▲, +20°.

All but two gauges were aligned with the toe of the beach, at distances of 3 m apart. Gauges were placed along the toe of the beach as it was decided to calibrate the wavefield at the same position as the focused waves would be focused later. Two additional gauges were placed in a line perpendicular to the toe of the beach, along the centre-line of the basin. They were placed at a distance of 2.78 m apart (to give a regular spacing between the toe-line and the paddles). The purpose of these gauges was to ascertain the extent of reflections off the beach.

4.1.4 Paddle control

The paddle control software of the UKCRF, *HR Wavemaker*, is designed to enable the user to select a desired sea-state from a suite of available options. These include regular waves and random waves of a variety of frequencies and amplitudes. These waves can be normally incident, oblique or multi-directional. The software writes a playback file containing the paddle positions (along with a specified paddle update period), incorporating theoretical

user-defined paddle transfer functions. This playback file is sent to the control cabinets and thence to the paddles. For the present experimental work it was desirable to bypass the control software and send positions direct to the paddles. This was because it was necessary to have complete control over the paddle positions in generating focused wave groups, in particular using paddle transfer functions determined for different angles of incidence. A patch to the software was written by HR enabling absolute paddle positions to be sent to the paddles. The paddle control software had built-in safety devices which would cut in if the requested paddle motion was above a safe limit.

4.2 Calibration of the UKCRF

4.2.1 Outline of calibration procedure

Calibration of the wave basin is necessary in order to find the relationship between the input signals sent to the paddles and the waves that are generated. The UKCRF has a set of standard theoretical transfer functions that were (originally) assumed to be independent of the angle of propagation. The validity of this assumption was tested as part of the present work.

Calibration of the facility was done in two different phases, first using regular waves then using focused wave groups. Regular wave groups provided a rough first pass. There are drawbacks in using regular waves, most notably due to the sheer number of experiments involved. Focused wave groups provide finer and more accurate calibration curves.

Regular waves

The calibration procedure using regular waves is illustrated in Figure 4.4. For a small number of pre-determined frequencies, several regular waves of small amplitude were generated. The measured amplitude of each wave is plotted as a function of input amplitude, yielding a straight-line graph. This process is repeated at each chosen frequency. The information from all frequencies is then combined in a single plot of amplitude gradient versus frequency. This graph gives a calibration curve.

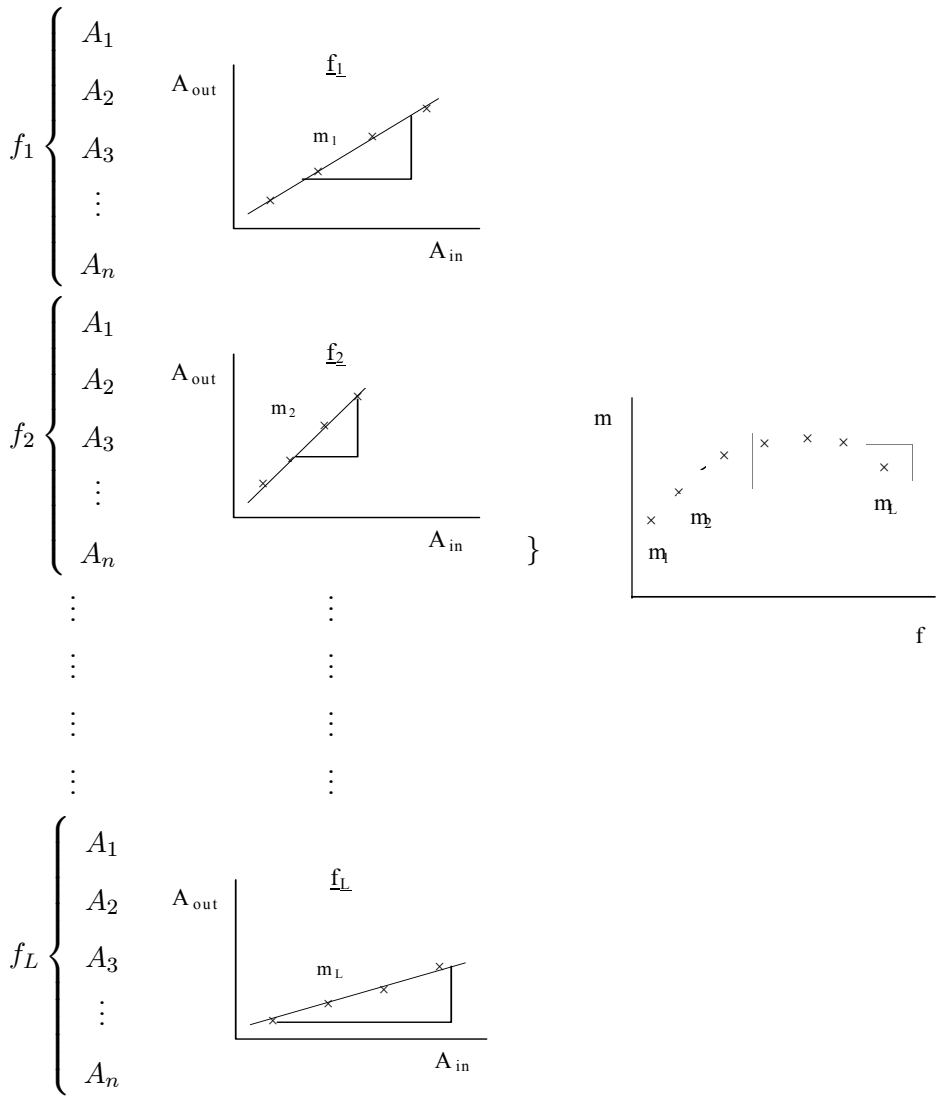

Figure 4.4: Schematic of regular wave calibration using L different frequencies, each with n different input amplitudes.

Focused wave groups

A focused wave group consists of the sum of many individual regular waves of different frequencies. A discrete Fourier Transform of the acquired time signal yields the amplitude spectrum. Focused waves with a number of input amplitudes are generated. Five such amplitude spectra are illustrated in Figure 4.5. For each individual frequency component it is possible to plot a graph of measured amplitude versus input amplitude. The gradients and intercepts of these graphs are then plotted as a function of frequency to yield a set of calibration curves of much finer resolution than have been obtained using regular waves. The gradient curve *only* is shown in Figure 4.5.

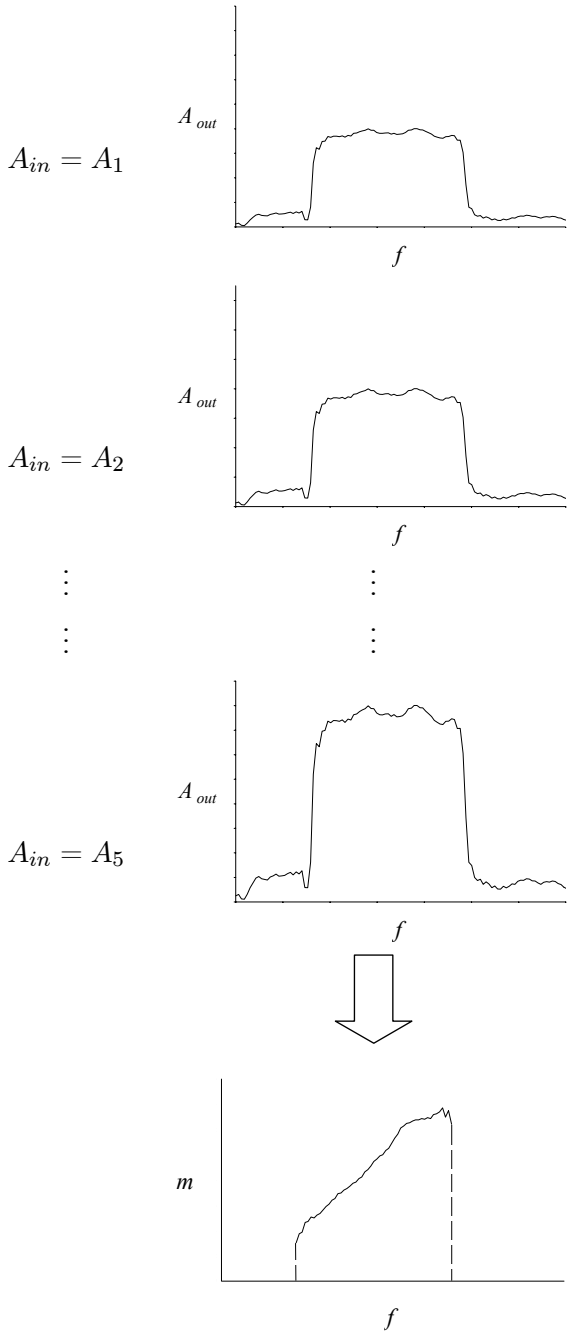

Figure 4.5: Schematic of focused wave group calibration using a number of different amplitude wave groups. Their amplitude spectra provides information necessary to plot measured amplitude spectra against input amplitude. This provides calibration data in the form of a gradient (m) and intercept (not shown) for each frequency.

This process of using regular waves and focused wave groups needs to be repeated for each propagation angle of interest.

4.2.2 Calibration results

Calibration results - regular waves - normally incident

Regular waves used in the preliminary calibration tests had periods of 0.6, 0.7, 0.8, 1.0, 1.2, 1.4, 2.0, 2.5 and 3.0 sec. The amplitudes of the waves were chosen to be 2.5, 5, 10 and 20 mm with an additional amplitude of 30 mm for the 3 sec period waves. This range of amplitudes was chosen to ensure that the waves were very close to linear, which made curve fitting much easier and more accurate.

The generated time signal consisted of a 4 sec ramp up, a 10 sec duration of maximum amplitude and a 4 sec ramp down. It was evident from the data that reflections from the beach *did* have some effect on the signal. This is shown in Figure 4.6 where data from Gauges 6, 7 and 8 are compared.

Positions relative to the paddle for these three gauges are shown in Table 4.1

Table 4.1: Positions of three central gauges.

Gauge number	**Distance to paddles (m)**
6	2.77
7	5.55
8	8.32

Gauge 6 is closest to the paddles and hence furthest from the beach. The maximum amplitude is nearly constant. Gauge 8 is closest to the beach and shows a significant variation of maximum amplitude; lowest during the middle portion and highest near both ramps.

Taking approximate account of the wave envelope it was possible to select only the part of the time signal not affected by reflections. It was also necessary to avoid the initial overshoot of the time series, due to the ramp up of the paddle motion. This process of avoiding problems at the beginning and end of the sequence was done manually, as each time signal exhibited these phenomena to a greater or lesser extent.

The measured amplitudes were obtained from the small wave gauge to the right of the basin centre-line (see Figure 4.1) using the least-squares fit method of the surface elevations.

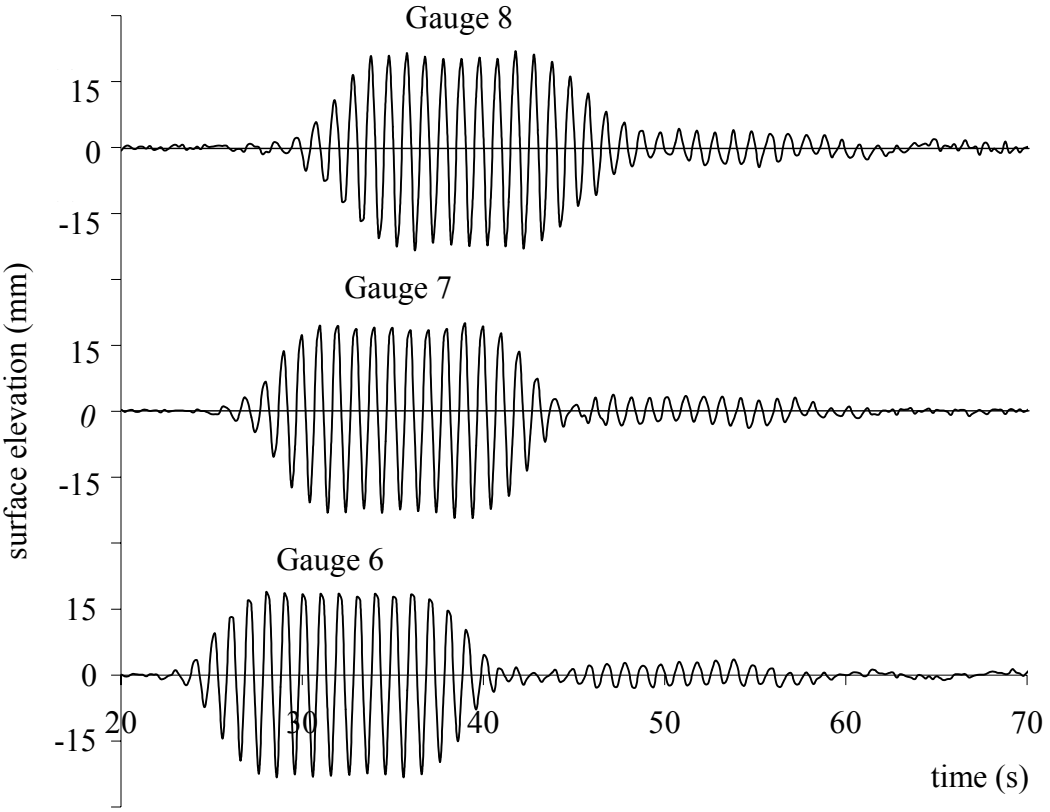

Figure 4.6: Surface elevation time histories of a 15 mm amplitude regular wave, measured at positions given in Table 4.1.

Graphs were plotted of the measured amplitude versus input amplitude. Figure 4.7 shows an example.

It can be seen from the two best-fit lines that although the graph is a straight line it does not necessarily go through the origin. This is probably due to 'slip-stick' friction of the paddles on start-up. Since the intercepts are very small and the regular wave calibration is used only as a first pass, these offsets are ignored when calculating the calibration curve. Figure 4.8 shows the resulting calibration curve.

A polynomial fit is made to the data and provides the necessary input for the focused wave group calibration. The polynomial is

$$m = 1.526f^4 - 6.720f^3 + 9.197f^2 - 3.383f + 0.8147 \tag{4.1}$$

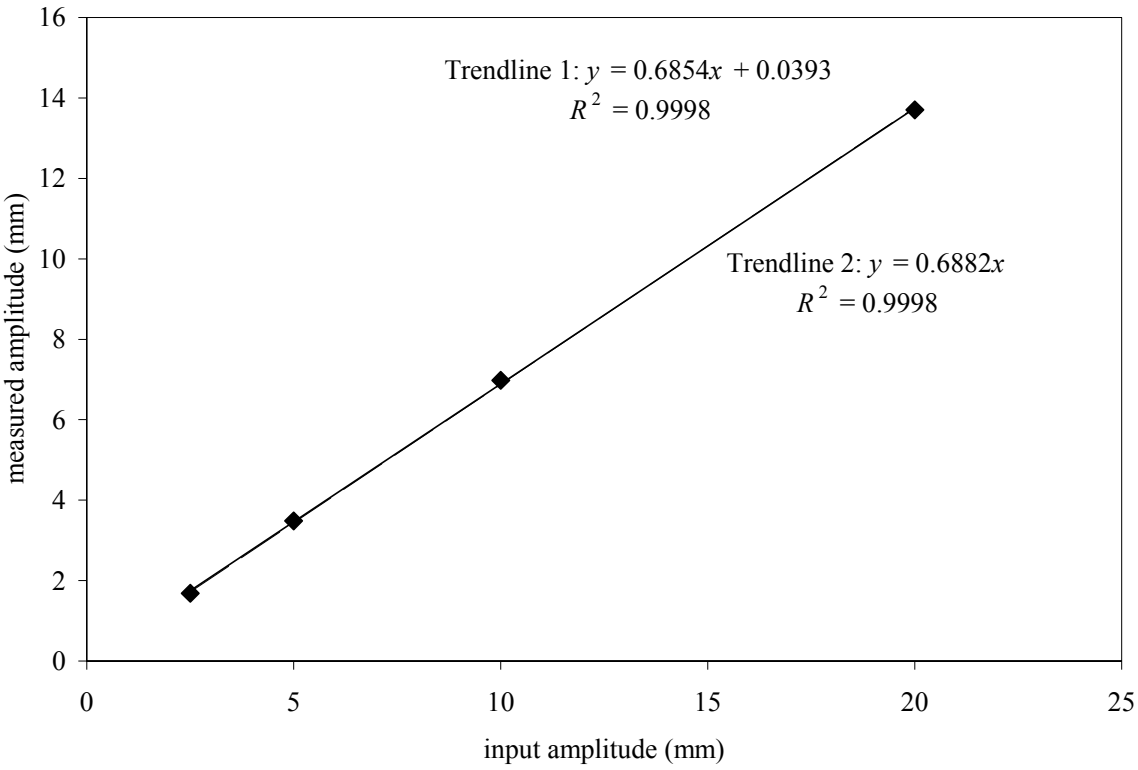

Figure 4.7: Relationship between input and measured amplitude for a 2 s period wave.

Calibration results - regular waves - oblique angles of incidence

As mentioned earlier it cannot be assumed that the calibration curve is applicable for all angles of propagation. Many further experiments would be needed in order to produce curves for all angles. Before carrying out these additional experiments, a few pilot experiments were undertaken to determine whether a more comprehensive calibration would be necessary. Measurements were taken at several angles for two different input amplitudes of 5 mm and 10 mm. The results for a 10 mm regular wave are shown in Figure 4.9.

There does appear to be a trend in this data, but since the variation was within ± 1 mm, i.e. within the margin of error of the readings, it was not possible to draw any firm conclusions. Therefore, the full range of experiments was undertaken, for every 10° between -30° and $+30^\circ$. It was not possible to run these experiments in rapid succession, as the water in the basin took some time to settle after each experiment. This was particularly the case for low frequency waves (T $>$ 2 sec), where up to 10 minutes was required to allow the water to settle. In order to reduce the number of experiments needed to provide a full data

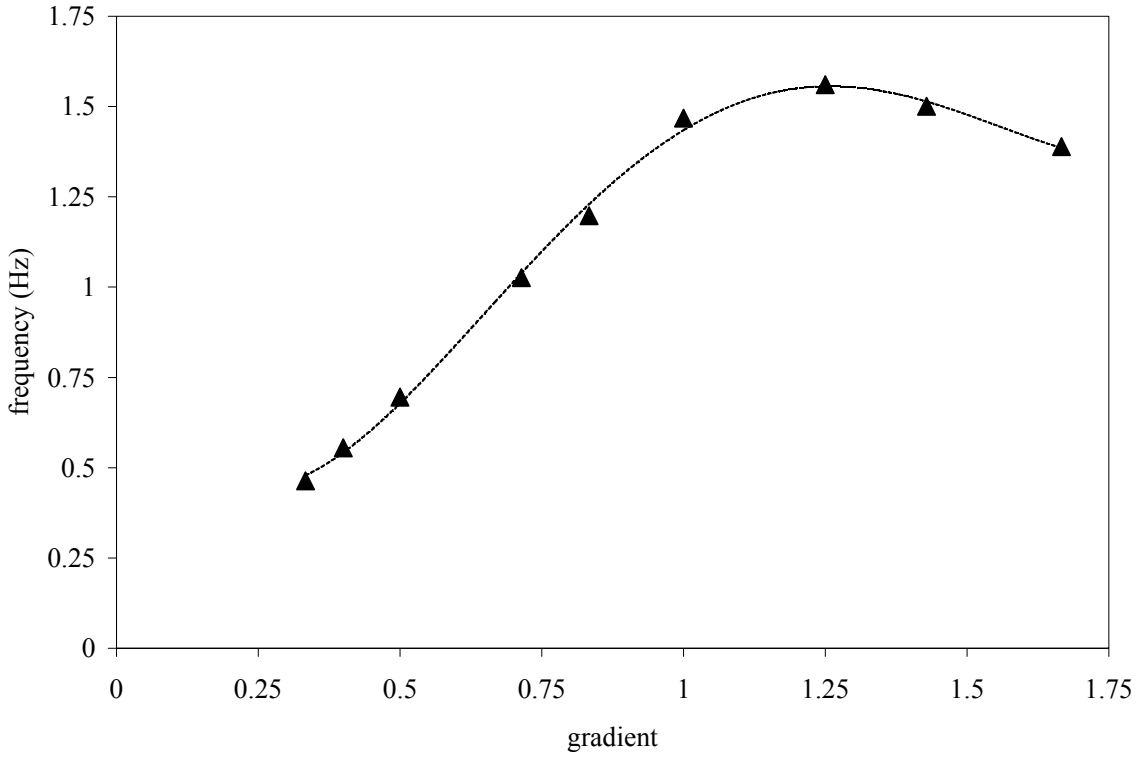

Figure 4.8: Polynomial fit to calibration curve obtained from normally incident regular waves.

set, the number of frequencies was reduced from nine to six. The chosen frequencies were: 0.333, 0.600, 0.867, 1.133, 1.400 and 1.667 Hz.

A total of 168 oblique regular wave experiments were carried out, allowing for some repeat measurements. Included in this number were repeats for the normally incident wave. Figure 4.10 shows the calibration curves obtained for the seven different angles.

It can be seen that there are some noticeable trends:

- The calibration curves are very similar for very low frequency waves, only showing significant variation above 0.5 Hz (T $<$ 2 sec)
- At angles $\leq 20°$, there is symmetry in the results i.e. curves for the $\pm$angles are very similar
- Waves generated at angles of $\pm 30°$ show a higher peak in the curve than for the other angles, and the $\pm$ results *are* significantly different from each other

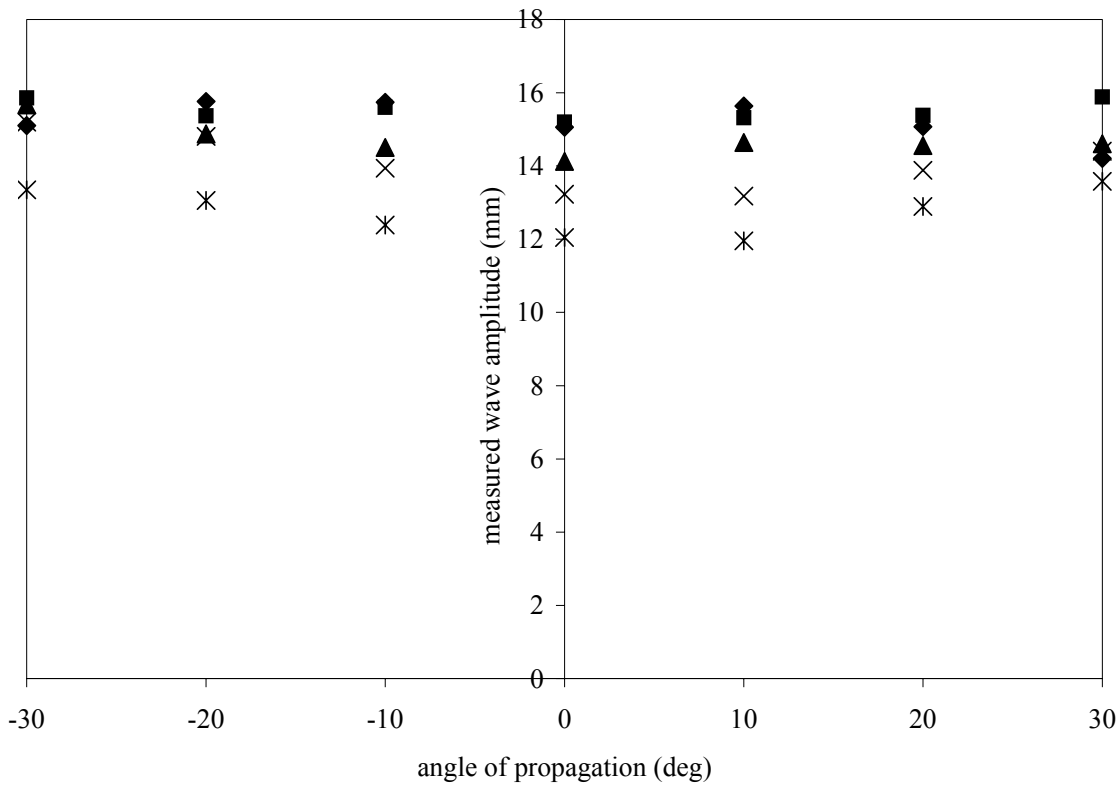

Figure 4.9: Measured amplitudes for five regular waves of different frequency at angles between -30° and +30°: ♦, 0.8 s; ■, 0.9 s; and ▲, 1.0 s; ×, 1.1 s; and ∗, 1.2 s.

Figure 4.11 shows two estimates of the calibration curve for a normally incident wave (i.e. 0°) obtained from the last round of experiments, and the initial experiments.

It can be seen that there is very little variation between the two, particularly below 1 Hz, indicating a high level of repeatability. A possible reason for the differences beyond 1 Hz lie in the fact that high frequency waves become nonlinear at smaller amplitudes than for comparable low frequency regular waves. This increases the error in deducing a gradient from the gradient graph for high frequency waves which in turn leads to greater uncertainty in the calibration curve.

The focused wave calibrations (described in the next section) required finer oblique angles, every 5° rather than at every 10°, and so it was necessary to interpolate the calibration curves. Where the ± calibration curves were very similar, an average value of the ± curves were used. i.e.

$$m_{\pm 10^\circ} = (m_{+10^\circ} + m_{-10^\circ})/2 \tag{4.2}$$

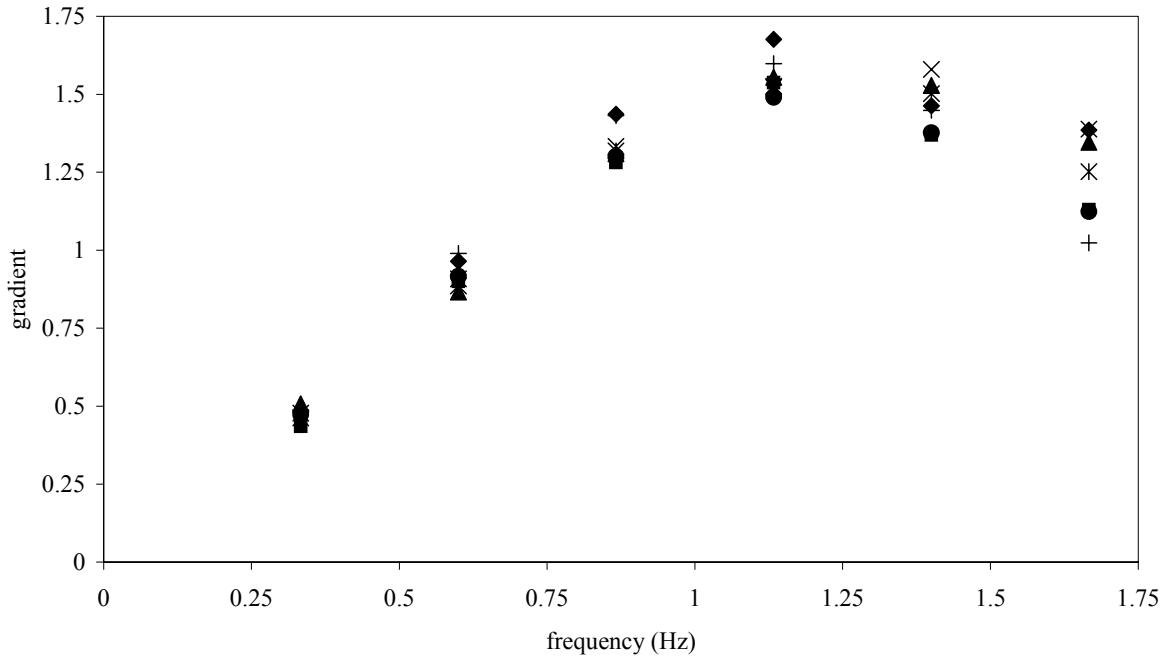

Figure 4.10: Calibration curves for all angles of incidence: ♦, -30°; ■, -20°; ▲, -10°; ×, 0°; ∗, +10°; •, -20°; +, +30°.

$$m_{\pm 20^\circ} = (m_{+20^\circ} + m_{-20^\circ})/2 \tag{4.3}$$

then

$$m_{\pm 5^\circ} = (m_{0^\circ} + m_{\pm 10^\circ})/2 \tag{4.4}$$

$$m_{\pm 15^\circ} = (m_{10^\circ} + m_{\pm 20^\circ})/2 \tag{4.5}$$

$$m_{+25^\circ} = (m_{\pm 20^\circ} + m_{+30^\circ})/2 \tag{4.6}$$

$$m_{-25^\circ} = (m_{\pm 20^\circ} + m_{-30^\circ})/2 \tag{4.7}$$

The equations for m_{0°, m_{+30° and m_{-30° are unchanged. The resulting calibration equations are as follows:

$$m_{0^\circ} = 1.526f^4 - 6.720f^3 + 9.197f^2 - 3.383f + 0.8147 \tag{4.8}$$

$$m_{\pm 5^\circ} = 0.9487f^4 - 4.346f^3 + 5.697f^2 - 1.253f + 0.4102 \tag{4.9}$$

$$m_{\pm 10^\circ} = 1.212f^4 - 5.471f^3 + 7.334f^2 - 2.222f + 0.6061 \tag{4.10}$$

$$m_{\pm 15^\circ} = 1.321f^4 - 5.785f^3 + 7.480f^2 - 2.112f + 0.5454 \tag{4.11}$$

$$m_{\pm 20^\circ} = 1.430f^4 - 6.100f^3 + 7.626f^2 - 2.002f + 0.4848 \tag{4.12}$$

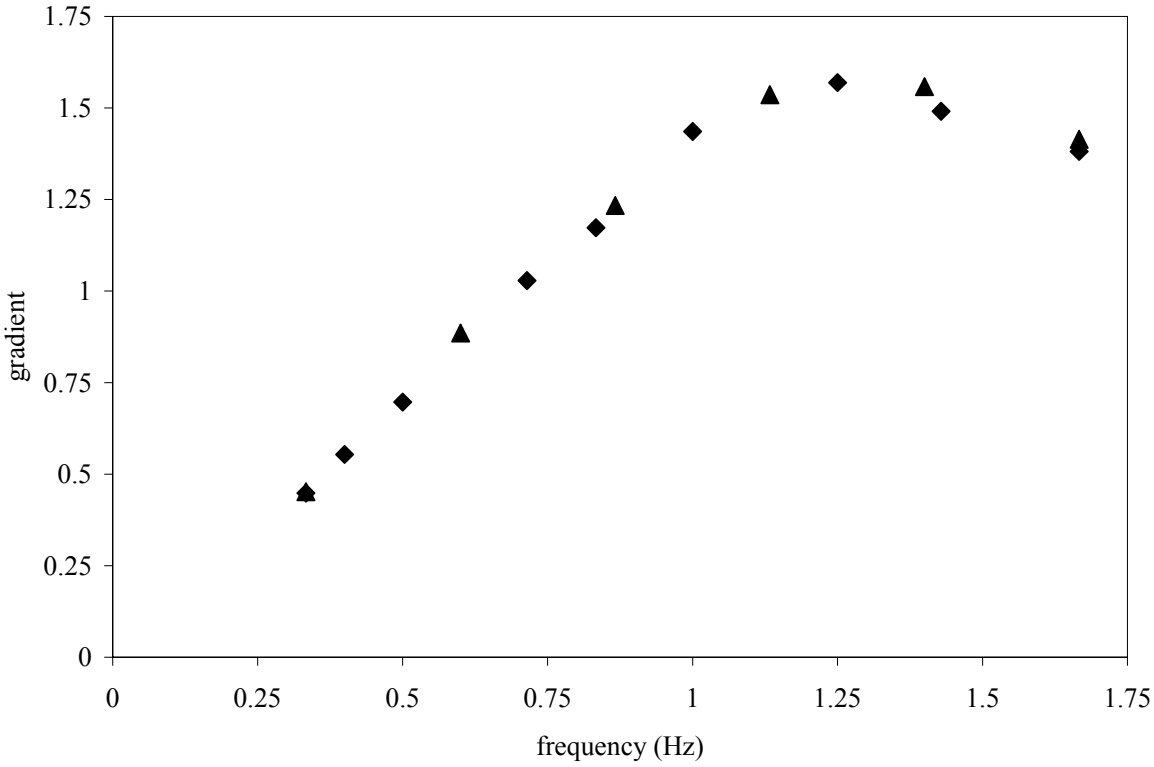

Figure 4.11: Comparison of calibration curve fornormally incident wave: ⧫, nine data point experiment; ▲, six data point experiment.

$$m_{-25^\circ} = 4.312f^5 - 19.18f^4 + 30.96f^3 - 23.47f^2 + 10.12f - 1.2274 \tag{4.13}$$

$$m_{+25^\circ} = 1.242f^4 - 5.449f^3 + 6.715f^2 - 1.385f + 0.3738 \tag{4.14}$$

$$m_{-30^\circ} = 5.054f^5 - 21.94f^4 + 34.37f^3 - 25.00f^2 + 10.33f - 1.210 \tag{4.15}$$

$$m_{+30^\circ} = 1.054f^4 - 4.799f^3 + 5.804f^2 - 0.7676f + 0.2628 \tag{4.16}$$

It should be noted that Eqns. (4.13) and (4.15) are only valid for $f \leq 1.133\ Hz$ since the polynomial fit for -30° is poor beyond this (m_{-25° uses m_{-30° in its derivation). Also Eqns. (4.13) and (4.15) are polynomials to the fifth power, whereas the others are quartic. There is no particular reason for this except that the given polynomial provided a better fit to the data points. These relationships are used in the program to generate all the initial focused wave groups.

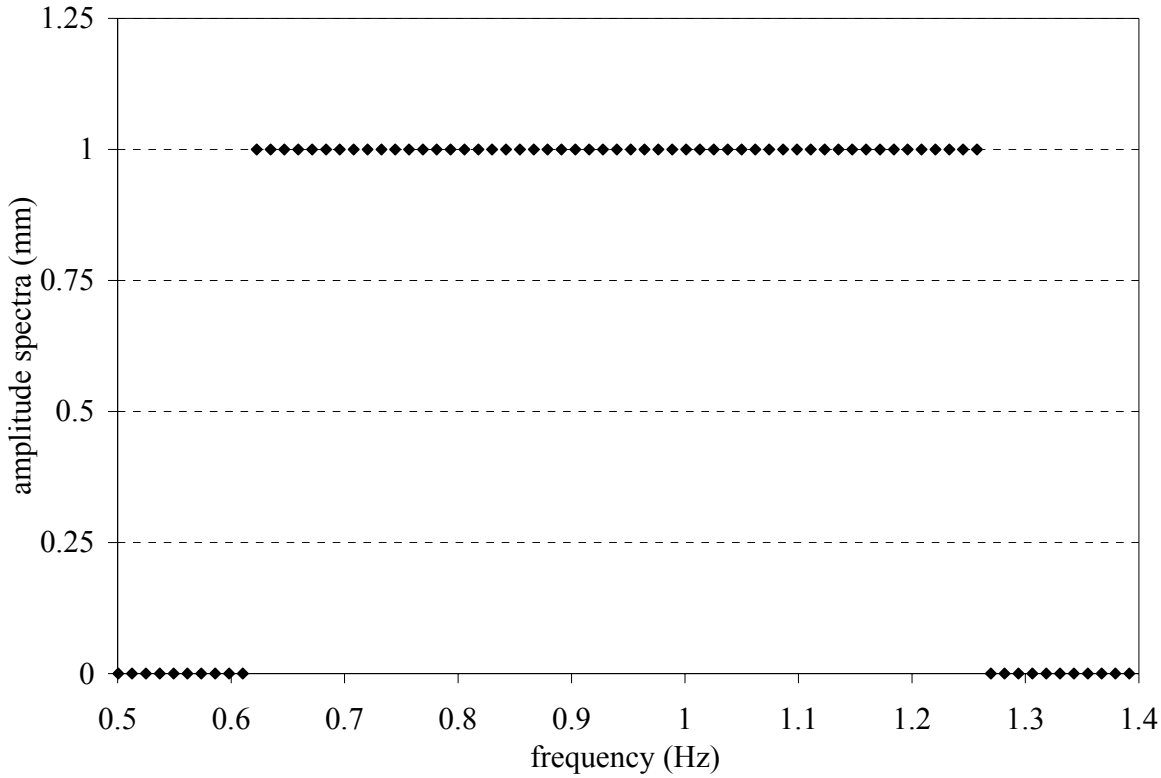

Figure 4.12: Top hat amplitude spectrum with 1 mm amplitude components.

Calibration results - focused wave groups - normally incident

Once regular waves have been used to generate an initial set of calibration curves, the next step was to take the regular wave calibration results and use them to generate focused wave groups. The amplitude spectra of these focused wave groups was then used to generate focused group calibration results as shown in Figure 4.5. Finally these calibrations are checked by generating a second tranche of focused groups and ascertaining how well their amplitude spectra compared to the initial input spectra.

As mentioned previously, the focused wave group used in the calibration is composed of a large number of equally-spaced frequency components (in contrast to the work by Baldock et al. (1996) using components equally spaced in period). Additionally the amplitudes of the frequency components are the same size. This is known as a *top hat* spectrum. Figure 4.12 shows an example of one such input amplitude spectrum used in the calibration procedure.

Table 4.2: Frequency ranges of focused wave groups.

	period (s)		**frequency (Hz)**	
	T_{min}	$T_{\max}$	$f_{\min}$	$f_{\max}$
Group 1	1.037	3.034	0.330	0.964
Group 2	0.942	2.340	0.427	1.060
Group 3	0.795	1.606	0.623	1.257

The time signal sent to the paddles is generated according to:

$$\eta(x_p, t) = \sum_{n=1}^{N} a_n \cos(\omega_n t + k_n x_p) \tag{4.17}$$

where x_p is the distance from the focus location to the paddles i.e. -8.33 m, (but see later note on movement of focus location), a_n is the amplitude of each individual frequency component, ω_n is the frequency of that component, k_n is the corresponding wave number, N is the number of frequency components, chosen to be 53 herein.

The frequency range and the amplitude have to be decided upon before focused waves are generated. In order to investigate the capabilities of the basin, three frequency ranges were used. The period and associated frequencies of these three groups are shown in Table 4.2. It was found that a focused wave group composed of the longest periods (lowest frequencies) produced the largest, non-breaking wave.

Individual amplitude components (a_n) of 0.25 mm, 0.5 mm, 0.75 mm and 1 mm were used in the focused group calibrations. With 53 wave components and an a_n of 1 mm this produced a maximum crest of 53 mm.

Movement of the focus location has been discussed in previous research, for example Baldock et al. (1996) and this phenomenon was clearly evident in the present results. The movement from the anticipated location of linear focus is due to non-linear wave-wave interactions and as a result it increases with the size of the wave group. Since the calibration is carried out at the toe of the beach, the wave groups should be brought to focus at the toe. In order to achieve this, the x_p value of Eqn. (4.17) is adjusted by trial and error until the measured surface elevation at the toe is focused. The definition of *focused* is where all components are completely in phase. This can be judged by eye to be the spatial location where the troughs either side of the central peak in the time signal are the same size i.e. it

is not necessarily where the largest crest occurs. A more rigorous test would be to calculate the phase of each component resulting from a discrete Fourier Transform.

Figure 4.13 shows amplitude spectra using both regular wave calibration results and focused wave calibration results, for the three different group frequencies as detailed in Table 4.2.

It can be seen that the amplitude spectra resulting from the regular wave calibrations gives very good results, but the results when focused group calibrations are used was even better. A second pass of the focused group calibrations was carried out in order to determine whether the calibration was further improved. Only two amplitude values of 0.5 mm and 1 mm were used. Figure 4.14 shows the results.

It can be seen from Figure 4.14 that the 'second pass' data produced a worse correlation between input and measured wave component amplitudes. The reason for this is not clear, but since the first round of focused waves produced such good results (as shown in Figure 4.13) the calibration values will be taken from the first pass.

It is not necessary to produce a polynomial fit to the focused group calibration results, instead they are written to an input file of gradients and intercepts, valid only at the specific frequencies that were calibrated.

Calibration results - focused wave groups - oblique incidence

Using Eqns. (4.8) to (4.16) it was possible to generate focused wave groups at 12 different angles with a regular wave calibration. For this set of experiments only the central position along the beach was used. Symmetry was not assumed, and all $\pm\theta_0$ experiments were run. In order to obtain the most accurate results a small wave gauge was used. Rather than removing the offshore gauge stand, the small wave gauge was attached to it, enabling remote calibration. The drawback of using the small wave gauge is that there appears to be some movement of the gauge when anything other than a very small ($\lesssim$ 30-40 mm) wave moves past it. Therefore, there was a restriction on the size of wave that can be used in these calibrations, compared to the normally incident waves when large wave gauges could be used to look at data from the larger waves. Also, for the normally incident wave experiments, three different frequency ranges were used. For the oblique wave work only the frequency range corresponding to the longest periods was used because it was this frequency range that gave

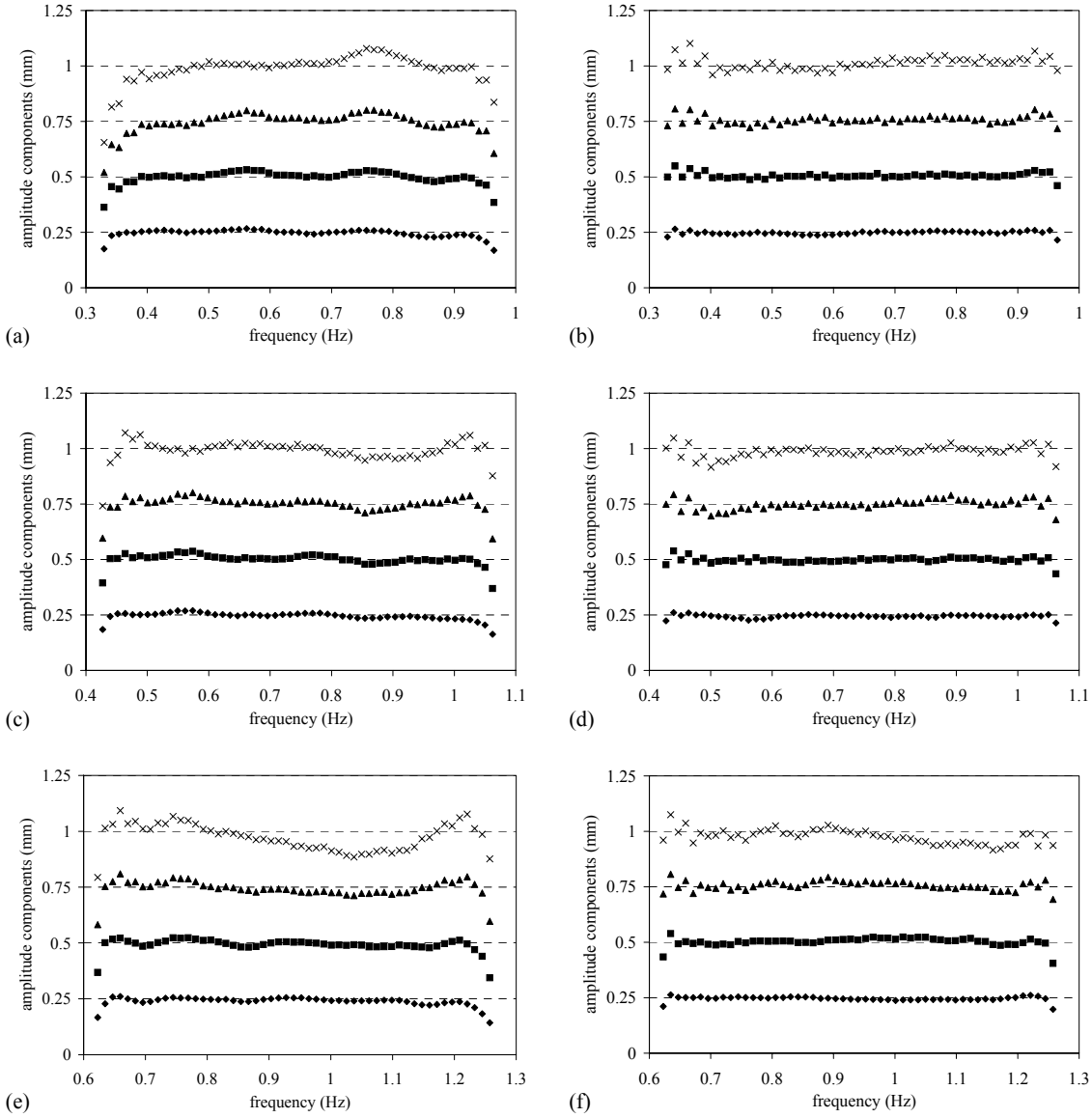

Figure 4.13: Amplitude spectra for focused wave groups. (a) Group 1 using regular wave calibration results. (b) Group 1 using focused group calibration results.(c) Group 2 using regular wave calibration results. (d) Group 2 using focused group calibration results.(e) Group 3 using regular wave calibration results. (f) Group 3 using focused group calibration results: ♦, 0.25 mm; ■, 0.5 mm; ▲, 0.75 mm; ×, 1.00 mm.

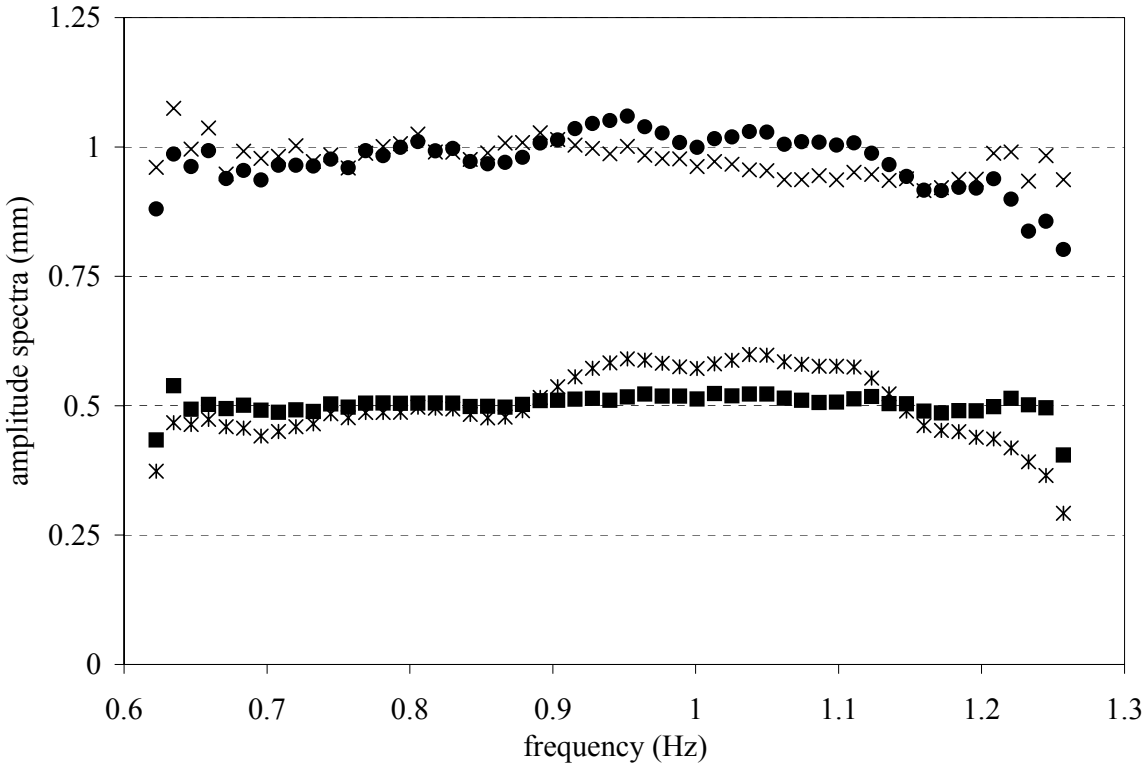

Figure 4.14: Amplitude spectra showing effect of using focused wave group calibration results for a second time: ■, 0.5 mm - first pass; ∗, 0.5 mm - second pass; ×, 1.0 mm - first pass; •, 1.0 mm - second pass.

the largest focused waves before breaking. Results again gave very close correlation between input and measured amplitudes when calibration data was incorporated in the paddle signal. Calibration data were written to frequency *and* direction-specific data files.

4.3 Instrumentation for test measurements

The tests were carried out several weeks after the wave basin calibration was completed and with a different experimental set-up. The tests comprised surface elevation, fluid velocity and wall over-topping measurements.

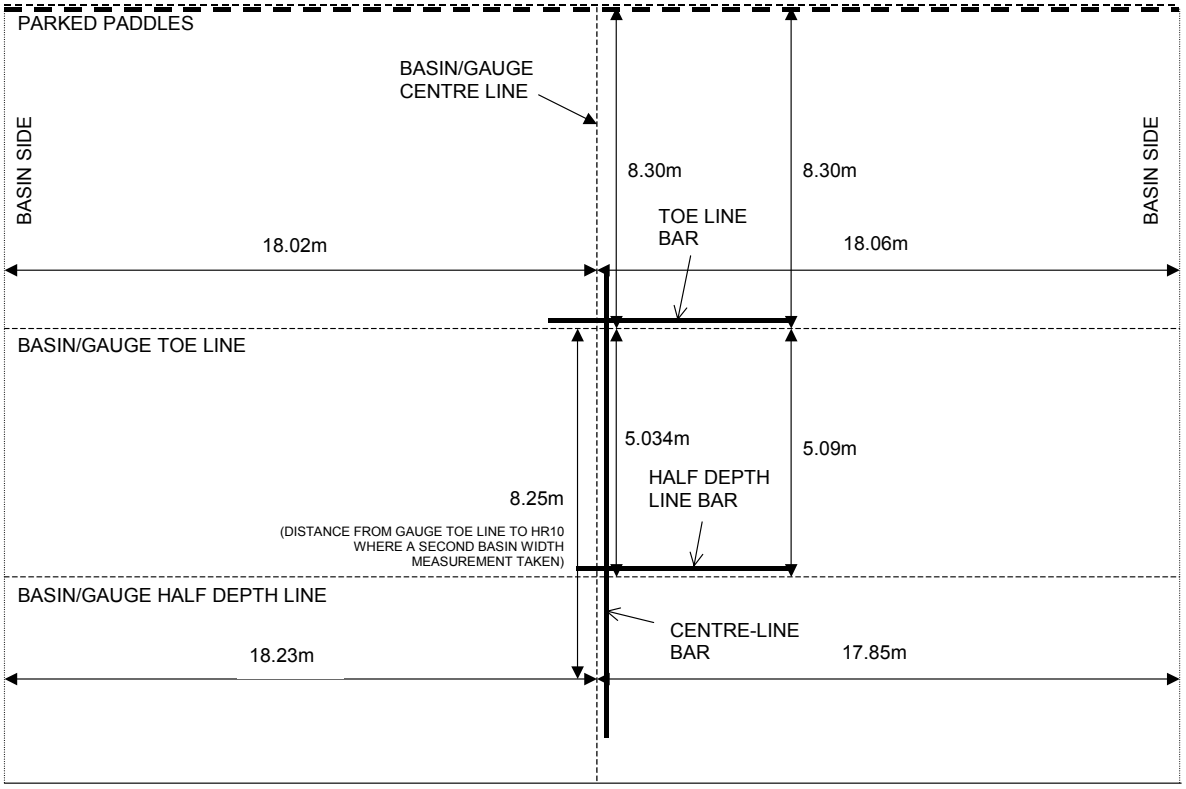

Figure 4.15: Layout of wave gauge rig for experimental tests.

4.3.1 Wave gauge array

Surface elevation measurements were required from a large area of the basin. Figure 4.15 shows the layout of the wave gauge rig used for the experimental tests.

The rig was designed and built at UMIST, and therefore needed to be reasonably lightweight and transportable. It was constructed from 6 m lengths of aluminium tubing of O.D. 34 mm. Photographs of the rig are shown in Figures 4.16 (a) and (b). The bars were connected by two or three way connectors shown in Figure 4.16 (d). The rig was supported by six very heavy circular feet, as shown in Figure 4.16 (e), that allowed pivotal motion about the foot. The vertical pole that was supported by each foot had a sleeve that allowed the entire rig to be raised and lowered. The stiffness of the rig was improved by the addition of several cross-members, though it still retained a little flexibility. The location of the array was chosen to be off-centre of the basin. This was because the spread seas were assumed to be symmetrical and nothing would be gained by measuring both sides. There was a slight overlap to the left of the centre-line, and this enabled symmetry checks to be made.

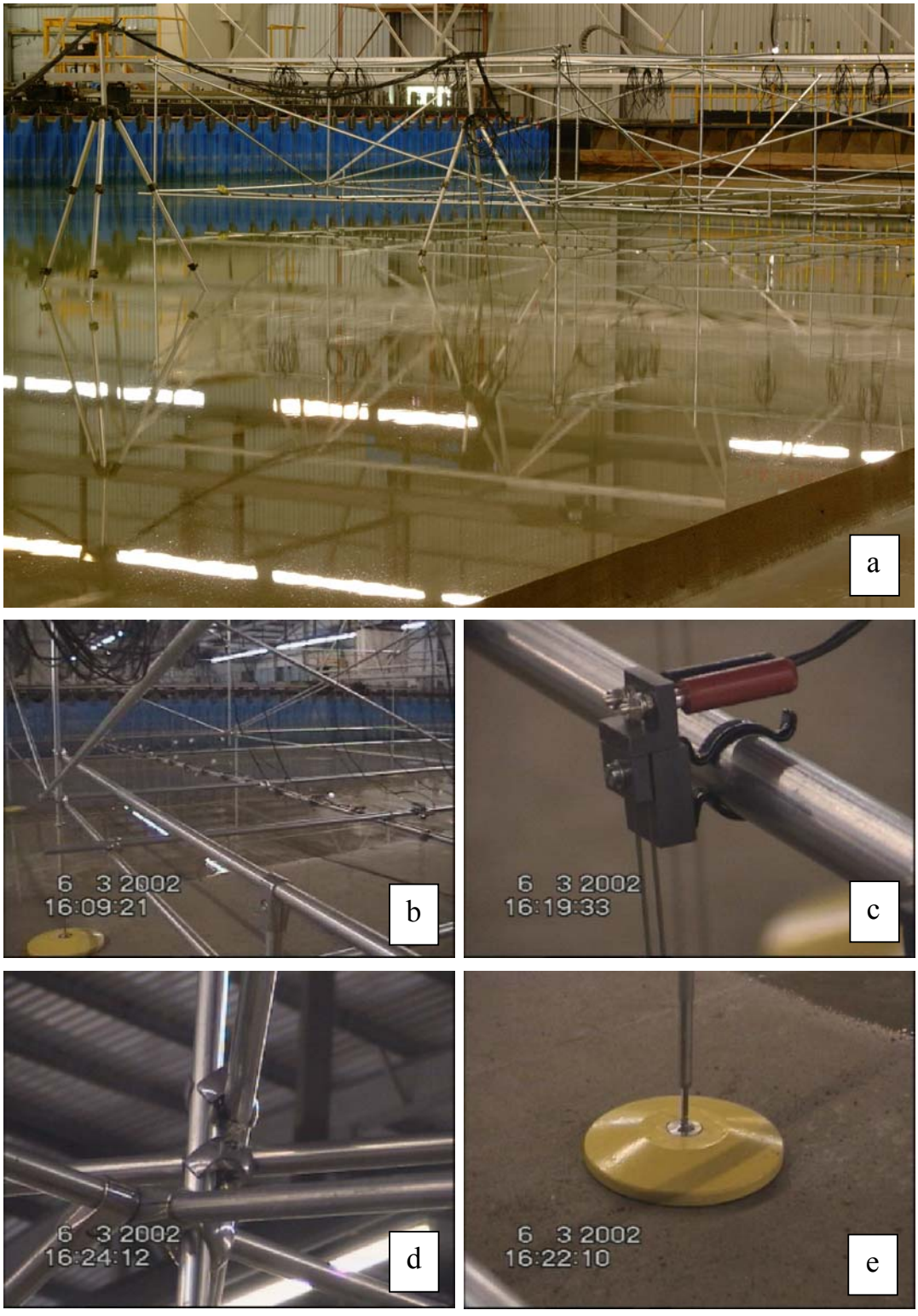

Figure 4.16: Photographs of the wave gauge rig. (a) Location of rig within the basin. (b) Close-up of tubular frame. (c) UMIST wave gauge and clip. (d) Aluminium connectors. (e) Supporting foot.

Wave gauges were attached to the array of bars with simple clips as shown in Figure 4.16 (c). These were held firmly onto the bars by fastening small cable ties onto the open end of the clips. This method of attachment meant that wave gauges in the longshore direction were placed conventionally with both arms of the gauge parallel with the paddles. The wave gauges that were along the centre-line of the basin were perpendicular to this i.e. the wires were in a line perpendicular to the paddles.

Wave gauges and additional wave gauge monitors were provided by UMIST. This enabled the use of 32 wave gauges in the basin. More wave gauges were available but to use them would have required data acquisition to be carried out in sequential rather than instantaneous mode[2].

Half of the 32 wave gauges used HR cables that were connected to the HR wave monitors. The other half were connected via UMIST cables to UMIST wave monitors. There was no operational difference between the two groups of gauges, though it was noted that gauges connected to HR equipment had a much higher signal to noise ratio (possibly due to better quality cable sheaths). These were therefore used in preference to UMIST gauges when only a small number of measurements were required.

Wave gauge calibration

During calibration, the gauges were raised and lowered individually by set amounts using accurately cut measurement blocks. The only exception to this was when gauges were used in shallow water where the range was too limited. Therefore, all gauges in shallow water were removed and calibrated on a bar in deep water. This bar could be raised and lowered accurately using holes and locating pins, enabling the gauges to be calibrated en masse.

4.3.2 Laser Doppler Anemometer (LDA) measurements

Fluid particle velocities were measured using a Dantec 2D Laser Doppler Anemometer (LDA) system. A photograph of the probe is shown in Figure 4.17. The principles of LDA will not be described here in detail. Briefly, velocities are measured using the Doppler effect[3]

[2] Sequential mode introduces time delays in the signals from different channels.

[3] The Doppler effect is an apparent change of frequency due to the relative motion of the observer and a source of radiation.

Figure 4.17: Dantec LDA probe

resulting from the interaction of a laser with particles. Two coherent laser beams form a small intersection volume. When a particle passes through the intersection volume it scatters light from both beams. The components of the scattered light form an interference pattern on a photodetector surface. The interference pattern has a pulsating light intensity due to the changing path lengths of the two components, as the particle moves. The velocity of the particle is deduced from the frequency of the fluctuating light.

Health and Safety measures were put in place to ensure that the risk of exposure to the laser beam was minimised. It was not possible to erect a screen around the laser probe, therefore all personnel except an experienced laser operator were cleared from the facility. Difficulties were experienced in getting the correct density of seeding particles to give best data acquisition rates.

The focal length of the laser was 80 mm, and its measurement volume approximately 1 mm^3. A list of the LDA measurements that were undertaken is as follows:

1. Normally incident focused wave - single measurement under the trough.

2. Oblique incidence focused wave - single measurement under the trough.

3. Repeated normally incident focused wave - through the water column, in 50 and 120

Figure 4.18: Photograph of the ADV probe.

mm water.

4. Repeated oblique incidence focused wave - through the water column, in 50 and 120 mm water.

5. Solitary wave - through the water column, in 48 and 12 mm water.

4.3.3 Acoustic Doppler Velocimeter (ADV) measurements

Water particle velocity measurements were also carried out with a Nortek Acoustic Doppler Velocimeter (ADV). The principle of the ADV, like the LDA, is based upon the Doppler effect. The basic operational principle of the ADV is to transmit an acoustic pulse of known frequency into a measurement volume, and receive the resulting echo from the water particles. The frequency shift between the transmitted and received signal is proportional to the water velocity in the measurement volume. Figure 4.18 shows the transmit transducer surrounded by three receive transducers.

There were a number of different sensor heads that could be placed on the probe arm, enabling different velocity orientations to be measured. It was possible to record either two or three velocity components, depending upon the sensor head that was used.

There were several advantages of the ADV over the LDA:

- No seeding of the water required to give good signal-to-noise ratios
- No specific health and safety requirements
- All three velocity components available from one set of data

However, the distinct disadvantage that the ADV system has when compared to the LDA, is the size of the sensor head, which limits its use as the water depth decreases. Also, the ADV has a larger measurement volume than the LDA, so the measured velocities will be subject to a higher degree of averaging and hence will not be as accurate. The measurement volume of the ADV is located approximately 100 mm from the transmit transducer and is approximately 0.25cm^3.

A list of the ADV measurements that were undertaken is as follows:

1. Normally incident focused wave - single measurement under the trough.
2. Oblique incidence focused wave - single measurement under the trough.
3. Repeated normally incident focused wave - through the water column, at toe of beach.
4. Repeated oblique incidence focused wave - through the water column, at toe of beach.
5. Repeated oblique incidence focused wave - at 40% depth, for nine positions up the beach (minimum water depth of 134 mm).

4.3.4 Sea wall

A sea wall was built along the entire basin length to enable overtopping volumes to be measured. The toe of the sea wall was 8.125 m from the toe of the beach as illustrated in Figure 4.19 (a). The central section of the wall had a flat top and sloping back wall. The slope of the front face of the sea wall was 1:2.18 and the top of the seawall horizontal (both taking into account the beach slope). The actual dimensions of the sea wall are shown in Figure 4.19 (b). The sea wall either side of the central section had a sloping face on the seaward side only, in order to save on building costs. This is illustrated in Figure 4.19 (c), which shows the sea wall when the basin is drained of water.

In order to enable over-topping measurements to be made, it was necessary to build a catchment area which incorporated a V-notch weir (shown in Figure 4.20 (a)) and to

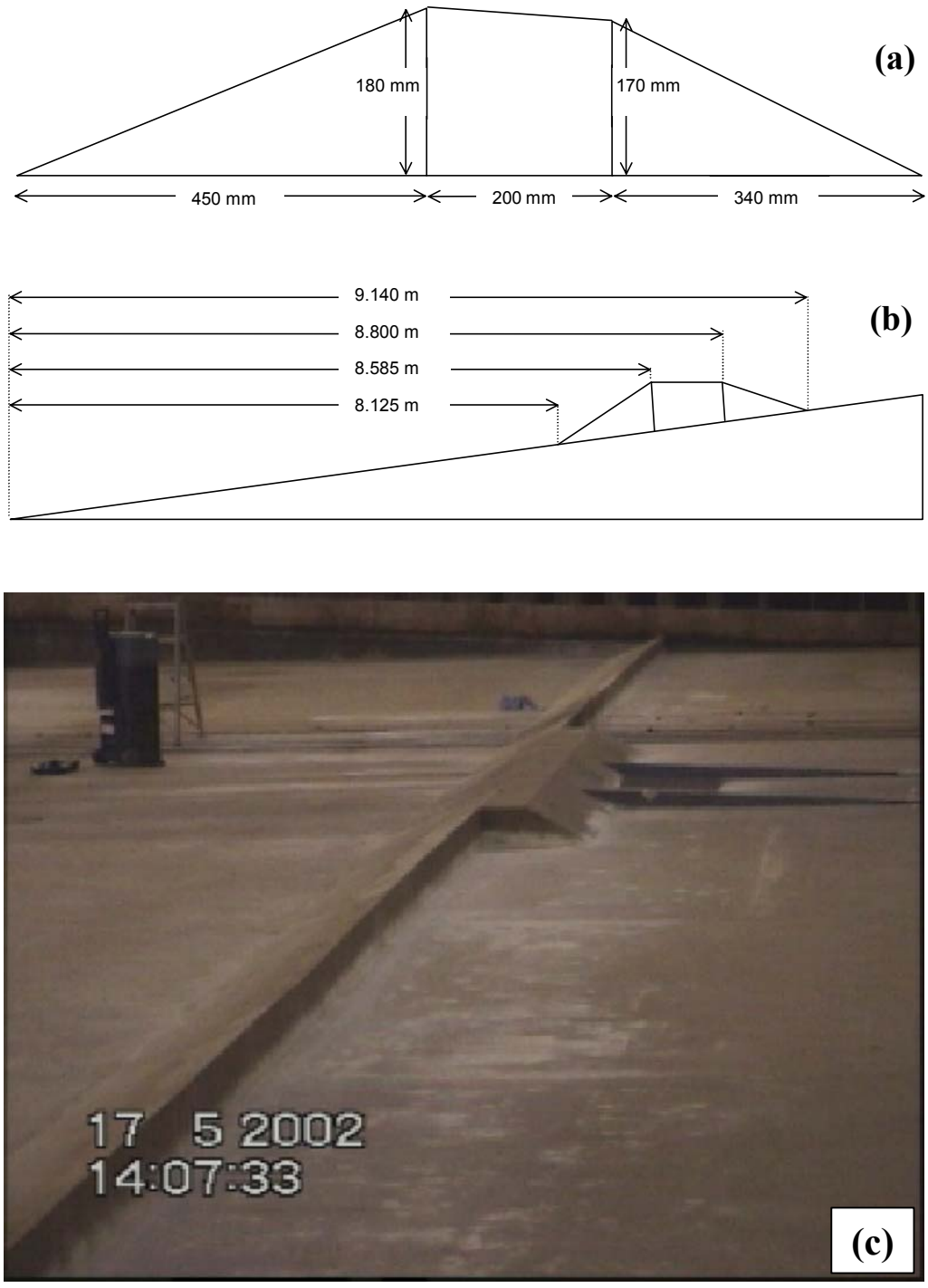

Figure 4.19: Sea wall constructed in the UKCRF. (a) Dimensions of the sea wall. (b) Location of the sea wall relative to the toe of the beach. (c) Sea wall in the dry basin showing full central section and sloping front face of remaining sections.

make surface elevation measurements at various positions over the wall. Surface elevation measurements were made possible by sinking wave gauges into PVC tubes set into the sea wall, as shown in Figure 4.20 (b). The catchment area was calibrated using known volumes of water.

4.3.5 Image Recording

In addition to the surface elevation, kinematics, run-up and overtopping measurements, a *visual* record of the experiments was made. This visual record provided invaluable information on how to interpret some of the experimental data.

Video recordings

Video footage was obtained using tripod-mounted digital cameras. The waves were filmed from two locations: View A - along the toe of the beach and View B - from the gantry beyond the top of the beach. Lines were painted on the beach parallel to the still water shoreline at 0.5 m spacings. Video footage from View B provided a useful cross-check for the runup measurements since it was possible to estimate the runup level up the beach to within 0.1 m.

Stills photography

A professional photographer recorded several high quality digital photographs of some of the most dramatic waves: the solitary wave, the largest normally incident focused group and an oblique incidence focused group. A selection are shown in Figure 4.21 (a) to (d). Figures 4.21 (a) and (b) show the oblique incidence focused wave group immediately before and during overtopping of the central portion of the sea wall. Figures 4.21 (c) and (d) shows the solitary wave moments before overtopping and then just afterwards. These photographs may provide useful insight into the physical behaviour of the waves as they overtop a structure.

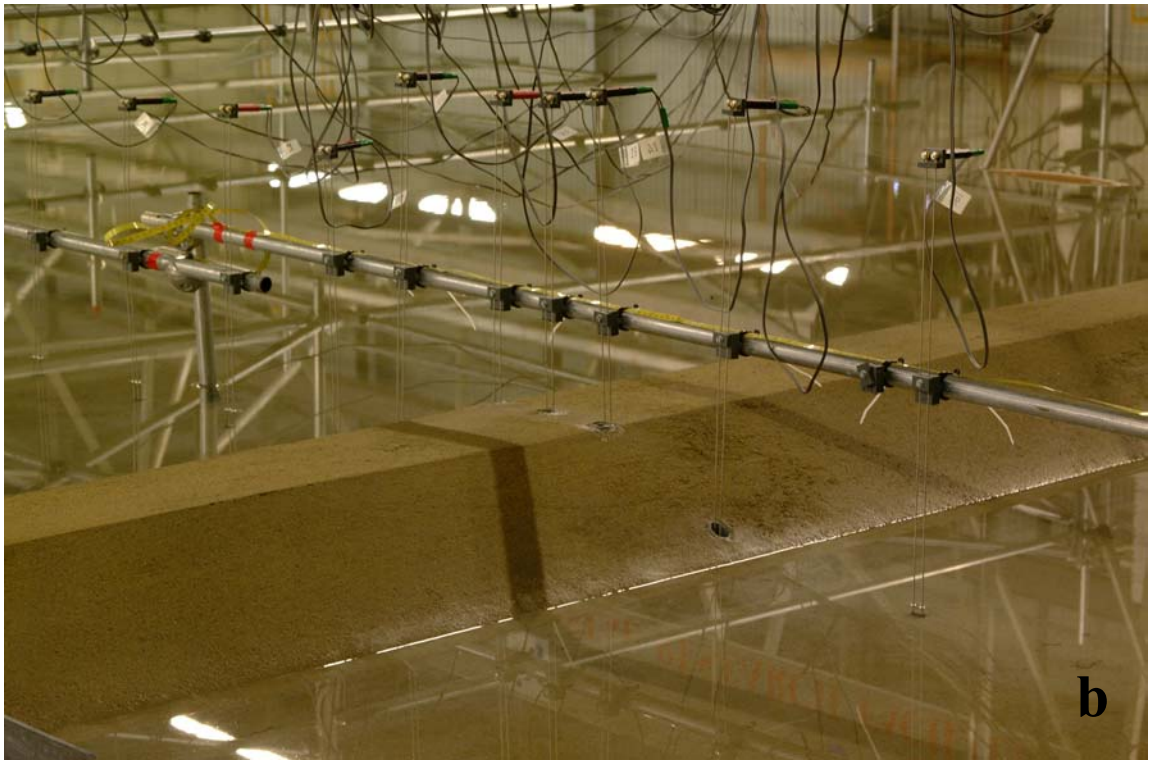

Figure 4.20: Sea wall constructed in the UKCRF. (a) Catchment area showing V-notch weir. (b) Close-up of wall, showing gauge placement in hollow tubes

Figure 4.21: Photographs of waves overtopping the sea wall (a) oblique incidence wave group immediately prior to overtopping (b) oblique incidence wave group during overtopping (c) solitary wave before overtopping and (d) solitary wave after overtopping.

Chapter 5

Visualisation of focused wave group dynamics and harmonic structure

The purpose of this chapter is to carry out analysis of the behaviour of focused wave groups as they undergo transformation in shallow water at a plane beach in the UKCRF. Most of the results are qualitative but they give an insight into generic properties of the dynamics of nonlinear systems and processes.

5.1 Focused wave group interacting with a plane beach

By presenting the surface elevation time histories in an appropriate manner it is possible to glean information about some of the underlying wave transformation processes. In this section, surface elevation data is displayed from WG 1 and WG 5. These are respectively the crest focused and trough focused groups with the largest amplitude and a focus location coinciding with the toe of the beach, as described in Appendix A1. There are 44 sequential wave gauge measurement locations along the centre-line of the basin, placed at 250 mm intervals beginning 1.5 m offshore of the toe of the beach (approximately 7 m from the paddles) and finishing 9.25 m onshore of the toe of the beach in a still water depth of 37.5 mm. This layout of wave gauges is shown in Figure 5.1. A total of 32 wave gauges were available for surface elevation measurements. Therefore to cover 44 positions it was necessary to have one arrangement (Layout C) for the deep water positions and other arrangement (Layout L) for the shallow water positions i.e. the wave group generation had to be carried out twice. The

use of two overlapping gauge arrangements proved useful for comparison purposes though in fact, the reproducibility of the experimental data was so good that it is impossible to tell from the stacked time histories (shown in this section) where the join between the deep and shallow water data occurs. The two wave gauge arrangements for the focused wave groups interacting with a plane beach are given in Appendix C, Table C1 and Table C2.

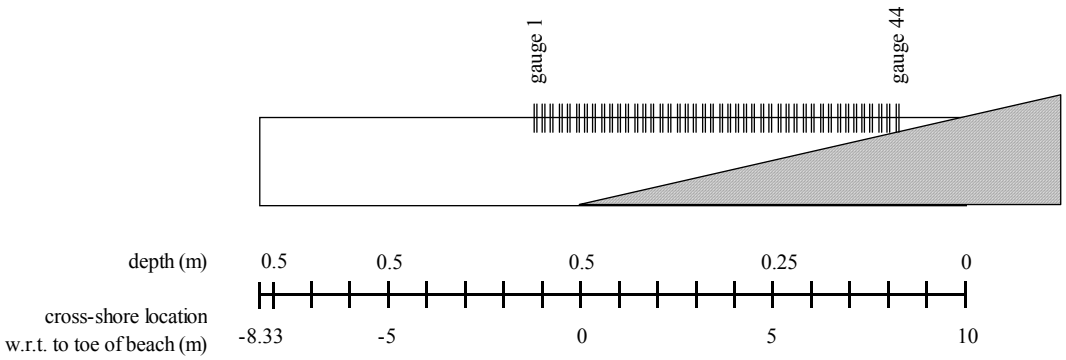

Figure 5.1: Location of wave gauges in the UKCRF.

5.1.1 Crest focused time series

Figure 5.2 shows stacked time histories of the crest focused wave group[1]. There are several interesting points to note about the plot. There is a gradual dispersion of the wave group from an initial group consisting of three large crests and two troughs over a period of about five or six seconds, to a rather less well-defined group of waves over a period of 15 seconds. This is primarily due to dispersion of parasitic waves from the main group, i.e. the high frequency waves travel more slowly and appear at later times.

It is possible to see how the size of the three crests of the group change as they travel up the beach. The first crest (to the left of the group) appears to increase in size until only two gauges from the end, though never achieving the same amplitude as the central (second) crest. The second crest appears to have an approximately constant amplitude until about gauge 30, when it dramatically reduces in size (presumably due to breaking). It then develops a saw-tooth shape which continues until the final measurement position. The shape of the

[1]N.B. Whilst the colours in the stacked plots are useful for visualising the structure they provide no quantitative information; therefore care must be taken when making comparisons between plots .

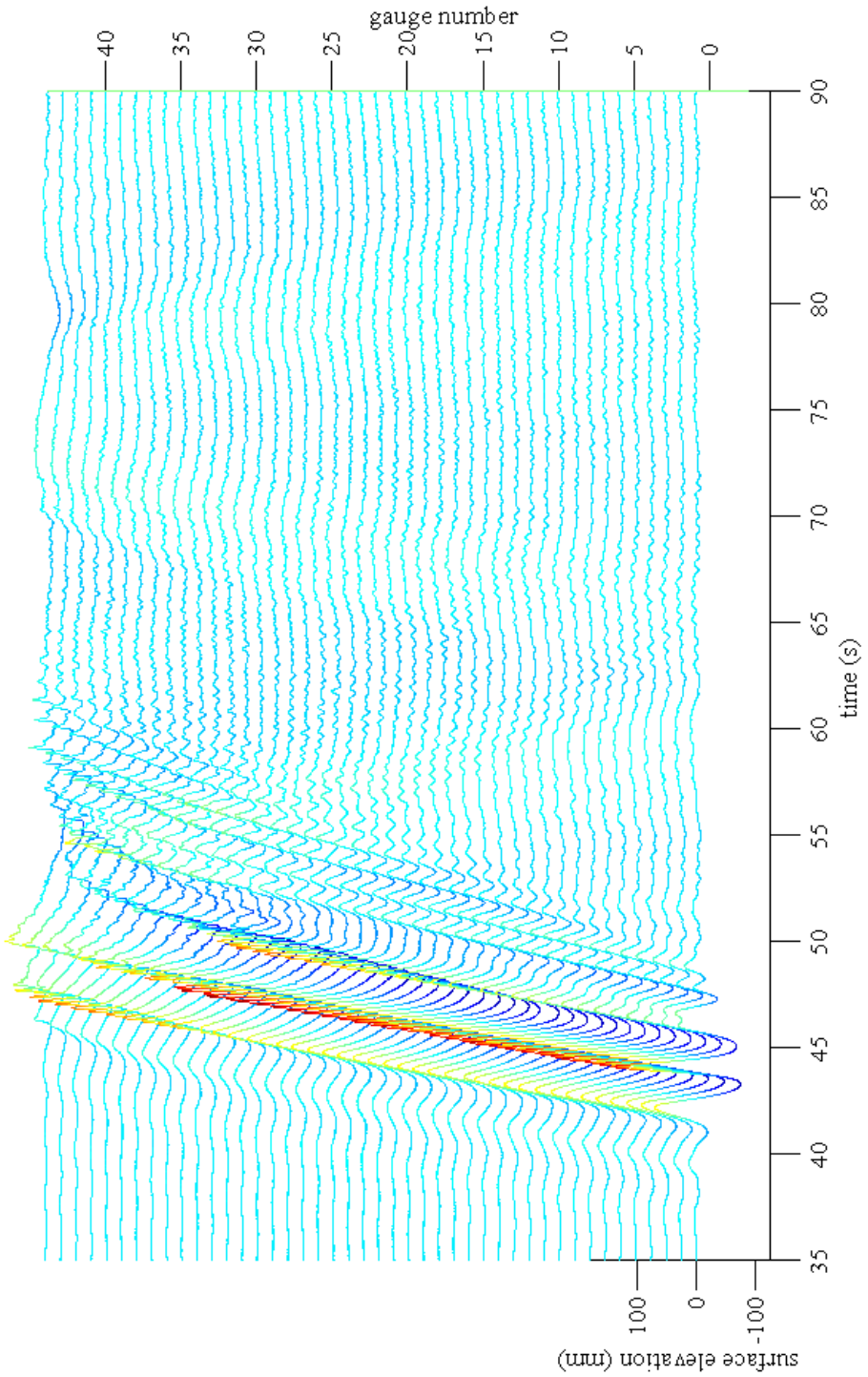

Figure 5.2: Stacked time histories of a crest focused time series.

third crest is initially modified by one of the high frequency parasitic waves, but this soon falls from the back of the group, and by the time the group reaches the toe of the beach (gauge 7), the crest is relatively 'clean'. From the toe of the beach onwards the crest increases in amplitude until a sharp reduction occurs, at a position similar to that of the reduction of the second crest. The crest then all but disappears in relation to the size of the other two crests.

Following the advent of the wave group, the surface elevation time histories become subject to some high frequency 'noise'.

Finally, and of considerable interest there is evidence of a low frequency wave coming off the beach and being re-reflected across the basin. This will be investigated in detail later in this section.

5.1.2 Trough focused time series

Figure 5.3 which shows stacked time histories of the trough focused wave group, exhibits characteristics very similar to that of Figure 5.2, most noticeably the low frequency wave reflected off the beach. The individual crests that make up the group also grow in size until a maximum value after which they become saw-tooth shaped.

5.1.3 Addition plots

Section 3.3.2 described how it is possible to separate the different harmonics of the generalised Stokes expansion. If this method is applied to the time signals from each of the wave gauges then it is possible to produce stacked time histories for odd and even harmonics. Figure 5.4 shows the effect of adding crest focus and trough focus time histories. This plot should show only even harmonics. Certainly the obvious wave group structure has been removed, leaving only higher frequency waves and the low frequency wave. It is interesting to note that high frequency waves travel up to the beach, then effectively disappear. This is in marked contrast to the low frequency wave which is reflected off the beach, off the paddles, and again off the beach, before being lost from the end of the time series. Greater clarity is possible by filtering the time signals at an appropriate frequency. For the 'addition plots' this frequency is 0.5 Hz.

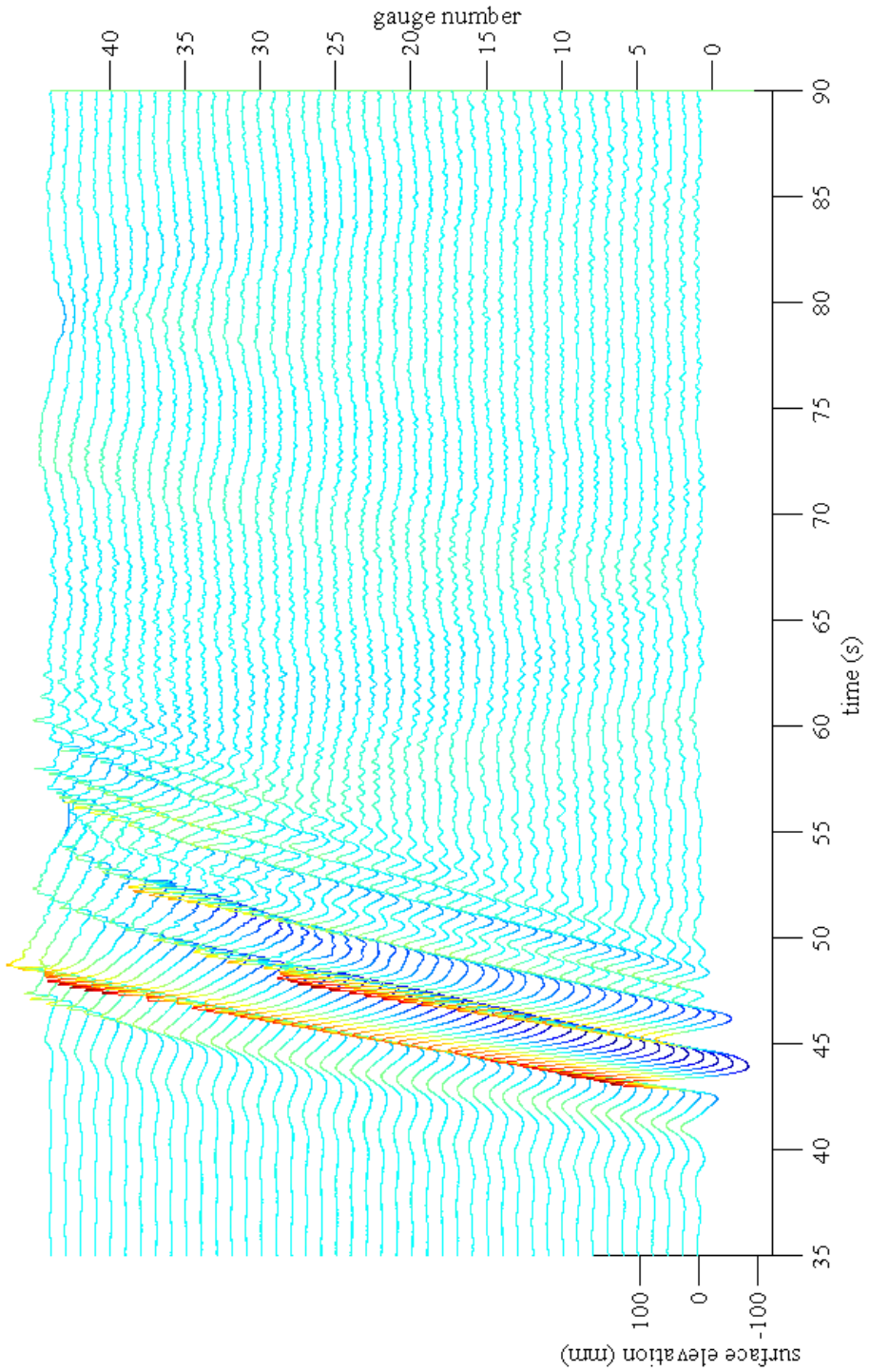

Figure 5.3: Stacked time histories of a trough focused wave group.

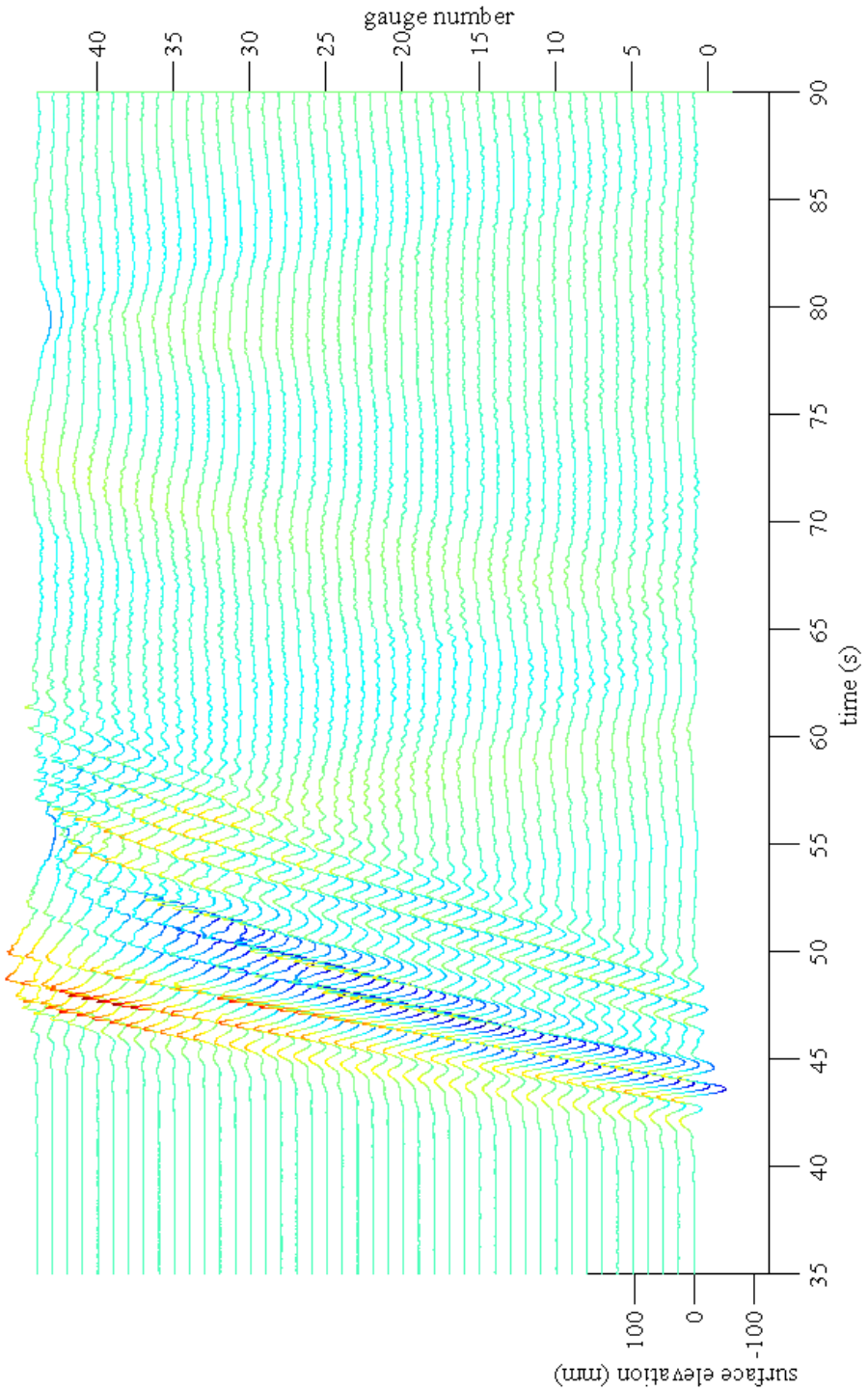

Figure 5.4: Stacked time histories of the addition of crest and trough focused wave groups.

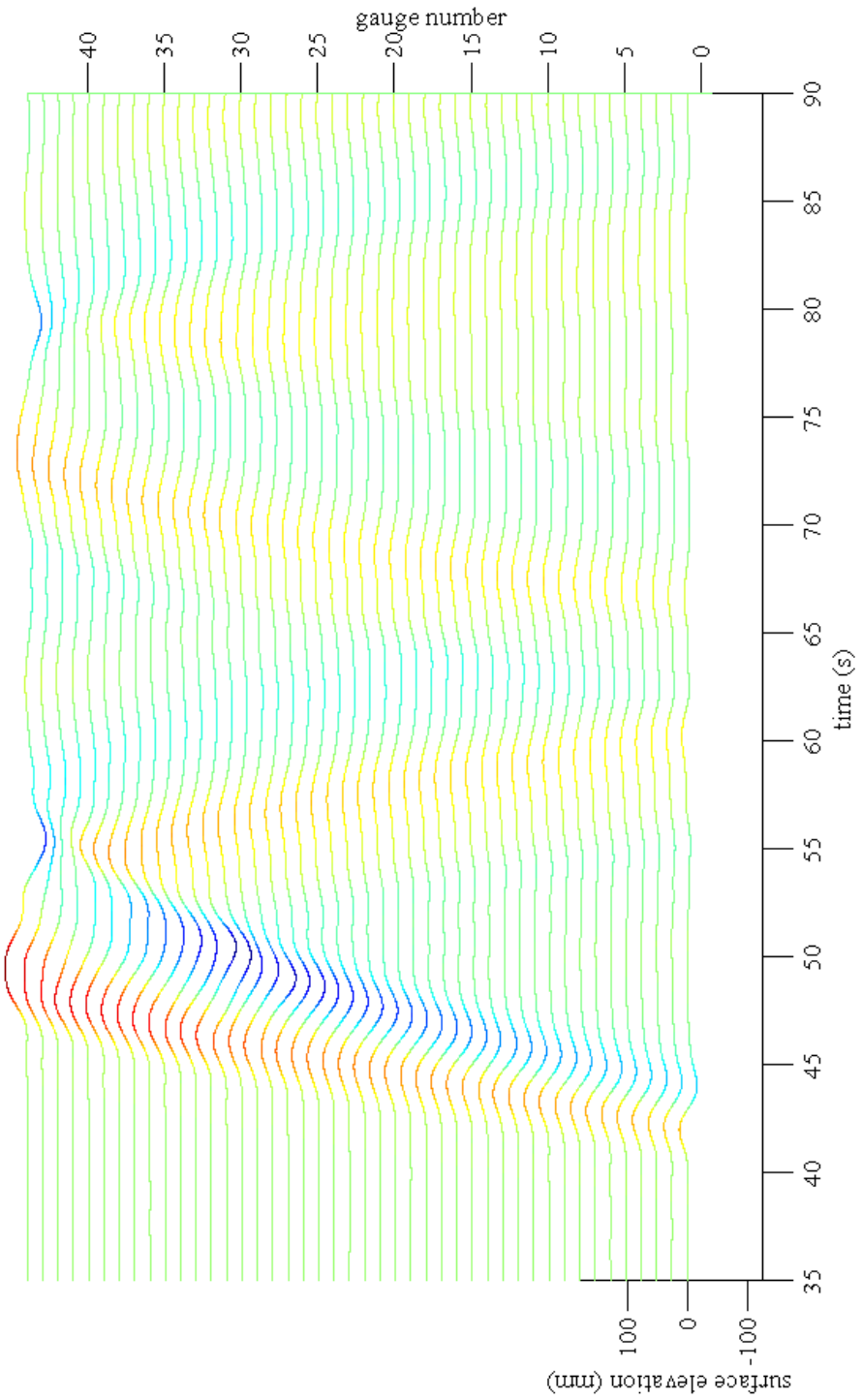

Figure 5.5: Stacked time histories of the addition of crest and trough focused wave groups, low frequency band-pass filtered at 0.5 Hz.

Low frequency band-pass filtered

Figure 5.5 shows the result of removing all frequency information above 0.5 Hz. The result is a very clean picture of low frequency waves. There is a low frequency hump followed by a depression of the water surface. The low frequency hump is the low frequency parasitic wave generated by the paddle which travels independently of the wave group; the depression is the local set-down term that lies underneath the wave group and is bound to the group i.e., it travels at the same speed as the group. These two waves remain together until the last measurement position, though their shape stretches from a period of about 5 seconds to 10 or 12 seconds at the furthest point up the beach. In principle the parasitic long wave should move off and separate from the bound set-down as the bound wave travels more slowly than the low frequency parasitic wave. In practice there is not enough distance to enable this to happen before both waves hit the shoreline.

It is not clear from the plot whether this wave is the reflection of the parasitic wave, the set-down term, or some combination, or indeed some new wave generated in the breaking process. This low frequency wave may give some insight into the phenomenon of 'surf beat' which is of great interest to coastal engineers.

High frequency band-pass filtered

Figure 5.6 shows the result of filtering Figure 5.4 with a 0.5 Hz high frequency band-pass filter. It is immediately obvious that there are considerable even (almost exclusively second order) harmonics travelling up the beach, and *nothing* returning, i.e. there is complete dissipation of the energy in this bandwidth of the second harmonics. As with the other stacked plots there is also clear evidence of a spreading in time of the group of waves. This plot is composed of the second order bound waves and the higher order parasitic waves that travel more slowly and so will begin to trail the main group, as is clearly shown.

5.1.4 Subtraction plots

Figure 5.7 shows the effect of subtracting the trough focus time series from the crest focus time series. This plot yields odd harmonics. The main wave group is evident, though there is some high frequency 'noise'. The size of the group is reduced in comparison to the crest focus time series of Figure 5.2, and the shape of the waves, beyond about gauge 30, looks distorted.

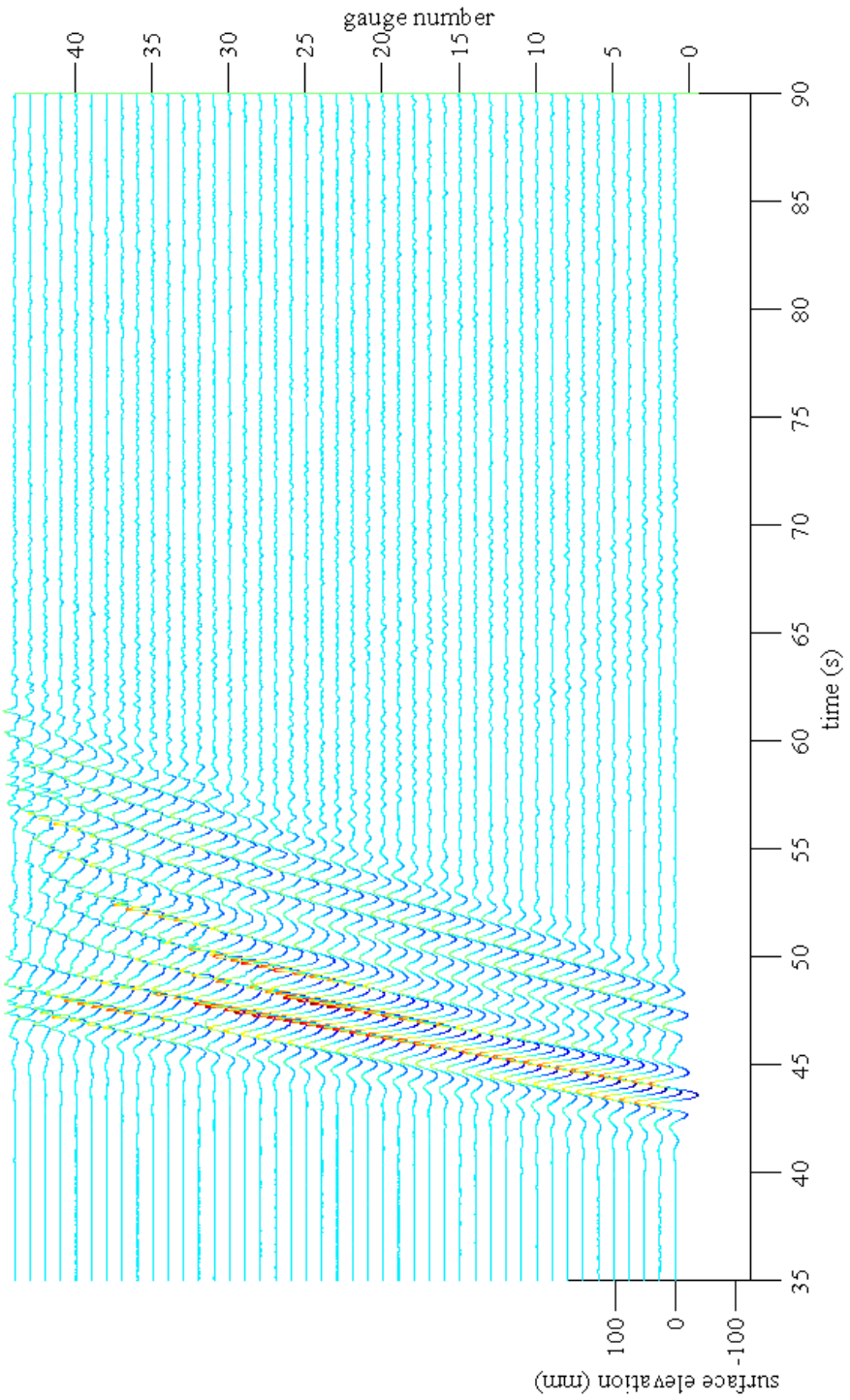

Figure 5.6: Stacked time histories of the addition of crest and trough focused wave groups, high frequency band-pass filtered at 0.5 Hz.

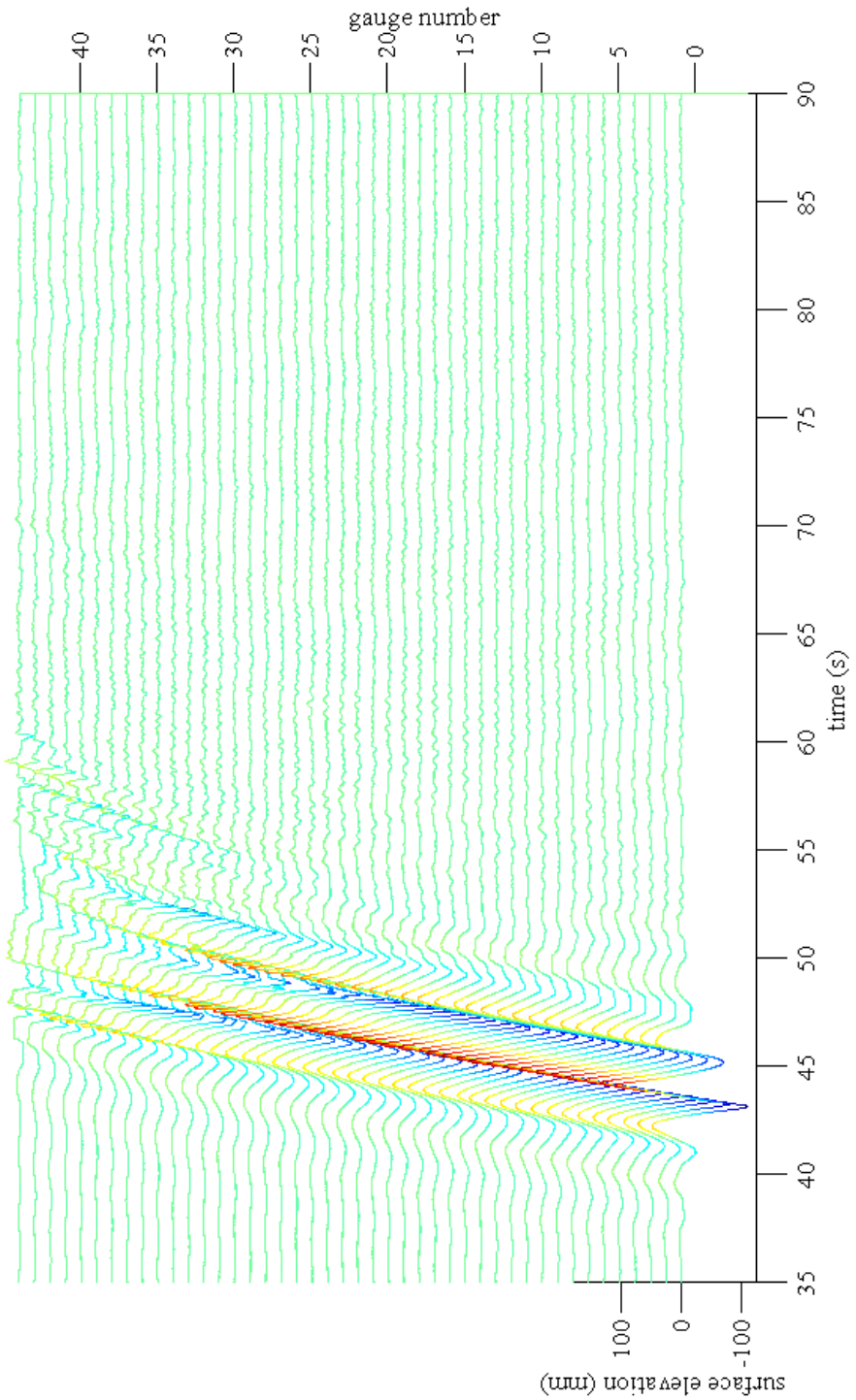

Figure 5.7: Stacked time histories of the subtraction of trough focused from crest focused wave group time series.

Further information may be gleaned by appropriately filtering these plots. Referring back to Figure 3.5, an appropriate place for a cut-off filter would be 1 Hz. This will split the linear group that peaks at 0.464 Hz from the third order harmonics around 1.39 Hz.

Low frequency band-pass filtered

Figure 5.8 shows the effect of applying a low pass filter at 1 Hz to the subtracted signals. Only the linear group is apparent. Noticeably, the distortion of the wave group in shallow water has been removed, leaving only a well-defined group of waves. Therefore the distortion in the shallow part of Figure 5.7 must have been due to third (or higher order) odd harmonics, rather than the effect of the failure of vertical time alignment of the crest and trough focused groups over the linear frequency range. Also, the waveforms appear not to exhibit any form of skew evident in Figure 3.4 for location D, which was not filtered to remove third order harmonics.

As in the case of high frequency second order waves, there is no evidence of any reflection of the linear group from the beach, implying that all this energy is used to drive some other local process.

High frequency band-pass filtered

Figure 5.9 shows the high pass signals of the subtraction series, i.e. third order harmonics. These are very small, relatively high frequency waves that disperse as they travel up the beach and then vanish in the surf zone.

5.1.5 Low frequency waves

In order to understand the generation mechanism of the low frequency wave it is necessary to carry out investigations into several aspects of its behaviour. The first aspect is the variation in size of the low frequency wave in the basin.

This is done for the initial low frequency parasitic (error) wave, the set-down (localised depression in sea level under a group), the released low frequency wave, and the reflected wave, for all unidirectional and spread sea cases. Figure 5.10 shows the four main long waves that are present in the basin, at three locations.

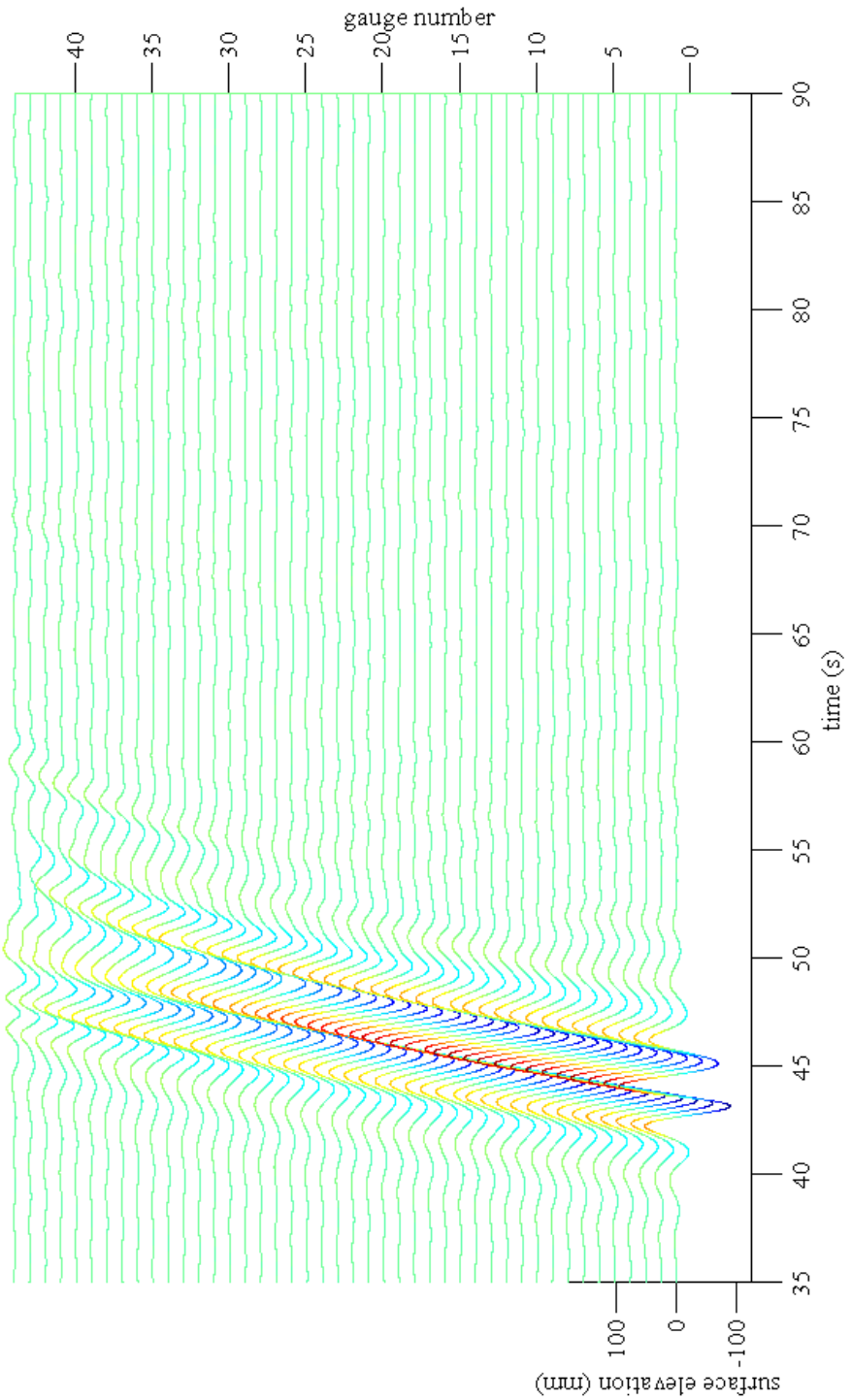

Figure 5.8: Stacked time histories of the subtraction of trough focused from crest focused wave group time series, low frequency band-pass filtered at 1 Hz.

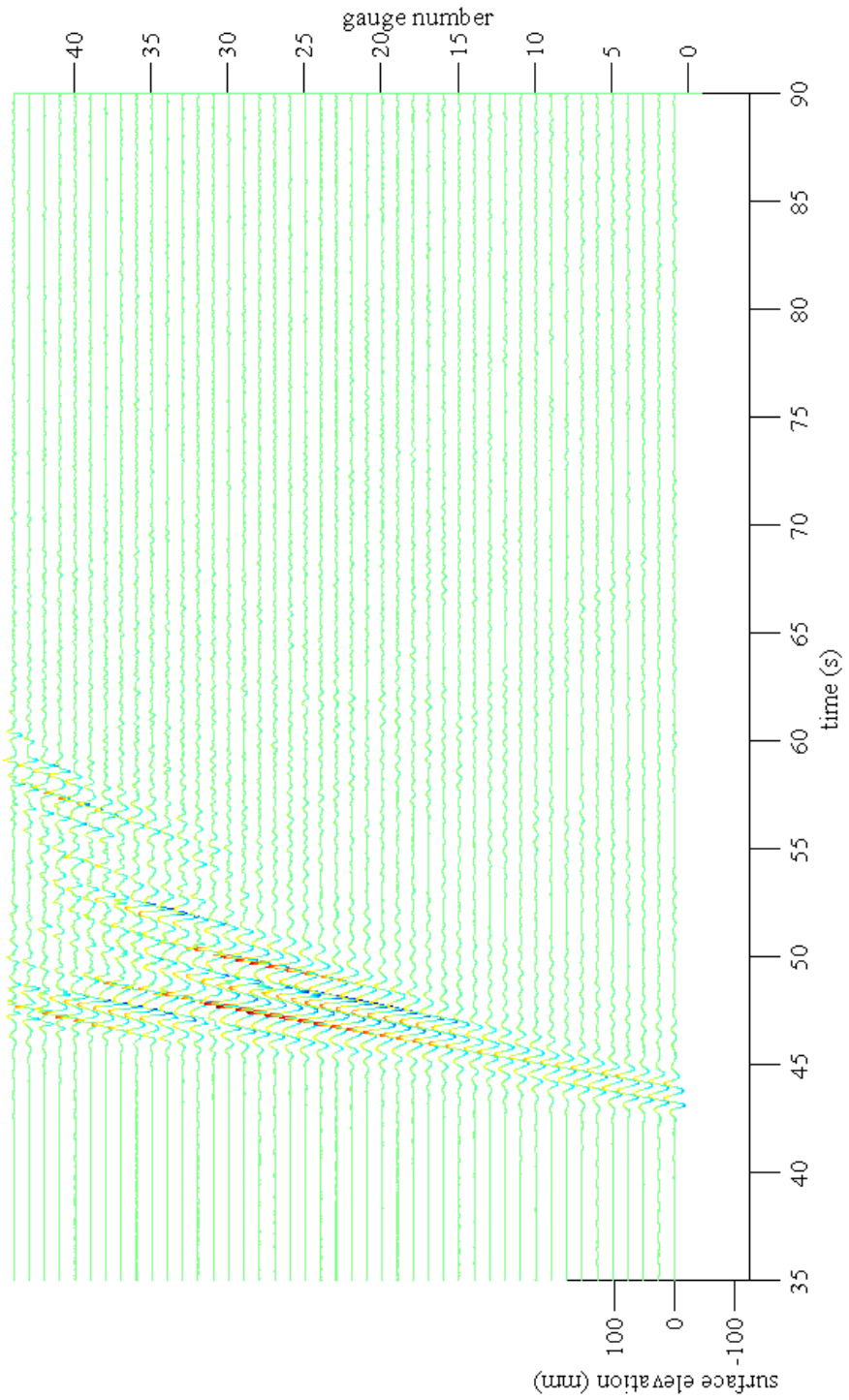

Figure 5.9: Stacked time histories of the subtraction of trough focused from crest focused wave group time series, high frequency band-pass filtered at 1 Hz.

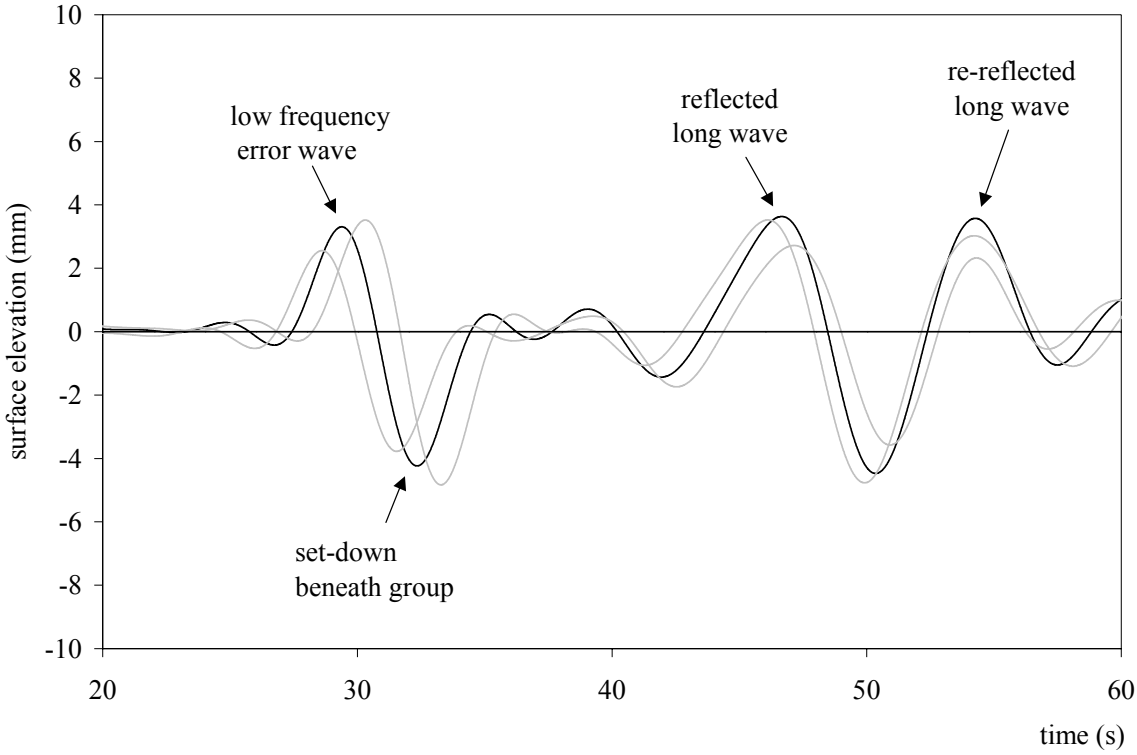

Figure 5.10: Long waves present in the UKCRF - dark line represents low frequency band-pass filtered time signal at toe, faint lines represent the signals from gauges 1.5 m either side.

Results will be presented from all 32 focused wave groups: WG 1 - WG 32. Details of these wave groups can be found in Appendices A1 and A2 and Chapter 2. The low frequency waves investigated in this section are obtained by adding the time series of the corresponding crest focused and trough focused groups, and low frequency band-pass filtering at 0.5 Hz.

Low frequency error wave

Figures 5.11 (a) to (d) show the size of the error wave that runs in front of the wave group and may influence the runup and overtopping experimental results discussed in the next chapter. Amplitude data are plotted against the dimensionless cross-shore distance. The value of zero on this axis corresponds to the toe of the beach and 1 corresponds to the still water shoreline.

It can be seen that for all these cases, there is a steady increase in the size of the error wave to a maximum closest to the shore-line.

Figure 5.11 (a) shows the large wave group that focuses at the toe of the beach. Each of the four series on this plot is for the same design wave i.e. a NewWave of crest amplitude 114 mm, focusing at a location of 8.33 m from the paddles (i.e. at the beach toe location). However, two are for unidirectional waves (one normally incident, one oblique) and the other two are for spread seas of different spreading factors ($\pm 10^\circ$ and $\pm 30^\circ$). In deeper water the error waves for both of the unidirectional cases are about the same size, though beyond about gauge 25 at a depth of 275 mm, the error wave from the normally incident wave becomes consistently larger. The error wave from the $\pm 10^\circ$ spread sea is around 2/3 the size of the unidirectional case and the $\pm 30^\circ$ spread sea case is about 1/3 the unidirectional case. This is to be expected because of the lateral structure of the wave group - the displacement of fluid beneath an energetic group (the long bound wave) is affected by the return flow beneath the group, which for spread sea cases can go sideways around the group as well as beneath i.e., it drives longshore transient currents. In the next chapter it will be seen that results from spread sea experiments are given some prominence due to the reduced size of the error

Looking now at Figure 5.11 (b), (c) and (d) which show three different wave group types, a similar pattern is evident. Figure 5.11 (b) is a large wave group that focuses 1/4 way up the beach i.e. in 3/4 maximum water depth. The input amplitude for this wave was again 114 mm. The error wave is of a comparable size as the large wave group focusing at the toe, for both the unidirectional and spread sea cases. Moreover, the reduction for spread sea cases is the same. Figure 5.11 (c) shows a 90 mm input wave group focusing halfway up the beach. A similar trend to Figures 5.11 (a) and (b) is observed, though the size of the error wave is much reduced. There is a comparable size of unidirectional cases and a smaller error wave for spread sea cases. Figure 5.11 (d) shows the size of the error wave for a 57 mm amplitude NewWave, focusing at the toe of the beach. The size of the error wave is now very small - less than 5 mm for most of the basin, but the same trends in reduction for spread seas is observed. The amplitude is close to the $\frac{1}{4}$ scaling consistent with 2nd order theory.

Set-down beneath wave group

As mentioned in the introduction of the thesis, the conventional definition of set-down is the depression of the water level seaward of the breaker line, associated with changes in the momentum flux due to wave shoaling and breaking. However the term can also be used to

describe the maximum depression in the apparent water level underneath wave groups. It is this second definition that will be investigated in this section. Figures 5.12 (a) to (d) show the size of the set-down beneath each of the wave groups. The set-down is shown as a negative displacement. Its amplitude increases up to a maximum value, then decreases to approximately zero closest to the shoreline. The position of the maximum value is dependent upon the input amplitude and degree of wave spreading. It is also dependent on the location of wave breaking which will be shown in the next chapter (see Figures 6.4 to 6.7).

Figure 5.12 (a) shows the set-down for the large focused wave of 114 mm input amplitude, focused at the toe of the beach. The amplitude of set-down is roughly the same for both unidirectional cases and the $\pm 10^{\circ}$ spread sea case. It reaches a maximum size of about -40 mm at about 60% the way to the still water shoreline. This in about 210 mm of water. Following this maximum set-down, it decreases quite rapidly to about zero closest to the shoreline. For the $\pm 30^{\circ}$ spread sea case the trend is identical to that of the unidirectional and $\pm 10^{\circ}$ spread sea case, but the magnitude is only around 2/3 of the size i.e. the maximum is approximately -28 mm. It must be mentioned that as the water depth decreases, it becomes increasingly difficult to measure the set-down (and the error wave and reflected waves) since the values become smaller and smaller, and hence less accurate.

Figure 5.12 (b) shows the set-down for the large wave with an input amplitude of 114 mm that focuses a quarter way up the beach. The values of set-down for all four wave types on the plot are the same as for the large wave focusing at the toe shown in Figure 5.12 (a).

Figure 5.12 (c) shows a 90 mm input wave focused halfway up the beach. The same trends are the same as 5.12 (a) and (b), though this time, all of the set-down values are reduced by approximately 15%. The peak of the set-down value occurs slightly closer to the shore.

Finally, Figure 5.12 (d) shows set-down for a 57 mm input amplitude group that focuses at the toe. Again, the set-down values for both unidirectional groups and the $\pm 10^{\circ}$ spread sea case are very similar and the set-down for the $\pm 30^{\circ}$ spread sea case is about 2/3 the value of those groups. The maximum value of the set-down for this smallest group occurs closest to the shoreline at about 75% up the beach from the toe. The maximum value of the set-down is about 25 mm - 60% of the value of the two largest wave groups.

The maximum value of the set-down is likely to be related to the location of wave breaking. Wave breaking will be investigated in the next chapter.

Reflected long wave

Figures 5.13 (a) to (d) show the size of the long wave that is released after the wave breaks on the beach. The first thing to note is that the size of this wave is smaller than either the error wave or the local set-down wave. It is only about half the size of the error wave and a little over a third the size of the set-down. Therefore it will be more prone to errors in measurement. The size of the reflected wave increases slightly for shallower water depths, reaching a maximum close to the shoreline before dropping sharply to zero and negative values for the last four gauges. Remember though that the reflected wave is transmitted from the beach and so actually travels from shallow to deep water, decreasing slightly in size. It can also be seen that, unlike the error wave and the set-down, the size of the reflected wave is clearly different for normally incident and oblique cases.

Figure 5.13 (a) shows how the size of the reflected wave varies for the largest wave group focused at the toe. At the toe, all values are of 10 mm or less, gradually rising to around 17 to 18 mm. The highest values are for the unidirectional waves: first normally incident, then oblique incidence, then the $\pm 10^\circ$ spread sea case with the smallest reflected wave occurring for the $\pm 30^\circ$ spread sea case. There are a restricted number of data points and not inconsiderable scatter, but there *does* appear to be some evidence of variation in the position of the maximum value of the reflected wave. For example the normally incident unidirectional wave group appears to be a maximum at a dimensionless distance of 0.775[2], whereas the wave group that gives the smallest reflected wave peaks at a distance of 0.85. The other two cases fall somewhere between and are a little difficult to distinguish. Figure 5.13 (b) which shows the reflected wave for the large wave focusing a quarter way up the beach shows the same trends and very nearly the same values as for Figure 5.13 (a). Figure 5.13 (c) shows the same pattern, but a reduction in the size of reflected wave, for the group that is a little smaller and focuses halfway up the beach. All but the $\pm 30^\circ$ spread sea case (which has a maximum at a dimensionless distance of 0.875) have their maxima at a distance of 0.825. Finally Figure 5.13 (d) shows the smallest reflected wave size, but the same pattern of decrease from unidirectional to spread seas. Again, the $\pm 30^\circ$ spread sea case has a maximum at the gauge furthest up the beach - this time between a dimensionless distance of 0.875 and 0.9. The other cases reach their maxima between about 0.825 and 0.85.

[2] These values were acquired from reading the graphs at a magnified scale.

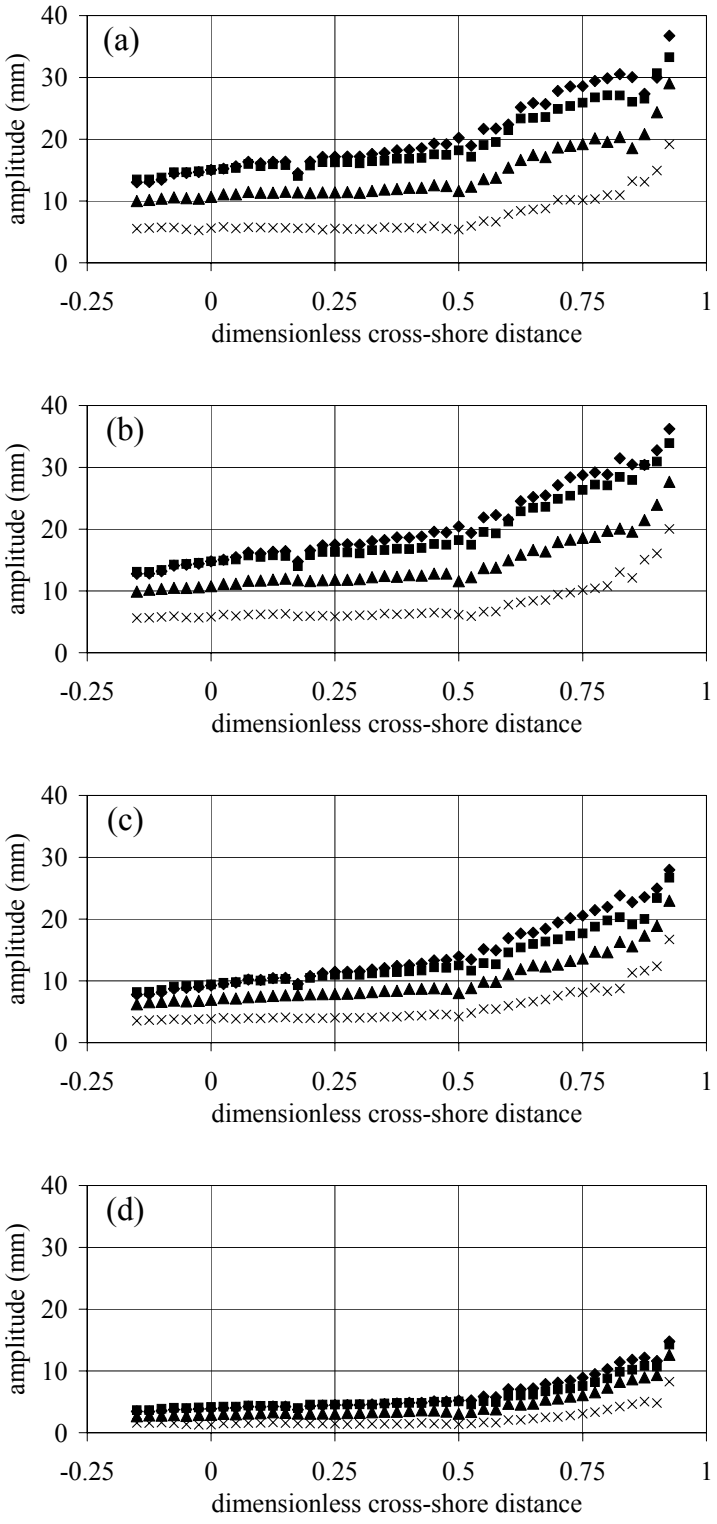

Figure 5.11: Size of error wave at all gauge locations for (a) large group focused at toe (b) large group focused at three-quarter depth (c) large group focused at half depth (d) small group focused at toe: ♦, unidirectional, normally incident; ■, unidirectional, oblique incidence; ▲, spread sea ±10°; ×, spread sea ±30°.

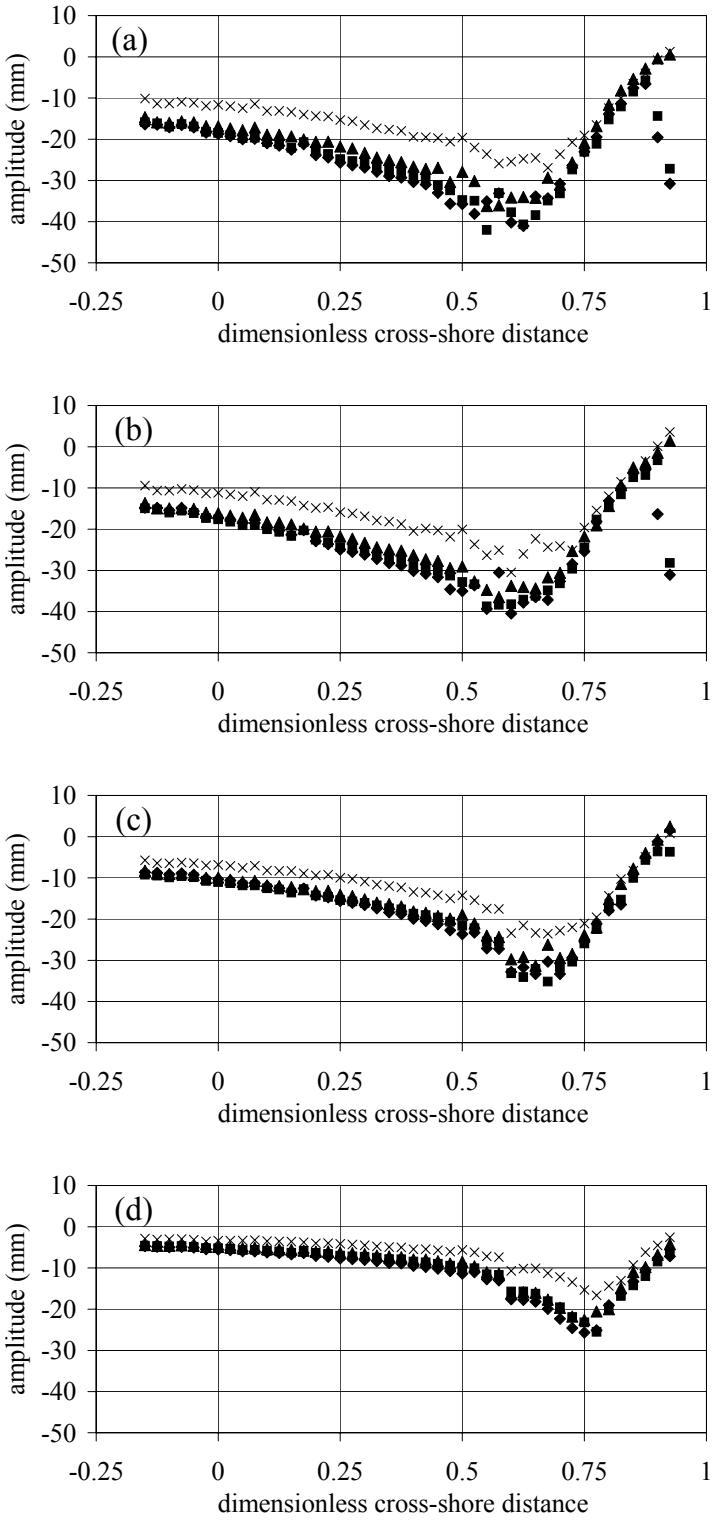

Figure 5.12: Size of setdown at all gauge locations for (a) large group focused at toe (b) large group focused at three-quarter depth (c) large group focused at half depth (d) small group focused at toe: ♦, unidirectional, normally incident; ■, unidirectional, oblique incidence; ▲, spread sea ±10°; ×, spread sea ±30°.

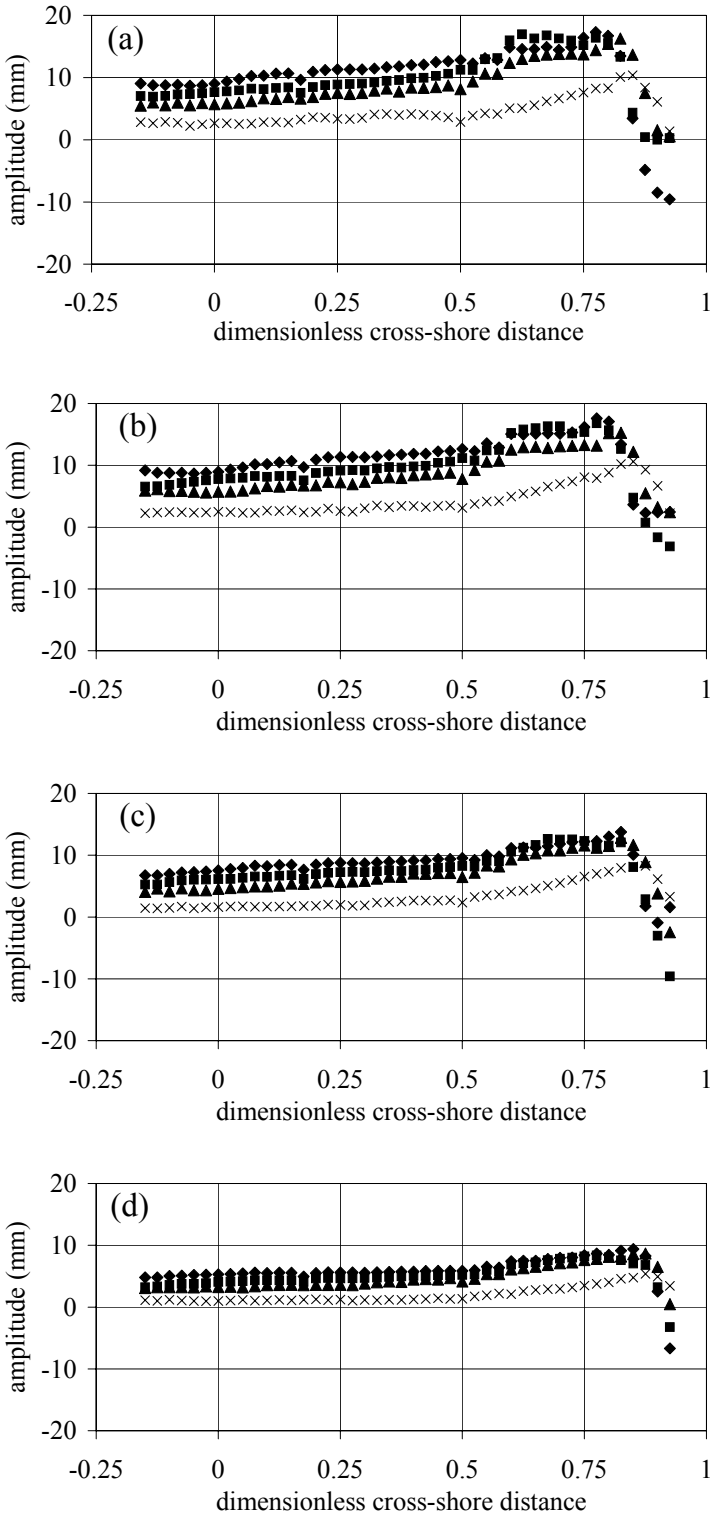

Figure 5.13: Size of low frequency reflected wave at all gauge locations for (a) large group focused at toe (b) large group focused at three-quarter depth (c) large group focused at half depth (d) small group focused at toe: ♦, unidirectional, normally incident; ■, unidirectional, oblique incidence; ▲, spread sea ±10°; ×, spread sea ±30°.

Comparison of size of low frequency wave with incoming wave group

The low frequency wave (LFW) that is generated when the incoming wave group breaks on the beach will be related in some way to the characteristics of that group. The exact dependence is governed by the generation mechanism of the LFW. As has been discussed earlier, several generation mechanisms have been proposed, some of which are complementary whilst others are not. Due to the low frequency error wave that precedes the wave group it will not be possible to completely disentangle the relationship between incoming group and LFW, but there is much information that may be obtained. Figures 5.14 (a) to (c) show how the size of the LFW compares with the size of the linearised group, the low frequency error wave and the set-down underneath the group, for unidirectional and spread sea cases. The measurement location for this analysis was chosen to be the toe of the beach. Each of the graphs of Figure 5.14 (a) to (c) show strong correlations between the LFW and the particular aspect of the incoming wave group. Figure 5.14 (a) shows an apparently linear relationship between LFW and linear envelope. Figure 5.14 (b) shows a more curved (square root like) relationship, and Figure 5.14 (c) more curved still. There are important points to note however. For each of the wave group types, i.e. normally incident, oblique incidence and spread sea, the relationships are of a similar nature, but results do not lie on the same line. As mentioned earlier, the preceding error wave adds confusion to the analysis, but looking carefully at Figure 5.14 (b), it can be seen that the error wave for the $\pm 30^{\circ}$ spread sea is around one-third the amount of the unidirectional cases and will therefore cause much less interaction. However, it is not known how the LFW of a spread sea focused wave group is related to the LFW of a similar unidirectional wave group.

Comparison of LFW for crest focus and trough focus groups

It is interesting to investigate whether the LFW is dependent upon the phase of the focused wave group, i.e. crest focused or trough focused, or whether it is related to the linear envelope. Figures 5.2 and 5.3 show evidence of the LFW, but the time series are contaminated by high frequency structure. In order to obtain a clearer picture it is necessary to filter out these high frequency data. Referring back to Figures 3.1 and 3.2 it would seem that a reasonably good cut-off frequency would be 0.3 Hz, in order to capture low frequency structure, but not the

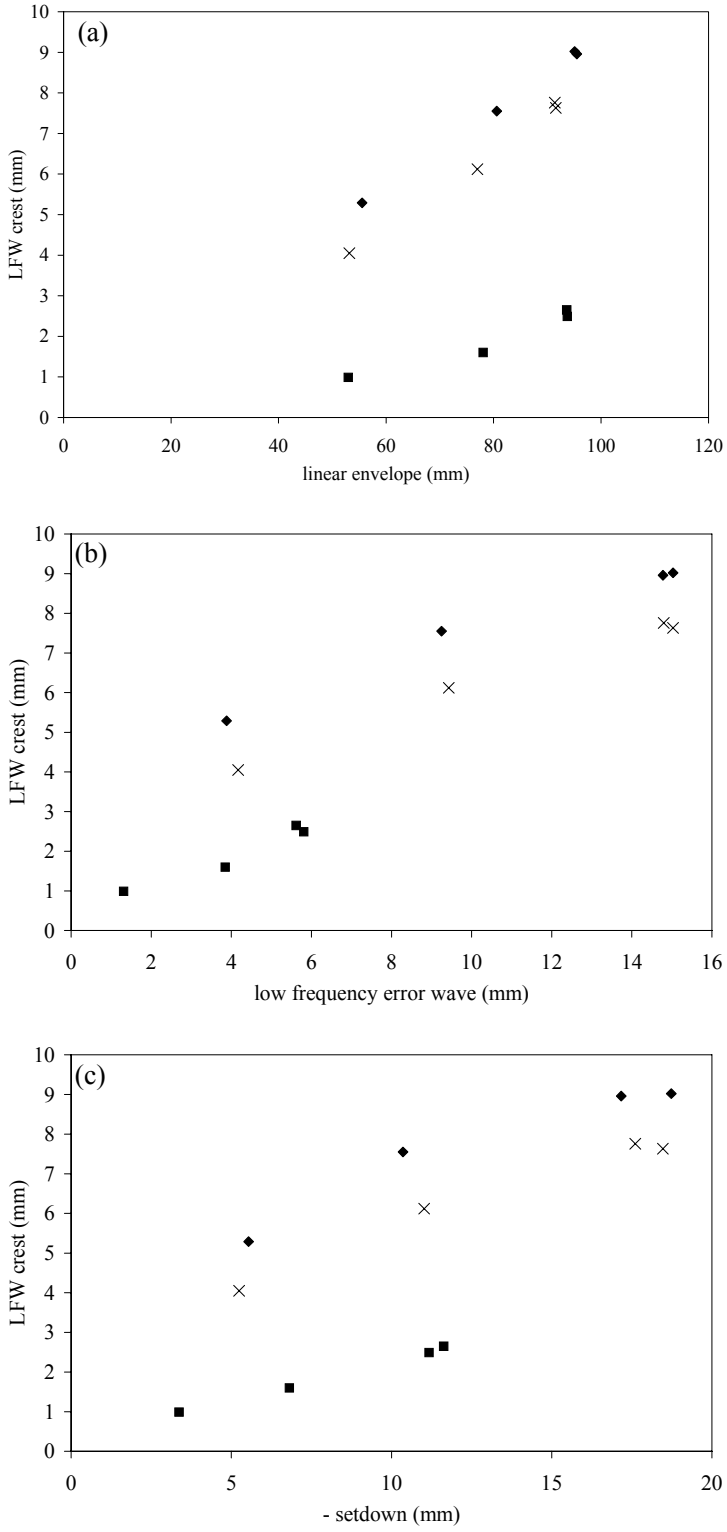

Figure 5.14: Size of low frequency wave reflected back off beach for 12 wave group pairs, as a function of (a) amplitude of linear envelope (b) amplitude of low frequency error wave and (c) magnitude of setdown beneath wave group: ♦, normally incident; ×, oblique incidence; ■, spread sea ±30°.

linear group. All filtered amplitude spectra use a linear ramp down to zero[3] to eliminate any problems associated with a sharp cut-off. This is particularly necessary in the case of Figure 3.2 where the amplitude spectra do not reduce to zero at 0.3 Hz. Figures 5.15 and 5.16 show the effect of applying the 0.3 Hz low pass filter to the crest focused and trough focused wave groups, respectively.

At first glance it would seem that Figures 5.15 and 5.16 are very similar, but there are some subtle differences:

- the error wave of the crest focused wave group is wider than the corresponding wave of the trough focused group
- the trough of the LFW is deeper for a trough focused group than for a crest focused group
- the LFW of the trough focused group lags that of the crest focused group, by about two seconds (at the gauge closest to the paddles)

The last two points are evidence of a phase lag of the trough focus LFW compared with the crest focus LFW. To further compare the differences between these two LFWs Figure 5.17 shows the effect of subtracting the LFW from the trough focused group from the LFW of the crest focused group. Figure 5.18 shows the same data but at a larger scale.

One point of note in Figures 5.17 and 5.18 is the relatively large crest closest to the shoreline. This is a result of the larger 'width' of the error wave for crest focused groups. The other obvious feature is the large number of long wave oscillations compared with the crest focused and trough focused cases. This is simply as a result of the size and phases of the LFW waves being slightly different for the two cases.

The fact that there are some phase differences between the crest and trough focused LFWs means that the technique of obtaining an LFW by adding the crest and trough focused time series and applying a low-pass filter needs to be used with care i.e. the LFW of Figure 5.5 is an averaged LFW with some of the phase information being lost.

[3]The linear ramp was applied over 0.0977 Hz or 0.1953 Hz depending on the nature of the amplitude spectra. These frequency ranges correspond to 8 and 16 data points respectively.

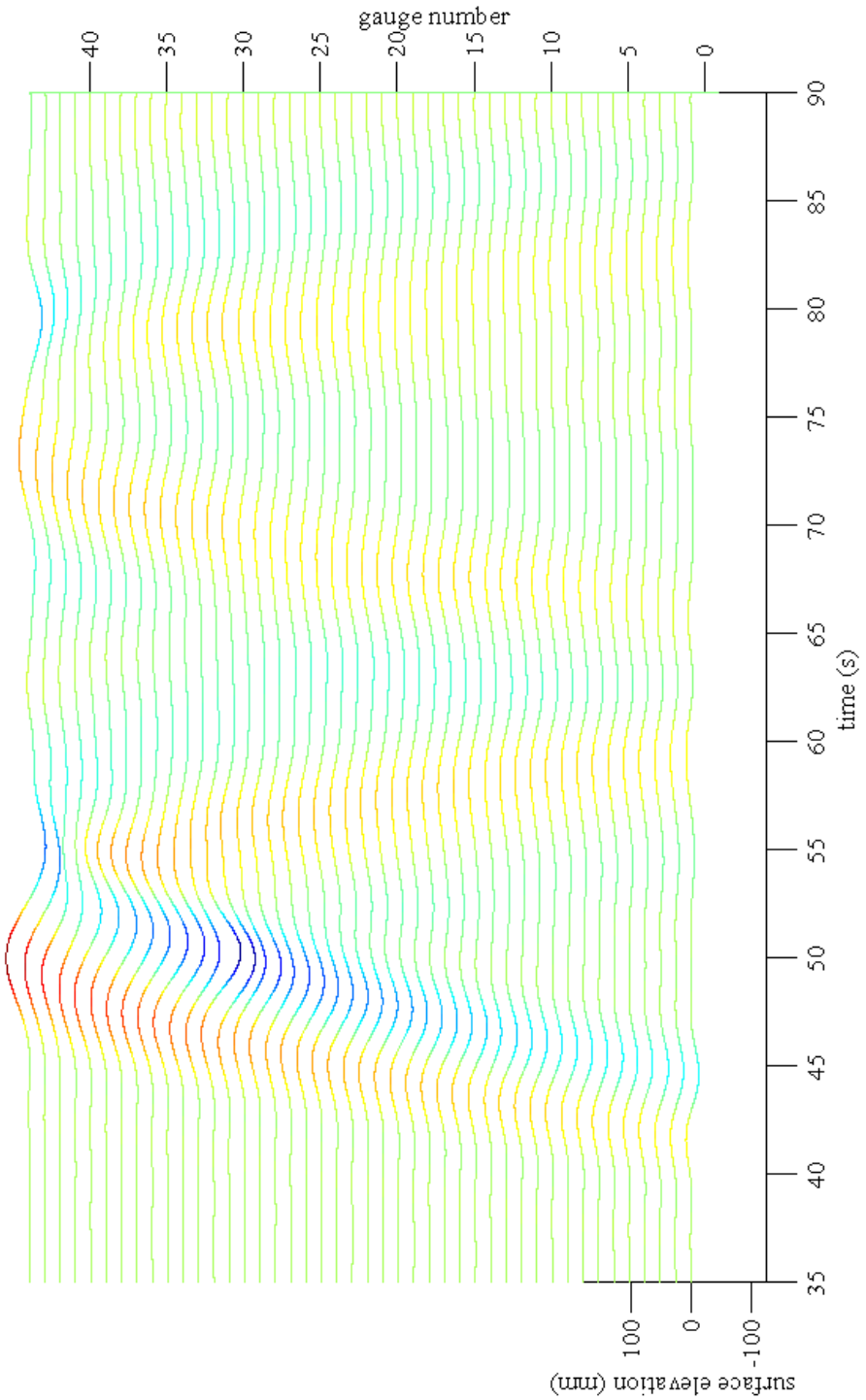

Figure 5.15: Stacked time histories of a crest focused low frequency wave.

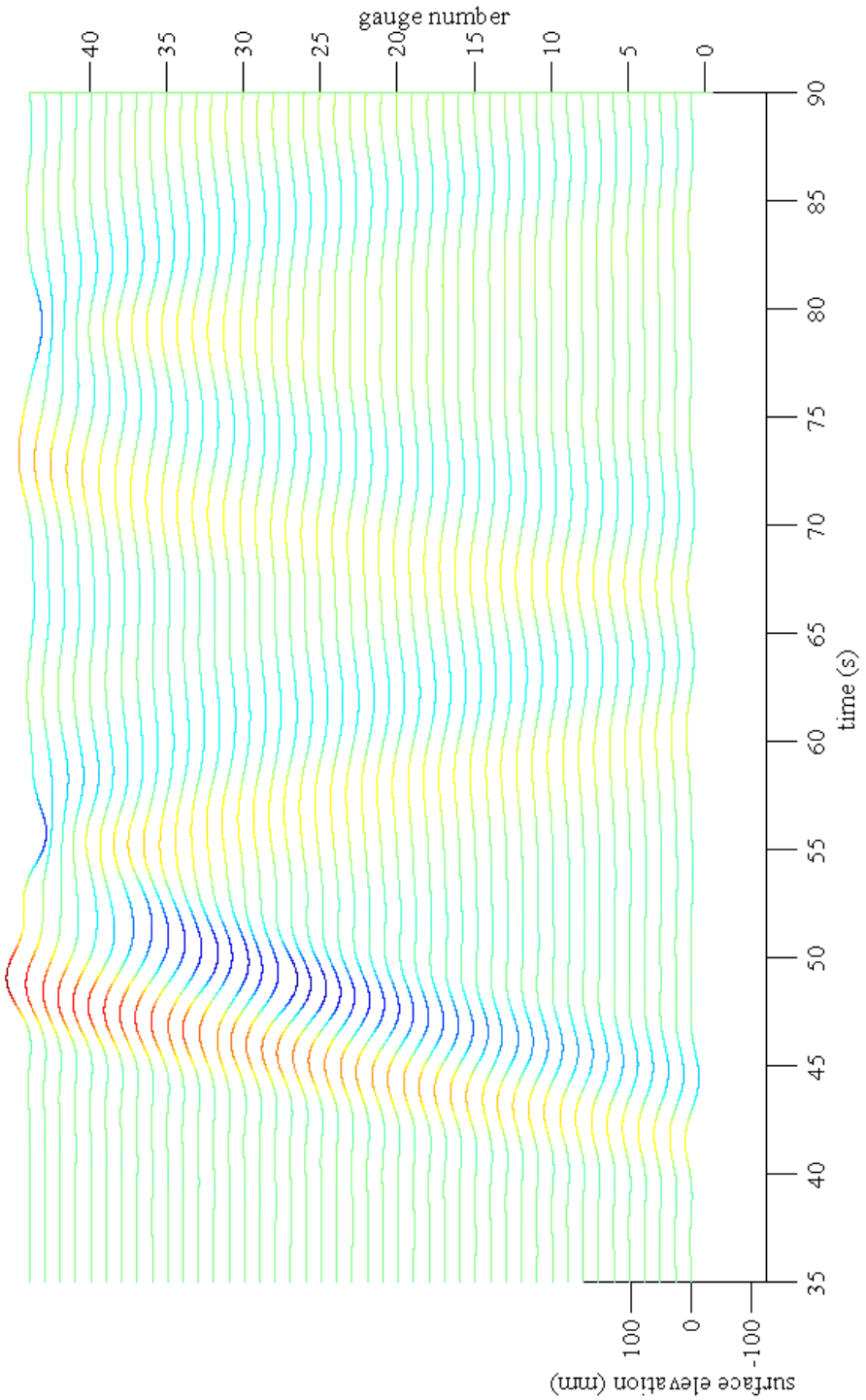

Figure 5.16: Stacked time histories of a trough focused low frequency wave.

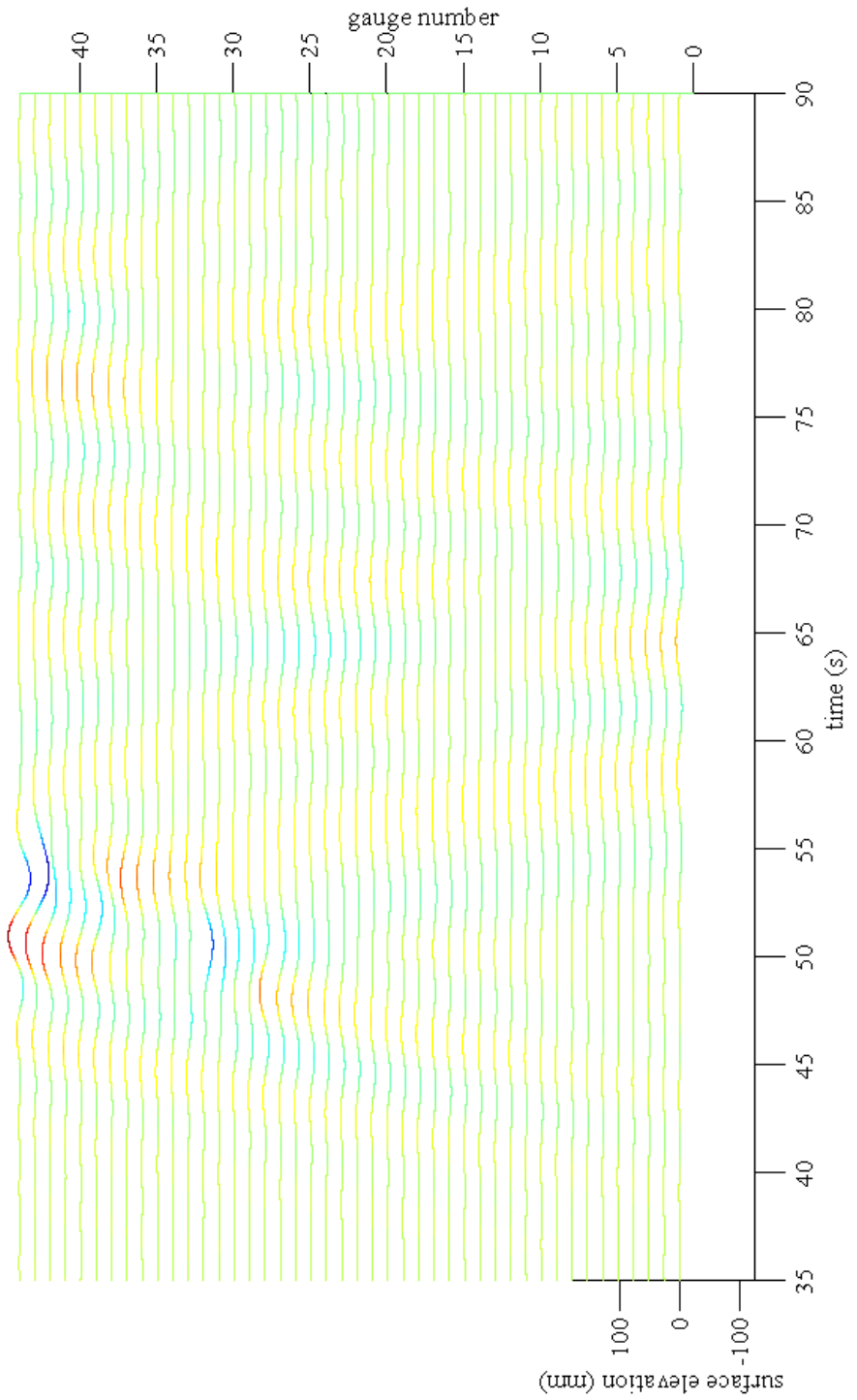

Figure 5.17: Stacked time histories of crest focused wave low frequency wave minus trough focused low frequency wave.

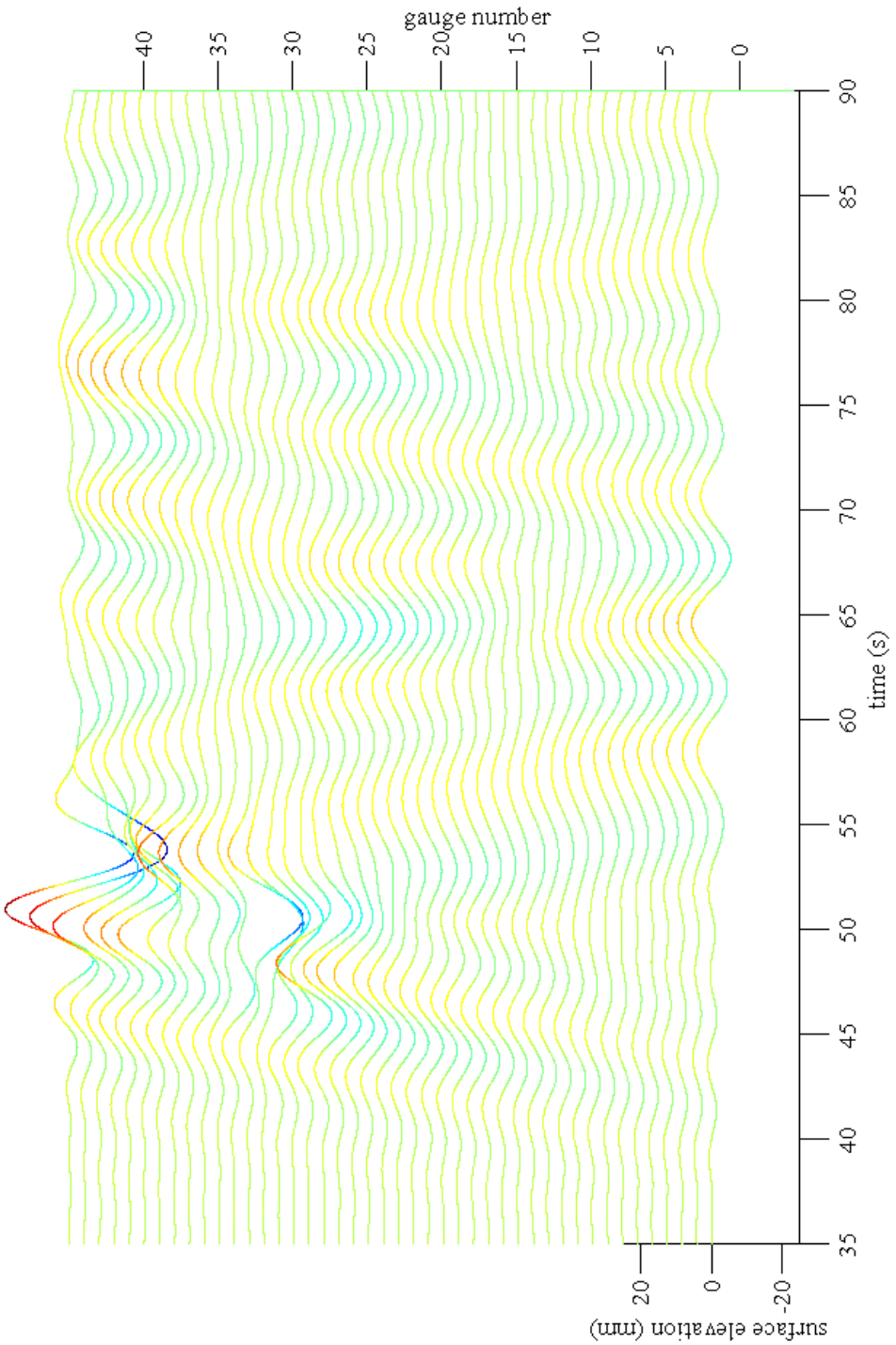

Figure 5.18: Stacked time histories of crest focused wave low frequency wave minus trough focused low frequency wave, elevation scale $\times$ 5.

5.1.6 Conclusions

The most obvious finding of the wave visualisation work is that there are *no* high frequency reflections, but low frequency waves both generated at the beach and reflected off the beach. These then continue to reverberate around the basin. The low frequency error wave generated by the paddles is considerably reduced for spread seas as would be anticipated. The high frequency waves are all dissipated in the wave breaking process.

The size of the local set-down beneath the incoming wave group reaches a maximum value which is associated with wave breaking.

The low frequency wave (LFW) generated after the wave group interacts with the beach reaches a maximum value, the position of which is determined by the size of the input amplitude of the group. Also, the temporal and spatial properties of the LFW are dependent on the phase of the wave group.

Re-reflections of the LFW are considerable.

5.2 Focused wave group interacting with a sea wall

The construction of a sea wall at the UKCRF was done primarily to investigate overtopping of waves. However, it can serve a secondary purpose of investigating how a slope steeper than the beach (1:20) affects the wave group structure. Barnes (1996) compared the generation of LFWs due to a wave group on slopes of 1:20 and 1:100. He found that the more gentle slope dramatically reduced the size of the LFW, probably due to greater energy dissipation. The converse may be true: a steeper slope generates a larger LFW.

5.2.1 Sea wall structure

The sea wall is described in detail in Chapter 4. It has a front slope of 1:2.17 (i.e., an order of magnitude steeper than the plane beach). The sea wall is built on top of the plane beach and the toe of the wall stands in approximately 10 cm of water. Therefore the waves interact with the beach, but generally do not break until they interact with the wall. Virtually all the waves in the main group then proceed to overtop the wall. In order to minimise erroneous results due to lost volumes of water the wave groups that will be investigated in this section are less than half the size of the wave groups used in the previous section, though they still have a focus location at the toe of the beach.[4]

5.2.2 Gauge placement for sea wall experiments

The gauge locations were different for the experiments carried out with the sea wall in place. Wave gauges were placed at half the previous spacing distance in the deep water, then at appropriate positions for measuring depth of water overtopping the sea wall and being captured on the leeward side of wall. Therefore the results shown in stacked plots in this section, have been interpolated in space to give time histories that coincide with those obtained without the wall, but they cease about 1.5 m before the toe of the wall (see Table C3, Appendix C for gauge locations). This interpolation process is undertaken at the final display stage, *not* with the original data, which would have led to phase errors.

[4] The wave groups are numbers 4 and 8, and have parameters defined in Appendix A1.

5.2.3 Crest and trough focus time series

Figures 5.19 and 5.20 respectively show stacked time histories of the crest and trough focused wave groups.

The primary difference between Figures 5.19 and 5.20 and Figures 5.2 and 5.3 are the large number of reflections present. This is to be expected since the reflection coefficient of the steeper wall will be far greater than that of the beach.

Figure 5.21 shows the time series and respective amplitude spectra for the crest focused wave group, at four locations in the basin[5]. Whilst the time series of the focusing event remain uncorrupted by reflections there is a great deal of additional structure in the amplitude spectra, at all frequencies. A similar picture is shown for the trough focused group in Figure 5.22.

5.2.4 Addition time series

The separation of harmonics method presented in section 3.3.2. showed that the addition of the crest and trough focused wave group time series yields even harmonics. The time series and amplitude spectra for this operation are shown in Figure 5.23. Fortunately there appears to be a natural trailing off of the amplitude spectra at 0.5 Hz. This can then be used, as before, as a point at which to filter the spectrum. Figure 5.25 shows the stacked time histories for the low frequency band-pass filter, and Figure 5.26 shows the effect of a high frequency band-pass filter.

Figure 5.25 shows a remarkably clean picture of the low frequency waves that looks very similar to that obtained in the previous section (see Figure 5.5), with no sea wall. The main differences between this LFW with the sea wall is that it is larger despite the smaller input amplitude, and the point of reflection is clearly visible within the stacked time histories because the LFW came from the sea wall which was offshore of the still water shoreline. Figure 5.26 shows the high frequency band-pass filtered 'addition' time signals. There is a marked contrast to the corresponding plot obtained with no sea wall in place in Figure 5.6. With the sea wall in place the high frequency second order harmonics are reflected back off the wall, unlike when there was no wall present and there were no high frequency reflections. This is probably due to the fact that there is so much less breaking of the incident waves.

[5] Gauge locations are shown in Figure 3.3.

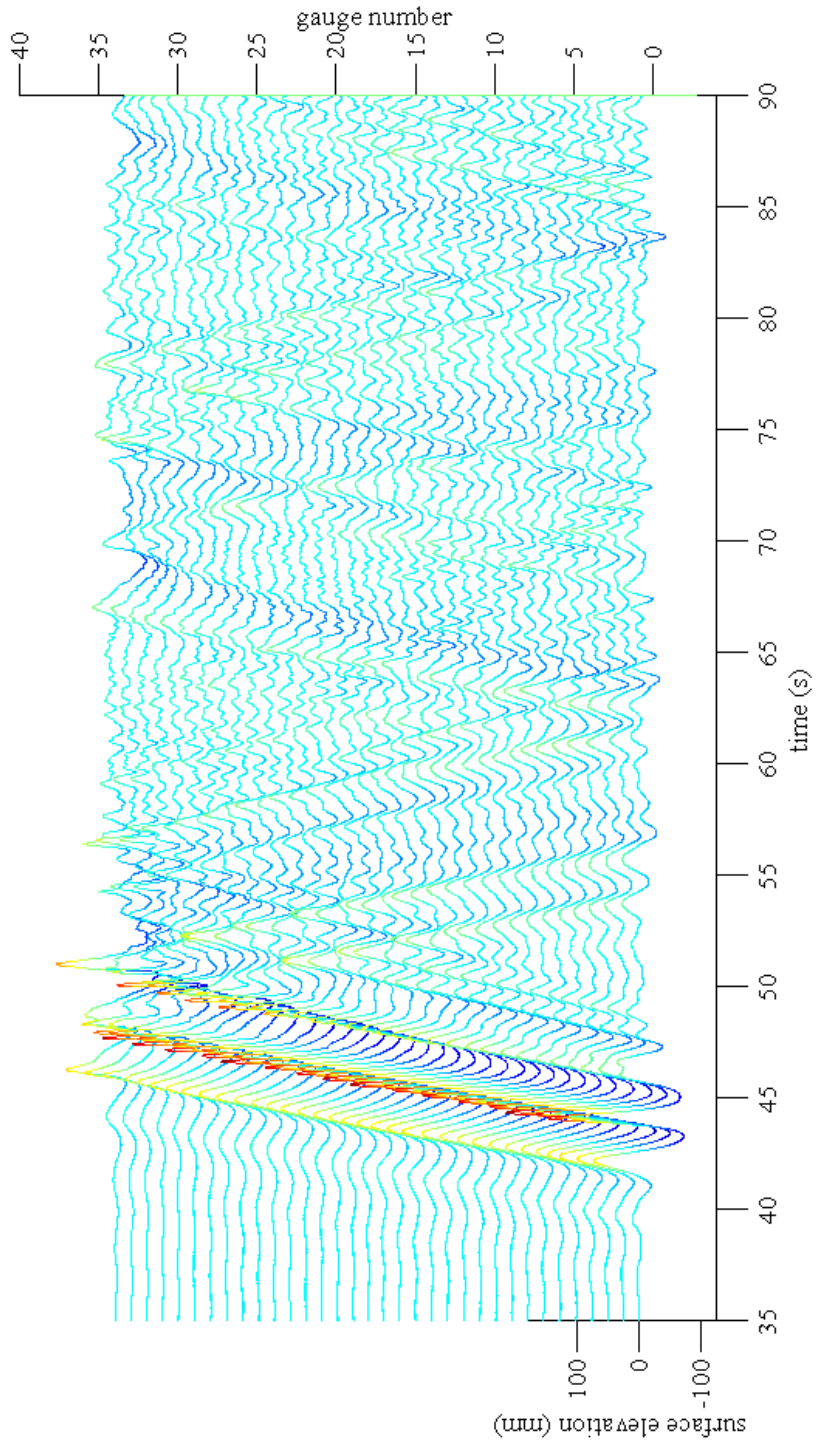

Figure 5.19: Stacked time histories of a crest focused wave group, with sea wall in place.

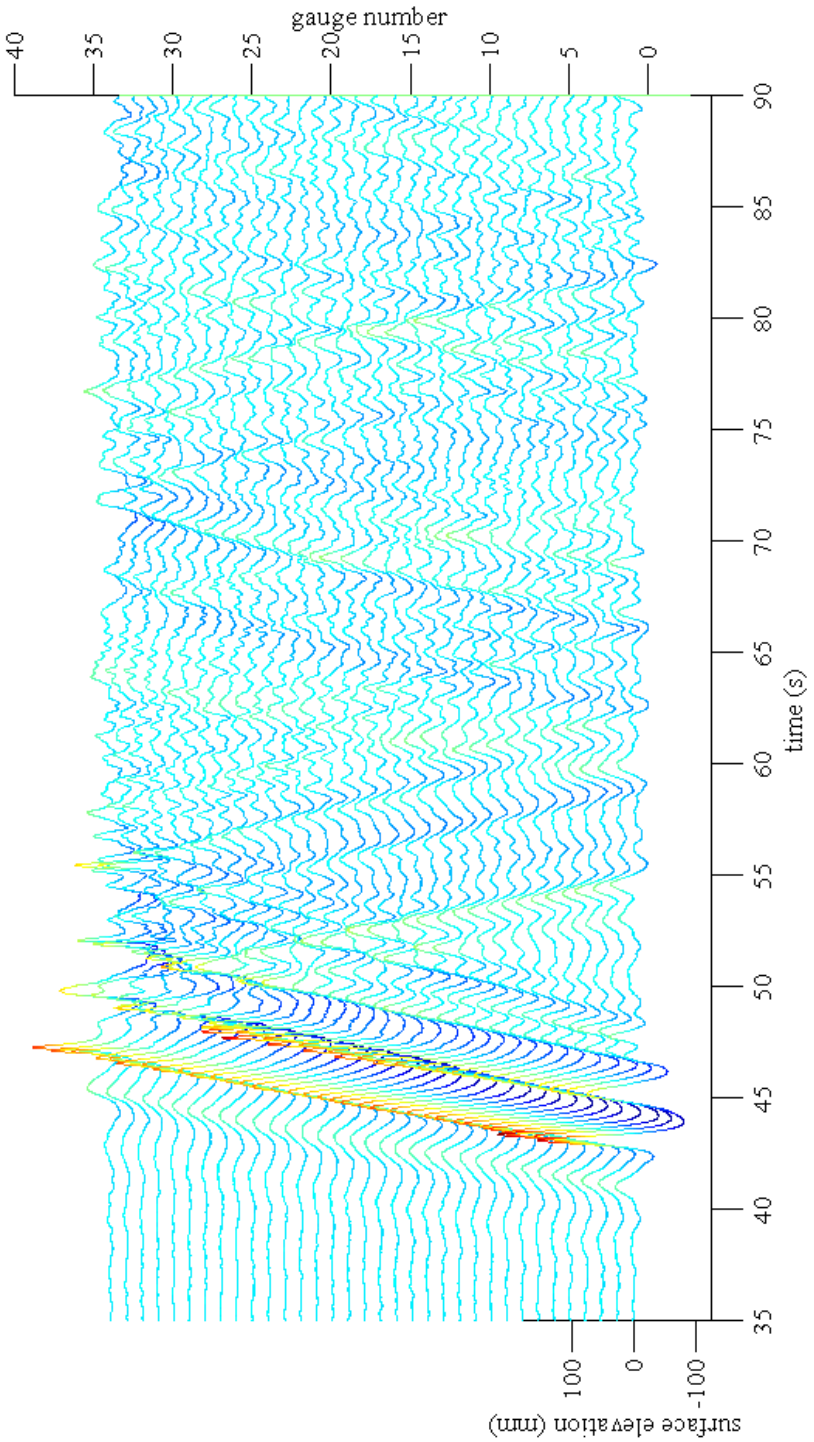

Figure 5.20: Stacked time histories of a trough focused wave group, with sea wall in place.

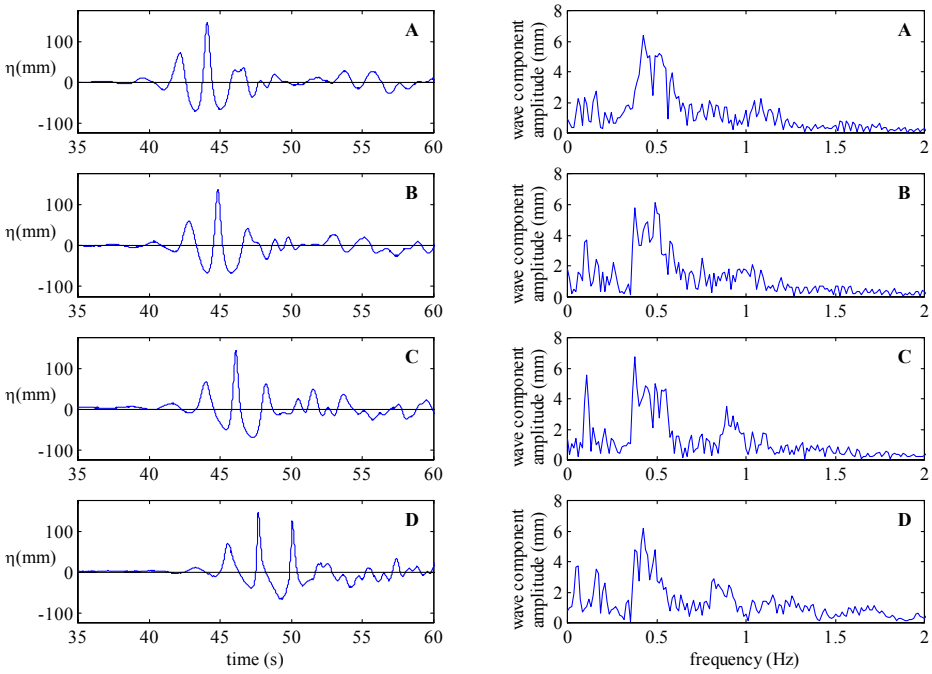

Figure 5.21: Time histories and amplitude spectra of a crest focused wave group at locations A, B, C and D, with sea wall in place.

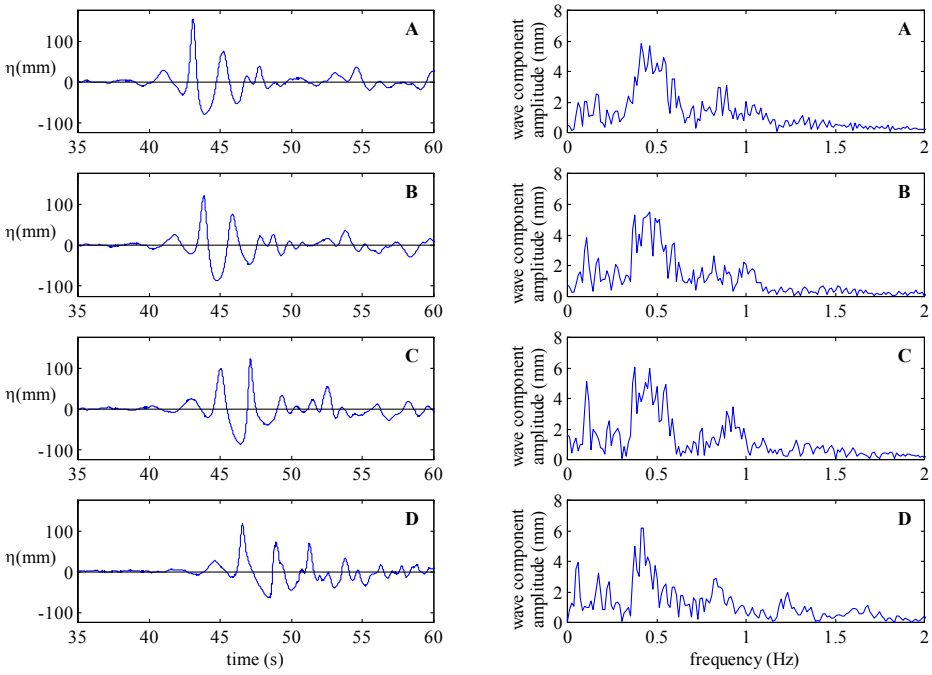

Figure 5.22: Time histories and amplitude spectra of a trough focused wave group at locations A, B, C and D, with sea wall in place.

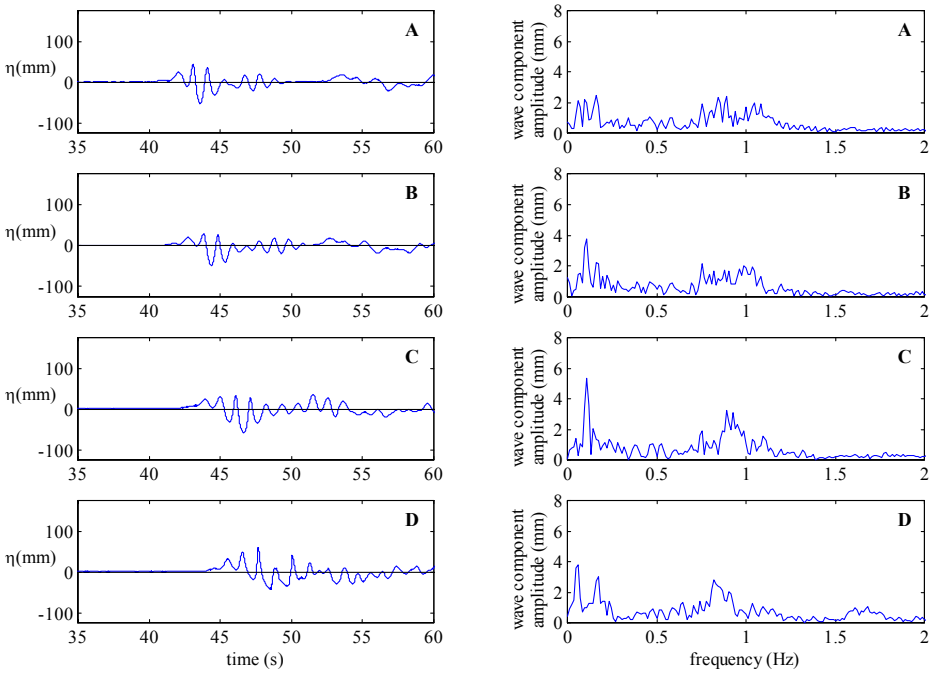

Figure 5.23: Surface elevation time histories and amplitude spectra of 'addition' terms, with sea wall in place.

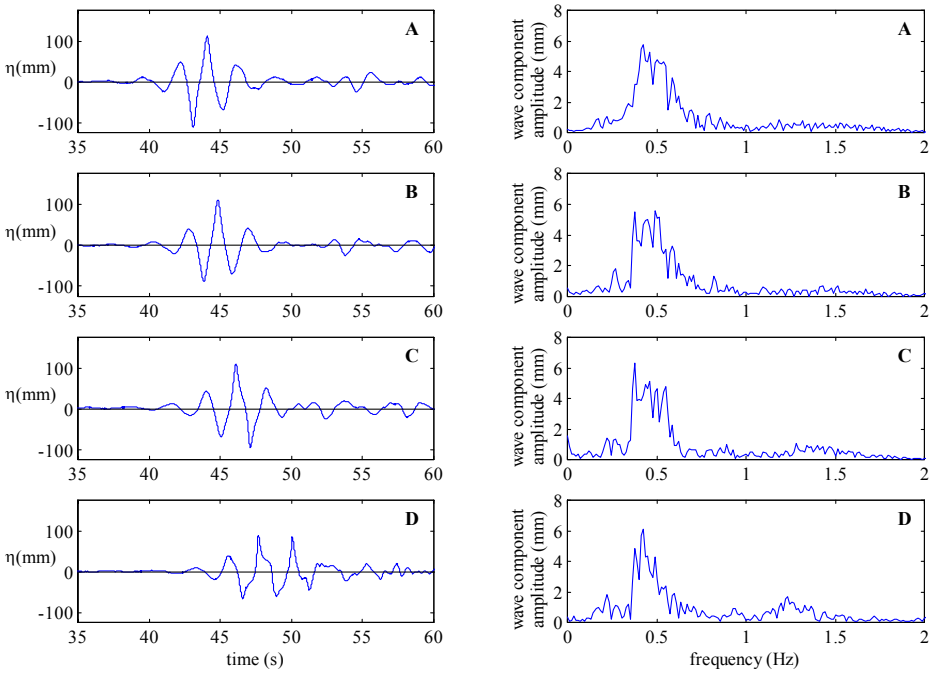

Figure 5.24: Surface elevation time histories and amplitude spectra of 'subtraction' terms, with sea wall in place.

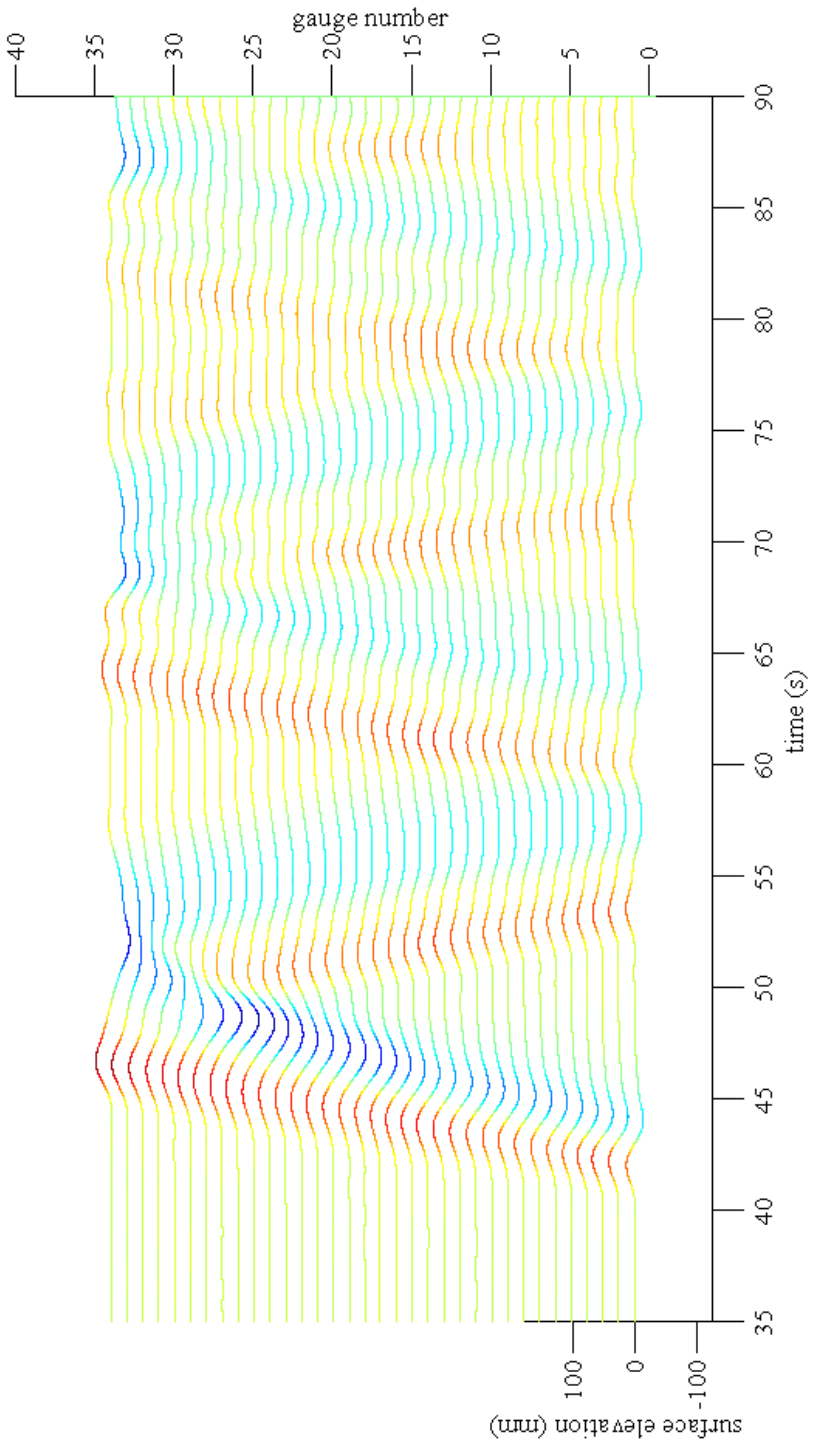

Figure 5.25: Stacked time histories of low frequency band-pass filtered 'addition' terms, with sea wall in place.

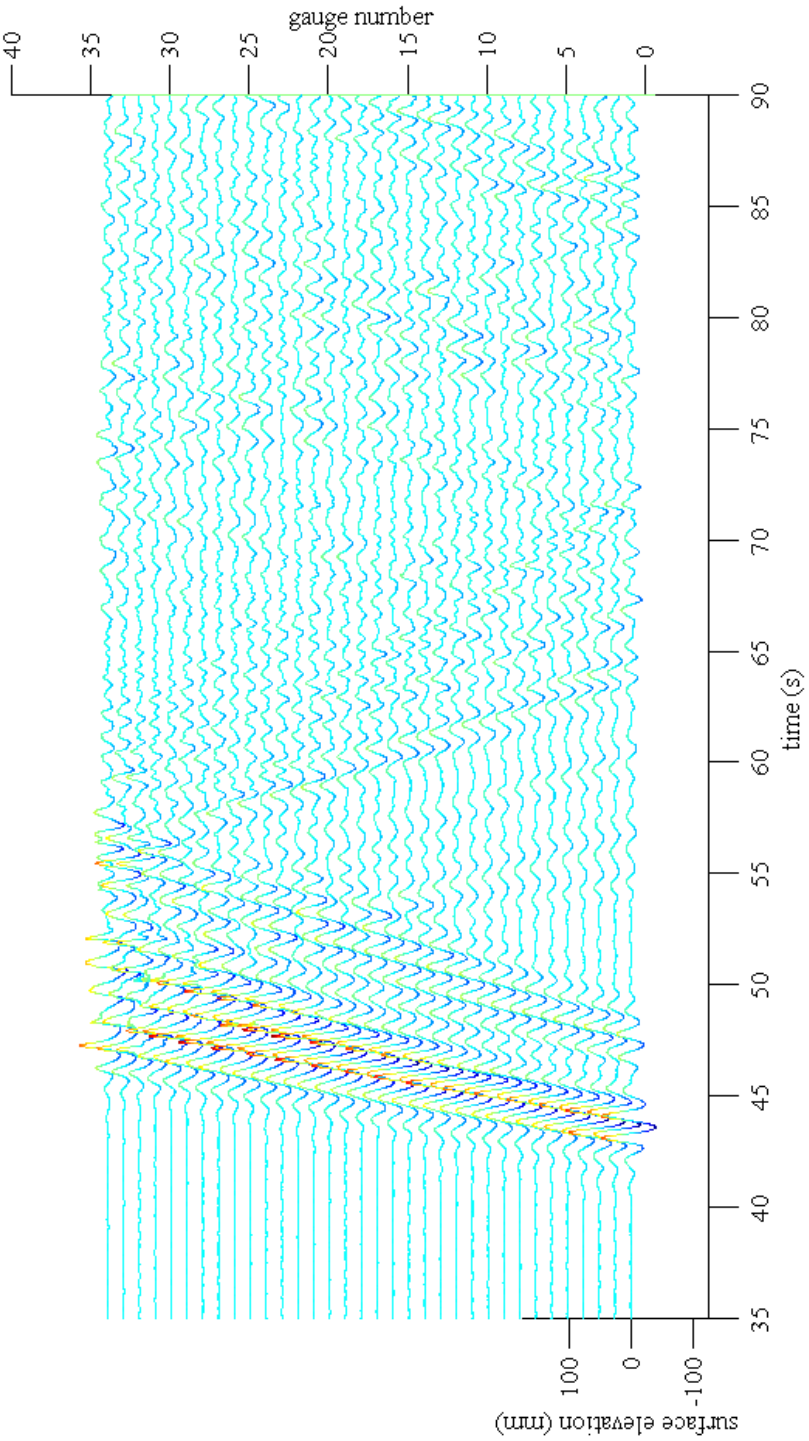

Figure 5.26: Stacked time histories of high frequency band-pass filtered 'addition' terms, with sea wall in place.

Some of the offshore moving double frequency components may be free waves - resulting from the release of 2nd harmonic bound harmonics from the linear waves during reflection.

5.2.5 Subtraction times series

The subtraction of a trough focused wave group from a crest focused wave group should yield the linear group and odd higher order harmonics. Figure 5.24 shows the times series and amplitude spectra at four locations in the basin. Whilst extraneous structure is obviously visible in the amplitude spectra, it appears to be less than that in Figure 5.23. Figures 5.27 and 5.28 show stacked time histories for a 1 Hz low pass filter and high pass filter respectively.

Figure 5.27 shows the linear group, but unlike in Figure 5.8 which showed the linear group interacting with a beach, there are significant reflections coming off the sea wall. The same is true for Figure 5.28 which shows high (triple) frequency reflections coming off the wall (in contrast to Figure 5.9).

5.2.6 Longshore variation of low frequency wave

It is interesting to investigate how the size of the LFW varies in the longshore direction for the cases of spread seas, since real waves that impact beaches are generally multidirectional. Figure 5.29 shows how the LFW varies at two depths in the basin for WG17 (see Appendix A2), the $\pm 30^{\circ}$ case, with the wall in place[6]. The gauge layout for this experiment is given in Appendix C, Table C4. Also plotted is the variation of the linearised group[7] in the longshore direction, for comparison purposes. It can be seen that at the toe of the beach the amplitude of the linearised wave group is a maximum at the centre-line of the basin, falling steadily along the longshore direction. This is to be expected as the $\pm 30^{\circ}$ wave group has a relatively small focused width. At the halfway depth the linearised group amplitude does not fall as sharply as at the toe of the beach. This is due to the gradual spreading of the wave after the focus location. The LFW for both the toe of the beach and the half depth location vary very little in the longshore direction. The greater variability in the points is due to the absolute error in the small measurements being more significant.

[6] It was necessary to use data acquired with the wall in place since a larger LFW is generated which enables more accurate comparisons to be made. For this spread sea case there was negligible overtopping.

[7] The term linearised refers to the low frequency band-pass filtered 'subtraction' time series, which has all sub- and super-harmonics removed. Refer back to section 3.3 for details.

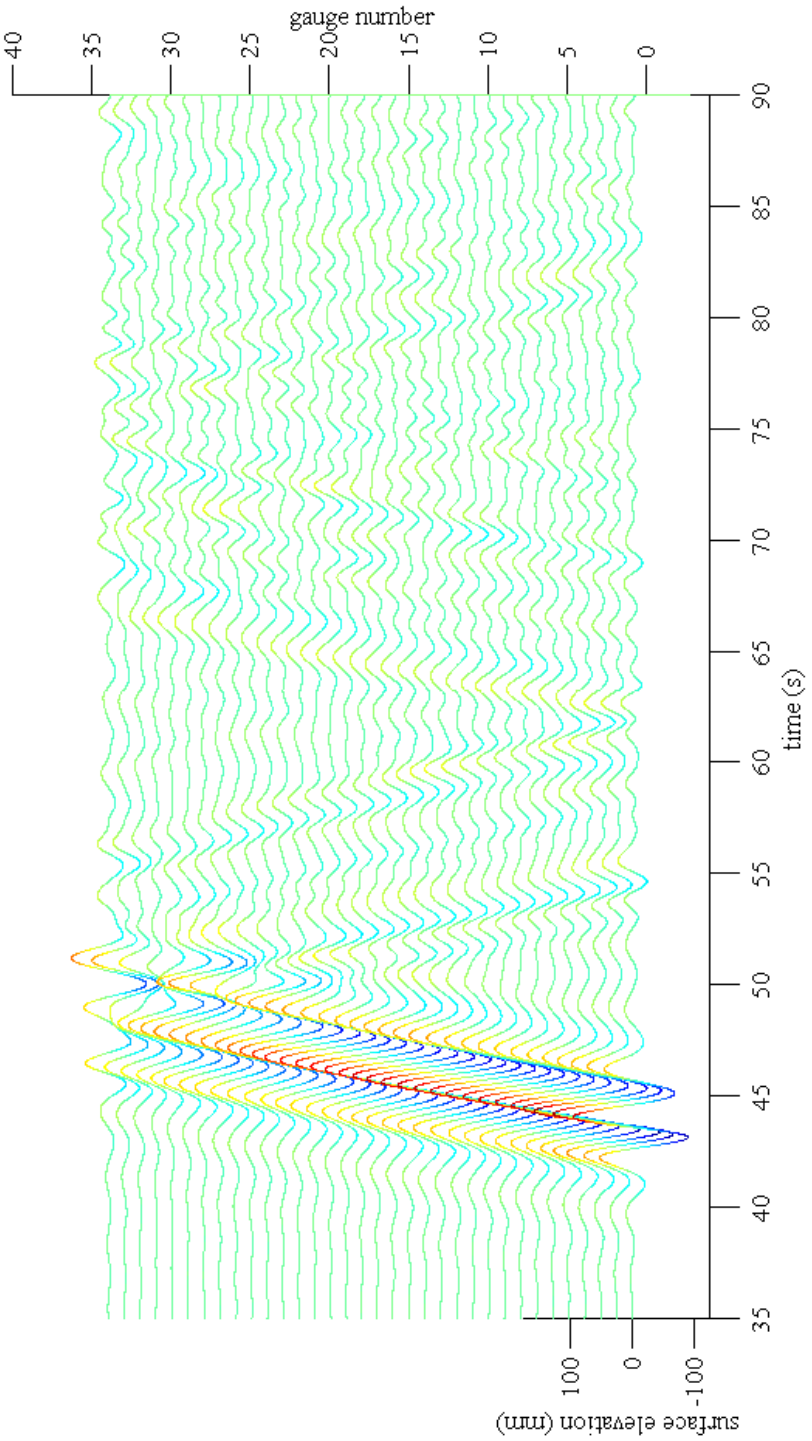

Figure 5.27: Stacked time histories of low frequency band-pass filtered 'subtraction' terms, with sea wall in place.

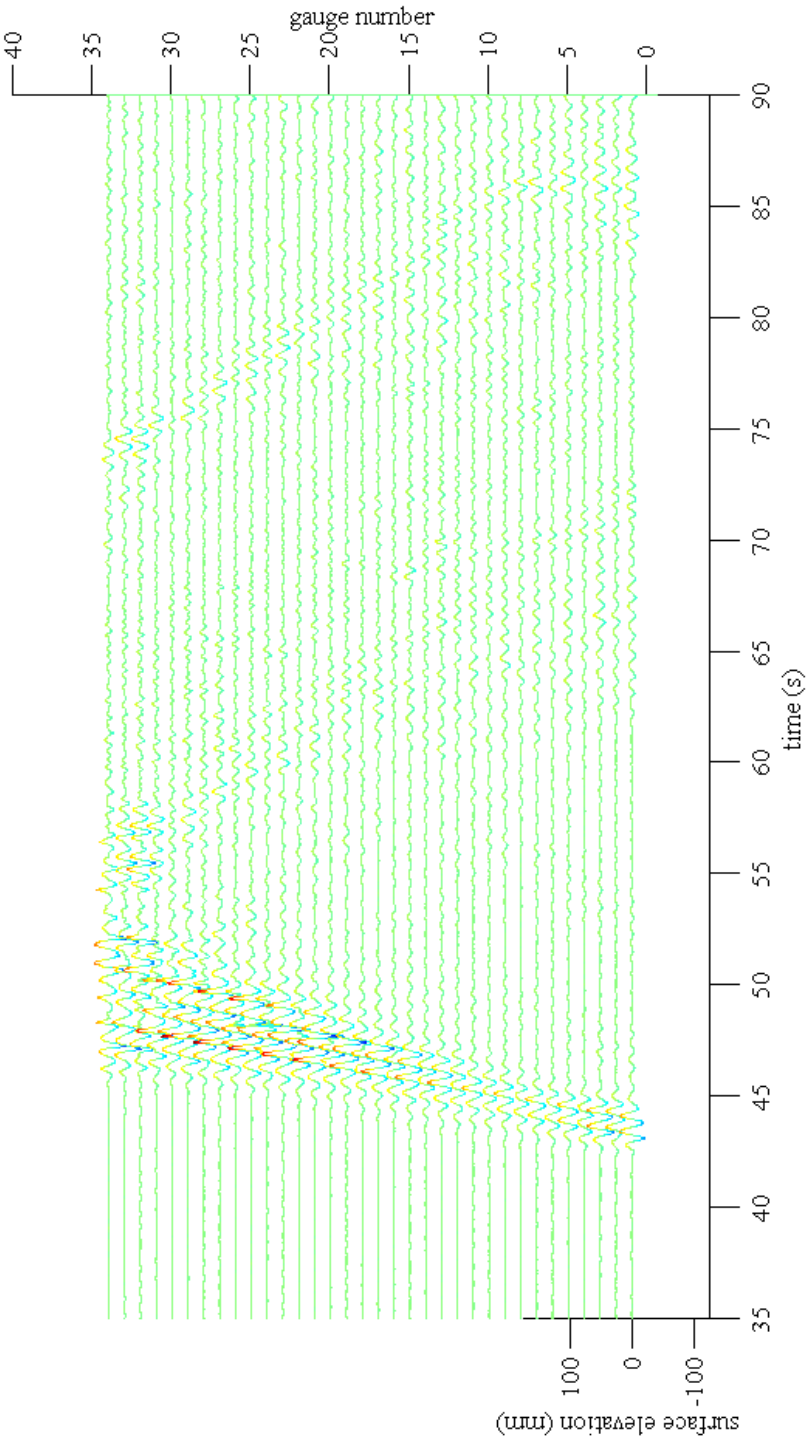

Figure 5.28: Stacked time histories of high frequency band-pass filtered 'subtraction' terms, with sea wall in place.

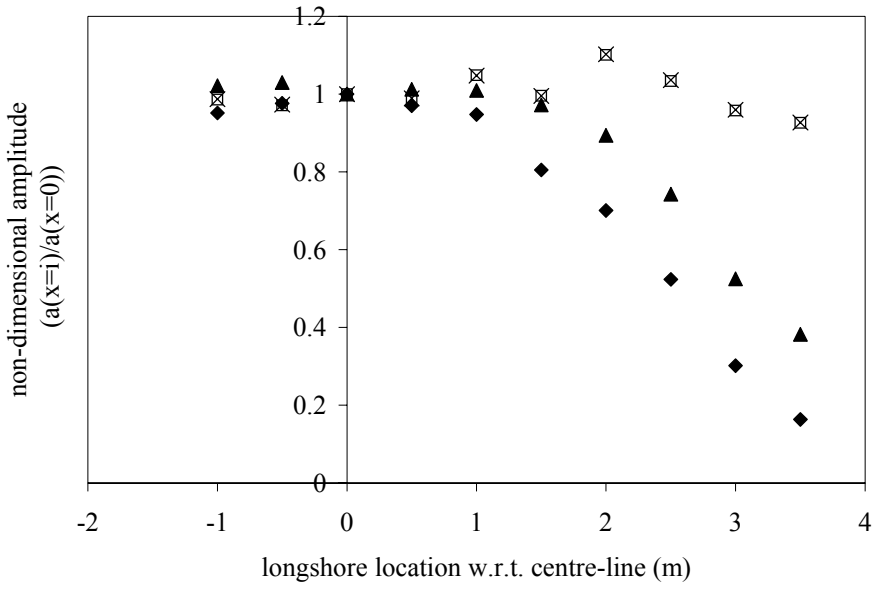

Figure 5.29: Non-dimensional wave amplitude as a function of longshore direction for ±30° wave group: ♦, linearised wave group halfway up beach; □, LFW halfway up beach; ▲, linearised wave group at beach toe; ×, LFW at beach toe.

Investigations were also made into the longshore variation for the ±10° case. However, this is a much longer crested wave that showed little variation in the linearised amplitude over the same distance as for the ±30° case.

5.2.7 Conclusions

The separation of harmonics is still possible for focused wave groups interacting with a highly reflective wall, though it would seem that there are reflections off the sea wall and possibly release of free waves for all harmonics of the wave group, in contrast to the situation without the sea wall. The size of the LFW is larger with the sea wall in place compared to the LFW generated by the interaction of a wave group with the beach.

The longshore variation in size of the LFW is much more uniform than the amplitude of the linearised group.

5.3 Solitary wave interacting with plane beach

5.3.1 Low frequency waves generated by a solitary wave

It is interesting to compare the size and behaviour of the LFW generated by a solitary wave, with those generated by focused wave groups[8].

Figure 5.30 shows a stacked plot of the solitary wave. The time scale has been shifted so that the initial LFW that is generated by the solitary wave lines up with the one generated by a focused wave as shown in Figure 5.5. The vertical scale of surface elevation is the same as that used for focused wave groups in Figure 5.2 to 5.9. There is remarkable similarity in the nature of the LFW from the solitary wave when compared to the LFW from the focused wave groups. There are two interesting features of the LFW. Firstly, the LFW generated by the solitary wave travels at the same speed as that generated by the focused wave group. Secondly, the time-shifted peak of the solitary wave lines up exactly with the peak amplitude of the focused wave group. This may imply that the same mechanism is involved in the generation of both waves' LFWs.

The high frequency structure that is evident close to the shoreline, following breaking of the wave, is likely to have been due to vibration of the wave gauge support frame.

Figure 5.31 shows how the size of the solitary wave and the LFW vary up the beach. The height of the LFW is about $\frac{1}{4}$ the height of the solitary wave. This is a much greater proportion than for focused wave groups, where the LFW is only about 10% of the linear wave group amplitude, and even less as a proportion of measured group amplitude maybe because of the different nature of the impact process. The solitary wave breaks dramatically by plunging in a very narrow region i.e., there is no gradual dissipation of energy over a larger region which happens in the case of focused wave groups.

There is no benefit in examining the LFW of the solitary wave which interacts with the sea wall as the overtopping volume is very large, i.e. most of the wave energy is lost to the landward side of the wall and is not available to drive a LFW.

[8] The term low frequency wave will continue to be used in this section to enable comparisons to be made with focused group LFWs, despite the fact that the time scale of the solitary wave LFW is very nearly the same as the incident wave.

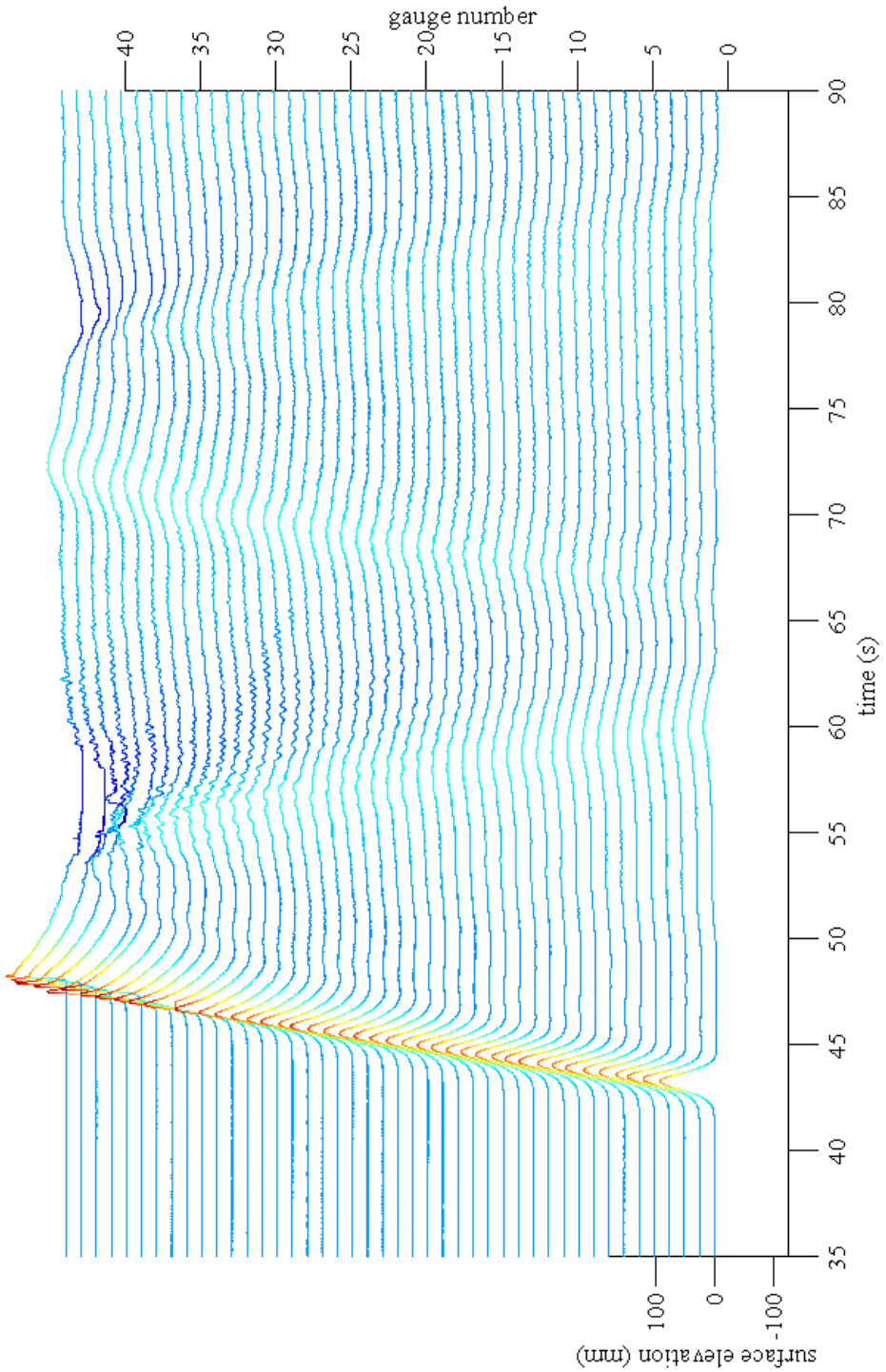

Figure 5.30: Stacked time histories of solitary wave generated in the UKCRF.

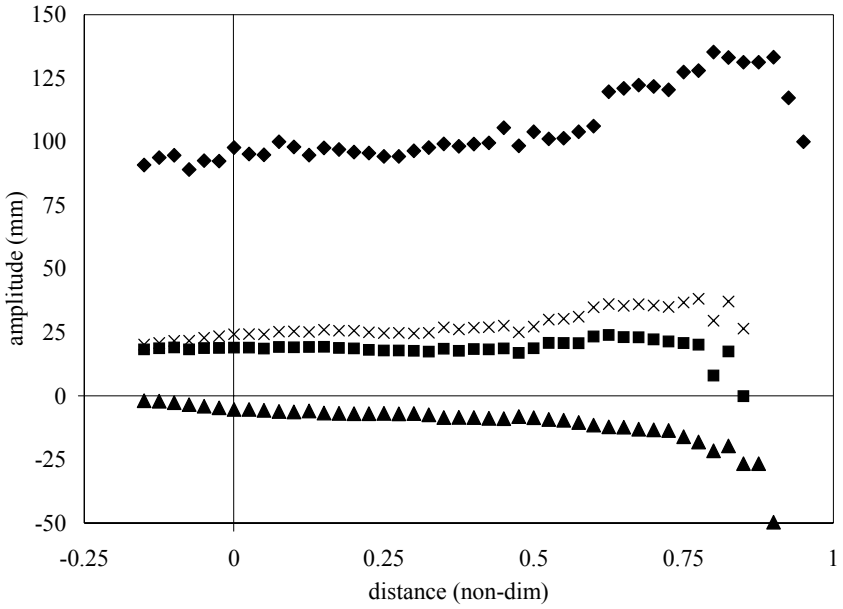

Figure 5.31: Wave amplitude variation in the basin: ♦, solitary wave amplitude; ■, LFW crest; ▲, LFW trough; ×, LFW height.

5.4 Embedded focused waves interacting with a plane beach

The process of embedding a focused wave group into a background regular wave produces a wave field that comes closer to what would be experienced in reality. This is obviously of tremendous benefit to coastal engineers. The background was chosen to be regular waves for this investigation, to minimise the number of variables, though the method can be used to incorporate a background of irregular waves.

The importance of this investigation is that waves preceding and following the focused group will have an influence on how the waves interact with a structure (in this case a beach). The background regular wave train had an input amplitude of 40.3 mm and a period of 1.747 sec, both chosen in some sense to give the best representation of the effects of a realistic random background. Further details are given in Chapter 2.

5.4.1 Generation of embedded wave groups

Four different embedded groups were used:

1. NewWave crest coincident with regular wave crest (EG1).

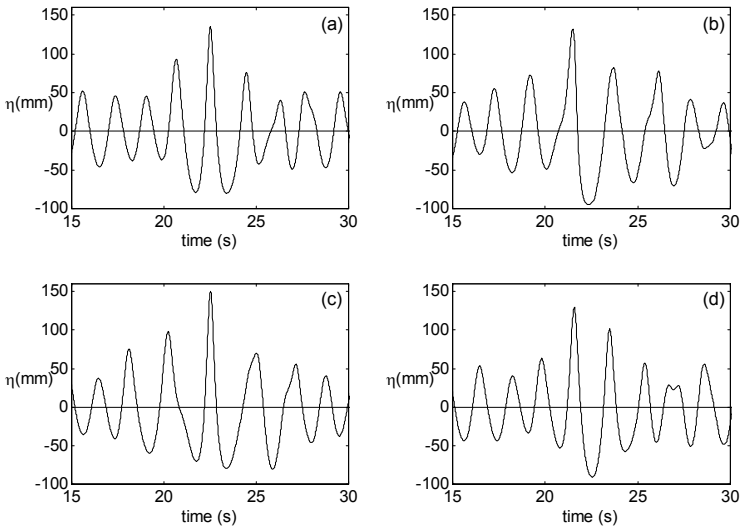

Figure 5.32: Time histories measured at the beach toe of embedded wave groups (a) EG1 (b) EG2 (c) EG3 (d) EG4.

2. NewWave trough coincident with regular wave crest (EG2).

3. NewWave crest coincident with regular wave trough (EG3).

4. NewWave trough coincident with regular wave trough (EG4).

Windowed surface elevation time histories of these four waves are shown in Figure 5.32.

It is interesting to compare how the surface elevations of the embedded focused waves compare with those of the lone NewWave. Figures 5.33 to 5.36 show the time histories and amplitude spectra for each of the four embedded cases, at four locations in the basin (as shown in Figure 3.3), alongside data from the associated lone NewWave.

Figure 5.33 shows that at the focus location, B, the embedded NewWave is nicely focused, and exhibits little distortion. The most obvious point to note is the spike in the amplitude spectra that corresponds to the frequency of the regular wave. The low frequency structure at round 0.2 Hz is roughly comparable with the lone wave data, but there is more high frequency structure at about 1 Hz.

Figure 5.34 shows that at focus the inverted (trough focused) NewWave shows a degree of distortion. The amplitude spectra at all locations do not have a clear spike corresponding to the regular wave, more a wider and higher peak around the linear group frequency (~ 0.3

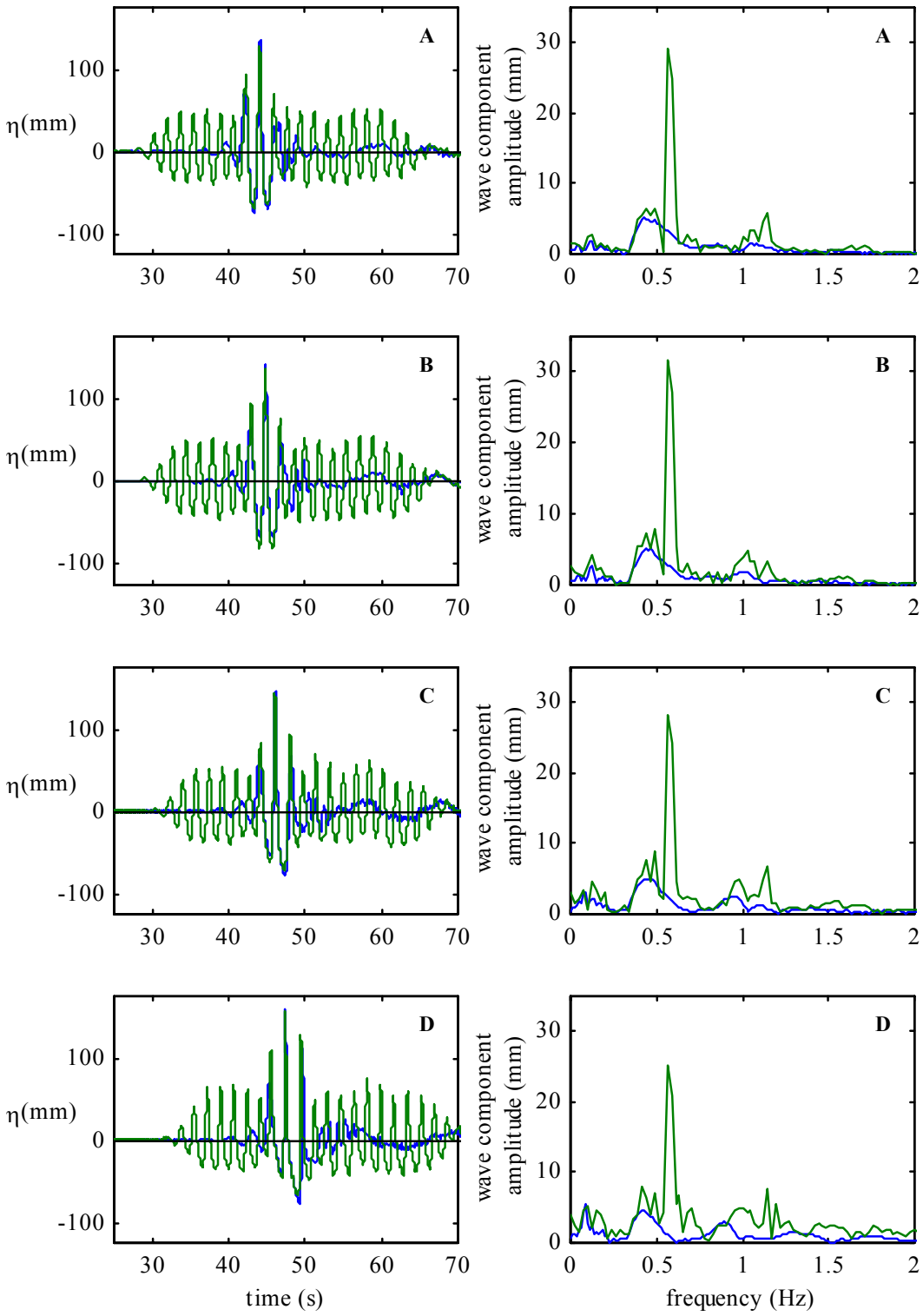

Figure 5.33: Surface elevation time histories and amplitude spectra measured at locations A, B, C and D of: (green) — New wave crest coincident with regular wave crest EG1; (blue) - - - lone crest focused NewWave.

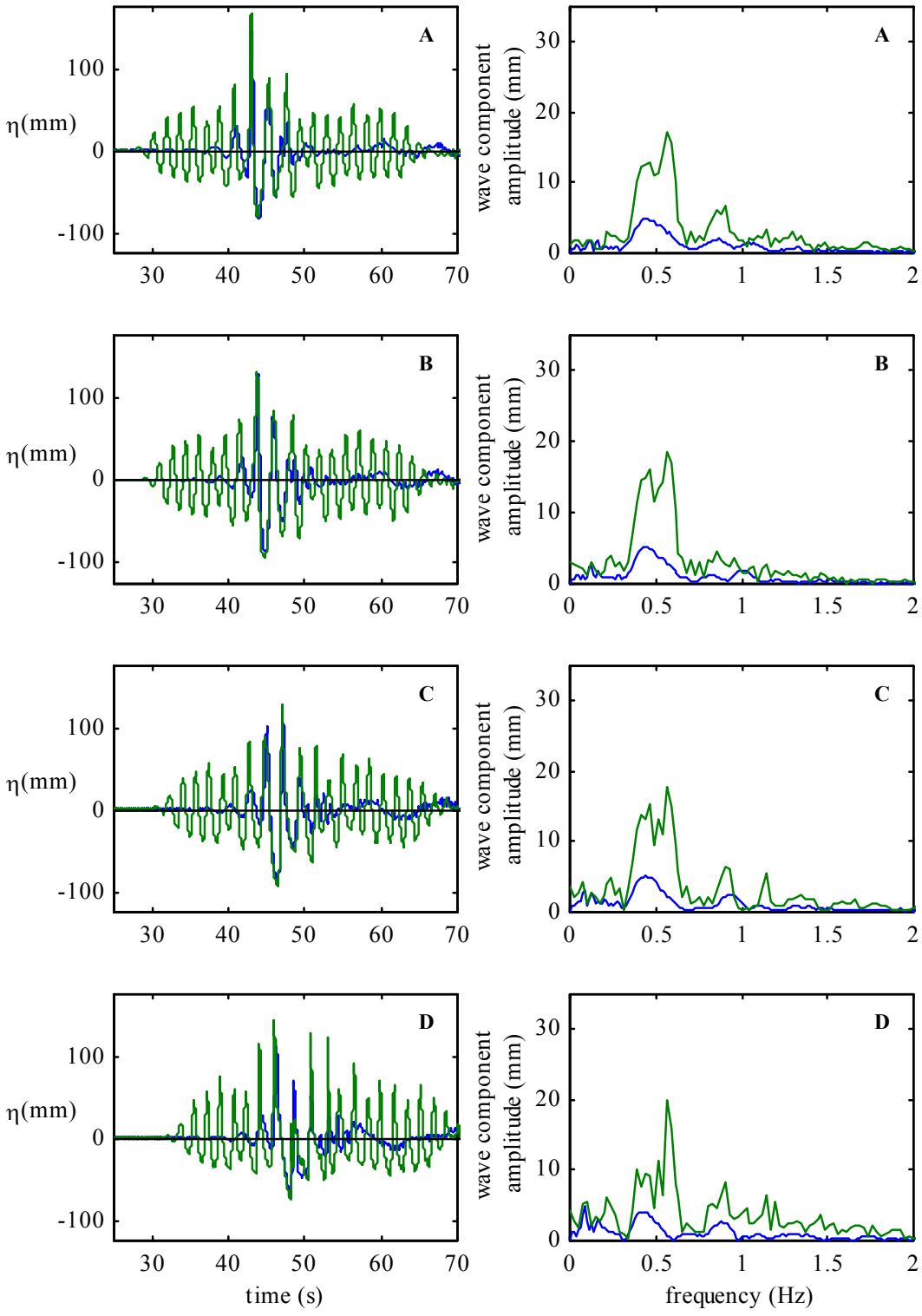

Figure 5.34: Surface elevation time histories and amplitude spectra measured at locations A, B, C and D of: (green) — New wave trough coincident with regular wave crest EG2; (blue) - - - lone trough focused NewWave.

to 0.7 Hz). The low frequency structure is roughly comparable for the embedded and lone groups, but again at higher frequencies there is more structure for the embedded wave.

Figure 5.35 which shows a NewWave crest coincident with a regular wave trough is virtually the same as the case of a NewWave trough coincident with a regular wave crest. The focused wave is out of phase with the regular wave, leading to very similar amplitude spectra as shown in Figure 5.35. There is no spike in the amplitude spectra - just a widening and increase at linear group frequency, and there is a little more high frequency structure. Again, the low frequency spectra are similar for lone and embedded groups.

Figure 5.36 shows the focused wave in phase with the regular wave. There is now a spike at the regular wave frequency, a little more high frequency structure, but a comparable amount of low frequency structure for the embedded case.

5.4.2 Removal of background regular waves

This can be achieved in a number of ways, and comparisons made to the lone NewWave data.

Removal of background waves from crest focused embedded group

Addition of the EG1 and EG3 time series should result in the removal of background regular waves from the embedded crest focused NewWave.

Figure 5.37 (a) shows the 'stripped' NewWave - the result of adding EG1 to EG3. The background waves are reduced considerably, and the focused wave is undistorted by the process. What *is* evident are the high frequency even harmonics from the regular waves, both before and after the main wave group. Figure 5.37 (b) shows the lone crest focused NewWave, as seen previously. The difference between the stripped NewWave and the lone NewWave is shown in 5.37 (c). There is evidence of some relatively high frequency background structure, and two low frequency waves that travel with the group. The largest differences between the 'stripped' NewWave and the lone NewWave occur as a result of the very sharp crests. These are very sensitive to any timing differences due to the presence of background waves.

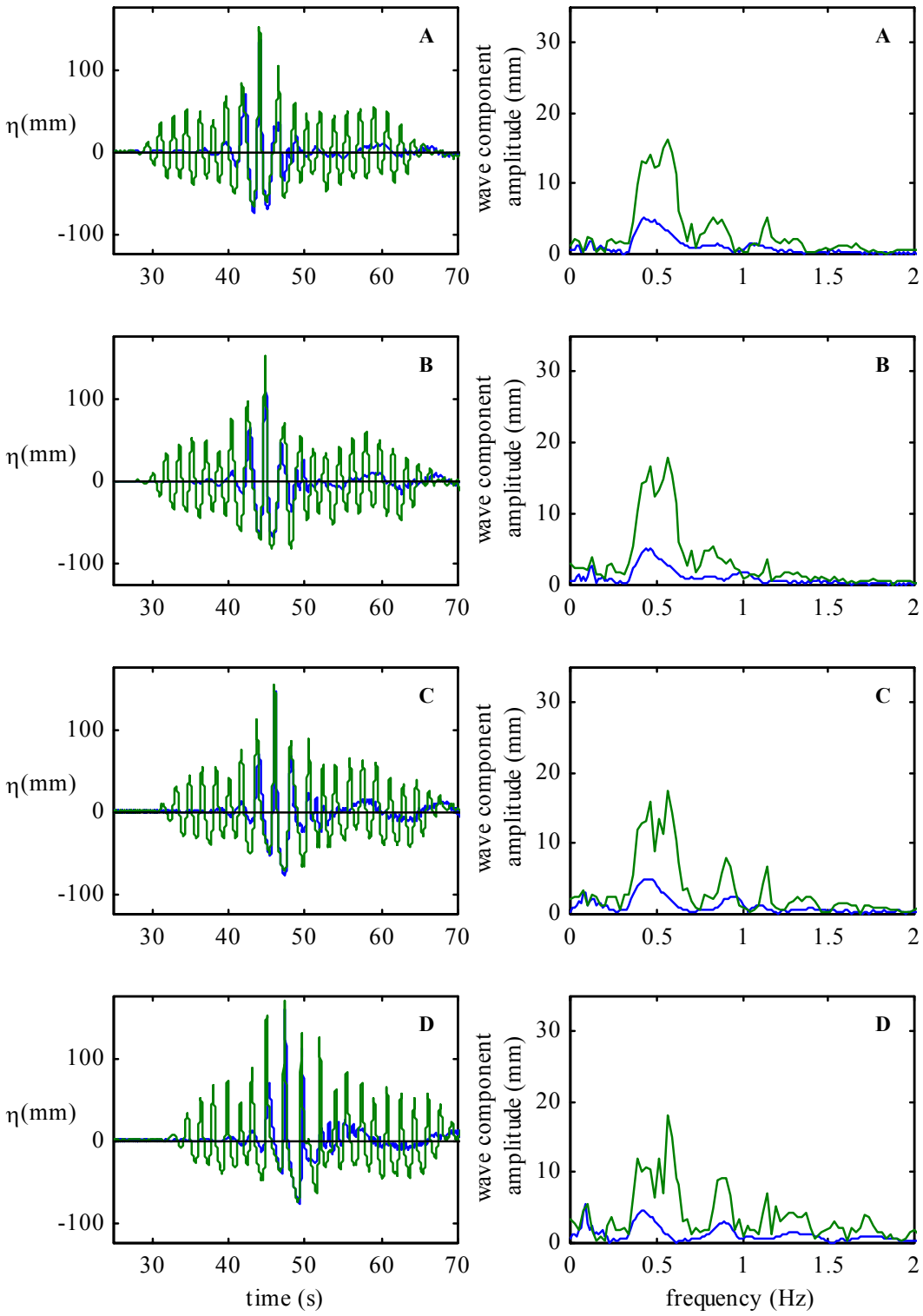

Figure 5.35: Surface elevation time histories and amplitude spectra measured at locations A, B, C and D of: (green) — NewWave crest coincident with regular wave trough EG3; (blue) - - - lone crest focused NewWave.

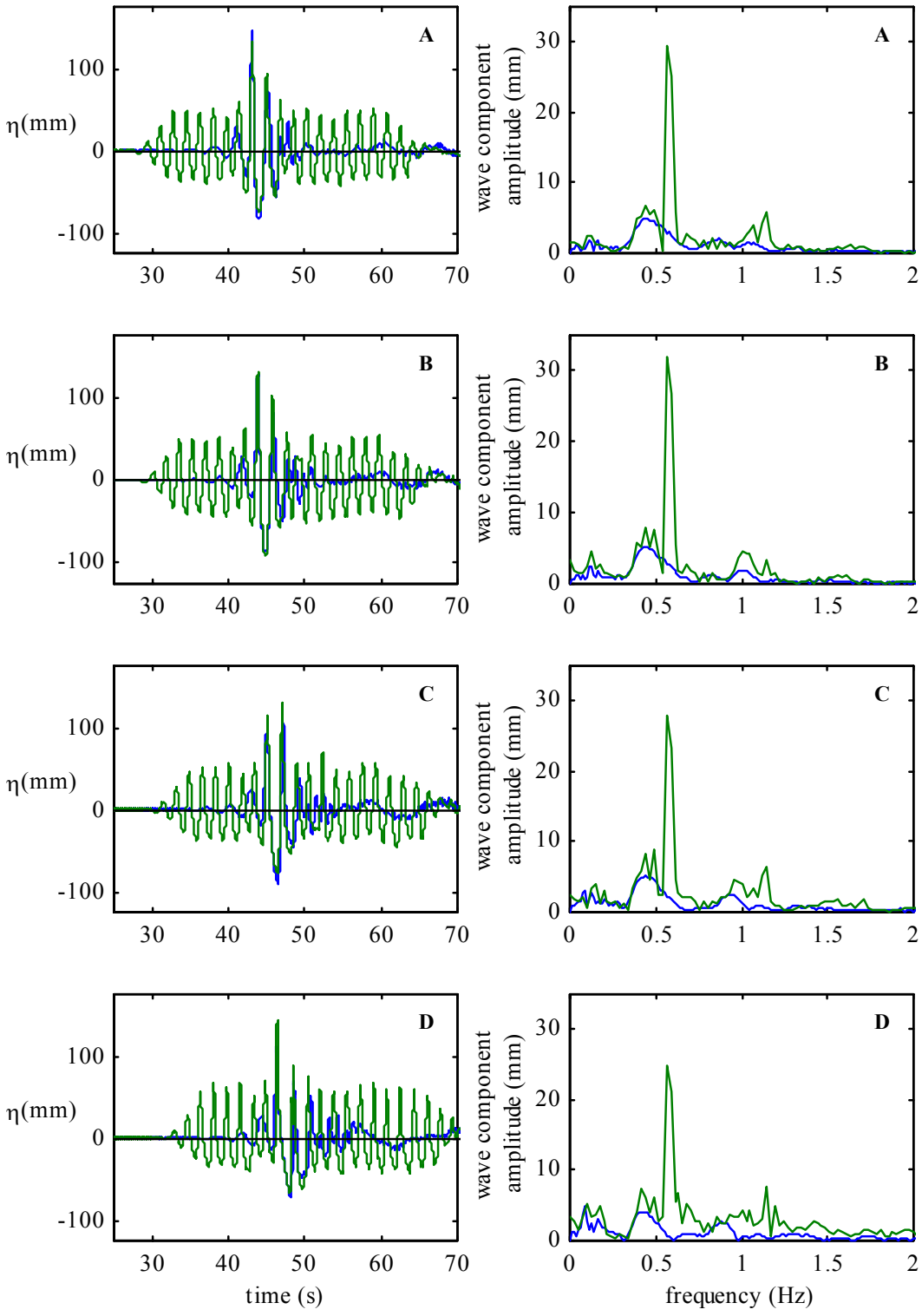

Figure 5.36: Surface elevation time histories and amplitude spectra measured at locations A, B, C and D of: (green) — NewWave trough coincident with regular wave trough EG4; (blue) - - - lone trough focused NewWave.

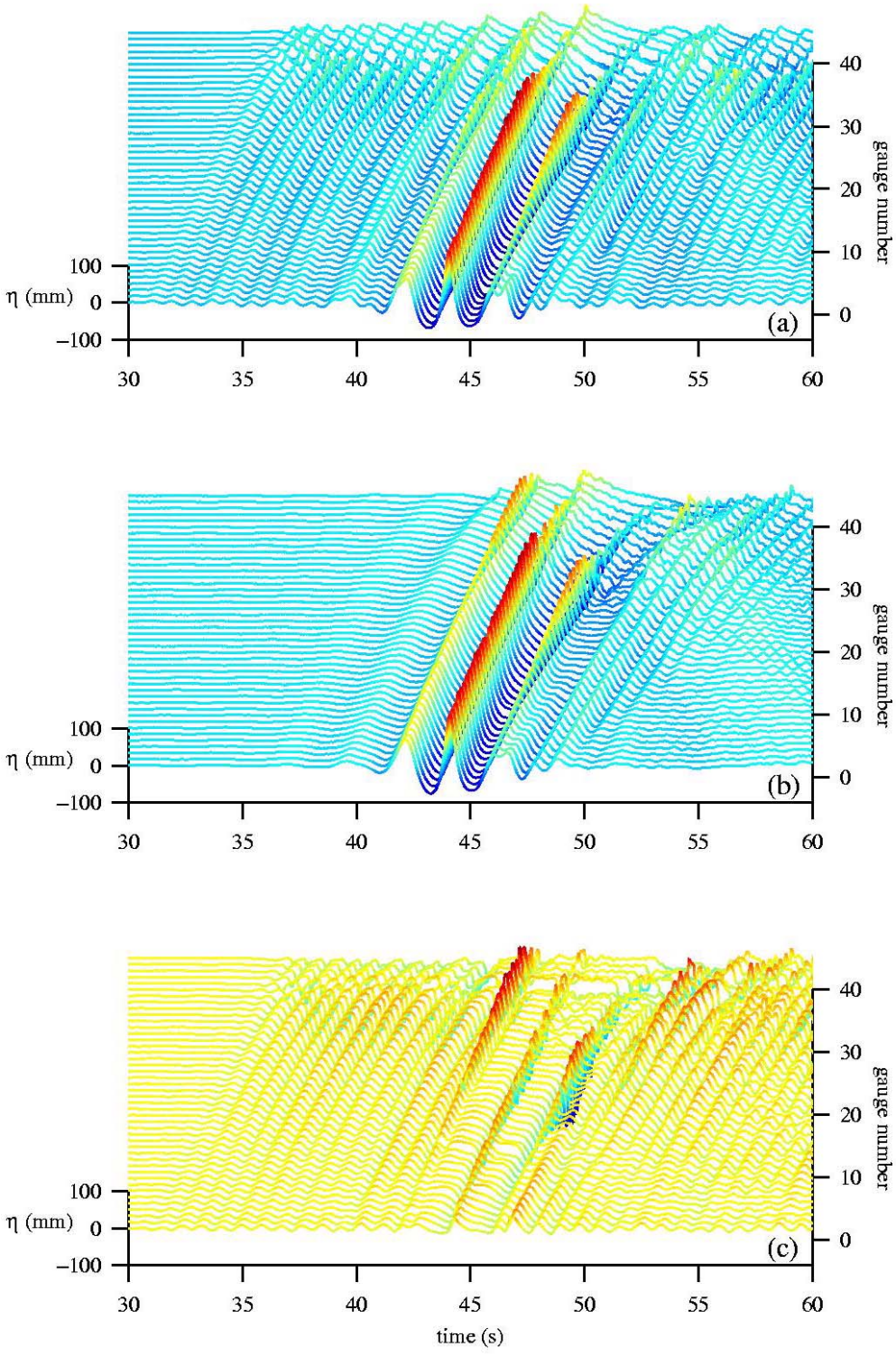

Figure 5.37: Stacked surface elevation time histories for (a) 'stripped' embedded crest focused wave group (b) lone crest focused wave group and (c) lone minus embedded crest focused wave group.

Removal of background waves from trough focused embedded group

In a similar manner as before, addition of the EG2 and EG4 time should result in the removal of the background regular waves from the embedded trough focused NewWave. This is illustrated in Figure 5.38.

As in the case of the stripped crest focused group, the background regular waves of the embedded trough group of Figure 5.38 (a) have diminished considerably but again show high frequency even harmonics due to the regular waves both before and after NewWave. In Figure 5.38 (c) there appears to be some low frequency structure underneath where the group would have been, as also shown in 5.37 (c). There are smaller differences in 5.38 (c) compared with 5.37 (c) because the less 'peaky' troughs are less sensitive to timing differences due to the presence of other waves.

5.4.3 LFW of embedded group compared with LFW of lone focused wave group

It is possible to compare the low frequency wave of the embedded wave with that obtained from the lone wave. This will be achieved by adding the time series of EG1 and EG4. The regular waves should cancel out, and only the even harmonics of the focused wave should remain. Time histories and amplitude spectra of this addition case are shown in Figure 5.39 for four gauge locations. Also plotted are data for the added crest focused and trough focused lone NewWave groups, as presented in Figure 3.4.

Both the time series and amplitude spectra of Figure 5.39 contain a lot of high frequency structure that is not present in the lone NewWave data. The low frequency structure is similar, but slightly larger for the embedded group.

A 0.5 Hz low pass filter can be applied to the data to generate low frequency stacked time histories. The result of this is shown in Figure 5.40. Figure 5.40 (a) shows the LFW from the embedded group which can be compared with Figure 5.40 (b) which is the LFW of the lone NewWave. It can be seen that there is a low frequency wave associated with the start-up of the paddles. However, there is no evidence that this is reflected off the beach. Figure 5.40 (c) shows the difference between the low frequency waves from embedded and lone NewWaves; however the colour scale is different so care must be taken to glean information from the size

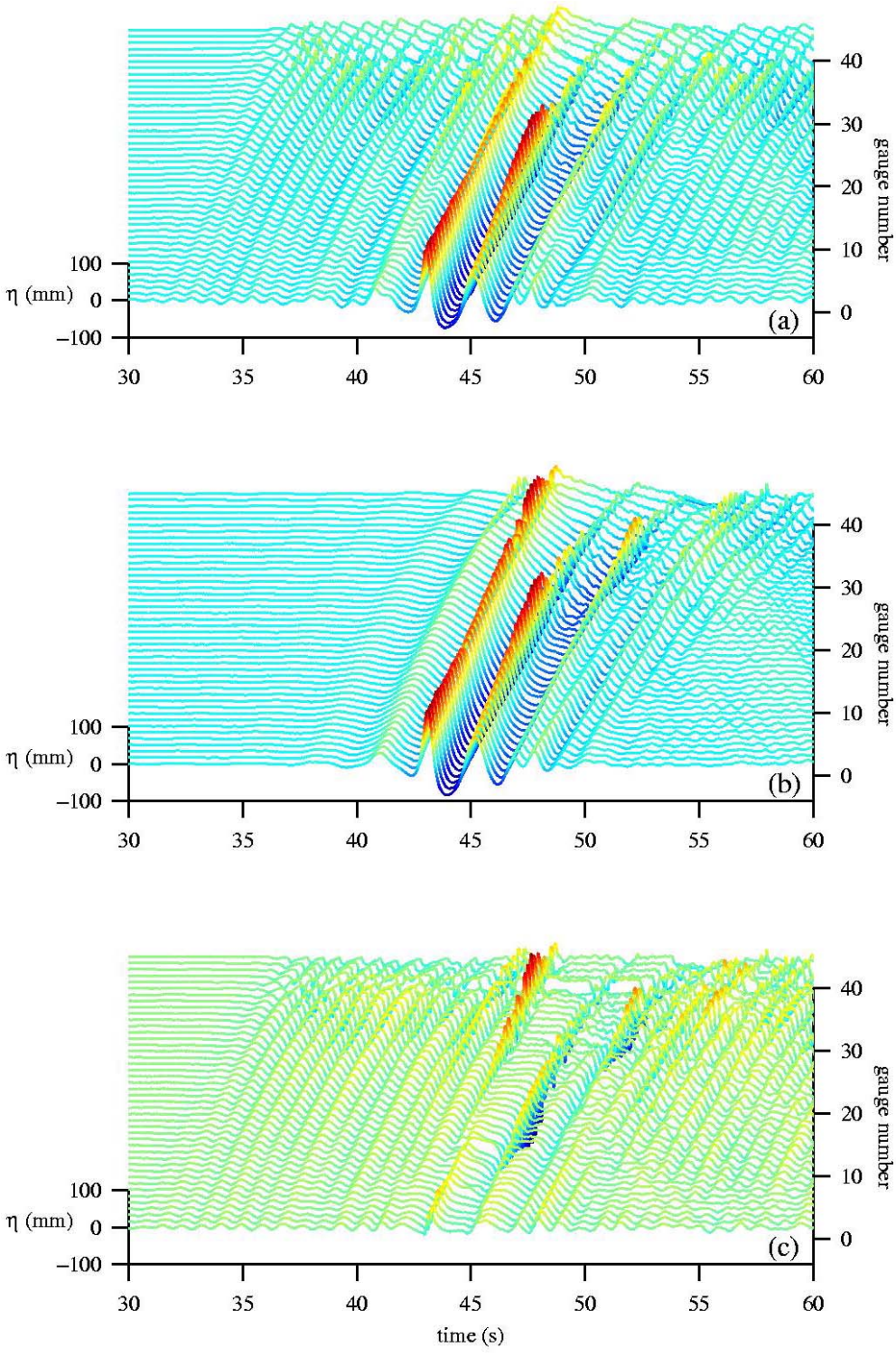

Figure 5.38: Stacked surface elevation time histories for (a) 'stripped' embedded trough focused wave group (b) lone trough focused wave group and (c) lone minus embedded trough focused wave group.

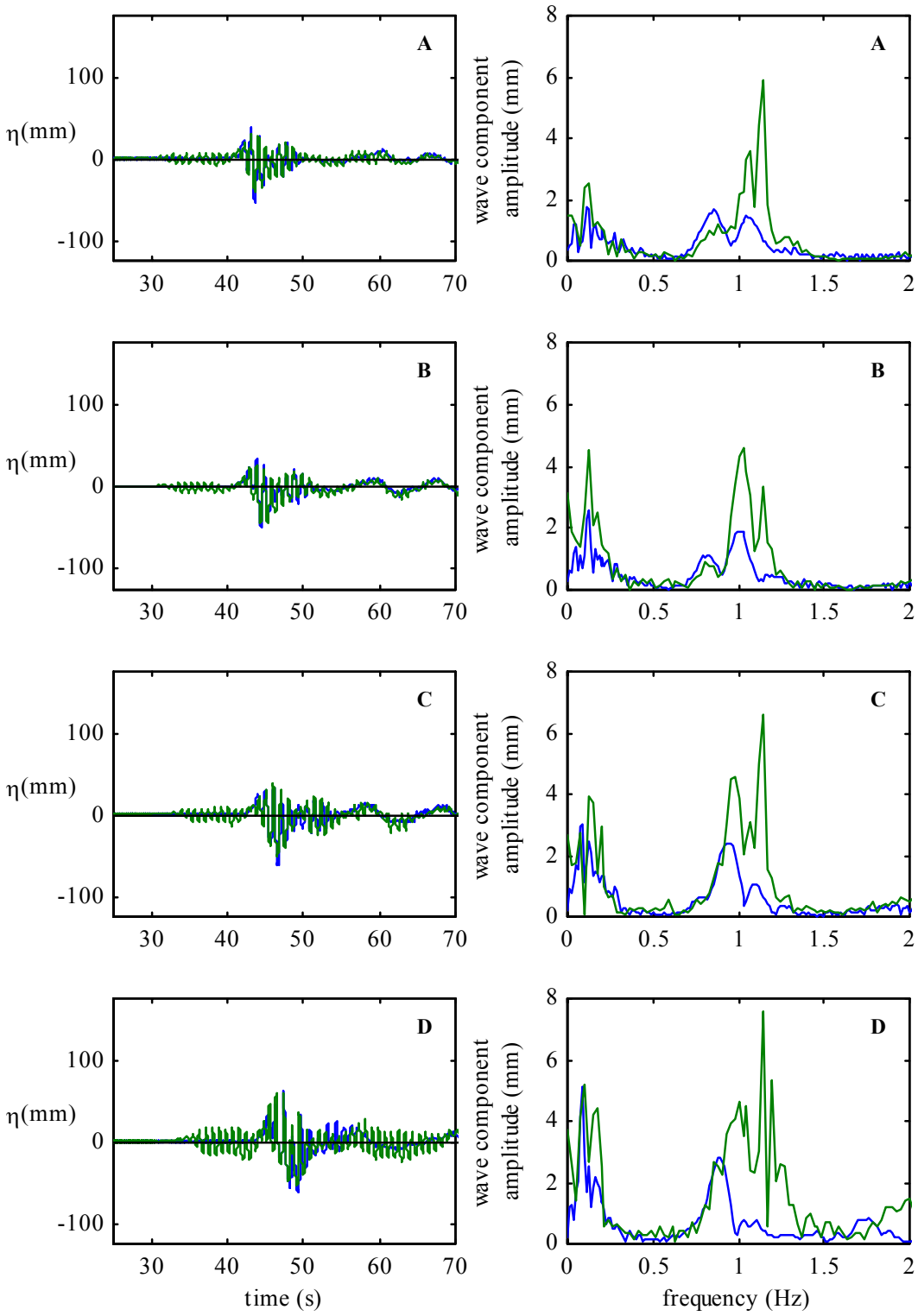

Figure 5.39: Time histories and amplitude spectra of 'addition' term, for embedded and lone crest focused wave group, measured at locations A, B, C and D: (green) — NewWave trough embedded in regular wave trough; (blue) - - - lone trough focused NewWave.

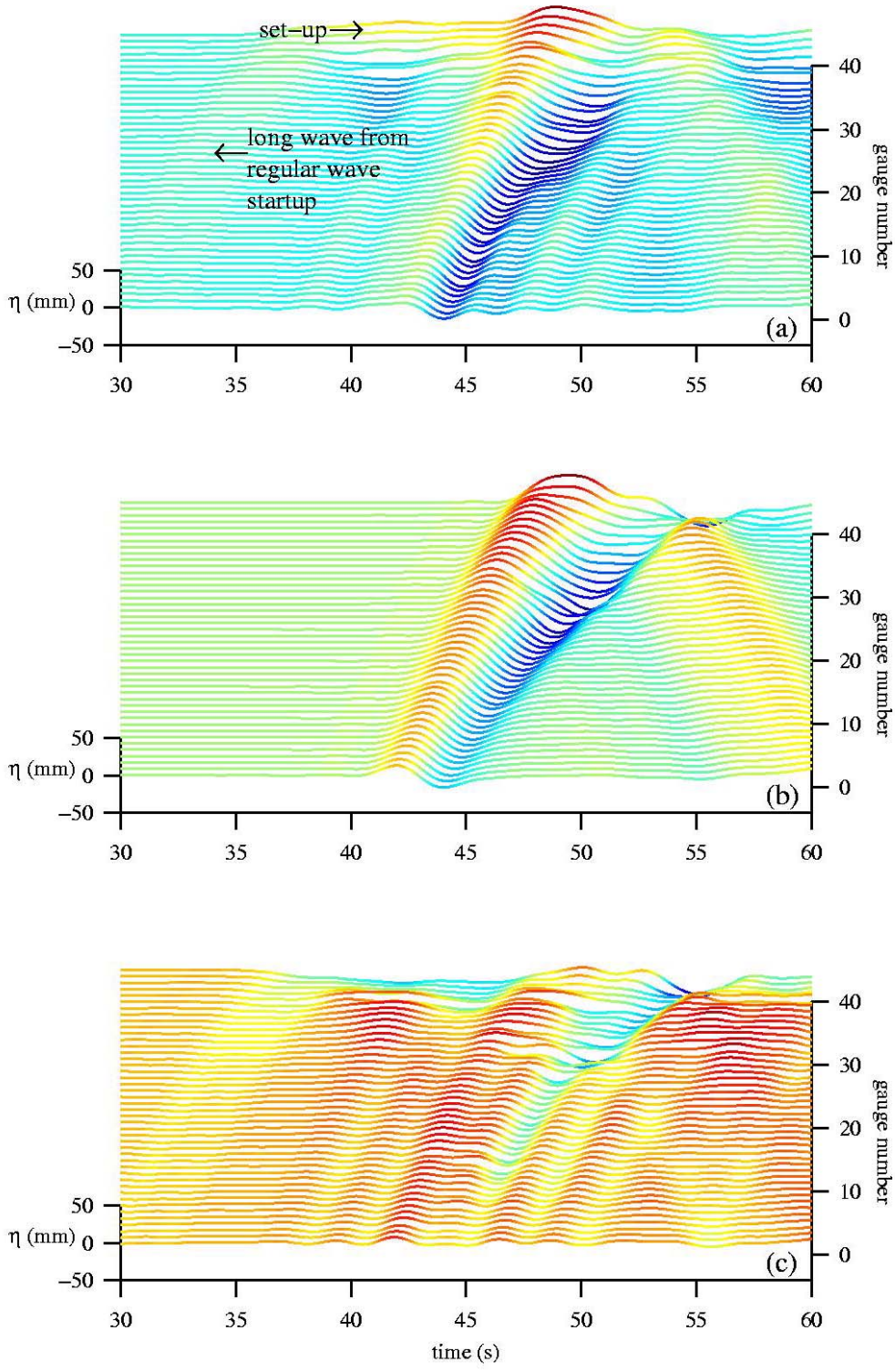

Figure 5.40: Stacked time histories of (a) low frequency band-pass filtered 'addition' time series from EG1 plus EG4 (b) low frequency band-pass filtered 'addition' time series from crest and trough focused lone NewWave and (c) subtraction of time series (b) from (a).

of the undulations. Other observations are that:

- the low frequency error wave that precedes the group is smaller for the embedded wave compared with the lone wave, until the water becomes very shallow when it becomes of comparable size;
- the local set-down underneath the group of the embedded wave is similar to the local set-down of the lone wave, both in terms of size and duration;
- there are additional low frequency waves that travel at the same speed as the error wave and set-down, both before and after the focused group;
- the LFW that is generated by the interaction of the waves with the beach is smaller for the embedded group but it appears to be generated from the same location, a little beyond the final wave gauge;
- there is evidence for the generation of a set-down of the water surface close to the shoreline due to the regular wave train;
- and finally, there do not appear to be any offshore moving low frequency waves that are generated by the regular waves that precede the main group.

5.4.4 Conclusions

It is possible to remove the background regular wave train from the embedded groups by simply adding inverted wave trains. It is also possible to use the separation of harmonics method to view the LFW generated by an embedded NewWave. Globally, the incorporation of a background system of waves to NewWave makes very little difference i.e., there is still only long wave radiation. The only significant differences to NewWave dynamics occur in shallow water where alignment of crests and troughs break down due to shocking of the crests. The embedding process reduces the size of the low frequency parasitic wave generated by the paddles.

5.5 Chapter Conclusions

The separation of harmonics method outlined in chapter 3 has been successfully used for to reveal some of the fundamental processes of wave groups interacting with structures: both a beach and a sea wall. It has also unravelled the harmonic structure of a focused wave embedded within a regular wave train.

The separation of harmonics was particularly able to shed light on the reflections of harmonics. The most noticable but perhaps a predictable finding was that the only waves that were outgoing from the beach were low frequency second order harmonics - the LFW. All other harmonics appeared to be completely dissipated. This is in stark contrast to the effect of the sea wall which reflected wave components at all frequencies. This fidning is probably due to the fact that when waves interact with the 1:20 beach they break, causing dissipation of much of the energy. However, with the sea wall in place (a much greater slope) very little breaking takes place - some of the water overtops the structure and the remainer is reflected unbroken - hence dissipation of the energy due to breaking is reduced.

The size of the LFW was greater as a result of interactions with the sea wall compared with interactions with the beach.

The size of the LFW generated by the interaction with a plane beach was compared with the one produced by a solitary wave. The solitary wave produces a much larger LFW, but it travels at the same speed as the one that comes from the focused wave group.

The temporal and spatial properties of the LFW were found to depend only weakly on the phase of the wave group i.e., a trough focused group LFW is slightly deeper than a crest focused LFW and the LFW of the trough focused group slightly lags that of the crest focused group.

It was found that the longshore variation in size of the LFW for a $\pm 30^{\circ}$ spread sea is much more uniform than the amplitude of the linearised group.

Of great interest was the fact that embedding NewWave into a regular wave background to produce a more realistic wave train results in very little difference to the generation of the LFW. It was evident that the LFW was generated as a result of the NewWave rather than the regular waves, however the amplitude of the LFW was slightly reduced.

Chapter 6

Extreme waves in the surf zone

6.1 Extreme wave breaking in the surf zone

The surf zone is the region between incipient breaking and the still water shoreline. Due to energy dissipation of wave breaking the surf zone is a very important region. There has been some recent laboratory work on the behaviour of breaking waves from wave groups on very shallow (1:35) slopes. Ting (2002) produced wave groups using a narrow-band spectrum. The groups comprised a large number of waves and the experiments were dogged by the generation of spurious long waves that reflected up and down the flume. Svendsen & Veeramony (2001) used repeating groups of five cnoidal waves, generated for more than thirty minutes in an attempt to achieve a steady-state condition. Cnoidal waves were chosen to reduce the size of the harmonics that would otherwise be generated, but they found that there were still some secondary crests present at the wave troughs.

The results that are reported here are from a specific type of focused wave group that realistically models the temporal and spatial variation of an extreme wave. The group is compact, comprising just three significant waves, and due to the transient nature of the experiment - just one single group - the results are free from wave basin reflections. This compact group should provide greater clarity on interpreting findings about wave breaking in wave groups.

6.1.1 Experimental setup

Unidirectional focused wave groups of normal and oblique incidence are analysed for their wave breaking characteristics. Details of these sixteen wave groups are given in Appendix A. Investigations are made into the behaviour of individual waves within the wave groups. These *intra*-group waves are given *roman* numerals to provide a distinction from the wave groups, which use *arabic* nomenclature. The waves are labelled in Figure 6.1 (a) and (b), for crest focused and trough focused wave groups. It is immediately obvious that only two waves have been investigated for trough focused groups, the reason for this being that the waves immediately before and after the two large waves are very much smaller and produce insignificant runup. Wave height, for the purposes of this investigation, is defined as being the amplitude of a trough plus the amplitude of the following crest.

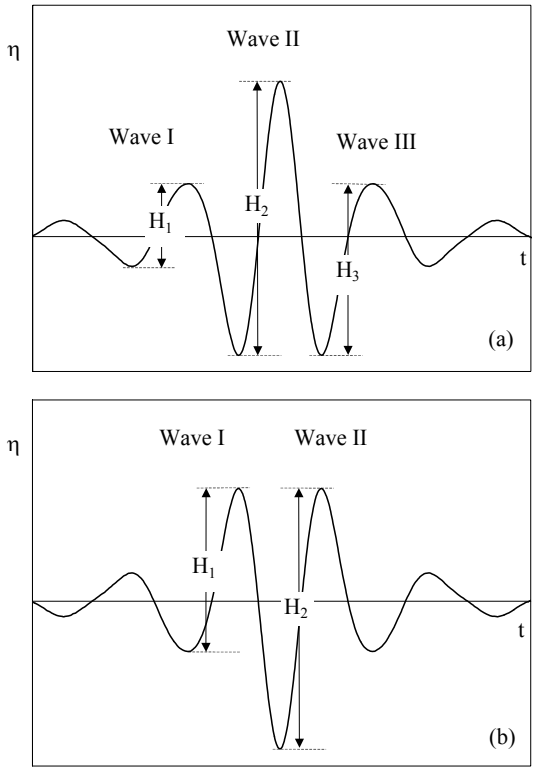

Figure 6.1: Definition of intra-group waves (a). crest focused and (b). trough focused.

Surface elevation measurements were made at forty-four locations along the centre-line of the basin as shown in Figure 6.2. The shallowest location was in a still water depth of 9.25 cm.

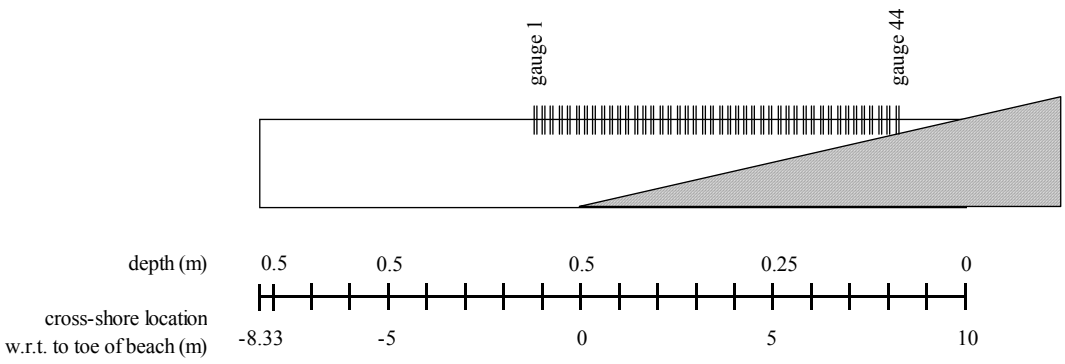

Figure 6.2: Location of wave gauges in UKCRF.

6.1.2 Height and position of wave breaking

Waves break when the particle velocities exceed the individual wave celerity. The depth at which this happens is influenced by bed slope, wave height and wavelength. There is also evidence to suggest that the 'groupiness' of the waves influences the location, and hence depth, of breaking (Svendsen & Veeramony, 2001). It is possible to analyse data from the focused wave groups generated in the UKCRF, to see how the wave heights vary as waves travel up the beach.

As discussed in the previous chapter, error waves were present in the basin because linear signals were sent to the paddles. The only error wave that will have a bearing on wave breaking is the low frequency error wave that travels in advance of the wave group. This low frequency wave *may* influence the position and depth of breaking as the incoming group could interact with the reflected wave. Wave groups that travel to the shore at an inclined angle will not interact with the reflected long wave. Therefore oblique wave groups will not be affected by any *potential* problems with the low frequency error wave. Figure 6.3 shows how the amplitude of the individual waves within WG12 varies as they move up the beach. Also plotted on the graphs is the wave-height-to-water-depth ratio H/d. The amplitudes are plotted as a function of dimensionless cross-shore distance with respect to the beach toe - negative values are off-shore of the toe, and the value of +1 corresponds to the still water shoreline.

The behaviour of Wave I shown in Figure 6.3 (a) is considerably different from Waves II and III shown Figure 6.3 (b) and (c) respectively. Firstly there is a gradual increase in the

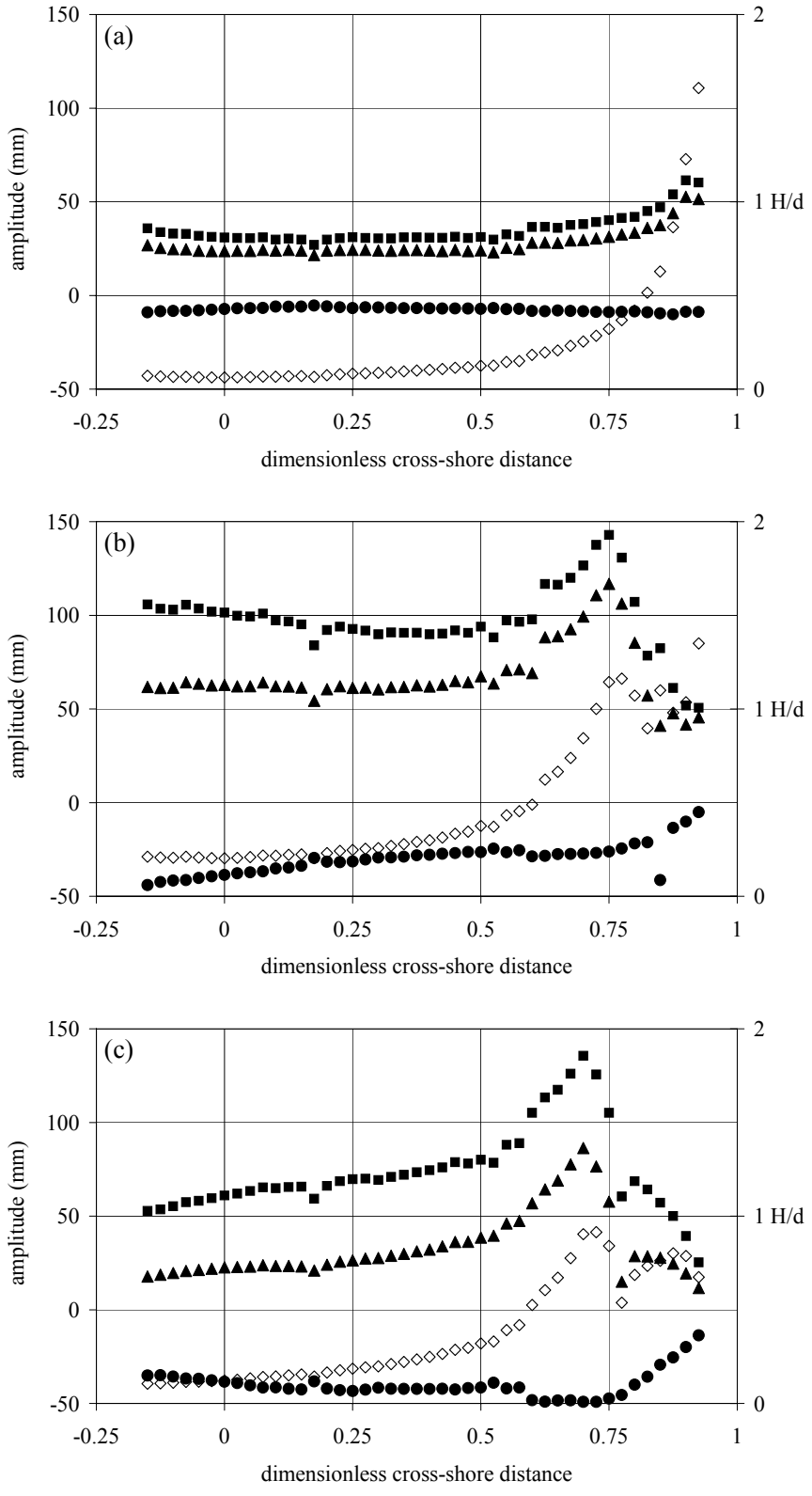

Figure 6.3: Wave height variation along the basin for a small oblique crest focused wave group. (a) Wave I (b) Wave II (c) Wave III: ▲, crest amplitude; •, trough amplitude; ■, wave height; ◊, wave-height-to-water-depth ratio H/d.

crest amplitude, and a corresponding but slower increase in trough amplitude, resulting in a steady increase in wave height as the wave travels up the beach. The breaker depth index climbs steadily up to a maximum value of about 1.6. However, Waves II and III show evidence of significant changes due to wave breaking. Wave II illustrated in Figure 6.3 (b) shows a constant crest amplitude and decreasing trough amplitude resulting in decreased wave height until about halfway between the toe of the beach and the still water shoreline. Thereafter the crest amplitude increases rapidly resulting in a larger wave height until approximately three-quarters of the way up the beach when the crest amplitude decreases suddenly. The breaker depth index also reached a local maximum at this point, but after the initial drop caused by wave breaking, it begins to increase again as the wave travels into shallow water, with a final value of about 1.4. Wave III shown in Figure 6.3 (c) is very similar to Wave II except that wave breaking occurs a little earlier and the final value of the breaker depth index is about 0.7. The surf zone region is from the point of wave breaking to the still water level, so, for WG12, Wave III is responsible for the surf zone beginning at a position about 70% up the beach from the toe.

Figures 6.4 to 6.7 show the wave-height-to-water-depth ratio (H/d) variation for each of the four types of wave group: crest focused normally incident, crest focused oblique incidence, trough focused normally incident and trough focused oblique incidence. Also shown on the graphs are the surf zone regions. These are deduced from the furthest offshore position of *wave height* reduction of any of the waves within the group.

The first important observation is that there is very little difference between the H/d variation of normally incident and oblique wave groups - compare Figure 6.4 with Figure 6.5, and Figure 6.6 with Figure 6.7. This is to be expected, and gives additional credibility to the quality of the results. Similarly the surf zone regions are very similar as would be expected.

Secondly, the size of surf zone is smaller for crest focused groups than comparable trough focused groups.

The third point to note, is that it can be seen from all four figures that, although Wave I is rarely the largest wave in the group in the deep water part of the basin it is always the largest wave in shallow water. For the crest focused groups, Waves II and III are usually larger than Wave I in the deeper part of the basin but break at a wave-height-to-depth-ratio H_b/d_d of approximately one - perhaps a little lower. However, Wave I peaks at between 1.6

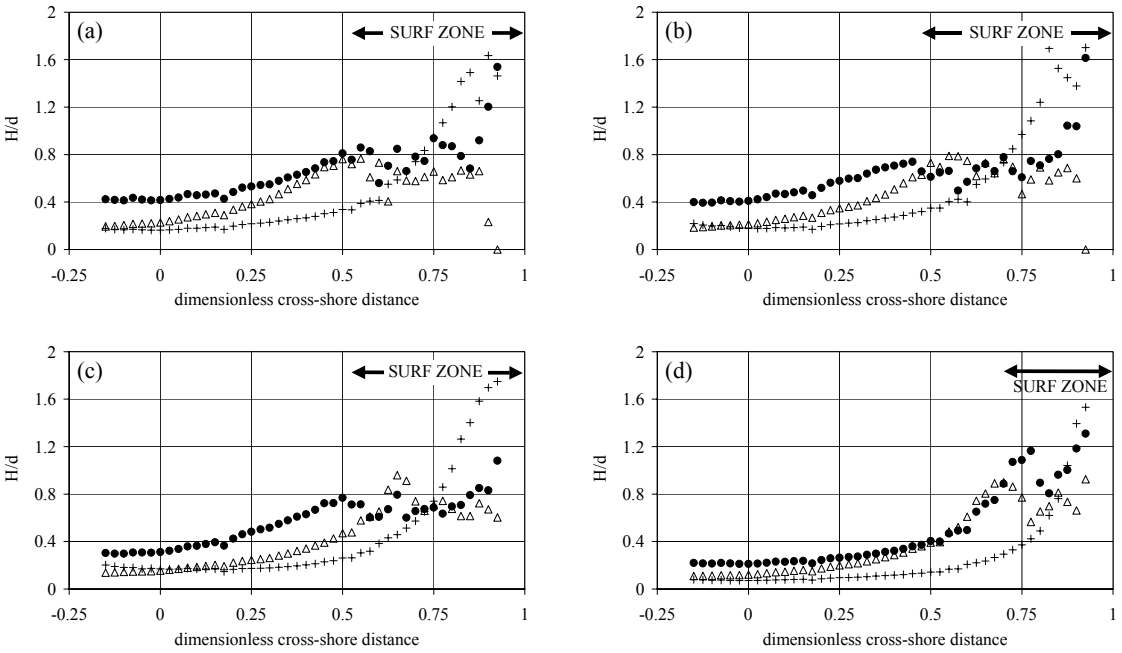

Figure 6.4: Wave height variation along the basin for normally incident crest focused waves. (a) wave 1 (b) wave 2 (c) wave 3 (d) wave 4: +, wave I; •, wave II; △, wave III.

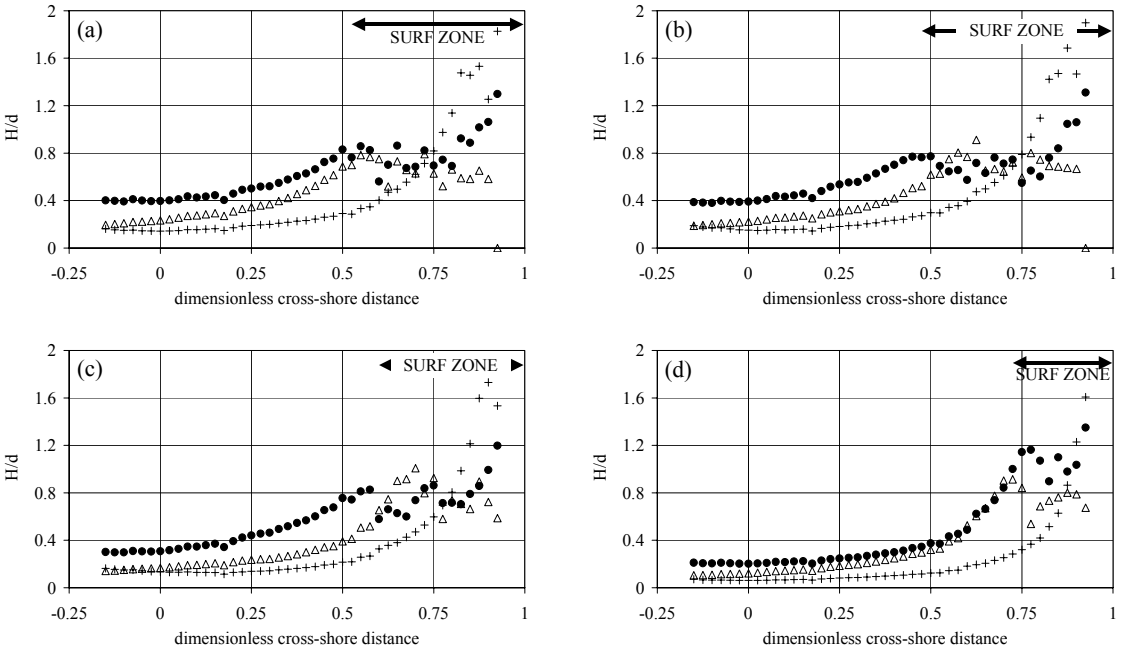

Figure 6.5: Wave height variation along the basin for oblique incidence crest focused waves. (a) wave 9 (b) wave 10 (c) wave 11 (d) wave 12: +, wave I; •, wave II; △, wave III.

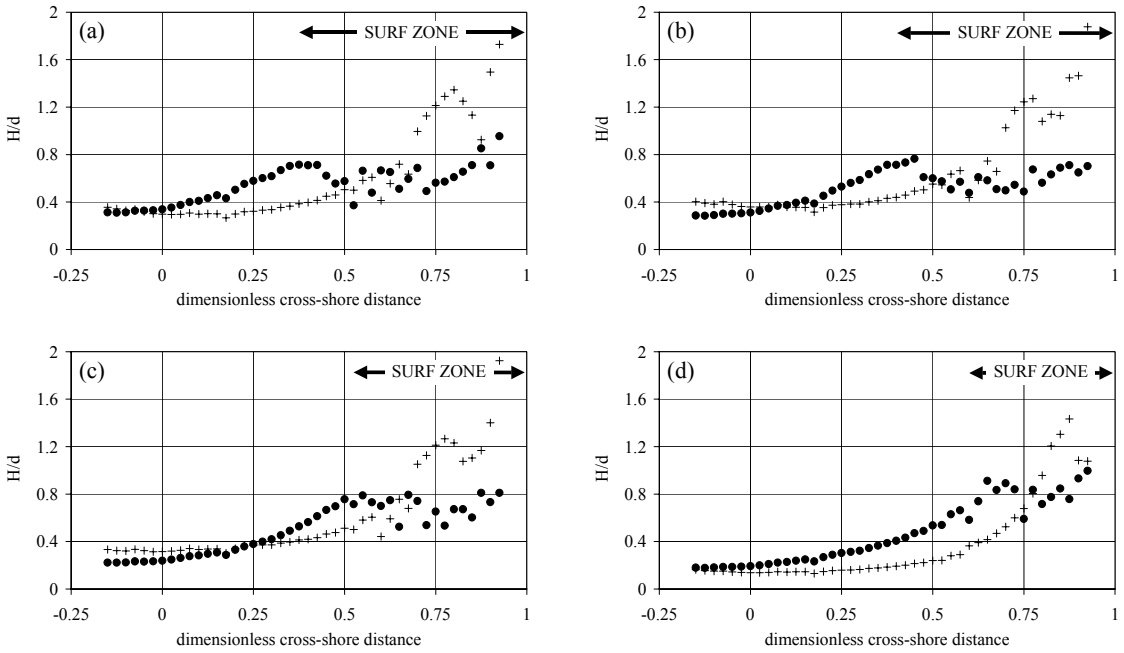

Figure 6.6: Wave height variation along the basin for normally incident trough focused waves (a) wave 5 (b) wave 6 (c) wave 7 (d) wave 8: +, wave I; •, wave II.

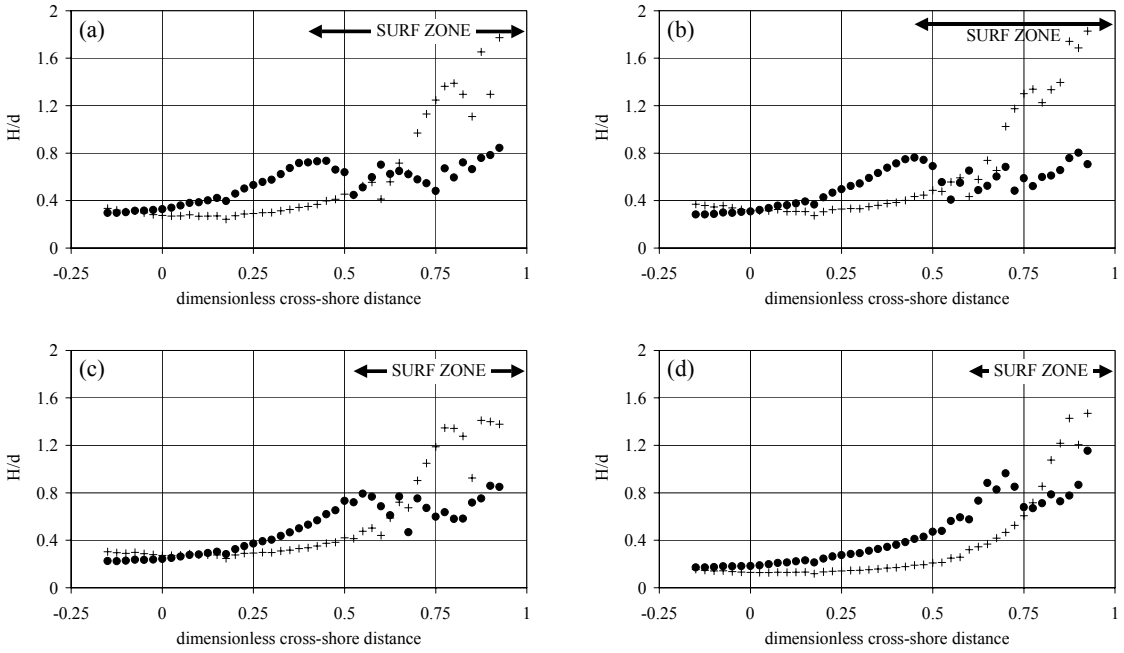

Figure 6.7: Wave height variation along the basin for oblique incidence trough focused waves (a) wave 13 (b) wave 14 (c) wave 15 (d) wave 16: +, wave I; •, wave II.

and 1.8.

These values of the breaker depth index are in agreement with results obtained by Svendsen & Veeramony (2001) who found that for wave groups the breaker depth index exceeded a value of unity. Svendsen and Hansen (1984) found a limiting value of $H/d = 2$ for saw-toothed waves. Irregular wave work by Thornton and Guza (1983) proposed a limiting value of $\overline{H}/d = 0.42$ in a saturated surf zone, where $\overline{H}$ is the root mean square wave height. This low value is probably due to the interaction of reflected waves back off the beach. The measured values are rather higher than those recorded by Ting (2002) who observed a maximum ratio of 0.9 for narrow-banded irregular waves. They are high compared to results obtained by Battjes (1974) who reported a breaking wave-height-to-water-depth ratio of between 0.8 and 1.2.

6.1.3 Frequency shifts

As the wave group breaks, the distribution of the energy within the amplitude spectrum changes. Figure 6.8 shows time series and amplitude spectra for WG1 (see Appendix A). Figure 6.8 (a) is the unfiltered data from the toe of the beach. A crude method to remove any reflections that come back off the beach which would otherwise complicate matters is to set the surface elevation to zero beyond an appropriate time. Of course care needs to be taken to choose a time at which the signal is tending to zero after the group has passed, otherwise truncation errors in the frequency spectrum will result. Figure 6.8 (b) shows the effect of truncating the signal after 50.9 sec. Figures 6.8 (c) and (d) show comparable time series and frequency spectrum for a gauge in the surf zone, 2.5 m seaward of the SWL, before and after truncation of the time signal. Figure 6.8 (d) can now be compared with Figure 6.8 (b) to show the effect that wave breaking has on the frequency spectrum. These two frequency spectra are reproduced in Figure 6.9, in a different format, comparable to that used by Svendsen & Veeramony (2001). Figure 6.9 shows the energy spectra replotted on a log scale as functions of the ratio of frequency to peak frequency, (a) at the toe of the beach, and (b) in the surf zone. It can be seen that there is a transfer of energy to both higher and lower frequencies compared with the peak frequency. This phenomenon is related to the generation of lower and higher order components following wave breaking. The shift in energy towards low frequencies, as waves progress shorewards, is a phenomenon oft reported in the literature (see for example Guza & Thornton 1982; Huntley 1976; Huntley et al. 1977;

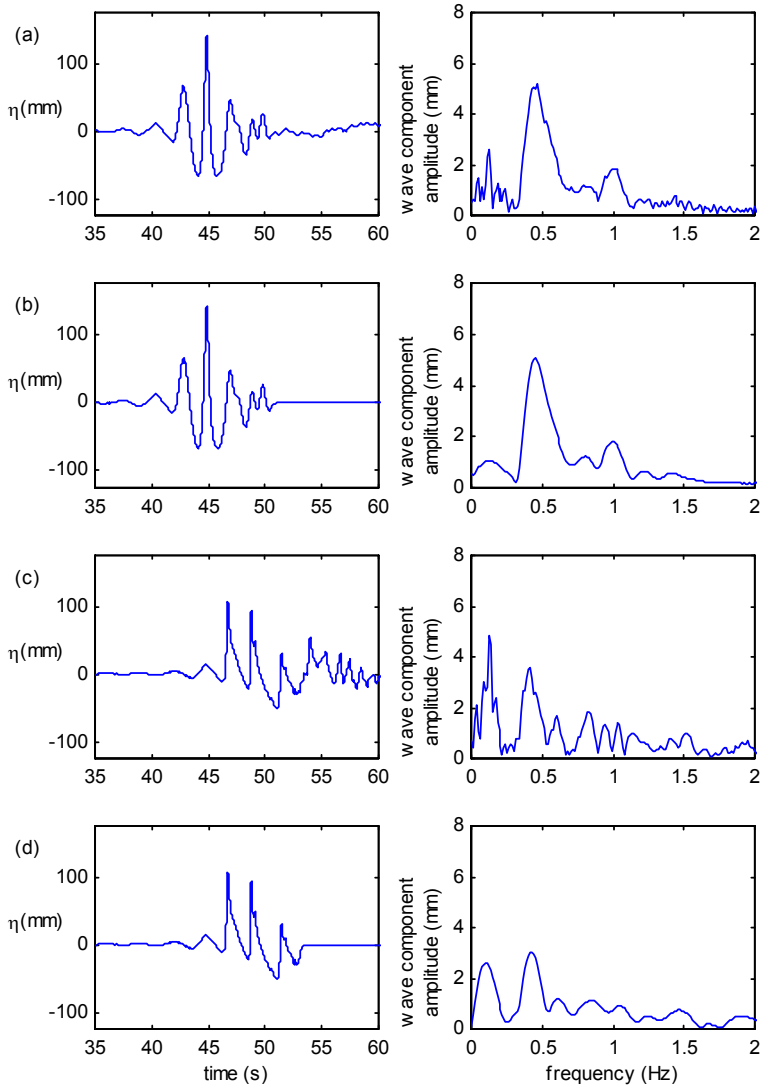

Figure 6.8: Time series and amplitude spectra at two positions in the basins (a) at toe of beach (b) at toe of beach but with relections removed (c) in surf zone, 2.5 m seaward of SWL and (d) 2.5 m seaward of SWL but with reflections removed.

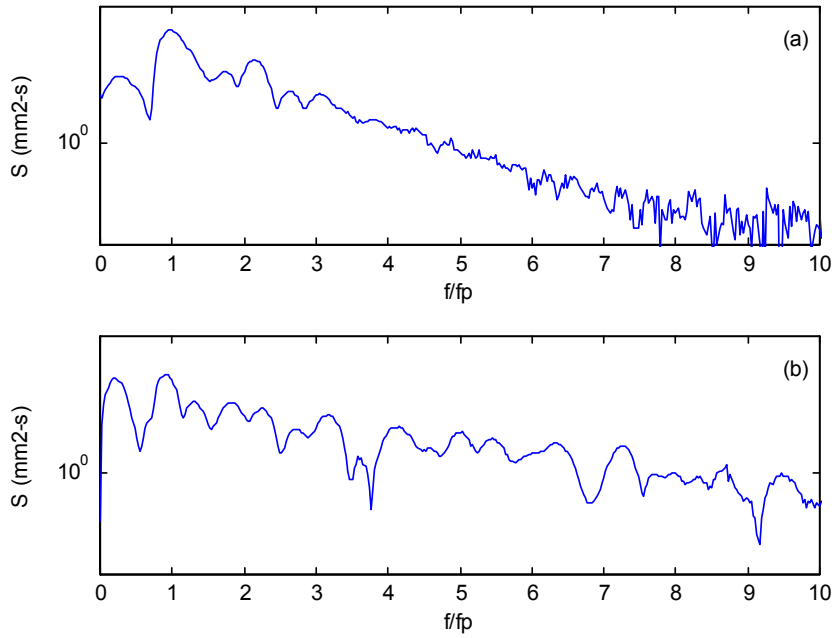

Figure 6.9: Energy spectra at (a) toe of beach and (b) in surf zone, 2.5 m seaward of SWL.

Mase 1994 and Mase 1995). Also, the slopes of the two energy spectra of Figure 6.9 are considerably different. This is likely to be due to the sharp, effectively discontinuous, jumps in time as the bore passes.

6.1.4 Wave group energy

It should in theory be possible to calculate the energy flux at every wave gauge from the envelope function, defined by Eqn. (3.27). It is necessary to separate the calculation into bound waves and free (error) waves i.e.

$$\begin{aligned} Energy\ Flux \quad = \quad & \rho g\{[(\eta_L^2+\eta_{LH}^2)+(\eta_{2\Sigma}^2+\eta_{2\Sigma H}^2)+(\eta_{2\Delta}^2+\eta_{2\Delta H}^2)]\times Cg_L \\ & +(\eta_{2\Sigma f}^2+\eta_{2\Sigma fH}^2)\times Cg_{2\Sigma f} \\ & +(\eta_{2\Delta f}^2+\eta_{2\Delta fH}^2)\times Cg_{2\Delta f}\} \end{aligned} \tag{6.1}$$

where Cg is the wave group speed and the subscripts represent the following: L - linear; H - Hilbert Transform; 2Σ- second order sum; 2Δ- second order difference; f- free wave.

Calculation of Group Speed

There are at least two methods of calculating the group speed, necessary for the calculation of the energy flux:

Method 1: $Cg = \frac{d\omega}{dk}$, using the linear dispersion relationship $\omega^2 = gk\tanh(kd)$ i.e.

$$Cg = \frac{gkd}{2\omega}\mathrm{sech}^2(kd) + \frac{g}{2\omega}\tanh(kd) \tag{6.2}$$

Method 2: Cg can be deduced from time of flight measurements of the wave group passing the gauges. For example, the time of the maximum of the envelope at each gauge could be deduced, leading to the speed of the envelope and hence the group.

There are drawbacks with both of these methods. Firstly, the accuracy of Method 1 is dependent on the choice of the wave number, k. This value was chosen to be the wave number corresponding to the peak of the spectrum. Method 2 may be more promising since it is based upon experimental results rather than theory. However, it brings its own difficulties, as will be outlined in the following section.

Envelope Tracking

The problem with envelope tracking is that for the linear envelope the original single peak splits into two and then three peaks as the wave group enters shallow water. This is illustrated in Figure 6.10. The calculated group speed obviously depends on which peak is being tracked.

An alternative way of carrying out Method 2 is to calculate the midpoint time of the envelope area. This provides a more robust estimate of the group speed.

Group speeds are required for three wave groups - bound waves, second order sum and second order difference free waves. The speed of the bound wave is the same for each of the harmonics, and was most easily derived from the second order difference (low frequency) term. The speed of the second order sum (high frequency) free wave was deduced with some difficulty by distinguishing by eye where the start and finish of the error wave was located and calculating the maximum of the envelope. Figure 6.11 is replicated from Chapter 3 and shows the high frequency bound and error waves.

It can be seen from Figure 6.11 that closest to the paddles, the free wave is quite distinct from the bound wave, but as the group moved up the beach it becomes less distinct. However, since the free wave is relatively small compared with the linear group it takes longer for it

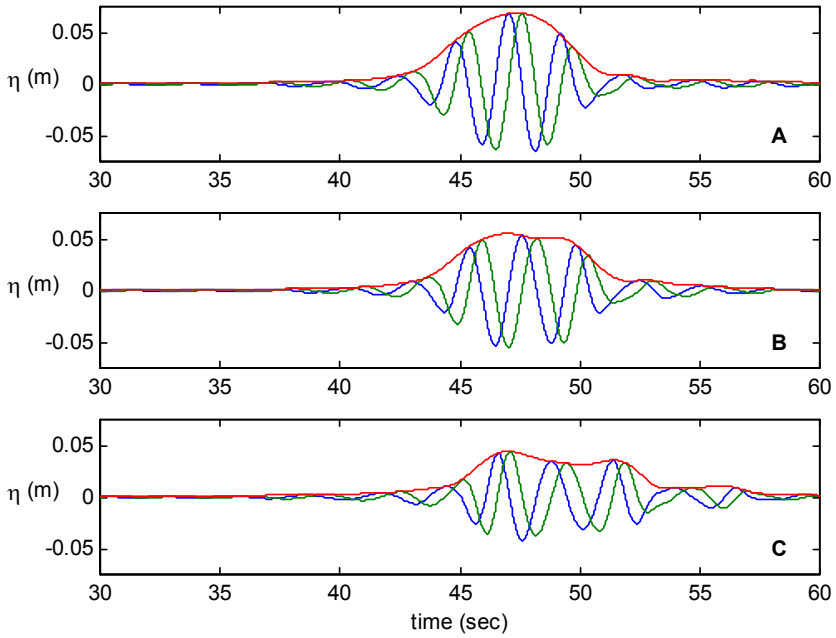

Figure 6.10: Wave groups entering into progressively shallower water (a) 4 m onshore of toe (b) 5 m onshore of toe (c) 7 m onshore of toe: — (blue), linear group; - - - (green), Hilbert Transform; – – – (red) envelope function.

to be affected by the bed and slow down. Therefore, a constant velocity was assumed. The speed of the second order difference free wave was identical to the second order difference bound wave. Figure 6.12 compares the speed of the bound wave and the constant speed second order sum free wave.

Once all terms in Eqn. (3.14) were determined it was possible to calculate the energy flux for all gauges. Figure 6.13 shows the energy flux for a number of wave gauges.

From the energy flux it is a simple process to integrate over time to arrive at a value for the energy at each gauge. This result is shown in Figure 6.14.

It was anticipated that the energy of the wave group would be constant until the onset of wave breaking. For this wave group this occurs at around the halfway up the beach. Clearly this is not the case. It appears that the energy is near constant until the dimensionless distance of 0.125. Why the energy should begin to decrease at this stage is not clear. The calculation procedure outlined in this section is obviously prone to error, many of the values used being dependent upon subjective decisions. There does however appear to be an underlying trend.

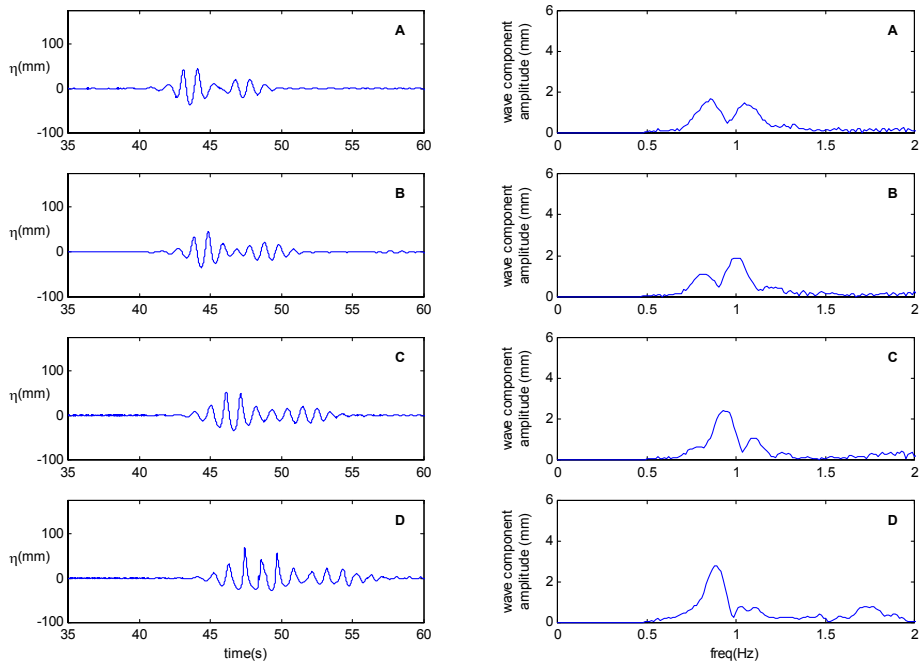

Figure 6.11: Surface elevation and amplitude spectra of second order high frequency 'sum' terms, showing bound and error waves.

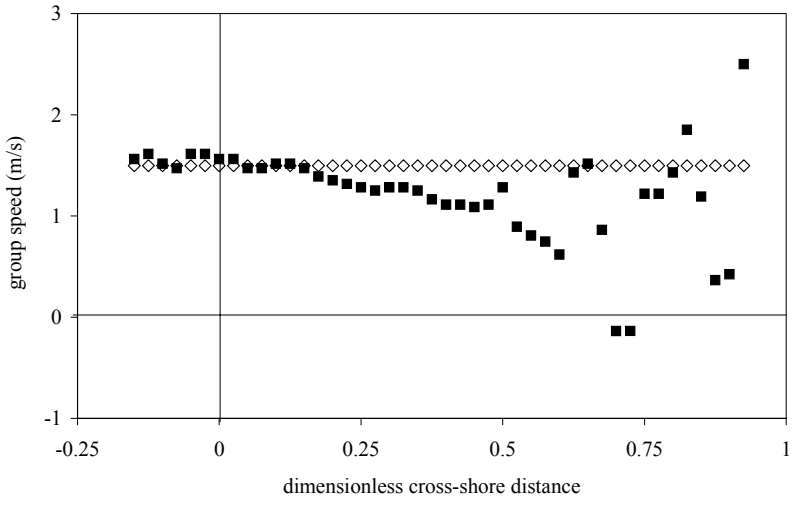

Figure 6.12: Group speed: ■, second order high frequency error wave and ◊, second order high frequency bound wave.

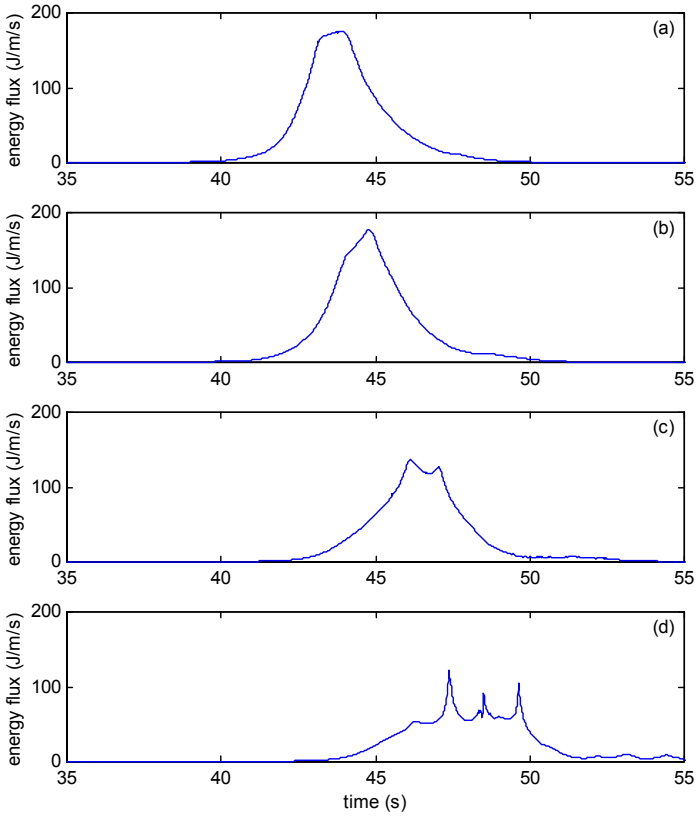

Figure 6.13: Energy flux per unit length of wavefront (J/m/s) at (a) 0.5 m water depth closest to the paddle (b) 0.5 m water depth at toe of beach (c) 0.375 m water depth (d) 0.25 m water depth.

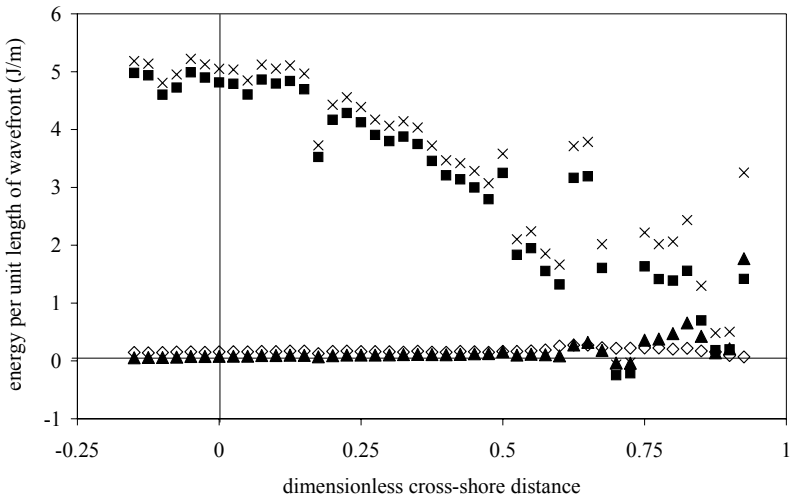

Figure 6.14: Calculated energy: ■, bound wave ; ◊, second order high frequency free/error wave; ▲, second order low frequency free/error; ×, total.

The wave gauge measurements further up the beach are more subject to reflections, which led to a subsequent breakdown of the analysis method.

6.1.5 Conclusions

The results show that the breaker depth indices for transient wave groups on a 1:20 beach are higher than the majority of published values, though less than the values published by Svendsen and Hansen (1984) for cnoidal waves.

Focused wave groups moving into shallow water exhibit the phenomenon of energy shifts to sub- and super-harmonics from the primary frequency range.

Calculation of energy flux in the basin is non-trivial. It would benefit from further investigations, particularly in calculating the group speed of focused waves in shallow water.

6.2 Runup on plane beach

This section investigates the runup of focused wave groups that model extreme temporal and spatial events in unidirectional and spread seas. The term NewWave has been applied to this useful category of focused wave, and is described in detail in Chapter 2.

Specific attention is paid to runup on a plane beach (rather than a structure). It is

of vital importance to be able to determine the extent of wave runup due to an extreme event, to permit the safe siting of buildings, roads and other structures. To date, laboratory investigations have been carried out to assess beach runup, but these studies have been limited to the use of regular (Hunt 1959, Battjes 1974), irregular (Mase 1989) and solitary waves (Synolakis 1987).

Regular waves do not adequately model real waves on a beach because they are too uniform in time and space. Irregular waves are conceptually better but laboratory studies are usually plagued by reflections in the basin. Solitary waves provide a good model for Tsunamis, but not for other extreme waves. The beauty of using NewWave is that it models the temporal and spatial event of an extreme wave without the complication of spurious reflections due to the transient nature of the experiment.

6.2.1 Experimental procedure

The experiments carried out in the UKCRF involved a 1:20 beach. The breaker type can be deduced from the value of the surf similarity or Iribarren number given by

$$\xi_0 = \frac{\tan\alpha}{\sqrt{H_0/L_0}} \tag{6.3}$$

where α is the angle of the slope, H_0 is the offshore wave height and L_0 is the offshore wavelength. If the 'offshore' value is defined to be the value at the toe, then H_0 for the focused wave groups varies between 92 mm and 208 mm. The offshore wavelength of the groups is assumed to be given by

$$L_0 = \frac{gT_p^2}{2\pi} \tag{6.4}$$

where g is gravitational acceleration and T_p is the peak period of the spectrum. Since the same spectrum was used to generate all groups, the offshore wave length is estimated to be 4.782 m. The Iribarren number for the focused waves generated on the beach has a range of 0.240 to 0.360. The breaker type is categorised as follows:

Surging/collapsing	$\xi_0 > 3.3$
Plunging	$0.5 < \xi_0 < 3.3$
Spilling	$\xi_0 < 0.5$

Therefore the waves that interacted with the plane beach were *spilling* breakers.

Additionally the beach can be described as being *dissipative* for $\xi < 1.75$ or *reflective* for $\xi > 1.75$. Therefore the UKCRF beach with the wave groups as defined, is highly dissipative.

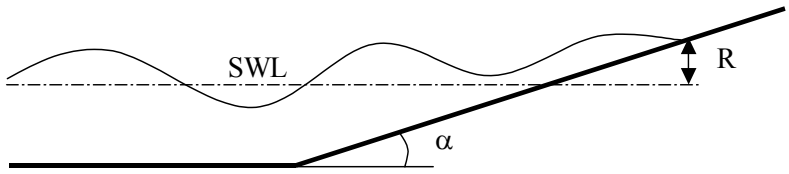

Figure 6.15: Definition of wave runup on a beach.

Figure 6.15 illustrates runup, R, on a plane beach of slope α. By definition, runup is the instantaneous elevation of surface elevation above the still-water-level i.e. it is a vertical rather than cross-shore measurement. In the UKCRF tests runup was estimated by noting visually the greatest extent to which a wave travelled up the centre-line of the beach. This was then converted into a vertical measure by taking account of the beach slope. This simple measurement was complemented by filming the swash zone. The digital pictures enabled runup to be determined to within +/-10 cm along the slope (corresponding to a vertical measurement of +/-5 mm) and also to give qualitative information on the relationship between the wave group parameters and maximum runup.

6.2.2 Effect of low frequency error wave on runup

Due to the method of wave group generation in the UKCRF, a low frequency error wave was present in the basin. This error wave is discussed in detail in Section 3.3.3 and 5.1.5, but briefly it is due to the fact that only linear surface elevation data was sent to the paddles and hence second order error waves are generated. It was not possible for the range of waves that were generated to produce second order signals for the paddles. There are both high and low frequency error waves, but only the low frequency waves give cause for concern since they precede the main wave group. The low frequency error wave manifests itself as a hump travelling just ahead of the main group oscillations.

The low frequency error wave may affect the runup results to some extent. It is possible to determine the effect of the low frequency wave using two different methods:

1. Numerical simulation of runup with and without low frequency wave

2. Estimate runup of isolated low frequency wave assuming behaviour of a solitary wave.

In parallel to the experimental work of this thesis, a numerical model was developed by

Weston (2003). This model has been validated against the results of the present UKCRF work and also against the solitary wave work of Synolakis (1987), with excellent agreement. For the representative wave group WG1, the numerical model predicted a runup of 115 mm with the low frequency error wave included but a reduced runup of only 53 mm when the error wave was removed. This is a little less then half the value and implies that the presence of the low frequency error wave increases the runup of Wave I of the wave group. For WG5 which is the inverted form of WG1, the numerical model predicts a runup of 140 mm with the low frequency error wave present, and reduces to 51 mm when it is absent. This is a very similar picture to the previous group.

For the second method, Synolakis (1987) provides a formula for estimating the runup of a non-breaking solitary wave. Eqn. (3.7) of Synolakis (1987) is

$$\frac{R}{d} = 2.831 \left(\cot \alpha\right)^{\frac{1}{2}} \left(\frac{H}{d}\right)^{\frac{5}{4}} \tag{6.5}$$

where R is the runup, d is the still water depth, α is the slope angle and H is the solitary wave height[1]. This formula is valid for $(H/d)^{\frac{1}{2}} \gg 0.288 \tan a$. Assuming that the low frequency error wave behaves as a solitary wave, the wave height is given by the crest elevation of the error wave. For the crest focused wave, $H = 10$ mm at the toe of the beach and for the trough focused wave, $H = 12$ mm, also at the toe. For the UKCRF beach, $0.288 \tan a = 0.0144$. For the crest focused case $(H/d)^{\frac{1}{2}} = 0.141$, and for the trough focused case $(H/d)^{\frac{1}{2}} = 0.155$. Therefore the inequality is satisfied. Using Eqn. (6.5), the predicted runups of the crest and trough focused error wave are respectively 48 mm and 60 mm. These values can be compared with the measured runup values of 98 mm and 135 mm for the crest and trough focused groups respectively. These values may be an overestimate, since for the corresponding values of H/d, Synolakis' (1987) data begin to stray from his formula towards lower values of runup. If the data of Synolakis are used to predict runup, then for the appropriate wave height to depth ratio the runup of the crest and focused groups are 40 and 50 mm, respectively. The runup of the low frequency error wave when treated as a solitary wave is therefore approximately 40-50% of the value of that recorded in the UKCRF.

Whilst the low frequency error wave generates a considerable runup, the maximum measured runup is that produced by the first wave in the wave group i.e., Wave I. The only

[1] The experimental tests on which this formula is based was carried out at a similar scale to that used in the UKCRF. Still water depths ranged from 62.5 mm to 383.2 mm.

effect of the error wave is thus to modify the behaviour of the following waves. At the very least the error wave provides a region of wetted surface for the wave group to runup on and therefore leads to potentially greater runup. On the other hand, the runup level of Wave I might be reduced if there is a considerable rundown from the error wave that interacts with the advancing bore of Wave I. Wave groups that are generated with an oblique angle of incidence will not be affected by the rundown of the error wave. Additionally, the size of the low frequency error wave reduces considerably for multidirectional wave groups and hence is there is a relatively small effect.

In conclusion, it must be borne in mind that the runup of normally incident waves will be modified by the presence of a low frequency error wave. The other wave group types (oblique and multidirectional) will be affected to a much lesser extent and there can be confidence in the quantitative results for those groups.

6.2.3 Relationship between wave height and runup

Intuitively it might be expected that the maximum runup would correspond to the largest wave in the group. Runup of individual waves within sixteen unidirectional wave groups were plotted as a function of:

1. maximum wave height at any position in the basin
2. maximum surface elevation at any position in the basin
3. maximum wave height at the toe of the beach
4. maximum surface elevation at the toe of the beach and
5. linearised wave height at the toe of the beach.

The plot that showed the strongest correlation with runup was the maximum wave height of the first wave (Wave I) in the group, at any position in the basin. This plot is shown in Figure 6.16, for both unidirectional and spread seas.

Looking closely at the data in Figure 6.16, there appear to be different linear relationships between runup and maximum wave height for the different types of wave group. For example, the normally incident wave group runup values lie approximately on a line that intersects the

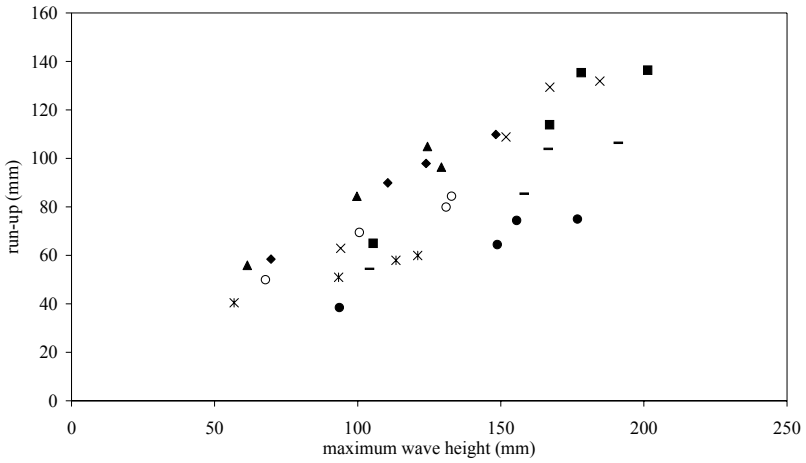

Figure 6.16: Relationship between runup and maximum wave height of Wave I at any position in the basin: ♦, normal incidence; ■, inverted normal incidence; ▲, oblique incidence; ×, inverted oblique incidence; ∗, ±30° spread; •, ±30° spread inverted ∘, ±10° spread; −, ±10° spread inverted.

vertical axis at 20 mm whereas the *inverted* normally incident wave group data lie on a straight line that intersects the vertical axis at about -20 mm. The differences in the wave groups will be explored further in Section 6.2.4.

Impact of other waves in the group

In Figure 6.16, all data came from runup of the first wave in the wave group. As mentioned before, this first wave always gave the greatest runup. It is interesting to examine whether there is a relationship between the runup of first and subsequent waves in the wave group. For the second wave in the group the relationship between runup and maximum wave height is less clear, but appears to be more of an inverse function. From video footage it was evident that the runup of the second wave was affected by the downwash of the first wave i.e., a large first maximum wave gives a large first runup *and* rundown which reduces the size of the second runup, even though the second wave height may be large. There was little or no runup contribution from the third wave in the group.

Figure 6.17 shows the ratio of the height of Wave II compared with Wave I at all points in the basin. It can be seen that although the height of Wave II is larger than Wave I for some positions in the basin, it is always smaller than Wave I in the shallowest region. Hence

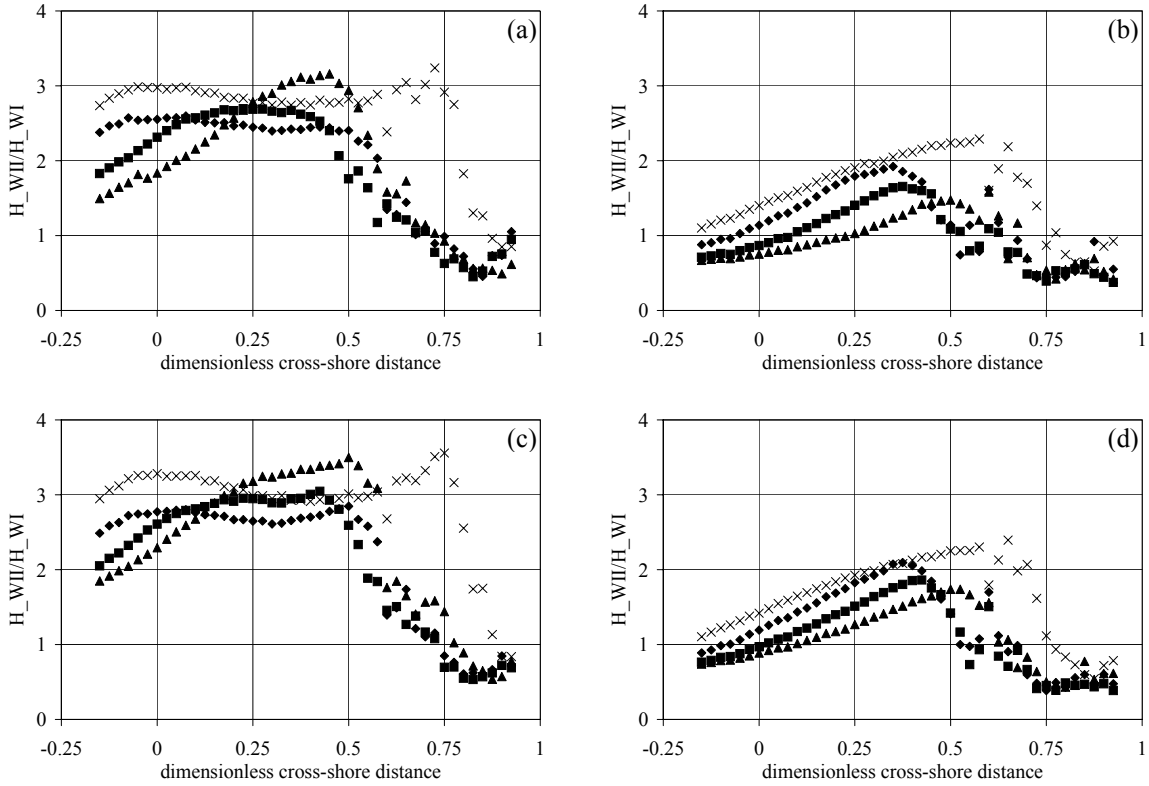

Figure 6.17: Relative height of Wave II compared with Wave I for different wave group types (a) normally incident, crest focused (b) normally incident, trough focused (c) oblique incidence, crest focused and (d) oblique incidence, trough focused: ♦, large, focused at toe; ■, large, focused at 3/4; ▲, large, focused at 1/2; ×, small, focused at toe.

a smaller onshore wave would be interacting with a large downwash.

It is possible to investigate the impact of preceding waves on the runup of the focused wave by considering an embedded focused group in a regular wave train. The embedded NewWave focuses at the toe and has the same input amplitude as that used for the lone, large NewWave focused at the toe (WG1). This embedded wave is described in detail in Chapter 4. Four different embedded groups were used:

1. NewWave crest coincident with regular wave crest (EG1).

2. NewWave trough coincident with regular wave crest (EG2).

3. NewWave crest coincident with regular wave trough (EG3).

4. NewWave trough coincident with regular wave trough (EG4).

Windowed surface elevation time histories of these four waves are shown in Figure 6.18. When the waves are in phase i.e. crest of regular plus crest of group (Figure 6.18 (a)), or trough of regular plus trough of group (Figure 6.18 (c)) the wave group is effectively undistorted as would be expected[2]. This is in contrast to waves that are out of phase and exhibit a degree of distortion.

Figure 6.19 shows how the surface elevation of the embedded NewWave (regular wave crest plus NewWave crest) compares with a lone NewWave (crest focused). There is excellent agreement between the NewWave shapes in the focus region, apart from slightly smaller troughs in the crest-crest wave train, and slightly smaller crests in the trough-trough wave train.

The runup of the first wave of the four embedded wave groups is plotted alongside the unidirectional results in Figure 6.20. It can be seen that the waves that are in phase fall within the scatter of lone wave group data, whilst the waves that are out of phase with the background regular waves have considerably reduced runup. This implies that for this size of regular wave, the runup of an extreme wave is not reduced unless the extreme wave is out of phase with the regular wave train.

6.2.4 Parametric study of extreme wave runup

It is possible to carry out dimensional analysis of the focused wave group runup. However, since there are not large enough variations on any of the parameters to provide any absolute relationships, it is more beneficial to investigate individual parameters. This section lists a number of parameters that can be used to define an extreme wave, and provide possible correlation with runup. These parameters are: input wave amplitude (A_0), focus location (x_f), group phase (ψ), angle of incidence (θ_0) and degree of wave front spread (θ_s).

Input wave amplitude, A_0

Table 6.1 shows the values of wave runup for two different input amplitudes, for waves focusing at the toe of the beach.

Figure 6.21 (a) shows that the increase in runup with wave amplitude for the crest focus

[2]The crests either side of the central trough are different sizes due to non-linearities, exhibited in a lone NewWave. They are *not* distorted due to the embedding process.

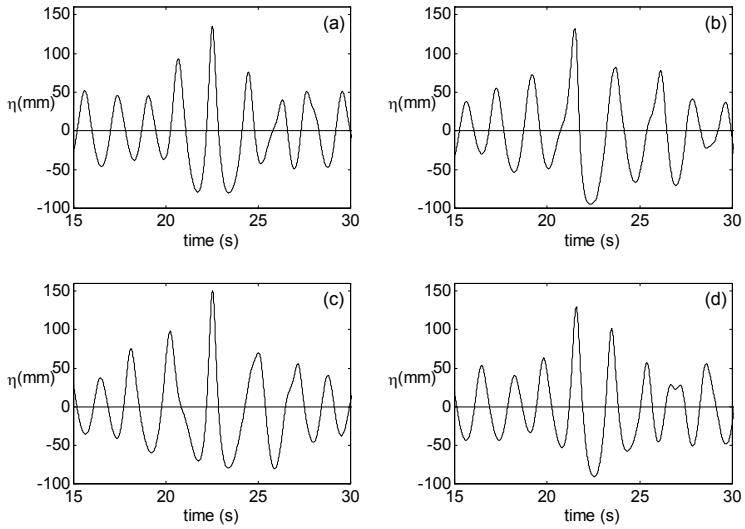

Figure 6.18: Time histories of four embedded wave groups (a) EG1 (b) EG2 (c) EG3 (d) EG4.

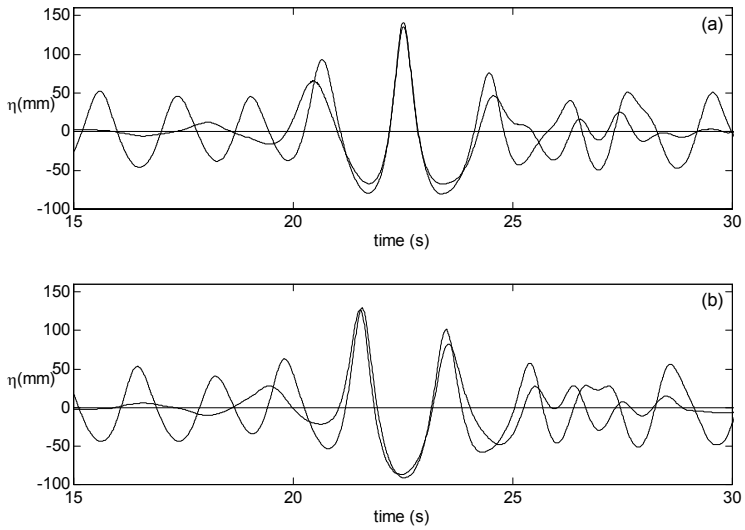

Figure 6.19: Time histories of embedded and lone NewWave, for (a) EG1 and (b) EG4: —, embedded NewWave; - - -, lone NewWave.

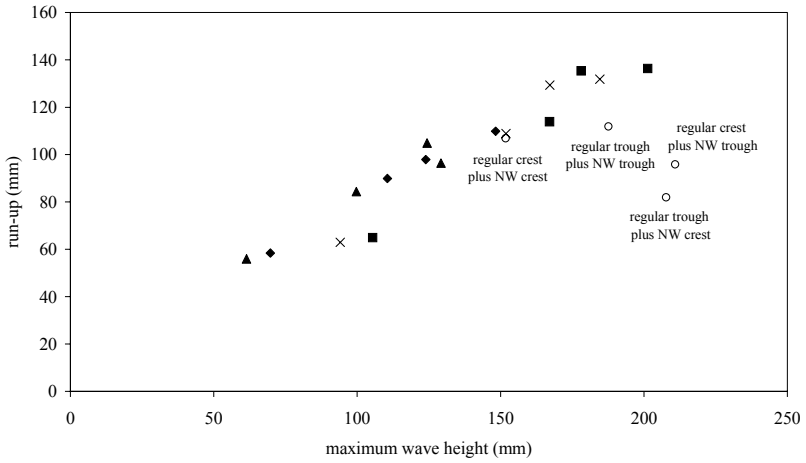

Figure 6.20: Runup as a function of maximum wave height of first wave, for unidirectional and embedded waves: ♦, normal incidence; ■, inverted normal incidence; ▲, oblique incidence; ×, inverted oblique incidence; ∘, embedded groups.

Table 6.1: Wave runup for two different input amplitudes (normal and oblique incidence waves).

	wave runup (mm)			
input amplitude (mm)	crest focus (normal)	crest focus (oblique)	trough focus (normal)	trough focus (oblique)
57	58	56	65	63
114	98	96	135	129

case is almost identical for normal and oblique incidence waves. For a doubling of the input amplitude, the runup increases by a factor of 1.68 for normal incidence and 1.72 for oblique incidence i.e. a multiplication factor of approximately 1.7. Similar behaviour is seen for doubling the input amplitude of normal and oblique incidence trough focus groups - though there is a slightly larger multiplication factor - 2.08 for normal incidence and 2.06 for oblique incidence. From this it can be deduced that there may be an approximately linear relationship between input amplitude and wave runup - particularly for trough focus wave groups; and that this relationship is independent of angle of incidence. At this time it is not clear why there should be a different multiplication factor for crest focus and trough focus wave groups, though results from numerical modelling (Weston et al. 2003) indicate a marked dependency

on group phase at the focus point.

Focus location, $\mathbf{x}_f$

It is possible to investigate the effect of changing the focus location whilst keeping the phase (at the focus point) and input amplitude constant. Table 6.2 shows the runup measurements for waves with an input amplitude of 114 mm, focusing at the toe of the beach and one-quarter way up the beach.

Table 6.2: Wave runup for two different focus locations (normal and oblique incidence waves).

	wave runup (mm)			
focus location	crest focus (normal)	crest focus (oblique)	trough focus (normal)	trough focus (oblique)
beach toe	98	96	135	129
$\frac{3}{4}$ depth	110	105	136	132

Figure 6.21 (b) shows that there is a slight increase in runup for a wave focused further up the beach i.e. in $\frac{3}{4}$ depth rather than at the toe of the beach. The increase in runup is greater for crest focused rather than trough focused groups. Again, there appears to be little difference between the action of normal and oblique incidence waves.

Phase of wave group, ψ

A crest focused wave group is one in which all *crests* are in phase, in contrast to a trough focused wave where all *troughs* are in phase. From Figure 6.21 (c) it can be seen that there is an increase in runup for trough focused groups when compared with crest focused groups, regardless of the focus location and of whether the wave group is normally or obliquely incident.

It should be noted that for each of the last three parameters, the order of the runup values are unaltered as the parameter is changed. For example, in Figure 6.21 (b), at the toe of the beach the highest value of measured runup is produced by trough focus (normal), then trough focus (oblique), then crest focus (normal) and lastly crest focus (oblique) giving the lowest value. This order of values is the same when the focus location is at the $\frac{3}{4}$ depth position. The same phenomenon exists in Figure 6.21 (a), and to some extent in Figure 6.21

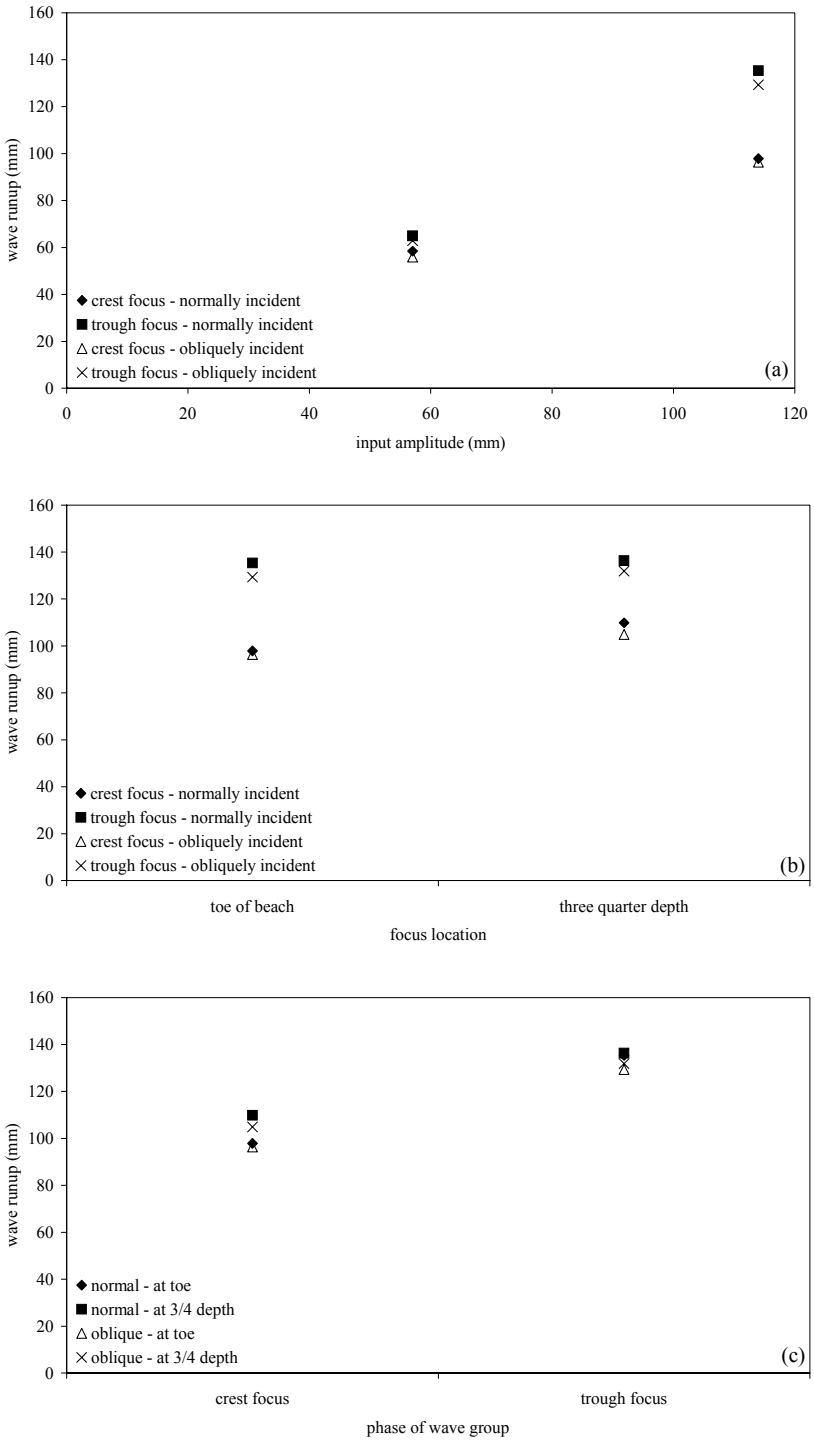

Figure 6.21: Wave runup as a function of (a) input amplitude, (b) focus location and (c) phase of the wave group.

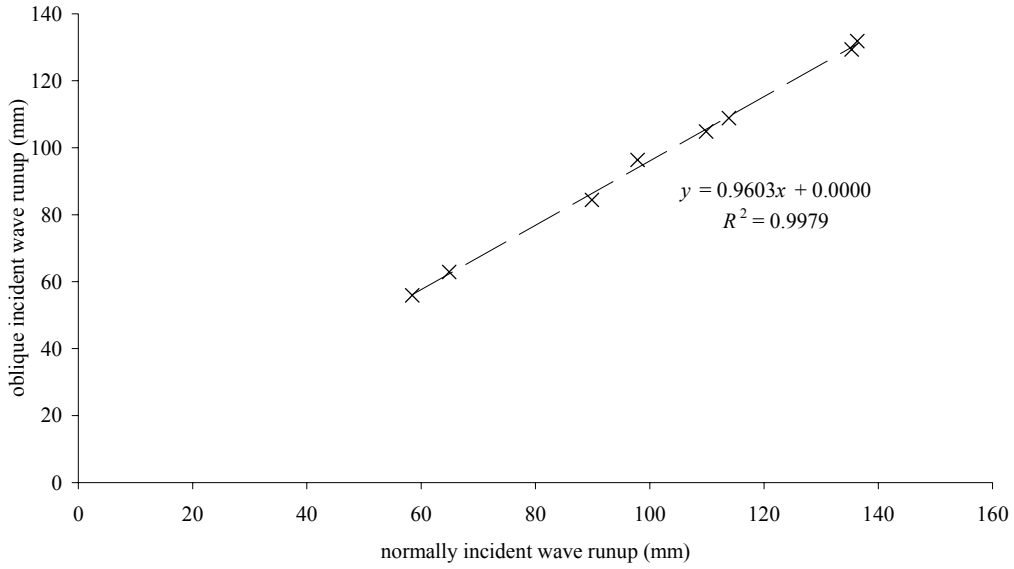

Figure 6.22: Wave runup of oblique waves compared to wave runup of normally incident waves.

(c) though for the trough focus the data points are very close in value to each other.

Angle of incidence of wave front, θ_0

The effect of the angle of incidence on wave runup is now investigated. Wave groups with two different angles - normal and oblique (20°) incidence were used. Figure 6.22 is a plot of runup of oblique wave groups versus that of normally incident wave groups for all unidirectional cases (of varying phases, focus locations and amplitudes). It can be seen that the runup of oblique waves is 96% of the normally incident waves, but otherwise identical. The best fit linear trend is near-perfect. An investigation of the effect of oblique incidence waves was carried out by De Waal & Van der Meer (1992). They estimated that the runup reduction factor for oblique long-crested waves is given by $\gamma_b = \cos(\theta_0 - 10^\circ)$. For an angle of 20° this is calculated to be 0.98. The results in the UKCRF are close to this value. The discrepancy may be due to the presence of the error wave producing a slightly larger runup of the normally incident wave groups.

Degree of wavefront spread, θ_s

In addition to measuring the runup of unidirectional wave groups, measurements were made for spread seas. A top hat distribution of two different spread angles was used: -10° to $+10^{\circ}$ and -30° to $+30^{\circ}$.[3] Comparisons between the runup of spread sea and unidirectional groups are shown in Figures 6.23 (a) and (b) for crest focus and trough focus groups respectively.

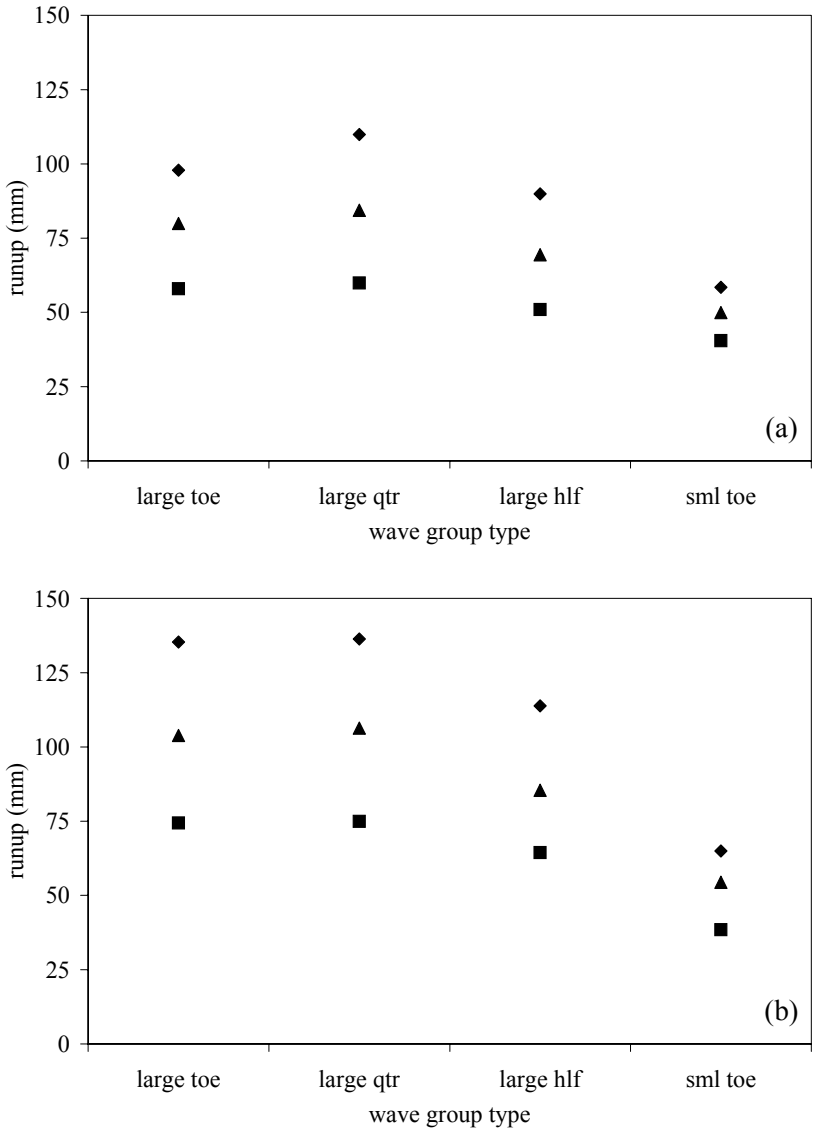

Figure 6.23: Wave runup as a function of wave front spread for (a) crest focus and (b) trough focus cases: ♦, normally incident - unidirectional; ▲, ±10° spread sea; ■, ±30° spread sea.

There is a very clear reduction of runup for spread sea states.

[3]The UKCRF was calibrated up to and including ±30° (see Chapter 4).

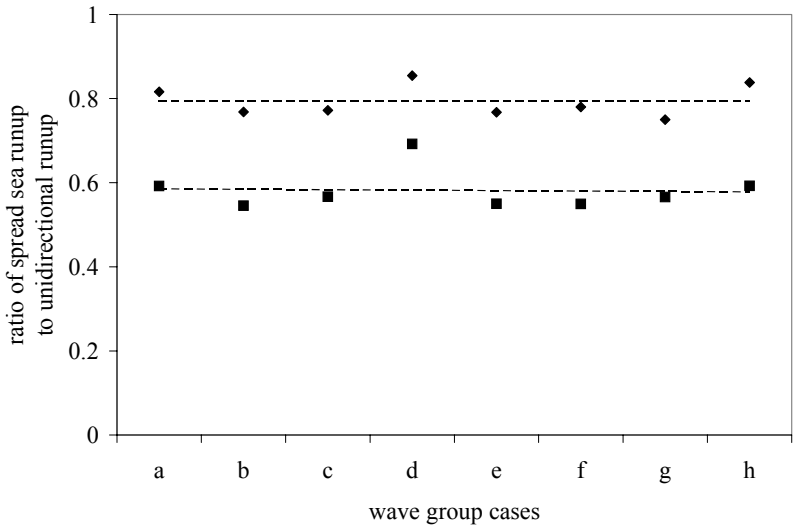

Figure 6.24: Ratio of runup reduction for spread seas for all wave group cases:♦, $\pm 10^\circ$ spread sea; ■, $\pm 30^\circ$ spread sea.

Figure 6.24 shows the reduction in runup for the two spread sea cases, for the eight different wave group types detailed in Table 6.3. Table 6.4 summarises these results showing

Table 6.3: Details of wave groups.

	size	focus location	inverted (Y/N)
a	large	toe	N
b	large	$\frac{3}{4}$ depth	N
c	large	$\frac{1}{2}$ depth	N
d	small	toe	N
e	large	toe	Y
f	large	$\frac{3}{4}$ depth	Y
g	large	$\frac{1}{2}$ depth	Y
h	small	toe	Y

the mean reduction in runup compared with a normally incident unidirectional wave.

Results for both crest and trough focused waves are very similar - approximately 20% reduction for a $\pm 10^\circ$ spread sea and 40% reduction for a $\pm 30^\circ$ spread sea. This robustness in the reduction factor is similar to the robustness of the 0.96 factor for 20° obliqueness, seen

Table 6.4: Ratio of spread sea runup to unidirectional normally incident runup.

	mean reduction factor (%)	standard deviation (%)
$\pm 10^{\circ}$ crest focus	80.2	4.1
$\pm 10^{\circ}$ trough focus	78.3	3.8
$\pm 30^{\circ}$ crest focus	59.8	6.5
$\pm 30^{\circ}$ trough focus	56.3	2.0

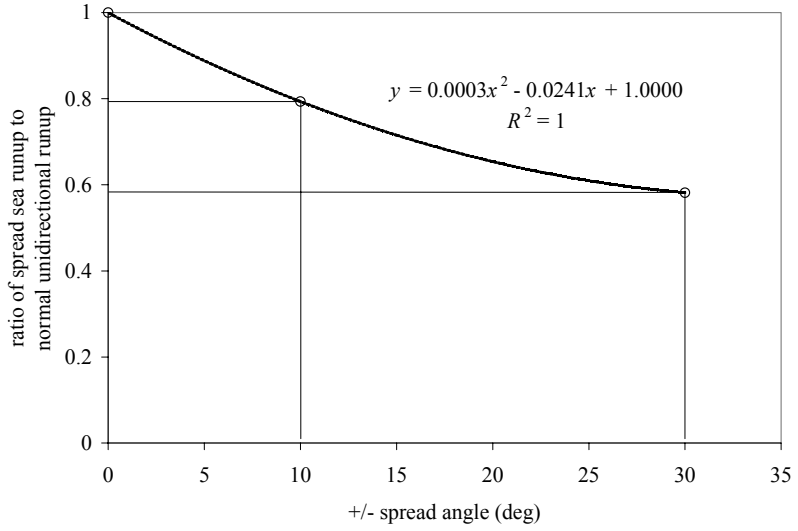

Figure 6.25: Ratio of spread sea runup to normally incident runup for different spreading values.

earlier. Figure 6.25 shows the results in another format with a suggested best-fit line.

In conclusion, runup increases with: increased input wave group amplitude; a focus location further up the beach; and with inversion of wave groups. Runup decreases with obliqueness and short-crestedness.

6.2.5 Correlation of runup with low frequency wave

In Chapter 5 it was seen that a low frequency wave was released when the wave group interacted with the beach. Barnes (1996) found that there was a linear relationship between the size of the released wave and the extent of runup. Figure 6.26 shows the relationship for focused wave groups generated in the UKCRF.

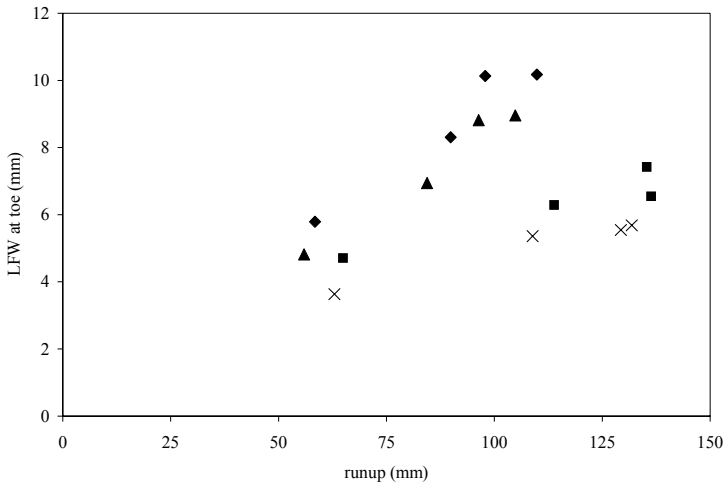

Figure 6.26: Crest amplitude of outgoing low frequency wave as a function of runup of Wave I : ♦, normal incidence; ■, inverted normal incidence; ▲, oblique incidence; ×, inverted oblique incidence.

The low frequency wave was obtained from surface elevation data measured at the toe of the beach and low frequency band-pass filtered. Figure 6.26 shows an approximately linear correlation between the size of the low frequency wave and the runup level, for all four unidirectional wave group types. A word of caution however in interpreting the data. Referring back to the influence of the low frequency *error* wave: both the outgoing low frequency wave (LFW) and the runup of the normally incident groups may be affected by the presence of the error wave. However, the oblique wave will be affected to a much lesser extent. Figure 6.26 shows that the size of the LFW is smaller for the oblique waves than for the normally incident waves. This may or may not be due to the presence of the error wave. Also evident, for the case of oblique waves, is the reduction in LFW as a function of runup for inverted groups. Numerical investigation of these issues is warranted.

6.2.6 Comparison with other wave runup investigations

Wave runup theories have been deduced from hydraulic model tests, but currently encompass regular, irregular and solitary waves separately.

Regular waves

For regular waves, Hunt's formula (Hunt, 1959) proposed over forty years ago is

$$\frac{R}{H_0} = \xi_0 \tag{6.6}$$

where R is runup, H_0 is the offshore wave height and ξ_0 is the surf similarity parameter given by Eqn. (6.3). Figure 6.27 compares the runup predicted from Hunt's formula with measurements. It is clear that the predicted values are around twice the size of the measured values.

Irregular waves

In order to compare the runup results it is necessary to find a representative significant wave height, H_s, for the wave groups. For irregular waves, the most probable maximum amplitude A, in N waves, is given by

$$A = \sigma\sqrt{2\ln(N)} \tag{6.7}$$

where σ is the standard deviation of the wave energy spectrum.

The significant wave height for irregular waves is defined in terms of σ as

$$H_s = 4\sigma \tag{6.8}$$

Rearranging Eqn. (6.7) to obtain σ, and making the substitution into Eqn. (6.8) gives

$$H_s = \frac{4A}{\sqrt{2\ln(N)}} \tag{6.9}$$

For irregular waves on a gentle beach, there are several formulae given by Mase (1989). These are

$$\frac{R_{\max}}{H_s} = 2.32\xi_0^{0.77} \tag{6.10}$$

$$\frac{R_2}{H_s} = 1.86\xi_0^{0.71} \tag{6.11}$$

$$\frac{R_{1/10}}{H_s} = 1.70\xi_0^{0.71} \tag{6.12}$$

$$\frac{R_{1/3}}{H_s} = 1.38\xi_0^{0.70} \tag{6.13}$$

$$\frac{\overline{R}}{H_s} = 0.88\xi_0^{0.69} \tag{6.14}$$

where $R_{\max}$ is the highest runup height[4], R_2 is the 2% excess runup height, $R_{1/10}$ is the one-tenth highest runup height, $R_{1/3}$ is the one-third highest runup height, $\overline{R}$ is the mean runup height, H_s is the deep water significant wave height and ξ_0 is the surf similarity parameter with the offshore wave height. Figure 6.28 shows the dimensionless runup predictions of Eqns. (6.13), (6.12), (6.11) and (6.10) alongside experimental results[5].

The first point to make is that the experiments were carried out within a restricted range of surf similarity parameter. Mase (1989) carried out experiments on four different beach slopes. For one case, which had a comparable slope of 1/20, the range of surf similarity parameter was between 0.21 and 0.85 (mean of 0.42, standard deviation of 0.19). Experimental results from the UKCRF tests fall in the bottom half of the Mase (1989) range.

From Figure 6.28 it is noticeable that non-dimensionalised runup is lower for inverted wave groups than for non-inverted groups. Also the predictions of Mase (1989) are more closely followed by inverted groups.

Solitary waves

When waves break they might act independently of each other: in effect their runup behaviour could be described in the same way as solitary waves (Bird & Peregrine (1997). In order to investigate whether or not this is the case for waves in a focused wave group, the experimental runup results were plotted alongside data provided by Synolakis (1987) for a 1:19.85 slope. Also included in the comparison is the runup of a 100 mm solitary wave that was generated in the UKCRF.

In plotting the measured values there is some uncertainty about which value of wave height should be used for the focused wave groups. Figures 6.29 (a) and (b) use wave height at beach toe, and maximum wave height, respectively.

The data provided by Synolakis (1987) on Figure 6.29 shows two distinct gradients. The data for lower dimensionless runup is for non-breaking waves whereas the larger dimensionless runup is for breaking waves.

[4]In fact there is no maximum runup since it is not possible to define a maximum wave, only a very large wave with a very small chance of occurring.

[5]Measurements of dimensionless runup were obtained from the measured runup divided by the significant wave height, H_s. H_s is obtained from Eqn. (6.9), using the appropriate value of N, e.g. for 2% exceedance, $N = 50$ and the measured wave amplitude A, at the toe of the beach. The *maximum* wave used $N = 10\,000$.

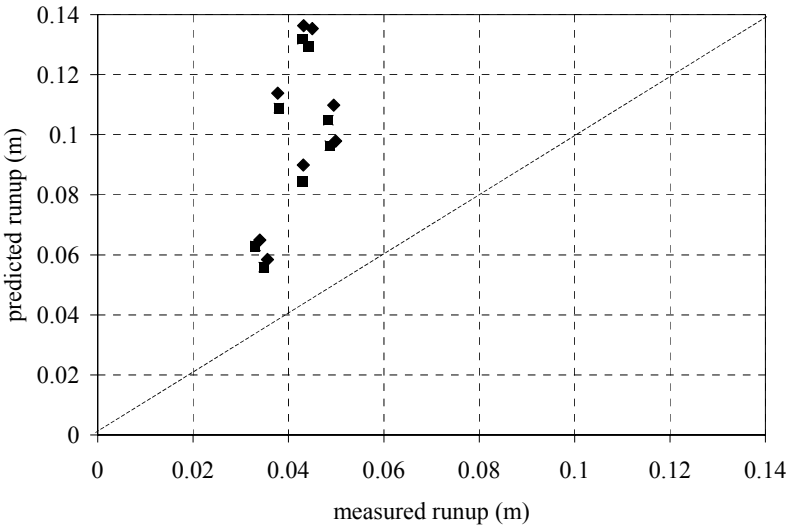

Figure 6.27: Predicted beach runup using Hunt's (1959) formula, compared with measured values: ♦, non-inverted groups; ■, inverted groups.

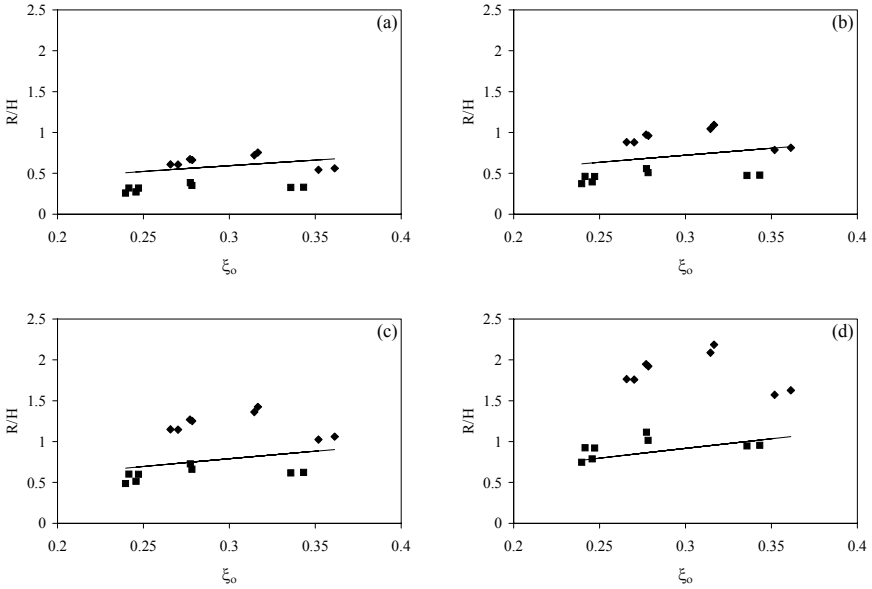

Figure 6.28: Relative height of wave II compared with wave I for different wave group types (a) $R_{1/3}/H_s$ (b) $R_{1/10}/H_s$ (c) R_2/H_s (d) $R_{\max}/H_s$: ♦, non-inverted groups; ■, inverted groups.

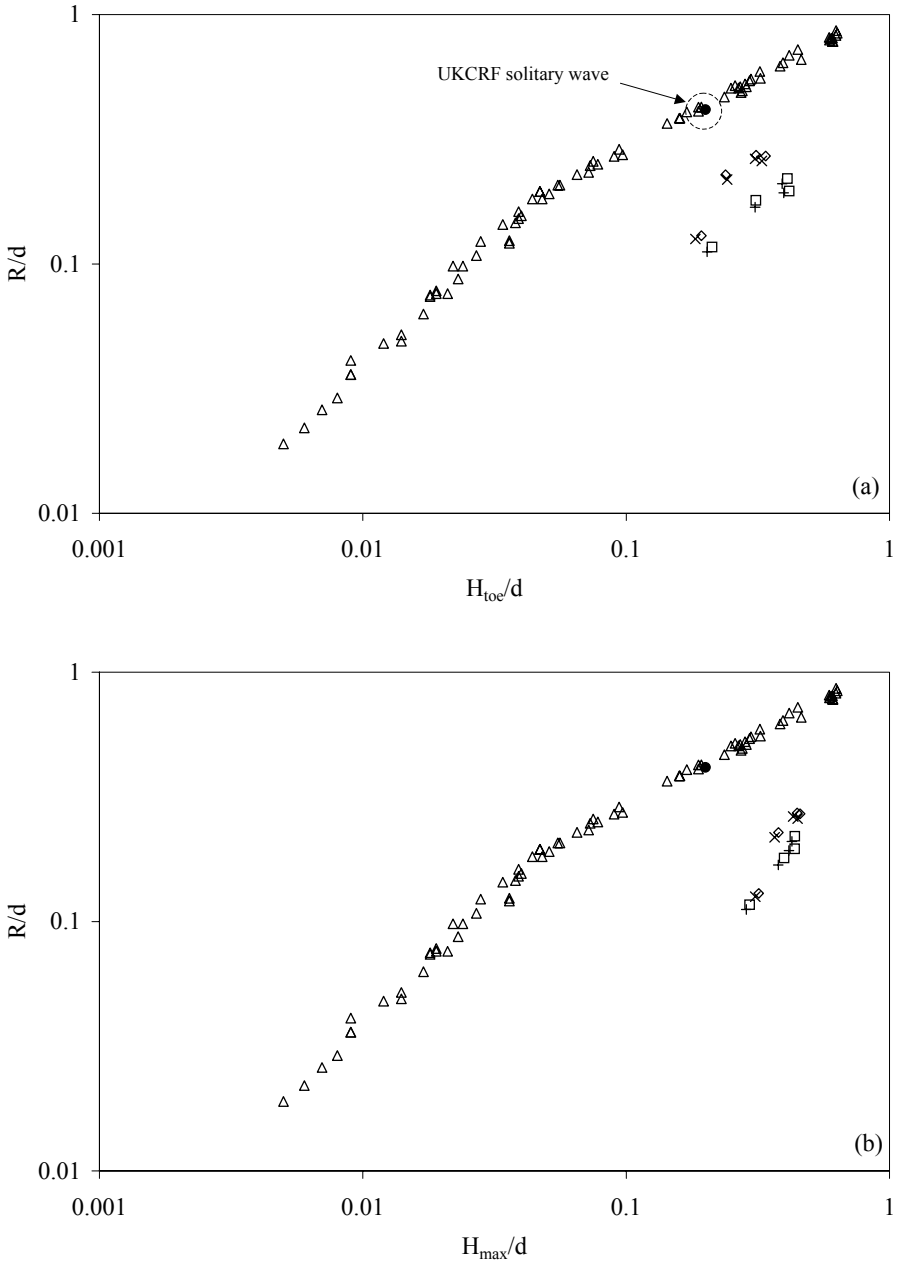

Figure 6.29: Comparison between solitary wave results and focused waves, using (a) Htoe and (b) Hmax: △, Synolakis solitary waves; □, normal incidence group; ◇, normal incidence group, inverted; +, oblique incidence group; ×, oblique incidence group, inverted; •, UKCRF solitary wave.

The first thing to note about the data in Figure 6.29 is the excellent agreement between the runup of the UKCRF solitary wave and the breaking solitary waves measured by Synolakis (1987). This gives confidence in the runup measurements in the UKCRF and provides confirmation of Synolakis' measurements.

The data for wave groups on Figure 6.29 shows that dimensionless runup is considerably less than that which would be obtained with a solitary wave, regardless of whether wave height at beach toe or maximum wave height is used. It can be concluded therefore that broken waves from focused wave groups do not have the same runup behaviour as solitary waves.

6.2.7 Conclusions

From the UKCRF data it is observed that Wave I in the focused group becomes the largest wave after it enters the surf zone. It produces the largest runup. There is a corresponding strong correlation between runup and maximum wave height of the first wave in all wave groups.

The effect of embedding a focused wave group within a regular wave train varies depending on the relative phases of the two waves. For waves that are out of phase with each other there is an attenuation of runup. For waves that are in phase the runup is little affected.

From a parametric study of the effects on extreme wave runup it was concluded that runup increases with increased input amplitude, a focus location closer to the still water shoreline and inversion of the wave groups. Runup decreases with obliquity and multi-directionality.

There is a linear relationship between the size of the outgoing low frequency wave (generated as the wave group reaches the shore) and the size of the wave runup.

The runup of focused wave groups is over-predicted by solitary waves but an irregular wave formulation gives reasonably close agreement particularly for inverted wave groups.

6.3 Overtopping of a sea wall

This section investigates the overtopping of a sea wall by extreme unidirectional and spread sea focused wave groups. Prediction of overtopping is critically important for coastal engineers when designing coastal structures to protect people and property. There is a fine balance

to be made between the financial cost of building a coastal structure that will provide the greatest security for what lies on the leeward side, and a pragmatic approach which allows a permissible rate of overtopping. In fact, the second approach is always followed to some extent since it is impossible to guard against the 'largest' wave since it probably does not exist - it is just less likely to occur than smaller waves.

It is necessary to make calculations of the rate of overtopping to enable appropriate drainage facilities to be constructed (Su et al., 1992), but it is also extremely useful to have estimates of individual overtopping volumes as these are important in predicting the effect on people and property (Allsop 1994, Owen, 1980, Jensen & Juhl, 1987). It is also useful to be able to measure the velocity of the overtopping water, to gauge the forces involved.

Overtopping investigations have been carried out primarily in laboratories because of lack of control of field environmental conditions and the sheer complexity and financial cost of field work. Earlier work (e.g. Saville 1955; Weggel 1976), used regular waves to provide empirical relationships between dimensionless parameters of structure crest freeboard and overtopping discharge. This was extended to cover irregular waves by assuming that each wave in the irregular wave train could be modelled as a regular wave (Ahrens 1977; Shore Protection Manual 1984). There are obvious flaws in this approach. Other work was based upon irregular wave overtopping in basins (Owen 1980; Van der Meer & Stam 1992), but as with laboratory irregular wave runup there are difficulties in carrying out such experiments. Overtopping tests may be greatly affected by very large reflections from the sea wall, which may reverberate around the basin or flume if not effectively absorbed. The use of NewWave for overtopping experiments eliminates the problem of reflections because it is a transient phenomenon.

6.3.1 Experimental procedure

Figure 6.30 shows a definition sketch of sea wall overtopping. An investigation into overtopping of waves over sea walls is more complicated than wave runup since it involves additional variables: water depth at toe of wall (h_m), crest of wall (R_c) and slope of sea wall (β). Dimensional analysis will not be undertaken for the same reasons that it was not carried out for runup, i.e. not enough variation of each dimensionless product or variable. The UKCRF tests used only one seawall geometry with $h_m = 0.0938$ m, $R_c = 0.117$ m and $\tan(\beta) = 1/2.18$.

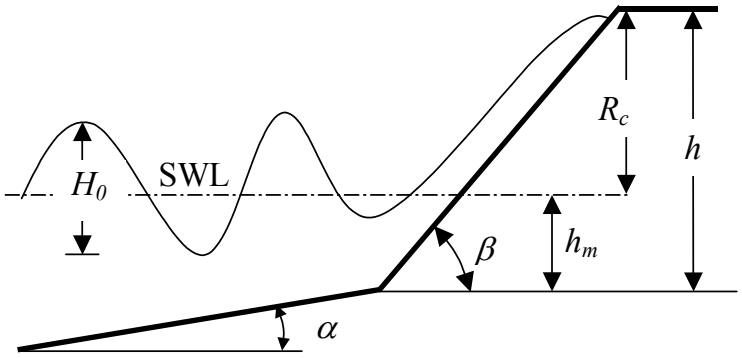

Figure 6.30: Definition sketch of sea wall overtopping in the UKCRF.

The Iribarren number for the wave groups, given by Eqn. (6.3) varies between 2.20 and 3.30. Referring back to Section 6.2.1 this means that the slope is *reflective* and the breaker types are mainly plunging breakers, but the smallest groups are defined as either collapsing or surging breakers.

Water surface elevations over the sea wall were measured by wave gauges placed in pre-cast holes in the sea wall, which were lined with plastic tubing. The gauges needed to be removed from the holes for calibration, along with all the other gauges in shallow water positions. This is in contrast to the method used by Kobayashi & Raichle (1994). They too had holes in the wall, but with the gauges permanently sunk in saturated sand. The gauges of Kobayashi & Raichle (1994) were calibrated by varying the still water level in the tank. This was not an option for the work in the UKCRF. Admitting fresh water into the basin causes seiching and may also introduce a temperature change with associated changes in conductivity. Figure 6.31 is a diagram of the wave gauges placed in the wall, attached to the wave gauge rig.

Wave overtopping volumes were measured using two methods:

1. Volume of water in catchment area.

2. Volume of water travelling over the top of the wall (from a knowledge of the water layer thickness and velocity of wavefront).

Method 1 can only measure the total amount of overtopped water, not the volume for each wave in a group. Method 2 requires careful calculation of volume from the thickness of the water layer travelling over the top of the wall, and the speed that it travels. The speed can be

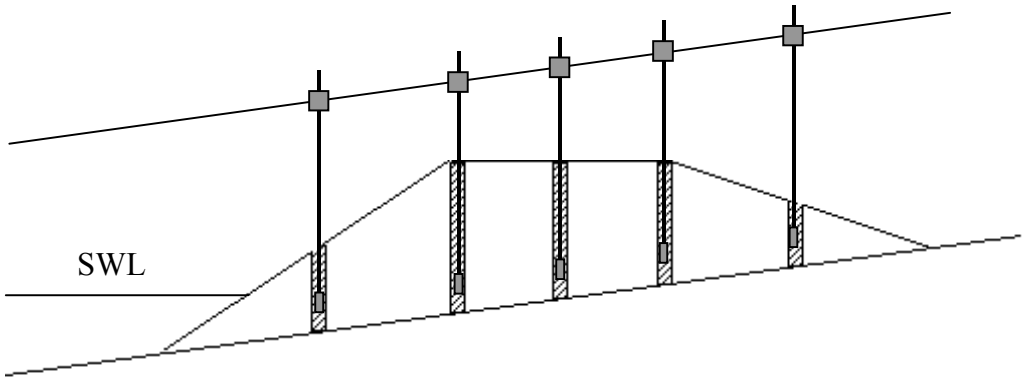

Figure 6.31: Placement of wave gauges in seawall.

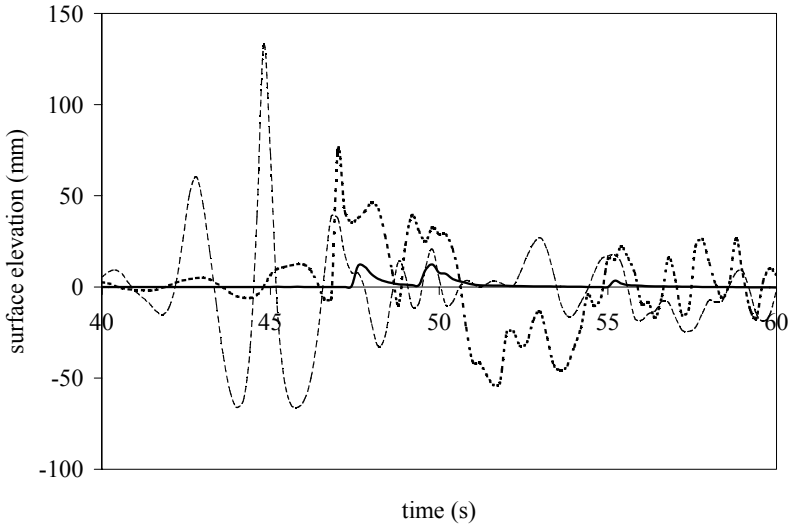

Figure 6.32: Surface elevation time histories at three points in the basin for wave group 1: — — —, toe of beach; − − −, toe of sea wall; and ——, top of sea wall.

deduced from the time that it takes the bore of water to travel between two wave gauges on the top of the wall. An attempt was made to use a Laser Doppler Anemometer to measure the velocity of the overtopping water, but this was not successful due to the entrained air within the sheet of water (Griffiths et al., 1992). Archetti et al. (1995) apparently had reasonable success measuring the velocity of the overtopping sheet of water using micropropellers, though this was for full-scale tests.

Figure 6.32 shows surface elevation time histories for three different locations in the basin, for wave group 1 (WG1 - see Appendix 1 for details). The focused wave group is recognisable at the toe of the beach, but at the toe of the sea wall considerable transformation of the shape of the group has taken place and it will have been affected by reflections back off the wall. The surface elevation time history from one of the gauges on top of the wall shows two comparably sized overtopping events, with a third smaller event occurring some time later at around 55 sec. With this second method it is obviously possible to calculate the volume of individual overtopping events.

Comparisons between the two methods for measuring wave overtopping volumes were generally very good. Figure 6.33 shows the agreement between the two methods for total overtopping volumes, for forty-two wave cases. This gives confidence that individual overtopping volumes can be obtained using Method 2.[6]

6.3.2 Effect of low frequency error wave on overtopping

As discussed in Section 6.2.6 there is a low frequency error wave in the basin. It is not possible to predict the effect of this wave on the overtopping results as there are no reliable methods analogous to those used for the error wave runup analysis. It is much more difficult even to determine the size of the low frequency error wave that runs up and overtops the sea wall.

It was clear from the data analysis that first overtopped volume was due to Wave I, not a preceding low frequency hump. Therefore there was no error in deducing the overtopping volumes. The only effect of the low frequency wave would have been to reflect off the wall

[6] A note on units: Overtopping volumes are given as volume per unit run. Due to the small scale of the UKCRF experiments units of litres/m rather than m^3/m have been used. The volume per unit run values have been calculated from the total overtopped volume in the catchment area divided by the length of the seawall in front of the catchment area. This is the conventional approach but it will lead to errors when analysing data from multidirectional seas that do not have a uniform distribution of overtopping along a seawall crest.

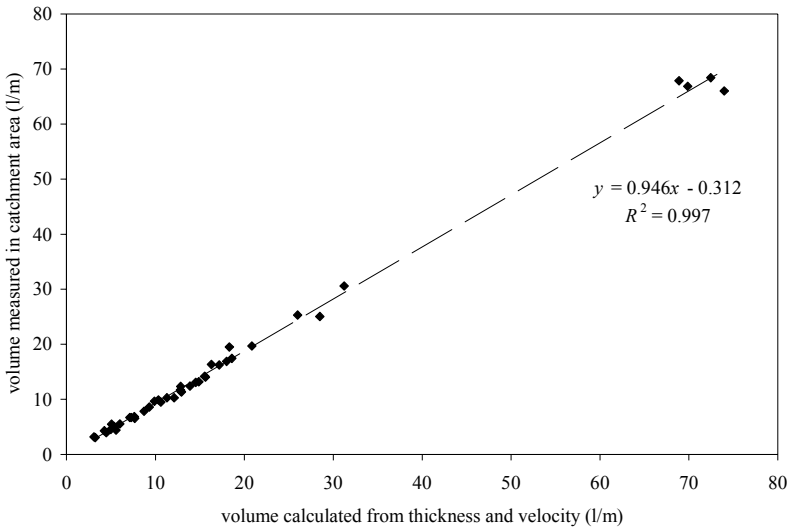

Figure 6.33: Comparison between total overtopping volumes (litres/m) using two different methods.

and interfere with incoming waves. The impact of this on the overtopping volume of Wave I is not known. It may be that the overtopping volume is reduced if the rundown of the error wave coincides with the runup of the next incoming wave. It is unlikely that the overtopping volume is increased. This would only happen if the next wave were travelling slightly faster than the first, catches up with it and travels over the wall on top of the first wave. The error wave is a low frequency free wave that travels slightly faster than the group and therefore will not be caught. There is also the possibility of a benign effect of the error wave depending on the relative phases.

The oblique wave groups have the same low frequency error wave as the normally incident wave groups. However, the reflected error wave will not interfere with the following waves. Therefore, there can be confidence in the quantitative findings concerning the oblique wave groups. Additionally since the error wave decreases in size with degree of wave front spreading, the multidirectional wave groups will be affected much less by reflections of the error wave than the normally incident groups.

In conclusion, it can be said that only the normally incident wave groups may be affected to any extent by the error wave. Also, the inclusion of an error wave puts these experiments in good company. The only laboratory overtopping experiment that makes mention of low

frequency error waves was carried out by Tsuruta & Goda (1968). They did not use data from the initial part of the time series because of low frequency start-up waves, though they continued to use data from when the low frequency wave would have come back off the paddles (but before reflections from the main wave train came back). All other experiments make no mention of low frequency error waves generated either spuriously from the paddle or those generated from the reflections of the waves off the sea wall, or subsequently being reflected off the paddles. The effect of these waves is that there is confusion about whether the waves are incoming or outgoing, part of the intended spectrum, or low frequency reflected components. This is problematic because it is necessary to separate the incident and reflected waves to define the significant wave height at the toe of the structure for use in the empirical formulae. However, methods to separate them are not necessarily valid for breaking waves (Kobayashi, 1999).

6.3.3 Relationship between wave height and overtopping

Given such a complex problem as wave overtopping volumes, many wave height parameters were investigated (in the same way as for runup). Figure 6.34 shows reasonable correspondence between the overtopped volume and maximum wave height of the first wave in the group. From Figure 6.34 it could be surmised that for this particular wall geometry and representative wave period, a minimum wave height of about 60 mm would be required to overtop the wall.

The waves that produce the largest overtopping are the normally incident inverted groups, though some of the smaller events are the oblique incidence inverted groups. Gunbak & Bruun (1979) suggest that deep troughs (which correspond to the inverted groups) may cause considerable rundown and are particularly damaging to seawall structures, particularly the toe of the structure. Figure 6.34 does not provide any evidence for this one way or the other.

Subsequent waves in the wave groups (i.e. Waves II and III) overtop much less, and there is no clear relationship. As with wave runup, subsequent waves to the first one in the group will be affected by wave reflections, though this time, more severe ones off the steeper wall.

6.3.4 Effect of obliqueness and multi-directionality

Figure 6.34 shows the overtopping volumes of both normal and oblique incident wave groups, as a function of maximum wave height. It is difficult to make quantitative predictions as to how the overtopping volume of extreme waves are affected by obliquity since there is no clear difference between the normal and oblique incident wave groups. The normally incident groups may be affected by the low frequency error wave but all the data lie along a reasonably well-defined line. The findings of De Waal & Van der Meer (1992) were that the effect of obliquity on overtopping was greater than on runup. Their reduction in overtopping due to obliquity is given by a multiplication factor $\gamma_b = \cos^2\left(\beta - 10^\circ\right)$. For an angle of attack of 20° this gives a reduction factor of 0.97. Obviously this is still very small and it is not possible to see from the scatter of data in Figure 6.34 whether this is the case.

The effect of multidirectionality of the wave front is shown in Figure 6.35. The overtopping values of the unidirectional wave groups are shown in a faded view. The key for the unidirectional groups is given on Figure 6.34. Figure 6.35 shows that the effect of multi-directionality appears to be a reduction in overtopping. There is a similar gradient for the data points, but a different intercept on the horizontal axis. It would also appear that the overtopping reduces for an increase in the spread from $\pm 10^\circ$ to $\pm 30^\circ$. This finding is in contrast to that of De Waal & Van der Meer (1992) who found that there was no reduction in overtopping rates for short-crested seas in comparison to long-crested seas and that overtopping rates remained the same regardless of the spreading angle of the multidirectional seas. This may be explained by the presence of the low frequency error wave or it may be a real phenomenon. The reduction in overtopping for multi-directionality to some extent confirms the findings of Franco & Franco (1999), though they investigated *vertical* wall overtopping. It may in fact be difficult to give a definitive answer to the question of the effect of obliquity and multi-directionality since it appears to depend both on structure slope (vertical vs. acute sloping angle) and, according to Juhl & Sloth (1994), on the structure crest too.

6.3.5 Relationship between overtopping and runup

Intuitively one would expect there to be a positive correlation between the volume of water overtopping the wall and the runup measured without the sea wall in place (the beach runup), for each of the wave groups. Figure 6.36 is a plot of overtopped volumes versus runup on

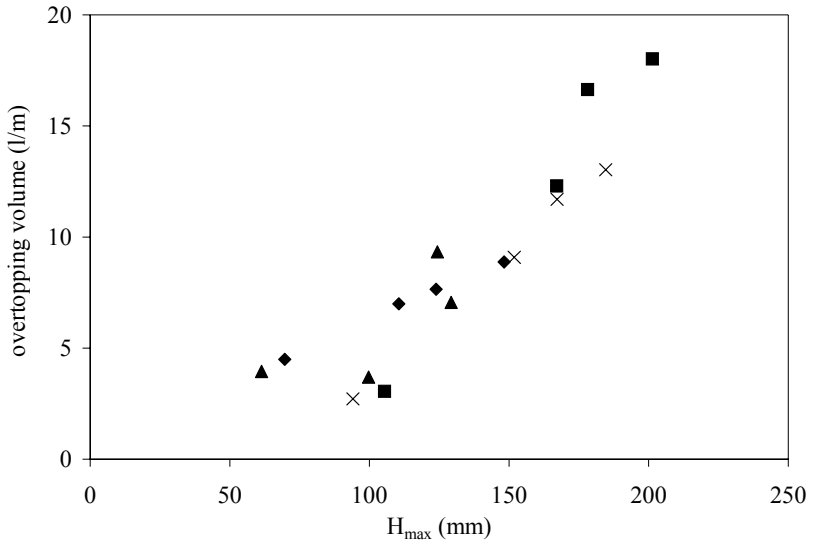

Figure 6.34: Overtopping volume as a function of maximum wave height for Wave I: ♦, normal incidence; ■, inverted normal incidence; ▲, oblique incidence; ×, inverted oblique incidence.

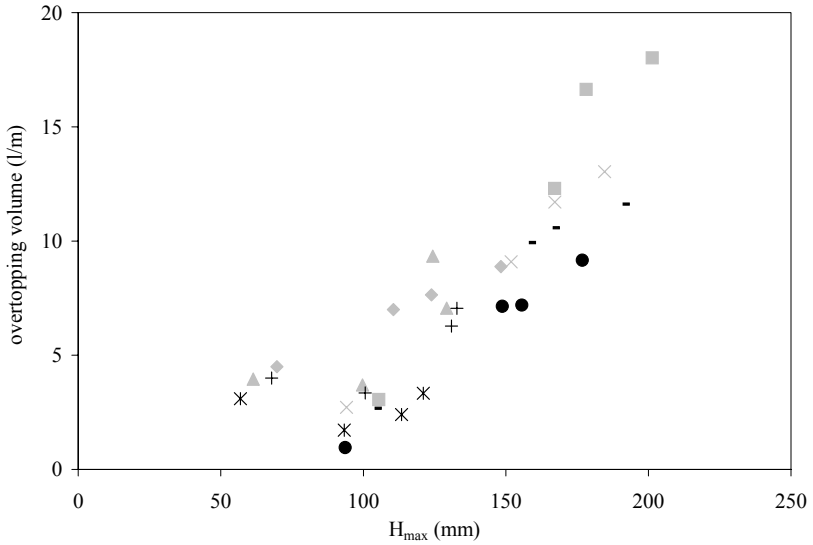

Figure 6.35: Overtopping volume as a function of maximum wave height for Wave I: ♦, normal incidence; ■, inverted normal incidence; ▲, oblique incidence; ×, inverted oblique incidence; ∗, $\pm 30^{\circ}$ spread; •, $\pm 30^{\circ}$ spread inverted +, $\pm 10^{\circ}$ spread; −, $\pm 10^{\circ}$ spread inverted.

the beach in the absence of the sea wall for the first wave in each group i.e., Wave I. There is indeed a positive correlation showing that waves that run furthest up the beach will also produce the greatest overtopping volumes. Waves II and III produced little if any overtopping and no clear correlation with their respective runup values.

Impact of other waves in the group

The previous section on wave runup on a plane beach investigated the extent to which the runup of the extreme wave was affected by the presence of other waves, by embedding the focused wave in a regular wave train. It would be possible to carry out a similar investigation into how the overtopping volume is affected by other waves. This analysis would suffer from a considerable drawback however. This is due to the reflections that are caused by the waves hitting the sea wall. These are *much* larger than the ones generated on the plane beach. Since the purpose of these investigations is to use focused groups to produce good quality clean data, there is no benefit in confusing the picture with adulterated data.

6.3.6 Comparison with other overtopping investigations

There have been a number of investigations into overtopping of coastal structures, with several different empirical formulae available. Three important approaches have been proposed by Owen (1980), Van der Meer and Janssen (1995), and the Shore Protection Manual (1984).

All three provide predictions of the mean overtopping discharge rate which has historically been the parameter of greatest interest to coastal engineers. However, a change in emphasis in the important overtopping parameters has led to methods for calculating maximum individual overtopping volumes. This extension to the formulae permits direct comparisons between overtopping volumes from the current work in the UKCRF to those values predicted by the above three theories.

When using empirical formulae for comparisons it is important to verify under what conditions the original formulae were obtained. It is difficult to obtain information about experimental conditions, particularly for the earliest work. Owen (1980) carried out tests at a very similar scale to those used in the current UKCRF work. He used a still water level of 480 mm and a maximum wave height of about 100 mm. These data come from a report that was never printed (Owen, 1980a). Van der Meer and Janssen (1995) refer to an earlier

paper that gives details on the experimental set-up (De Waal & Van der Meer, 1992). The tests are described as being small scale with a significant wave height of 200 mm. The water depth is not given explicitly but it can be inferred to be not more than 800 mm. Finally the guidance given in the Shore Protection Manual (1984) was based on small-scale laboratory experiments carried out by Saville in the 1950s. In Saville (1958) it states that data (for the curves) comes from small scale tests but there is additional data "with much larger waves (heights two to five feet)". Assuming that these larger tests are an order of magnitude higher than the small scale tests this would give wave heights of up to 150 mm. Therefore, all three emperical formulae probably come from tests that are of a comparable magnitude to the UKCRF tests.

In order to compare the overtopping results it is necessary to find a representative significant wave height, H_s, for the wave groups. This is done in an identical manner as for wave runup, by using Eqn. (6.9). For the first wave (Wave I) of wave group 1, at the toe of the sea wall, the measured wave amplitude $A = 81$ mm. Any choice of number of waves N is possible, but a typical value would be $N = 1000$.[7] Substituting $A = 81$ mm and $N = 1000$ into Eqn. (6.9) yields a significant wave height $H_s = 0.087$ m. It should be noted that this is the significant wave height of the focused wave group *at the toe of the sea wall.*

Owen 1980

Owen proposes a dimensionless freeboard, R_O^*, defined as

$$R_O^* = \frac{R_c}{T_m \sqrt{g H_s}} \tag{6.15}$$

where R_c is the crest elevation of the sea wall above still water level, T_m is the mean wave period and H_s is the significant wave height at the toe of the structure. Owen also proposes a dimensionless discharge, Q_O^*, defined as

$$Q_O^* = \frac{Q}{T_m g H_s} \tag{6.16}$$

where Q is the mean overtopping discharge per unit length of sea wall and g is the gravitational acceleration. These two dimensionless parameters are related according to the following

[7] Assuming a 10 sec average period for a three hour storm gives the number of waves $N = \frac{3 \times 3600}{10} = 1080 \approx 1000$.

expression

$$Q_O^* = A_O \exp\left(-B_O R_O^*\right) \tag{6.17}$$

where A_O and B_O are constants, dependent on sea wall geometry. The following is a calculation of mean overtopping rate, for Wave I of wave group 1:

1. Substitution of R_c=0.117 m, T_m = 1.75 s, g = 9.81 m/s^2 and H_s = 0.087 m into Eqn. (6.15) gives R_O^* = 0.0724.

2. Substitution of R_O^* = 0.0724, A_O = 0.00971 and B_O = 22.7[8] into Eqn. (6.17) gives Q_O^* = 1.89 $\times 10^{-3}$.

3. Eqn. (6.16) is rearranged to yield $Q = Q_O^* T_m g H_s$, with substitution of values Q_O^* = 1.89 $\times 10^{-3}$, T_m = 1.75 s, g = 9.81 ms^{-2} and H_s = 0.087 m giving Q = 2.83 $\times 10^{-3}$ m^3/s/m.

In order to calculate the overtopped volume (rather than the overtopping rate) it is necessary to use an extension to this theory, detailed in the HR Wallingford report W178 (1999). Firstly, the number of overtopped waves is given by

$$N_{ow} = N_w \exp\left(-C\left(R^*/r\right)^2\right) \tag{6.18}$$

where N_w is the number of waves, C is a parameter which depends on the sea wall slope and r is a roughness coefficient. For a slope of 1:2.18, C = 37.8[9], the roughness coefficient for smooth concrete is r = 1, which gives the number of overtopping waves N_{ow} = 502, i.e. 50% of waves overtop the structure. The average overtopping volume per overtopping wave is given by

$$\overline{V} = Q T_m N_w / N_{ow} \tag{6.19}$$

which, for this particular wave, is calculated to be $\overline{V}$= 0.00985 m^3/m. Finally the maximum overtopping volume is given by

$$V_{\max} = a\left(\ln N_{ow}\right)^{\frac{1}{b}} \tag{6.20}$$

[8] These values are interpolated values from a 1:2 and 1:2.5 seawall slope of Table 1, HR Wallingford report W178 (1999) which are an update of Owen's coefficients.

[9] There are values of C for only three seawall slopes (1:1, 1:2 and 1:4). There is no clear pattern to interpolate through the values for these slopes, therefore the value for the 1:2 slope is used.

where

$$a = 0.85\overline{V} \tag{6.21}$$

and

$$b = 0.76 \tag{6.22}$$

Making the substitutions into Eqn. (6.20) gives $V_{max} = 0.0946$ m^3/m. The measured overtopped volume for Wave I of wave group WG1 in the UKCRF is 0.00765 m^3/m. Therefore, the Owen formulation predicts an overtopping volume that is more than an order of magnitude higher than the measured value.

Van der Meer and Janssen (1995)

Van der Meer and Janssen (1995) propose a dimensionless freeboard, R_V^*, given by

$$R_V^* = \frac{R_c}{H_s} \frac{1}{\gamma_b \gamma_h \gamma_f \gamma_\beta} \tag{6.23}$$

where the γ variables are reduction factors for:

γ_b - berm

γ_h - shallow foreshore

γ_f - roughness

γ_β - angle of wave attack

These factors are based upon empirical formulations. There is no berm in the UKCRF experiments, therefore $\gamma_\beta = 1$. A shallow foreshore is defined, for these purposes, as one in which $h_m/H_s < 4$, where h_m is the water depth at the toe of the structure. The reduction factor is given by

$$\begin{aligned} \gamma_h &= 1 - 0.03\left(4 - \tfrac{h_m}{H_s}\right)^2 \quad for \quad \tfrac{h_m}{H_s} < 4 \\ \gamma_h &= 1 \qquad\qquad\qquad\quad for \quad \tfrac{h_m}{H_s} \geq 4 \end{aligned} \tag{6.24}$$

For Wave I of wave group WG1 this expression gives a value of $\gamma_h = 0.744$. The slope of the sea wall was smooth cement, with a reduction factor $\gamma_f = 1$. The reduction factor γ_β, for obliquity, is given in De Waal & Van der Meer (1992) as $\gamma_\beta = \cos^2(\beta - 10^\circ)$. Therefore, for normally incident waves, $\gamma_\beta = 1$, and for a wave attack angle of 20°, $\gamma_\beta = 0.97$.

For Wave I of wave group WG1 (a normally incident wave group), substituting the reduction factors, and R_c and H_s into Eqn. (6.23) gives R_V^* =1.81.

A dimensionless overtopping discharge is given by

$$Q_V^* = \frac{Q}{gH_s^3} \tag{6.25}$$

where Q is the average overtopping discharge per unit length. The dimensionless variables R_V^* and Q_V^* are related by

$$Q_V^* = 0.2\exp(-2.6R_V^*) \tag{6.26}$$

Substituting $R_V^* = 1.81$ into Eqn. (6.26) gives $Q_V^* = 1.82 \times 10^{-3}$. Rearranging Eqn. (6.25) and substituting for Q_V^* yields $Q = 1.46 \times 10^{-4}$ m^3/s/m, i.e. about a 1/20 of the overtopping discharge predicted using the Owen (1980) formulation. In order to obtain overtopping volumes it is again necessary to find the number of overtopping waves. In Van der Meer and Janssen (1995) the number of overtopping waves is given by

$$N_{ow} = N_w \exp\left(-\left(\frac{R_c/H_s}{c}\right)^2\right) \tag{6.27}$$

where

$$c = 1.62\gamma_h\gamma_f\gamma_\beta \tag{6.28}$$

Substituting the reduction factors into Eqn. (6.28) gives $c = 1.21$ and using Eqn. (6.27) with $N_w = 1\ 000$, the number of overtopping waves, $N_{ow} = 288$. This number of waves is nearly 50% less than the value obtained using Owen's formulation. Finally the maximum overtopping volume is given by

$$V_{\max} = a\left[\ln\left(N_{ow}\right)\right]^{\frac{4}{3}} \tag{6.29}$$

where

$$a = 0.84\frac{T_m N_w Q}{N_{ow}} \tag{6.30}$$

Using the appropriate values in Eqn. (6.30), $a = 7.46\times10^{-4}$. When the values of a and N_{ow} are substituted into Eqn. (6.29), the maximum overtopping volume is predicted to be V_{max} = 0.00753 m^3/m. This is almost identical to the value of 0.00765 m^3/m measured in the UKCRF.

Shore Protection Manual (1984)

This US CERC method given in the Shore Protection Manual (SPM) is used extensively by coastal engineers worldwide. In order to calculate the overtopping rate of coastal structures

by irregular waves it is necessary to:

1. calculate the hypothetical runup of regular waves on the coastal structure then
2. calculate the overtopping rate of regular waves based upon the hypothetical runup of regular waves and finally
3. calculate the overtopping rate of irregular waves based upon the overtopping rate of regular waves.

In the SPM (1984) runup for the structure is obtained from various design curves, the appropriate one depending on the value of h_m/H_0', where H_0' is offshore wave height. The value of H_0' used in this calculation is the significant wave height given by Eqn. (6.9), but using the measured amplitude at the toe of the *beach*. For Wave I of wave group WG1 this is $A = 61$ mm, which gives a significant wave height $H_0' = 66$ mm using Eqn. (6.9) with N =1 000. Therefore,

$$\frac{h_m}{H_0'} = 1.42 \tag{6.31}$$

This value of h_m/H_0' falls halfway between ones used in Figure 7-10 ($h_m/H_0' = 0.8$) and Figure 7-11 ($h_m/H_0' = 2$) of the SPM. To use the design curve it is necessary to calculate the following factor

$$\frac{H_0'}{gT^2} = 0.00220 \tag{6.32}$$

Reading from Figure 7-10 for a slope of 1:2.18, dimensionless runup is

$$\frac{R}{H_0'} = 2.6 \tag{6.33}$$

whilst from Figure 7-11 for the same slope it is

$$\frac{R}{H_0'} = 3.15 \tag{6.34}$$

An average of these two values gives $\frac{R}{H_0'} = 2.875$. This value would normally then be adjusted for scale effects since the design curves are for small-scale laboratory tests, and a coastal engineer would be more concerned with prototype scale. However, the purpose of this exercise is to compare predictions from small-scale models with laboratory measurements. Therefore,

$$R = 2.875 \times H_0' = 0.190 \text{ m} \tag{6.35}$$

This is the hypothetical runup for the structure, assuming regular waves.

The second step is to calculate the overtopping rate for regular waves, based upon this hypothetical runup. The overtopping rate for regular waves is given by

$$Q_S = \sqrt{gQ_S^* H_0^3} \exp\left(-\left[\frac{0.1085}{\alpha^*} \ln\left(\frac{R+h-h_m}{R-h+h_m}\right)\right]\right) \tag{6.36}$$

where α^* and Q_S^* are empirically determined coefficients that depend upon incident wave characteristics and structure geometry. Note that this is rate of overtopping of regular waves i.e. it is a single value. The variables h and h_m are shown in Figure 6.30. From SPM Figure 7.25 for a 1:1.5 structure,

$$\left.\begin{array}{c} \alpha_S = 0.067 \\ Q_S^* = 0.0135 \end{array}\right\} \text{ at } \frac{h_m}{H_0'} = 1.5 \text{ and } \frac{H_0'}{gT^2} = 0.0016 \tag{6.37}$$

From SPM Figure 7.26 for a 1:3 structure

$$\left.\begin{array}{c} \alpha_S = 0.08 \\ Q_S^* = 0.0240 \end{array}\right\} \text{ at } \frac{h_m}{H_0'} = 1.0 \text{ and } \frac{H_0'}{gT^2} = 0.0012 \tag{6.38}$$

(Both of these sets of values are for small-scale tests). Interpolating between these values to get coefficients for 1:2.18 slope gives, $\alpha_S = 0.074$ and $Q_S^* = 0.0193$. Substituting these values into Eqn. (6.36) yields $Q_S = 8.84 \times 10^{-4}$ m^3/s/m. This value, using regular wave overtopping theory, is about five times the size as that obtained by the method of Van der Meer and Janssen (1995).

The third step to calculate the overtopping rate for irregular waves uses more design curves of the SPM manual. Figure 7-35 of the SPM (1984) is a plot of Q/Q_S against relative freeboard, $(h-h_m)/R_s$, (where R_s is the wave runup of the equivalent deepwater significant wave height) for different values of α. The value of R_s is taken to be the same as the regular wave runup, R, which for this wave is 0.19 m. The relative freeboard is therefore $(h-h_m)/R_s = 0.619$. Using $\alpha = 0.074$ and reading from Figure 7-35 of the SPM gives $Q/Q_S = 0.340$, giving the mean overtopping discharge per unit length of structure, $Q = 3.01 \times 10^{-4}$ m^3/s/m. This value is an order of magnitude smaller than that obtained using Owen's (1980) formulation, and double the value obtained using the method of Van der Meer & Janssen (1995).

There is no method given in the SPM (1984) for calculating the overtopping volumes from the mean overtopping discharge, so the method given in Van der Meer & Janssen (1995) will

be used to enable comparisons to be made with UKCRF overtopping volumes. The number of overtopping waves will be the same, since this depends on R_c, H_s and c which are the same regardless of whether the Van der Meer & Janssen (1995) or SPM (1984) methods are used. Working through the calculation as before, the maximum overtopping volume is calculated to be $V_{max} = 0.0156$ m^3/m. This is approximately double the value using Van der Meer & Janssen (1995), which is to be expected, since the SPM (1984) predicted double the mean overtopping rate.

Overtopping values have been calculated using all three overtopping formulae for the first wave in one wave group only. Figure 6.37 is a plot of measured and predicted values for the first wave in all sixteen unidirectional wave groups. It can be seen that the predictions from Owen (1980) greatly exceed the measured overtopping values, but the values predicted by Van der Meer and Janssen (1995) seem to be roughly comparable with the UKCRF measurements.

The Van der Meer and Janssen (1995) predictions are shown again in Figure 6.38 in more detail. It can be seen that the formulation of Van der Meer and Janssen (1995) produces a scatter of results, but within an acceptable range. There may be a trend of increasing over-prediction at higher overtopping volumes.

6.3.7 Comparison of measured overtopping volumes with present permissible rates

In order to compare overtopping volumes measured in the UKCRF with published permissible rates it is necessary to scale the measured rates from model to prototype. To ensure geometric similarity

$$L_m = \lambda_L L_p \tag{6.39}$$

where L_m is the model length, λ_L is the model length scale and L_p is the prototype length. To ensure kinematic similarity it is necessary that the time scale ratio is the same for both model and prototype i.e.,

$$T_m = \lambda_T T_p \tag{6.40}$$

where T_m is the model time, λ_T is the model time scale and T_p is the prototype time. It is necessary to use the following Froude number (Fr) criterion

$$Fr_m = Fr_p \tag{6.41}$$

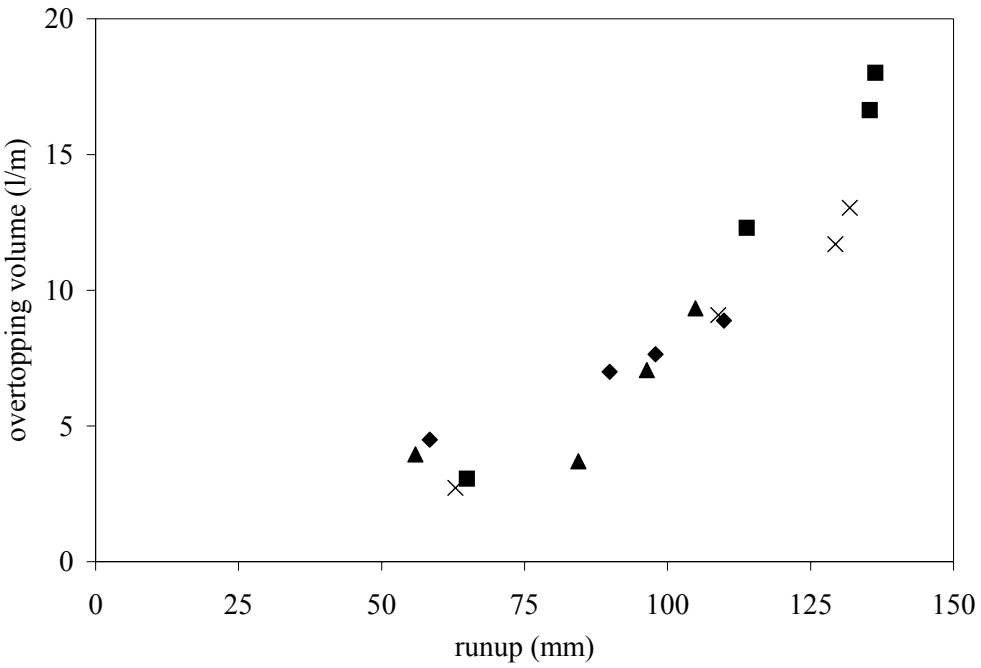

Figure 6.36: Overtopping volume as a function of wave runup for wave I: ♦, normal incidence; ■, inverted normal incidence; ▲, oblique incidence; ×, inverted oblique incidence.

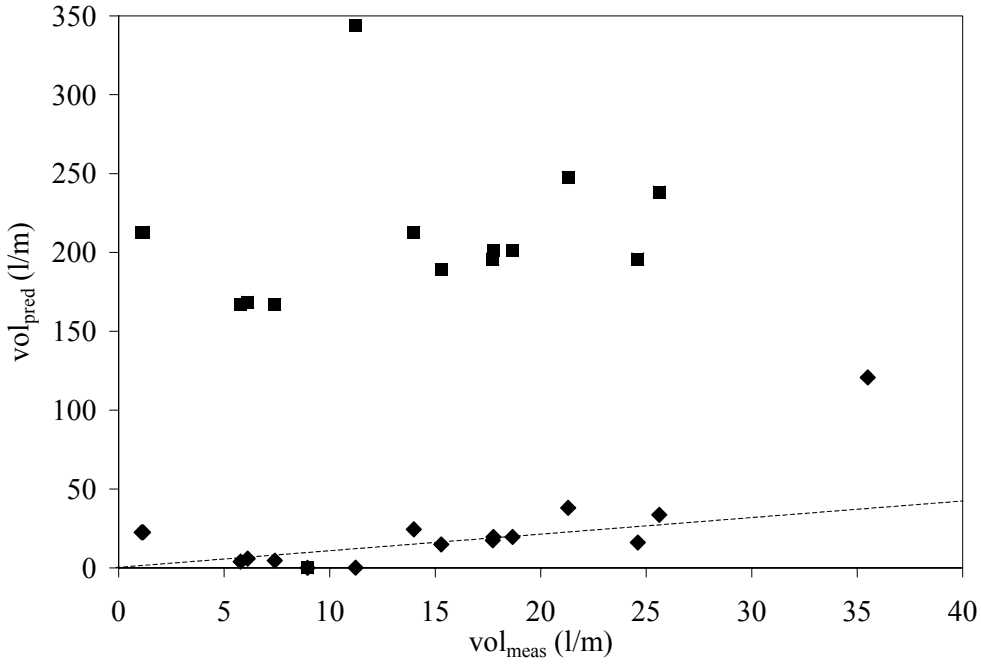

Figure 6.37: Predicted versus measured overtopping volumes: ♦, Van der Meer and Janssen (1995); ■, Owen (1980) and Besley (1999).

where the subscripts m and p refer to model and prototype respectively. The Froude number is given by

$$Fr = \frac{u}{\sqrt{gL}} \tag{6.42}$$

where u is velocity, g is gravitational acceleration and L is length. From Eqn. (6.41)

$$\frac{u_m}{\sqrt{gL_m}} = \frac{u_p}{\sqrt{gL_p}} \tag{6.43}$$

where the subscripts m and p again refer to model and prototype respectively. Gravitational acceleration, g, is the same at both scales and making substitutions for u in terms of L and T (time), Eqn. (6.43) can be rearranged thus

$$\frac{\sqrt{L_m}}{T_m} = \frac{\sqrt{L_p}}{T_p} \tag{6.44}$$

Making substitutions of λ_m and λ_p from Eqns. (6.39) and (6.40) yields

$$\sqrt{\lambda_L} = \lambda_T \tag{6.45}$$

Converting overtopping rates, which are in units of $m^3/s/m$, from model to prototype scale requires

$$\begin{aligned} Q_p &= Q_m \left(\lambda_L\right)^{-3} \left(\lambda_T\right)^1 \left(\lambda_L\right)^1 \\ &= Q_m \left(\lambda_L\right)^{-3} \left(\lambda_L\right)^{\frac{1}{2}} \left(\lambda_L\right)^1 \\ &= Q_m \lambda_L^{-3/2} \end{aligned} \tag{6.46}$$

The model time scale is obtained by assuming that a shoreward propagating wave would typically have a period of 10 sec whilst the wave period corresponding to the peak frequency of the wave group in the UKCRF was 2.16 sec. From Eqn. (6.40) this gives a model time scale $\lambda_T = 0.2156$. Substituting this value into Eqn. (6.45) gives the model length scale $\lambda_L = 0.0465$. The final substitution gives the overtopping rate of the prototype $Q_p = 99.8\ Q_m$.

It is then necessary to calculate the overtopping rates of the model from the measured overtopping volumes of the model. To do this a procedure it is necessary to carry out calculations according to Van der Meer and Janssen (1995), but in the reverse order.

From Eqns. (6.29) and (6.30)

$$\begin{aligned} V_{\max} &= a \left[\ln(N_{ow})\right]^{\frac{4}{3}} \\ &= \frac{0.84 T_p Q N_w}{N_{ow}} \left[\ln(N_{ow})\right]^{\frac{4}{3}} \end{aligned} \tag{6.47}$$

Substituting for N_{ow} from Eqn. (6.27) gives

$$V_{\max} = \frac{0.84 T_p Q}{\exp\left(-\left(\frac{R_c/H_s}{c}\right)^2\right)} \left[\ln\left[N_w \exp\left(-\left(\frac{R_c/H_s}{c}\right)^2\right)\right]\right]^{\frac{4}{3}} \tag{6.48}$$

Rearranging to obtain Q

$$Q = \frac{V_{\max} \exp\left(-\left(\frac{R_c/H_s}{c}\right)^2\right)}{0.84 T_p \left[\ln\left[N_w \exp\left(-\left(\frac{R_c/H_s}{c}\right)^2\right)\right]\right]^{\frac{4}{3}}} \tag{6.49}$$

Figure 6.39 shows the overtopping rates for 16 unidirectional waves at prototype scale, based upon measured overtopping volumes and geometric and kinematic similarity. Also plotted are three permissible or tolerable discharge rates that have recently been published in the Coastal Engineering Manual (2002).[10] It can be seen that there is considerable scatter. This is to be expected since the wave groups had widely varying characteristics. It can be seen from Figure 6.39 that the focused waves produced in the UKCRF produce overtopping rates that would be unsafe for both pedestrians and vehicles; one wave group (WG5 - large trough focused normally incident) produces mean overtopping rates that might damage the seawall.

6.3.8 Influence of wind on overtopping

The UKCRF does not have the capability of generating wind. Therefore it has not been possible to investigate the effect that wind has on the overtopped volumes. As discussed in Section 1.4.3 there have been previous investigations into the effect of wind on overtopping rates, but the general concensus is that the effect of wind is only significant for waves that produce high levels of breaker spray rather than green water overtopping. Juhl & Sloth (1994) provide a 'rule of thumb' for determining the type of overtopping. They found that if the structure crest to significant wave height ratio, R_c/H_s was less than unity green water overtopping will dominate, but for R_c/H_s greater than unity breaker spray would be dominant. For the sixteen unidirectional wave groups generated in the UKCRF, only one group (wave group 5) should be green water dominant. It can be seen from video footage that this is not the case - green water overtopping is dominant for all wave groups. This contradictory

[10] The permissible rates data are shown pictorially on a log plot in the Coastal Engineering Manual i.e. no specific values are given. The accompanying text warns that they are rough guidelines.

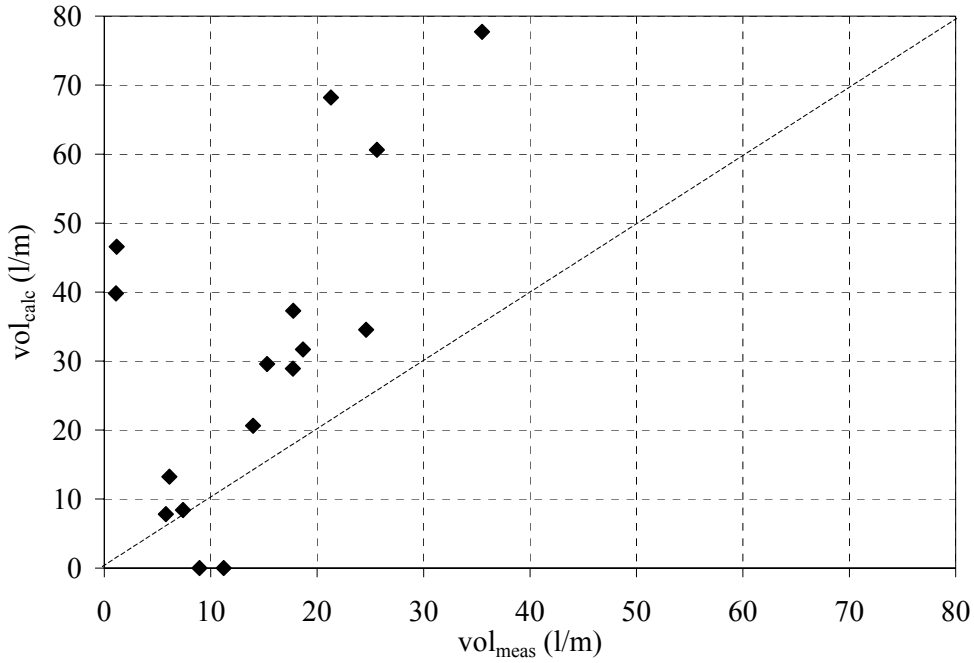

Figure 6.38: Predicted versus measured overtopping values using method of Van der Meer and Janssen (1995).

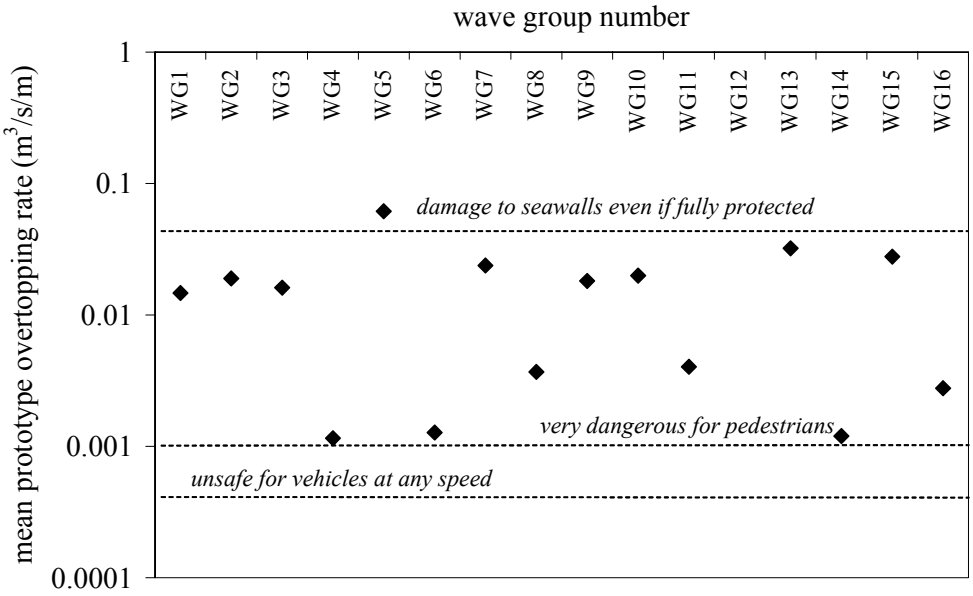

Figure 6.39: Prototype overtopping rates inferred from UKCRF measurements, compared with published permissible values.

finding may be due to scale effects which are problematic when investigating spray, because of surface tension considerations.

6.3.9 Conclusions

Reasonable correspondence was found between the overtopping volume and the maximum wave height of the first wave in all groups. There was also a positive correlation between the overtopping volume and the runup of the first waves.

Overtopping volumes were reduced by increasing multi-directionality. It was unclear as to whether there was a decrease due to obliquity.

Overtopping predictions of Owen (1980) and the SPM (1984) were considerably larger than measured values of the UKCRF extreme waves, but predictions by Van der Meer & Janssen (1995) were in remarkably close agreement.

Chapter 7

Kinematics

7.1 Background

Conventionally, coastal and offshore engineers use wave kinematics derived from Stokes theory of regular waves to determine loadings on structures. This simplification leads to inaccuracies - either over-design of a structure with associated costs when the fluid loading is over-estimated, or potentially dangerous under-design when the combined inertial and drag force of the Morison equation is under-predicted. A more realistic model for wave kinematics will lead to an improved loading analysis for fitness of purpose of offshore and coastal structures, as suggested by Tromans et al. (1991).

There has been much work on the kinematics of extreme waves in deep water, but little research to date on kinematics of focused waves in the coastal environment, particularly in the presence of a sea wall. This section presents kinematics results for both deep and shallow water.

7.2 Experimental procedures

Wave kinematics were measured using two different instruments: an Acoustic Doppler Velocimeter (ADV) and a Laser Doppler Anemometer (LDA). The operating principles of these instruments are briefly described in Chapter 4, but a recap is given here. The ADV has a relatively large probe head which therefore restricts its use to a minimum depth of around 70 mm. However, the ADV acquired three orthogonal velocity components at a sampling rate

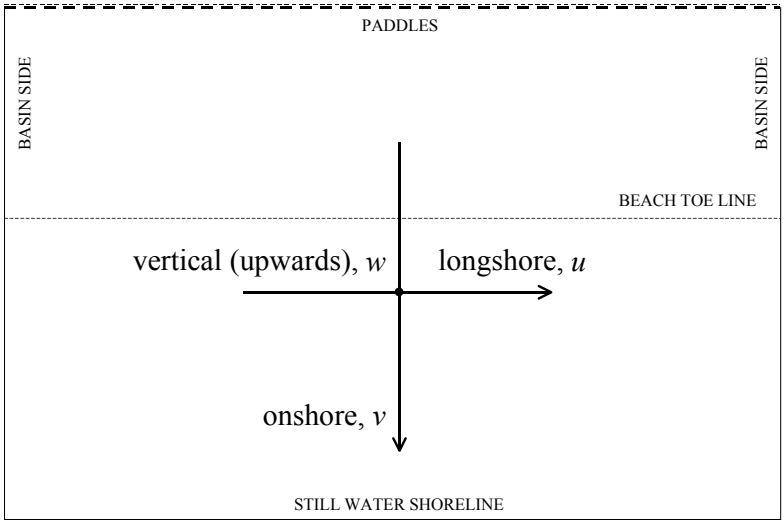

Figure 7.1: Direction of velocity components with respect to basin layout.

of 25 Hz. No seeding was required.

The LDA is more difficult to operate than the ADV since the laser beam is a radiation hazard out of the water, and the water had to be seeded with fine particles [1] to achieve acceptable data rates. However, the LDA potentially provides very useful data because it is capable of a faster sampling rate, has a much smaller measurement volume and the probe itself smaller than the ADV. Hence the LDA disturbs the flow less and may be used in shallow water down to depths of 12 mm. It was also possible to trigger the LDA acquisition from the wave generation signal enabling accurate comparisons to be made between velocity and surface elevation data. The sampling rate of the LDA was variable, depending on the detection of seeded particles in the measurement volume.

It is necessary to define the direction of the velocity components that will be presented in this Chapter. Figure 7.1 shows the directions of the three orthogonal velocity components u, v and w.

[1] Timiron®

7.3 Kinematics of single focused wave group at the toe of the beach

Normal and oblique incidence wave groups were generated in the UKCRF as described in Chapter 2. The wave groups considered here are WG1 and WG9 respectively (see Appendix A1). These were the largest groups and focused at the toe of the beach. The oblique group had an angle of incidence of 20°.

7.3.1 Normally incident wave group

Velocity measurements were made at the toe of the beach, 7.7 cm below the still water level, with both the ADV and LDA. This vertical distance corresponded with a position just below the two main troughs of the crest focused wave group.[2] The normally incident group would be expected to have an onshore and vertical water particle velocity component, but no longshore component. Figure 7.2 shows the onshore velocity component. It can be seen that there is very good agreement between the LDA and ADV measurements. The only difference occurs between 47 and 48 secs where the LDA records a small wiggle at approximately 47.5 sec which is missed by the ADV.

Figure 7.3 shows the upward vertical velocity component measurements below the level of the trough of the group. This also shows close agreement between the two measurement methods. Again there is a disparity between the two when the LDA records a sharp peak at 45.5 sec, which is not registered by the ADV.

Finally, Figure 7.4 shows the longshore velocity component of the normally incident group. As expected the velocity component is negligible. This component is measured by the ADV only, as the LDA measures just two perpendicular components. The negligible amplitude of the signal in Figure 7.4 is both confirmation of the correct alignment of the ADV probe and the low level of background noise for the ADV signal.

[2] The ADV probe was positioned at progressively deeper depths until an uninterrupted signal was acquired when the focused wave group passed the probe.

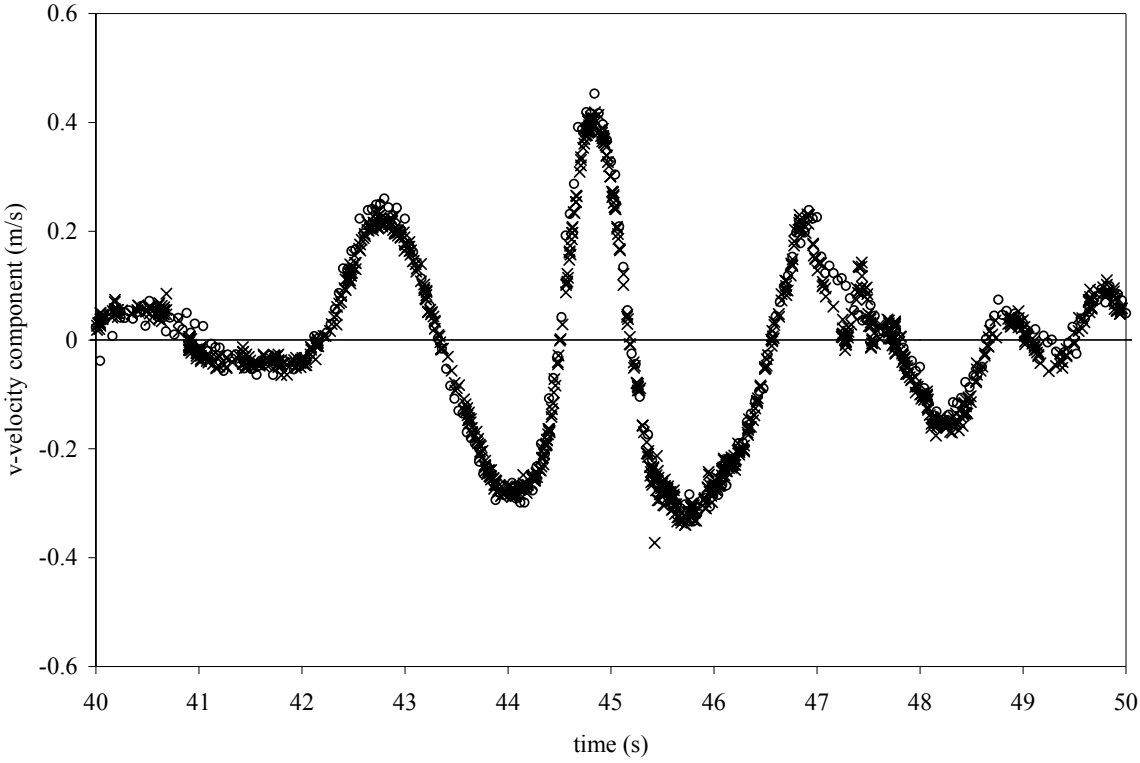

Figure 7.2: Time history of onshore velocity component of a normally incident crest focused wave group, measured at the toe of the beach beneath the trough: ×, LDA; ∘, ADV.

Separation of harmonics

The velocity components under a single inverted normally incident wave group were also measured. In this case, the probe was a little high and failed to record the velocity as the trough passed by i.e., the measurement volume emerged above the water surface. Onshore velocity component data are shown in Figure 7.5, along with a spline fit to bridge the gap in the measurements. These velocity data enable the separation of harmonics for the velocity field in a similar manner as was done for surface elevations in Chapter 3 and 5. Recapping on Section 3.3.2., the addition of information from crest focused and trough focused wave groups yields even harmonics, whilst the subtraction of information from trough focused from crest focused groups yields odd harmonics, which include the linear group information.

Figure 7.6 shows time histories and spectra of the original LDA velocity data (from Figures 7.2 and 7.5) with the resulting addition and subtraction time series and spectra. The first

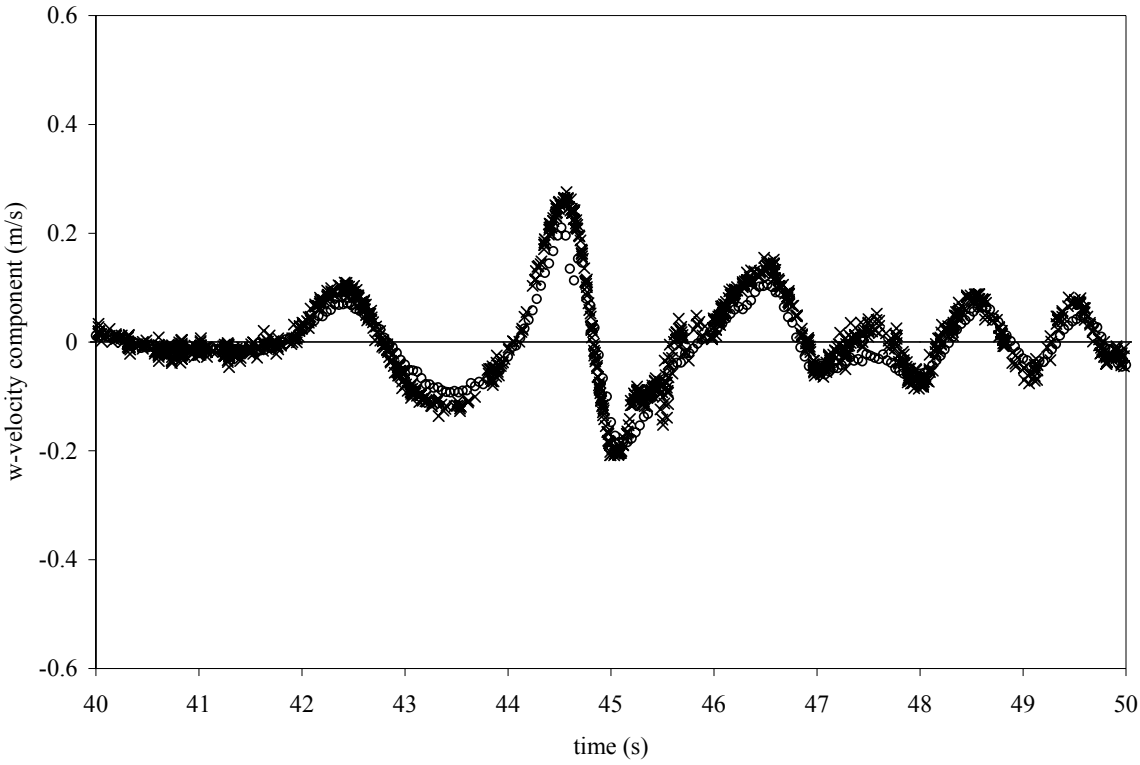

Figure 7.3: Time history of vertical velocity component of a normally incident crest focused wave group, measured at the toe of the beach beneath the trough: $\times$, LDA; $\circ$, ADV.

point to note is that the crest focused spectrum of the onshore velocity components shown in Figure 7.6 (a) contain more noise than the trough focused spectrum of Figure 7.6 (b). Also, the crest and trough focused spectra are of similar magnitude except that the trough focused spectrum has a considerable peak at 1.25 Hz. The time-dependent even harmonics of Figure 7.6 (c) show a recognisable set-down-like flow and a high frequency oscillation. The time-dependent odd harmonics of Figure 7.6 (d) have obviously linear behaviour, but with an additional bump on the third crest of the group at about 47.5 sec.

It is possible to produce filtered time histories by truncating the addition and subtraction spectra at an appropriate frequency. The effect of this is to separate the odd harmonics into linear and third order terms and even harmonics into second order difference (low frequency) terms and sum (high frequency) terms. This is analogous to the method used in Chapter 3 for the surface elevation data. The linear terms generated in this way can be compared with the theoretical linear velocity derived from surface elevation data. Linear theory gives the

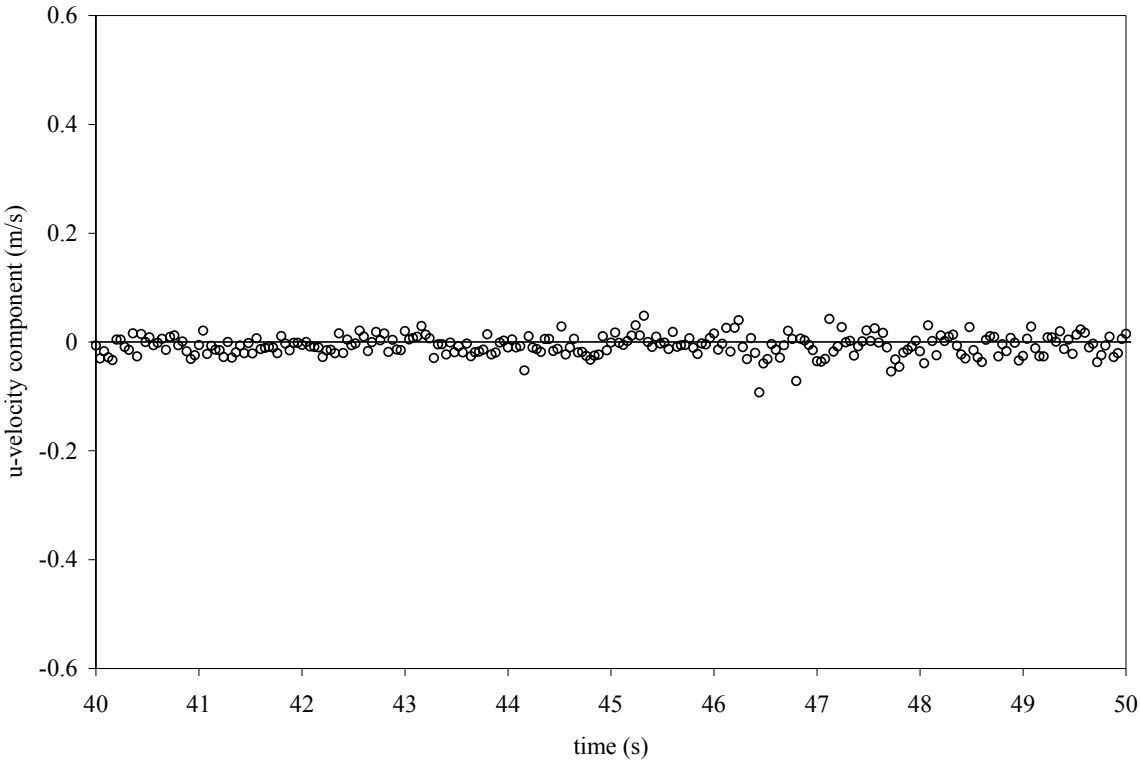

Figure 7.4: Time history of longshore velocity component of a normally incident crest focused wave group, measured at the toe of the beach beneath the trough using ADV.

velocity potential of a regular wave as

$$\phi = \frac{Ag}{\omega} \frac{\cosh k(z+d)}{\cosh(kd)} \cos\psi \tag{7.1}$$

where A is the wave amplitude, g is the gravitational acceleration, ω is the wave frequency, k is the wave number, z is the distance measured vertically upwards from the still water level, d is the still water depth and the phase function ψ is given by

$$\psi = \omega t - \mathbf{k}.\mathbf{x} \tag{7.2}$$

where t is time and

$$\mathbf{x} = \mathbf{i}x + \mathbf{j}y \tag{7.3}$$

where x is the distance in the longshore direction and y is the distance in the onshore direc-

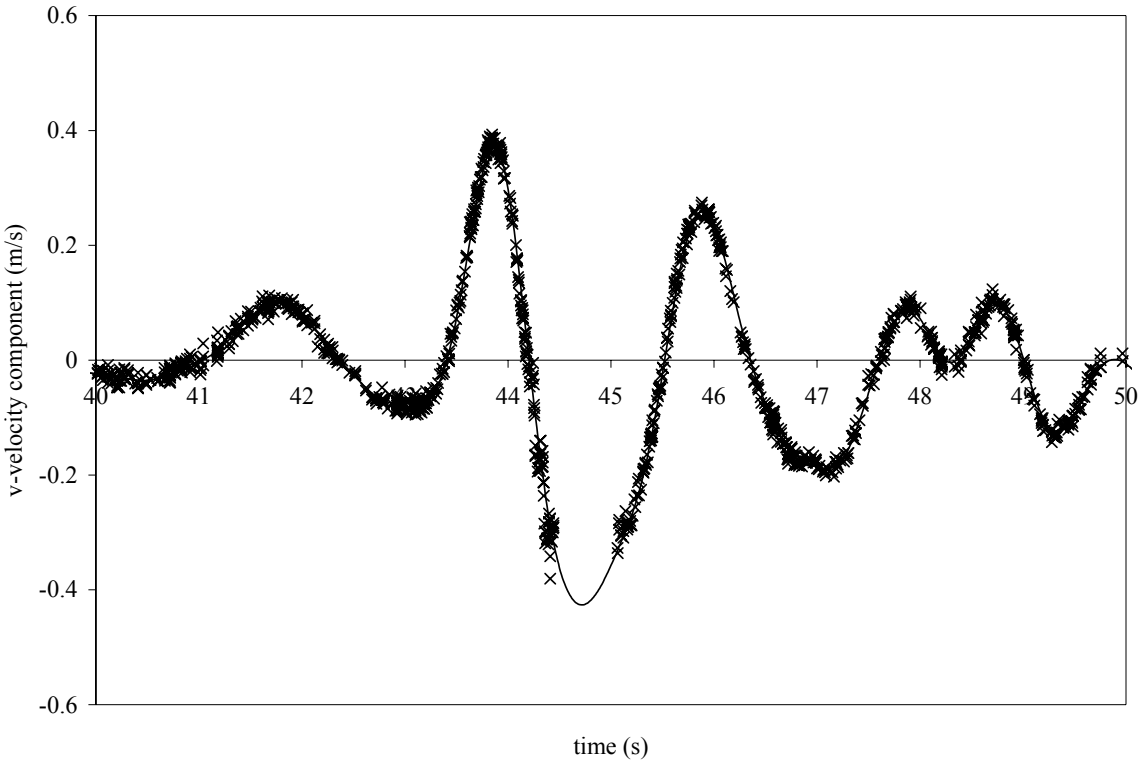

Figure 7.5: Time history of onshore velocity component of trough focused wave group, measured at toe of beach: ×, LDA measurement; —, spline fit to LDA data.

tion.[3] The water particle kinematics are obtained from the velocity potential thus

$$u = \frac{\partial \phi}{\partial x} = \frac{kAg}{\omega} \frac{\cosh k(z+d)}{\cosh(kd)} \sin(\omega t - kx\cos\theta - ky\sin\theta)\sin\theta \tag{7.4}$$

$$v = \frac{\partial \phi}{\partial y} = \frac{kAg}{\omega} \frac{\cosh k(z+d)}{\cosh(kd)} \sin(\omega t - kx\cos\theta - ky\sin\theta)\cos\theta \tag{7.5}$$

$$w = \frac{\partial \phi}{\partial z} = \frac{kAg}{\omega} \frac{\sinh k(z+d)}{\cosh(kd)} \cos(\omega t - kx\cos\theta - ky\sin\theta) \tag{7.6}$$

where θ is the wave angle measured anti-clockwise from the onshore y-direction. For a wave *group*, rather than a single frequency wave, a first approximation of the velocity components can be deduced from the linear superposition of individual velocity components of the wave group. Of interest is the onshore velocity v, which for the case of the normally incident wave

[3] The horizontal coordinates x and y correspond to the velocity components u and v respectively, shown in Figure 7.1.

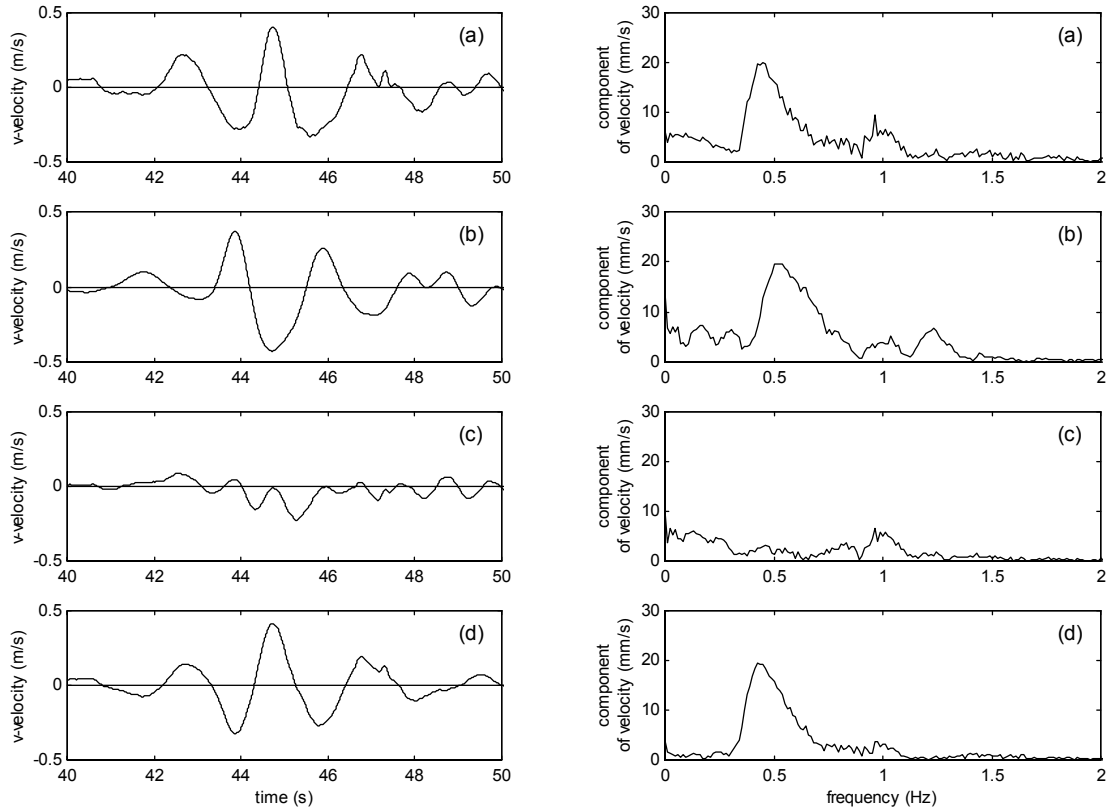

Figure 7.6: Onshore velocity component time histories and spectra measured below trough at toe of beach for (a) crest focused group (b) trough focused group (c) addition of crest and trough focused group time history and (d) subtraction of trough from crest focused time history.

group is given by

$$v = \sum_{n=1}^{N} \frac{k_n c_n g}{\omega_n} \frac{\cosh k_n(z+d)}{\cosh(k_n d)} \sin(\omega_n t - k_n x + \phi_n) \tag{7.7}$$

where N is the number of individual waves that compose the group, c_n are the individual wave component amplitudes and ϕ_n are the phases of the wave components. The amplitude components may be derived from the amplitude spectra of the low frequency band-pass filtered 'subtraction' time series. The amplitude spectra comprise both real and imaginary data i.e., $c_n = a_n + ib_n$ so that in practice the velocity may be deduced from

$$v = \sum_{n=1}^{N} \frac{k_n g}{\omega_n} \frac{\cosh k_n(z+d)}{\cosh(k_n d)} \left(a_n \sin(\omega_n t - k_n x) + b_n \cos(\omega_n t - k_n x)\right) \tag{7.8}$$

Figure 7.7 shows the amplitude spectra and time histories of the low and high frequency

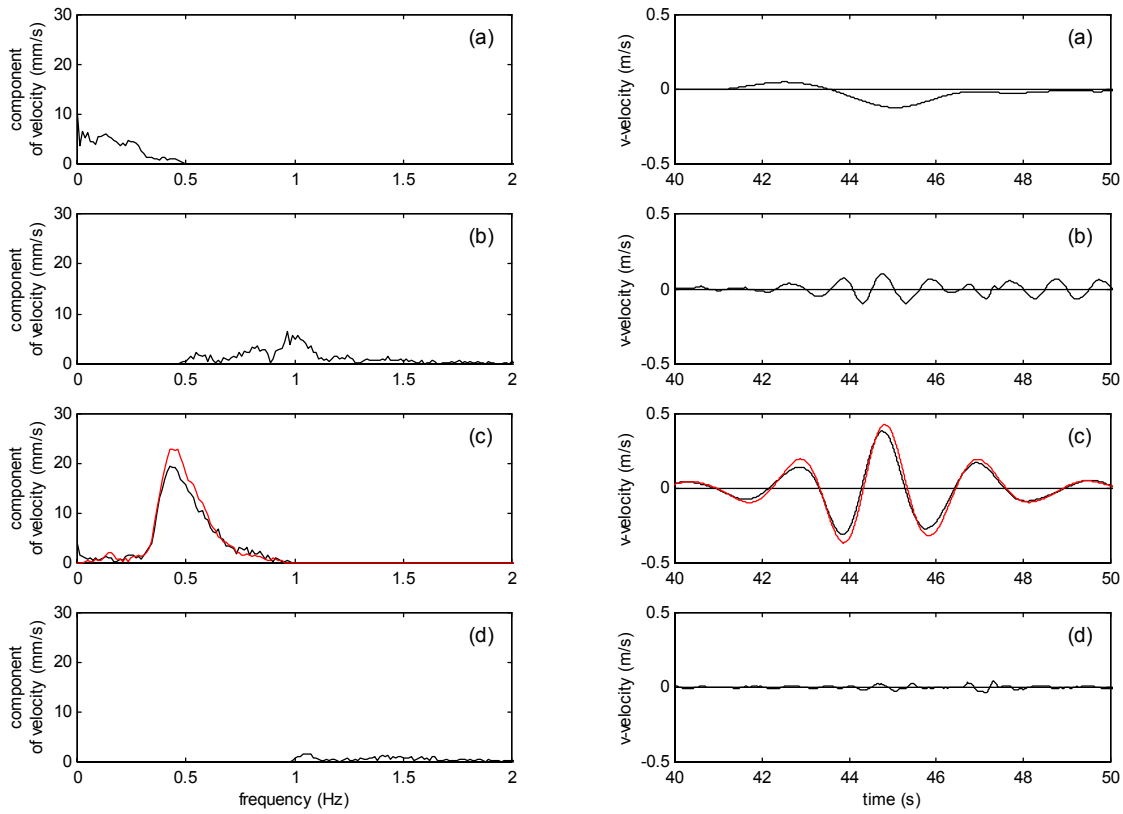

Figure 7.7: Spectra and resultant onshore v-velocity component time histories measured below trough at toe of beach for (a) low frequency band-pass filtered 'addition' harmonic term (b) high frequency band-pass filtered 'addition' harmonic term (c) low frequency band-pass filtered 'subtraction' harmonic term and (d) high frequency band-pass filtered 'subtraction' harmonic term: —, measured data; - - - (red), linear superposition theory.

filtered even and odd harmonics. The theoretically derived linear velocity component is also shown for comparison. A clearer picture of the harmonic structure now emerges. The trough in the time series of Figure 7.7 (a) shows the low frequency even harmonic that can be thought of as a flow associated with the surface set-down term. The preceding hump in this time series will be associated with the low frequency free/error wave. Figure 7.7 (b) shows the high frequency even harmonics. These are again due to bound second order sum components together with flow associated with the later arriving paddle error waves. Figure 7.7 (c) shows the horizontal velocity of the linear group with no high frequency contamination. The theoretically derived velocity component is larger than the measured data. The reason

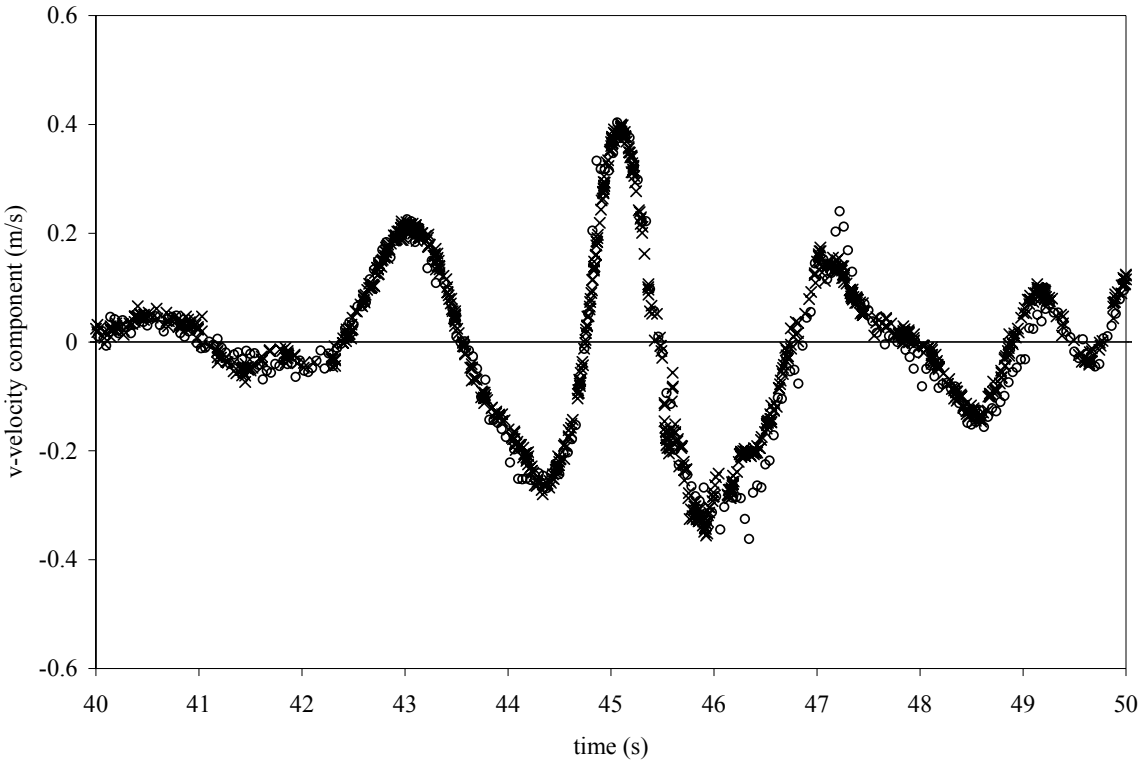

Figure 7.8: Time history of onshore velocity component of an oblique incidence crest focused wave group, measured at the toe of the beach beneath the trough: ×, LDA; ∘, ADV.

for this is not clear, but it does warrant future investigation. Finally, Figure 7.7 (d) shows the third order harmonics. These are of very low magnitude and are almost negligible, though it can be seen from the time history, that the crest at 47.5 sec was obviously responsible for the additional bump in the time series of Figure 7.6 (d). This small group of waves is probably a 3rd order error wave produced at the paddle propagating freely across the tank.

7.3.2 Oblique incidence wave group

Figure 7.8 shows the onshore velocity component measured under the trough of an oblique incidence wave group with the probe located at the toe of the beach. Again, there is generally good agreement between the ADV and LDA measurements though the ADV records more structure at about 46 sec and about 47.2 sec. When Figure 7.8 is compared to the normally incident case shown in Figure 7.2 there are a couple of differences. The main peak is a little lower for the oblique wave group. This is to be expected since the onshore direction is

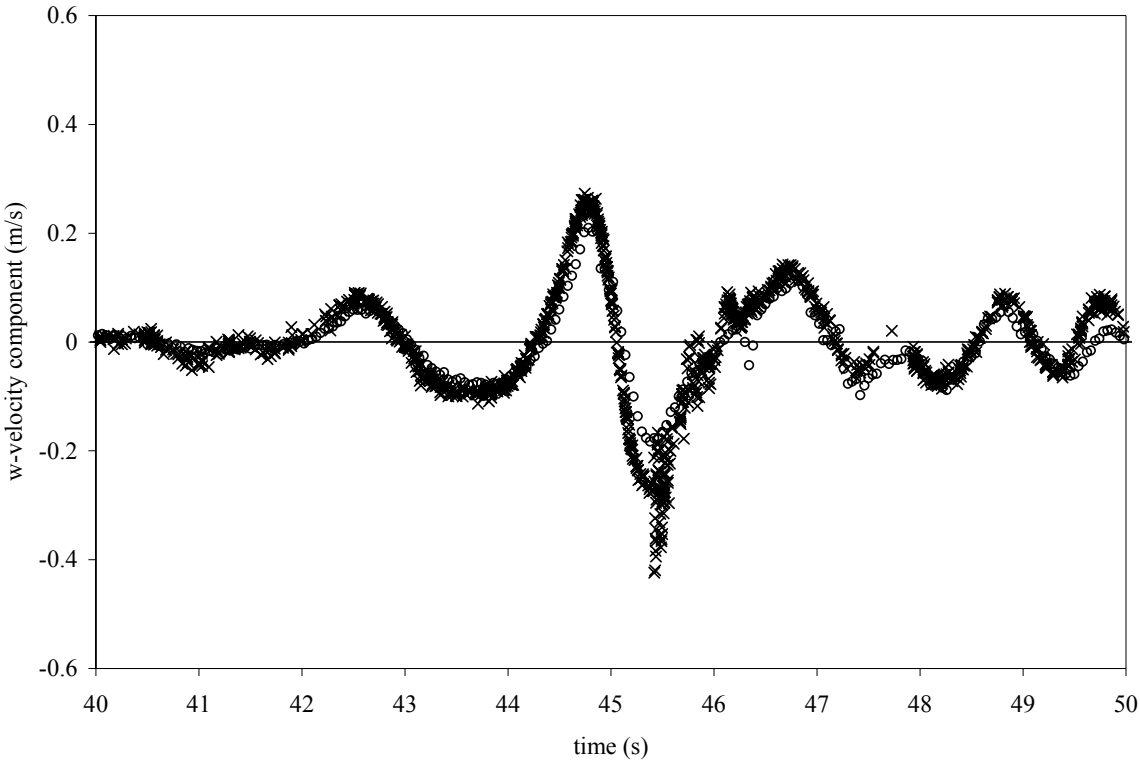

Figure 7.9: Time history of vertical velocity component of an oblique incidence crest focused wave group, measured at the toe of the beach beneath the trough: ×, LDA; ∘, ADV.

no longer the travelling direction of the group. For an oblique angle of 20°, the maximum velocity in the onshore direction should be reduced to about 94% of that of the normally incident wave group.[4] Also, the LDA no longer registers a small peak following the third main crest of the group.

Figure 7.9 shows the time-dependent behaviour of the vertical component of the water particle velocity for the oblique case, again at the toe of the beach. This is almost identical to the time history of the vertical velocity component given in Figure 7.3 except that the LDA records a significant downwards spike at about 45.5 sec. The cause of this is not known.

For the oblique wave group it is useful to gather data for the longshore component of velocity. This was only done using the ADV since it alone could measure three orthogonal

[4]From simple trigonometry, $v = V_{\max} \times \cos\theta$ where $V_{\max}$ is the maximum horizontal velocity of the group in the direction of travel, v is the onshore component and θ is the angle of incidence of the wave group. For $\theta = 20^{\circ}$, the onshore component would be reduced to 0.94 of the maximum normally incident onshore value.

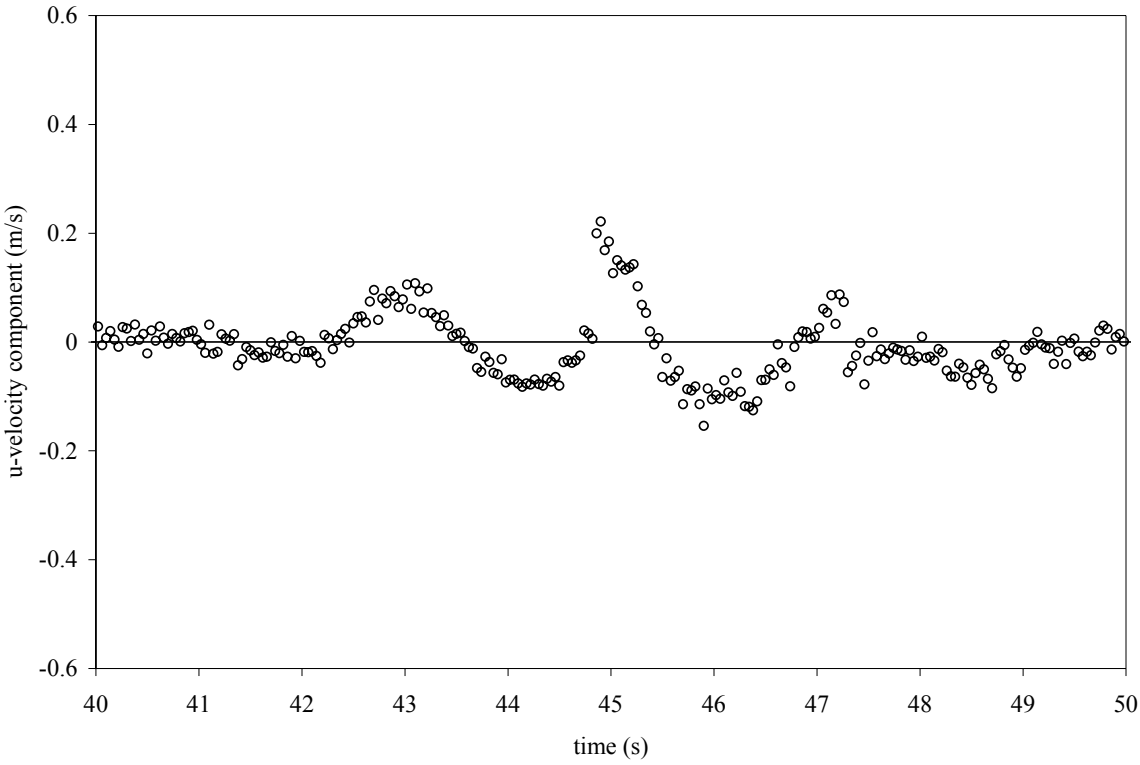

Figure 7.10: Time history of longshore velocity component of an oblique incidence crest focused wave group, measured at the toe of the beach beneath the trough, using ADV.

components simultaneously. Figure 7.10 shows the results. It can be seen that the shape of the data follows that of Figure 7.8 which is to be expected. The maximum velocity should be about 0.15 m/s.[5] Taking into consideration the noise level at 45 sec, the data would appear to be consistent.

7.4 Kinematics of repeated focused wave groups at beach toe

In addition to measuring the velocity components under the wave group trough for a single wave group, further water particle velocity measurements were undertaken under repeated focused wave groups. This experiment involved repeating the entire wave group generation

[5] From simple trigonometry, $u = V_{\max} \times \sin\theta$ where $V_{\max}$ is the maximum horizontal velocity of the group in the direction of travel, u is the longshore velocity component and θ is the angle of incidence of the wave group. $V_{\max} = 0.45$ m/s from the normally incident group shown in Figure 7.2, which combined with $\theta = 20^{\circ}$ gives $u = 0.45 \times \sin 20 = 0.15$ m/s.

at regular intervals of 30 sec. The aim of this experiment was to examine whether a longshore current is produced along the beach that in turn causes large scale recirculation in the main part of the basin, driven by the oblique incidence wave groups. Data from a total of twenty repeated groups were obtained. Initial analysis showed that the surface elevation was approximately the same for each wave group.

Measurements were carried out at regular spaced levels through the water column, at the toe of the beach. The measurement locations were at z = -422 mm, -372 mm, -322 mm, -272 mm, -222 mm, -172 mm and -122 mm where z is measured vertically upwards from the still water level. Data are presented for onshore and vertical velocity components for normally incident groups, and onshore, vertical *and* longshore velocity components for oblique groups.

7.4.1 Normally incident repeated wave group

Figure 7.11 (a) shows the time series of the ensemble mean μ, and $\mu \pm 2\sigma$ where σ is the standard deviation, of the onshore water particle velocity component at the measurement location closest to the water surface ($z = -122$ mm). Figure 7.11 (b) shows the variation of the mean horizontal velocity component with depth. Note that the kink in the time history of Figure 7.11 (a) at about 47.5 sec becomes less obvious as the measurement depth increases. This kink might be associated with a double frequency freely propagating error wave from the paddles. The reduction in the size of the kink with depth is consistent with this. Figure 7.11 (c) gives the depth profile of the mean peak velocities, at all seven depths. Also plotted on Figure 7.11 (c) is a line which represents the linear superposition theory outlined in the previous section and given in Eqn. (7.8). The data points follow a similar trend with fairly good agreement between the two curves. The linear superposition approach will lead to a very rough approximation since it ignores both higher order terms of the regular wave and any interaction between the individual wave components. It is therefore to be expected that the measured values of the peak mean velocities exceed the theoretical curve. It can be seen that there is increasing disparity between the linear approximation and the measured data as the measurement location nears the surface. This is possibly because higher order terms are increasingly important closer to the surface as has just been suggested as the explanation of the magnitude of the kink in Figure 7.11 (b).

Figure 7.12 shows the vertical velocity component of the normally incident repeated

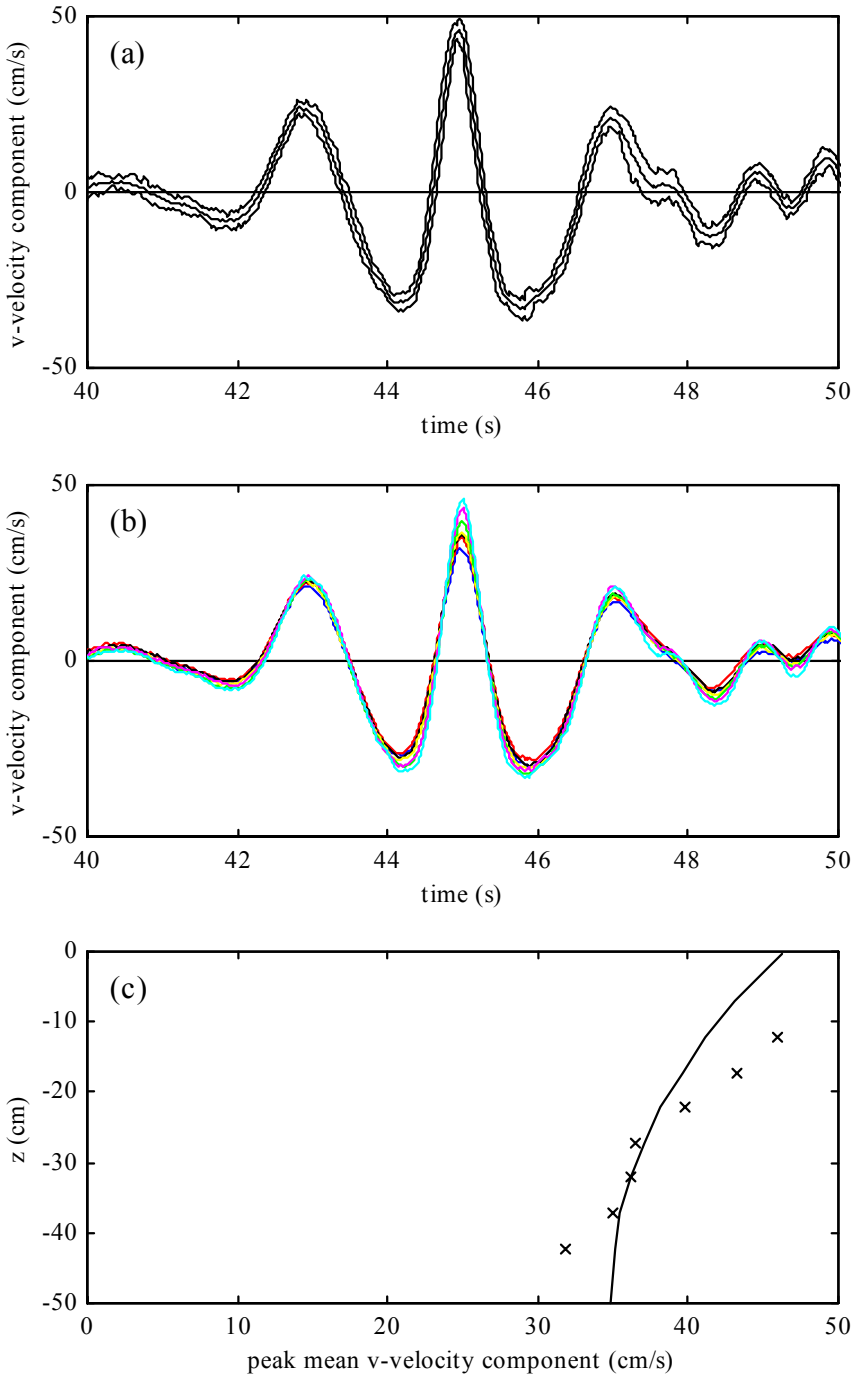

Figure 7.11: Onshore velocity component of normally incident repeating focused wave group measured at toe of beach by ADV (a) measured at z = -122 mm: —, mean μ; - - -, $\mu \pm 2\sigma$ (b) mean velocity through the column: — (blue), z = -422 mm; — (red), z = -372 mm; — (black), z = -322 mm; — (yellow), z = -272 mm; — (green), z = -222 mm; — (pink), z = -172 mm; — (turquoise), z = -122 mm (c) variation of peak mean velocity with depth: - - -, linear theory; $\times$, measured data.

groups. Figure 7.12 (a) shows μ and $\mu \pm 2\sigma$ at the deepest measurement location, at z = -122 mm. There is possibly a greater spread in the data set, particularly after the main event at about 47 sec. Figure 7.12 (b) shows how the mean peak vertical velocity components vary through the depth of the water column. They appear to be more evenly spaced than in Figure 7.11 (b). This is confirmed by the data curve of Figure 7.12 (c) which shows close to linear variation in peak mean velocity upwards from the bed. Figure 7.12 (c) also shows the curve derived from the linear superposition theory of the vertical velocity component. This is derived from Eqn. (7.6) in the same way that Eqn. (7.8) was derived from Eqn. (7.5) hence

$$w = \sum_{n=1}^{N} \frac{k_n g}{\omega_n} \frac{\sinh k_n(z+d)}{\cosh(k_n d)} \left(a_n \cos(\omega_n t - k_n x) + b_n \sin(\omega_n t - k_n x)\right) \tag{7.9}$$

As for the onshore velocity component, there is a similar trend for the two curves but there is increasing departure of measured data from linear theory as the measurement location nears the surface. Again, this may be due to the neglect of increasingly important higher order terms near the surface.

7.4.2 Oblique incidence repeated wave group

Data for the variation of horizontal velocity component with water depth of repeating oblique incidence wave groups at the toe of the beach are presented in Figure 7.13. Figure 7.13 (a) shows the time history of the mean μ and $\mu \pm 2\sigma$ of the horizontal velocity component at the beach toe. It is very similar to the normally incident case of Figure 7.11 (a) except that there is greater variation around the central peak and the second trough. The variation of velocity with depth in Figure 7.13 (b) and (c) show deviations from a smooth curve, probably due to noise-induced scatter. The theoretical curve of 7.13 (c) uses the normally incident curve derived from Eqn. (7.8) multiplied by $\cos(20°)$ to take into account the oblique angle. There is the same level of deviation from linear theory in Figure 7.13 (c) as for 7.11 (c), presumably for the same reasons: neglection of both higher order terms and interactions between individual wave components.

Figure 7.14 shows the vertical velocity component and is almost identical to the normally incident case shown in Figure 7.12.

Figure 7.15 shows the longshore velocity component through the water column for the repeating oblique wave group. Figure 7.15 (a) which shows the μ and $\mu \pm 2\sigma$ longshore u-

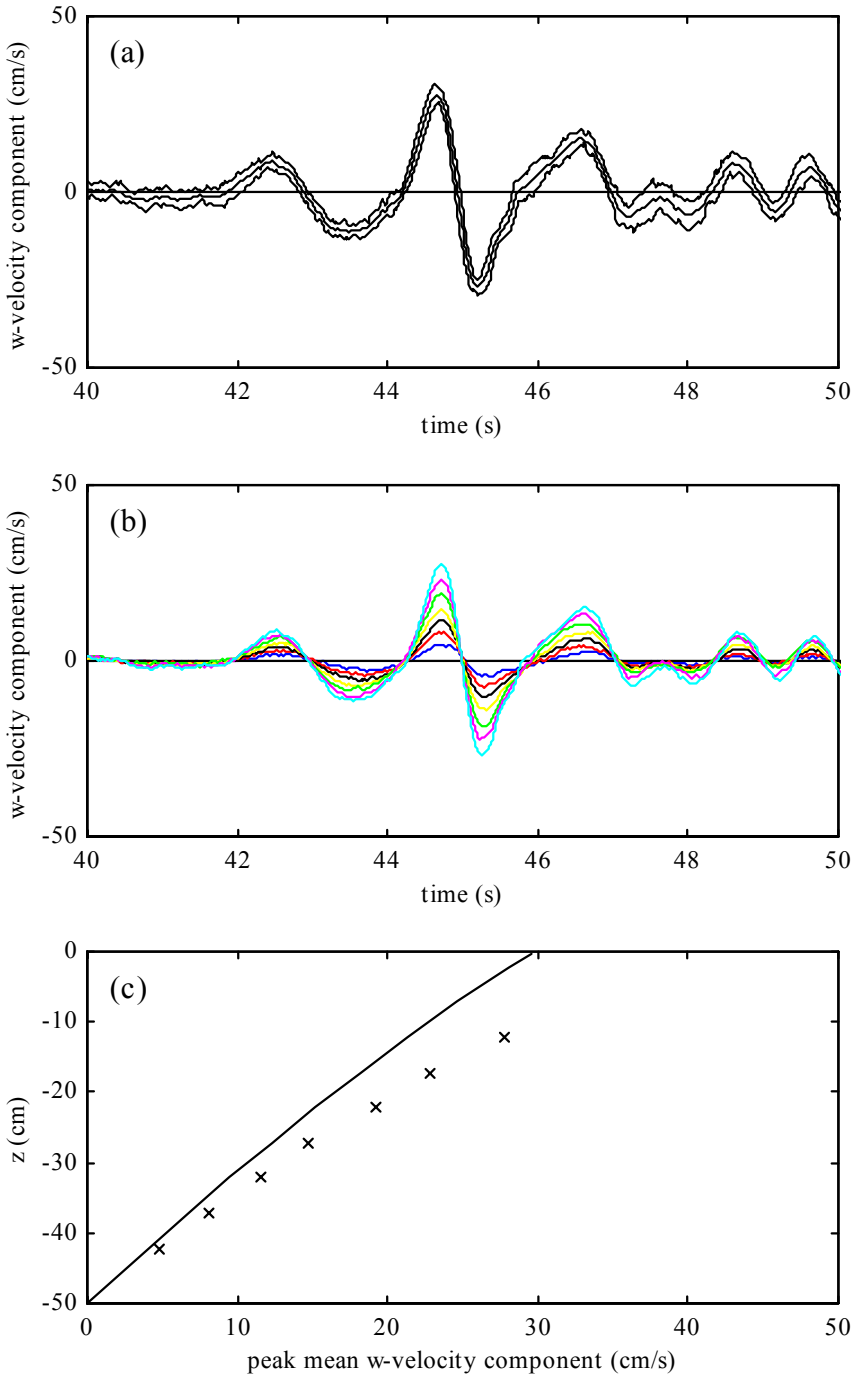

Figure 7.12: Vertical velocity component of normally incident repeating focused wave group measured at toe of beach by ADV (a) measured at z = -122 mm: —, mean μ; - - -, $\mu \pm 2\sigma$ (b) mean velocity through the column: — (blue), z = -422 mm; — (red), z = -372 mm; — (black), z = -322 mm; — (yellow), z = -272 mm; — (green), z = -222 mm; — (pink), z = -172 mm; — (turquoise), z = -122 mm (c) variation of peak mean velocity with depth: - - -, linear theory; $\times$, measured data.

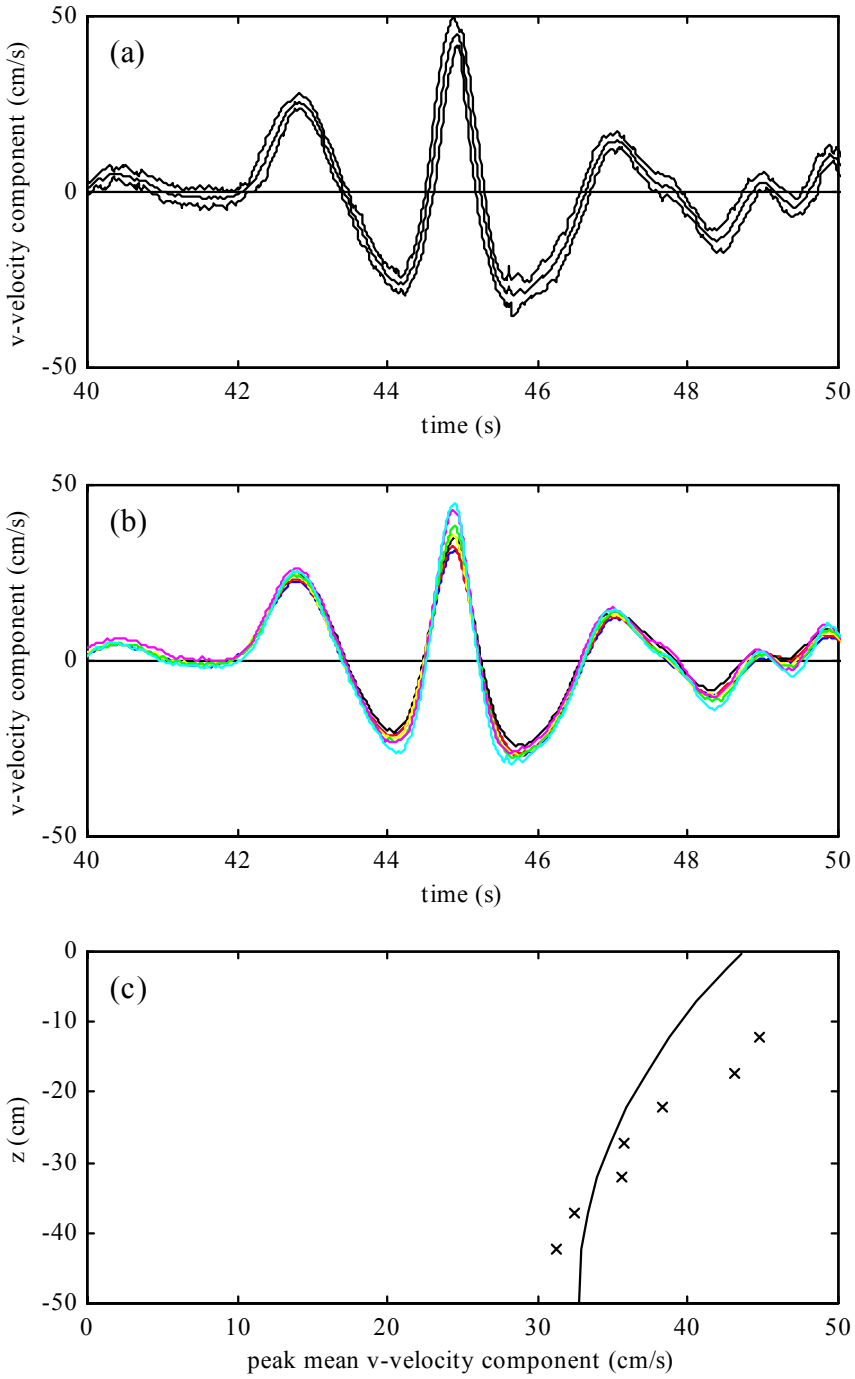

Figure 7.13: Onshore velocity component of oblique incidence repeating focused wave group measured at toe of beach by ADV (a) measured at z = -122 mm: —, mean μ; - - -, $\mu \pm 2\sigma$ (b) mean velocity through the column: — (blue), z = -422 mm; — (red), z = -372 mm; — (black), z = -322 mm; — (yellow), z = -272 mm; — (green), z = -222 mm; — (pink), z = -172 mm; — (turquoise), z = -122 mm (c) variation of peak mean velocity with depth: - - -, linear theory; $\times$, measured data.

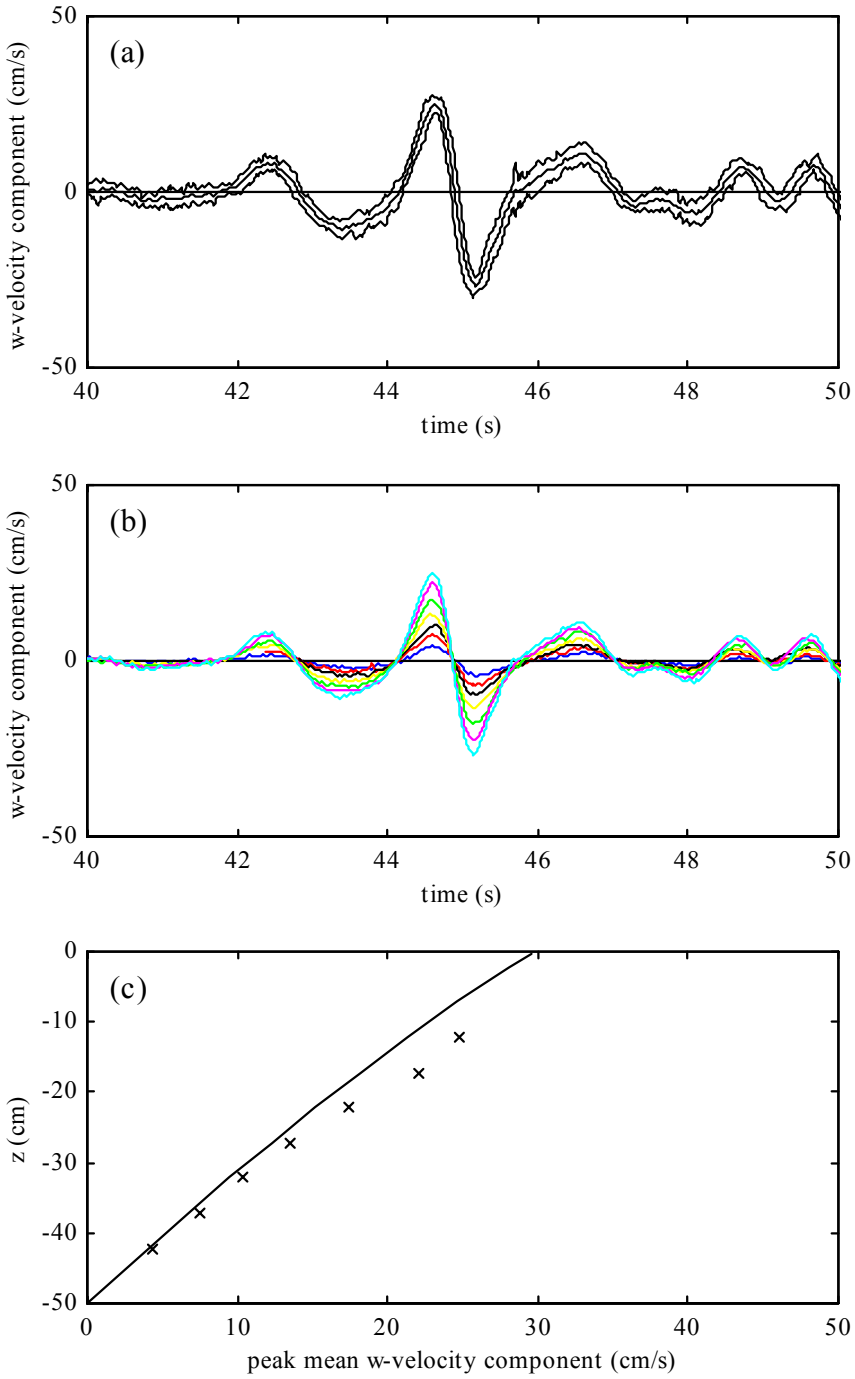

Figure 7.14: Vertical velocity component of oblique incidence repeating focused wave group measured at toe of beach by ADV (a) measured at z = -122 mm: —, mean μ; - - -, $\mu \pm 2\sigma$ (b) mean velocity through the column: — (blue), z = -422 mm; — (red), z = -372 mm; — (black), z = -322 mm; — (yellow), z = -272 mm; — (green), z = -222 mm; — (pink), z = -172 mm; — (turquoise), z = -122 mm (c) variation of peak mean velocity with depth: - - -, linear theory; $\times$, measured data.

velocity components closest to the free surface has significant levels of noise at just under 46 sec, but is otherwise of good quality. Figures 7.15 (b) and (c) show that there is little variation of the longshore velocity with depth. The theoretical curve of 7.15 (c) is obtained from Eqn. (7.8) multiplied by sin(20°) - the modification due to an oblique angle. There is reasonable agreement between the theoretical curve and the data points, though the measurements are lower than the theoretical curve, contrary to what would be expected. It is unlikely that poor alignment of the probe head is responsible as this would lead to a random error rather than a systematic error. It is possible that the wavefront has been refracted and the angle of incidence is less than 20°. Even a small reduction in the angle of incidence would have a considerable effect on the theoretical curve since the sine function varies rapidly for small angles, i.e. 20° or less. A reduction in the angle of incidence would reduce the theoretical curve, perhaps to below the measured values. Refraction of the wavefront would also affect the theoretical curve of Figure 7.13 (c) but the cosine function, used to modify the onshore v-velocity, is not as sensitive at these angles and any modification to the angle of incidence would be relatively insignificant. This explains the fact that there appears to be reasonable agreement between theory and measurement of the v-velocity, but not the u-velocity.

There does not appear to be an increasing disparity between the two curves of Figure 7.15 (c) nearer the free surface. It could therefore be surmised that higher order terms of the longshore velocity component vary less with depth than for the onshore or vertical components.

7.5 Kinematics of repeated focused group in the outer surf zone

Repeated focused wave groups were also measured in shallower water near the breaker zone where it was anticipated that the longshore current would be stronger. As a result the LDA data acquisition rates of the longshore velocity component were improved. As mentioned previously, the LDA system does not provide a constant data rate, unlike the ADV system - the acquisition of data depends upon the availability of a seeding particle in the laser beams. Therefore, when it comes to presenting LDA data it is not possible to provide averaged data without the errors inherent in splining the measurements. Hence, all LDA data from these

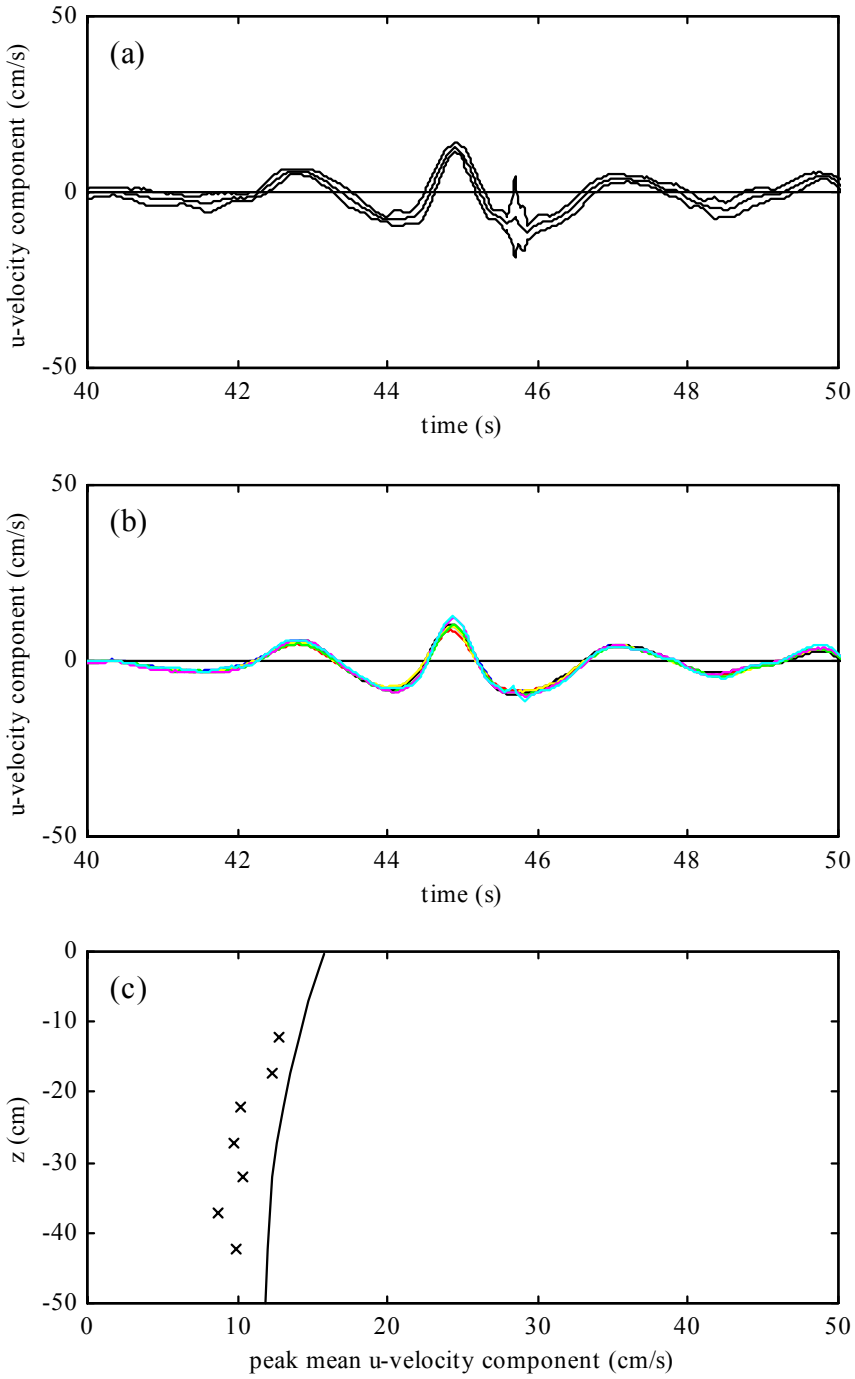

Figure 7.15: Longshore velocity component of oblique incidence repeating focused wave group measured at toe of beach by ADV (a) measured at z = -122 mm: —, mean μ; - - -, $\mu \pm 2\sigma$ (b) mean velocity through the column: — (blue), z = -422 mm; — (red), z = -372 mm; — (black), z = -322 mm; — (yellow), z = -272 mm; — (green), z = -222 mm; — (pink), z = -172 mm; — (turquoise), z = -122 mm (c) variation of peak mean velocity with depth: - - -, linear theory; $\times$, measured data.

repeating experiments will be presented on a scatter plot, which gives the added advantage of showing the range of values. ADV data given later in this section will be presented in terms of *mean* values over the twenty repeated groups.

LDA measurements in the surf zone were undertaken for normal and oblique incident repeated groups at a depth of 120 mm, 7.6 m onshore of the toe of the beach, 2 m to the right of the centre-line[6] and at elevations with respect to SWL of -100 mm, -90 mm, -80 mm, -60 mm and -40 mm. For the normally incident wave group (Wave Group No. 1) the first wave in the group breaks at 8.75 m onshore of the toe, the second wave breaks at 6.5 m and the third wave breaks at 5.75 m. For the oblique incidence wave (Wave Group No. 9) the first wave in the group breaks at 9.0 m onshore of the toe, the second wave breaks at 6.0 m and the third wave breaks at 6.25 m.[7] Therefore, the second and third main waves of the group have broken before reaching the measurement location at 7.6 m.

ADV measurements were also taken of the oblique incident wave group at a number of positions up the beach in the surf zone. These locations are detailed later in this Section.

7.5.1 Normally incident repeated wave group

Figure 7.16 shows the raw LDA measurements of the onshore velocity component at five elevations in the water column. The time at the origin is entirely arbitrary, but is consistent for all data sets. The data in Figures 7.16 (a) to (e) are from shallowest to deepest position. A low frequency wave is evident between 0 and 15 sec, followed by higher frequency waves. As would be expected, the peak horizontal velocity component increases steadily as the measurement location gets closer to the free surface. It is evident from the gap in the data in Figure 7.16 (a) that the LDA probe emerges from the water between approximately 20.5 and 21.5 sec. This would correspond to the largest trough passing the probe. There is clear evidence of the saw tooth behaviour of broken waves in the form of bores passing followed by higher scatter due to breaker-induced turbulence.

Figure 7.17 shows the corresponding vertical component of the water particle velocity data. The vertical water particle motions are almost negligible. However there are signs of high frequency oscillations between 25 and 30 sec, which increase in amplitude as the probe

[6] Using same direction convention as in Figure 3.1.

[7] Actually, the gauge time history at this location shows that the wave has *already* broken.

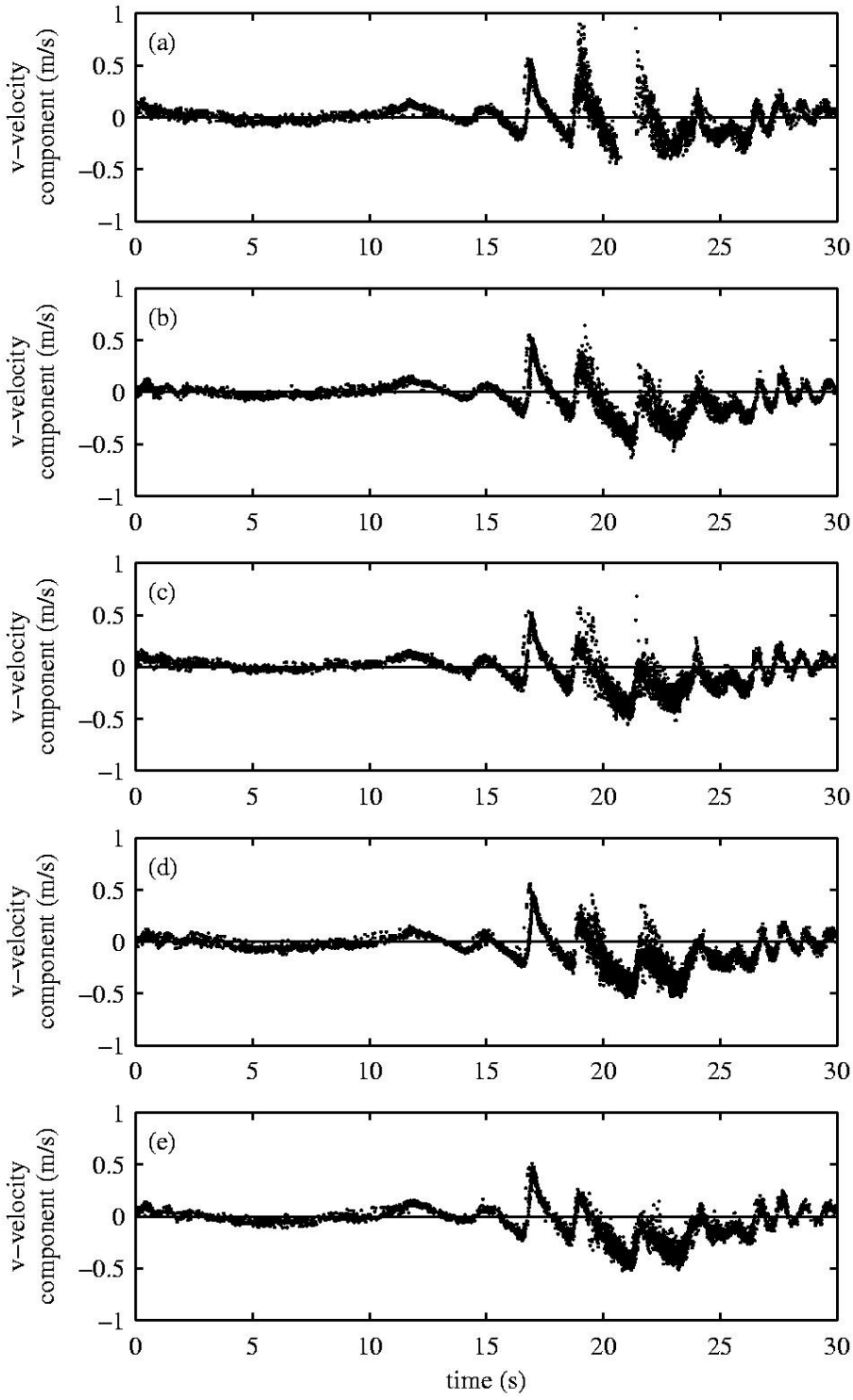

Figure 7.16: Time history of onshore velocity component of normally incident repeating focused wave group, measured with LDA at a still water depth of 120 mm for (a) z = -40 mm (b) z = -60 mm (c) z = -80 mm (d) z = -90 mm and (e) z = -100 mm.

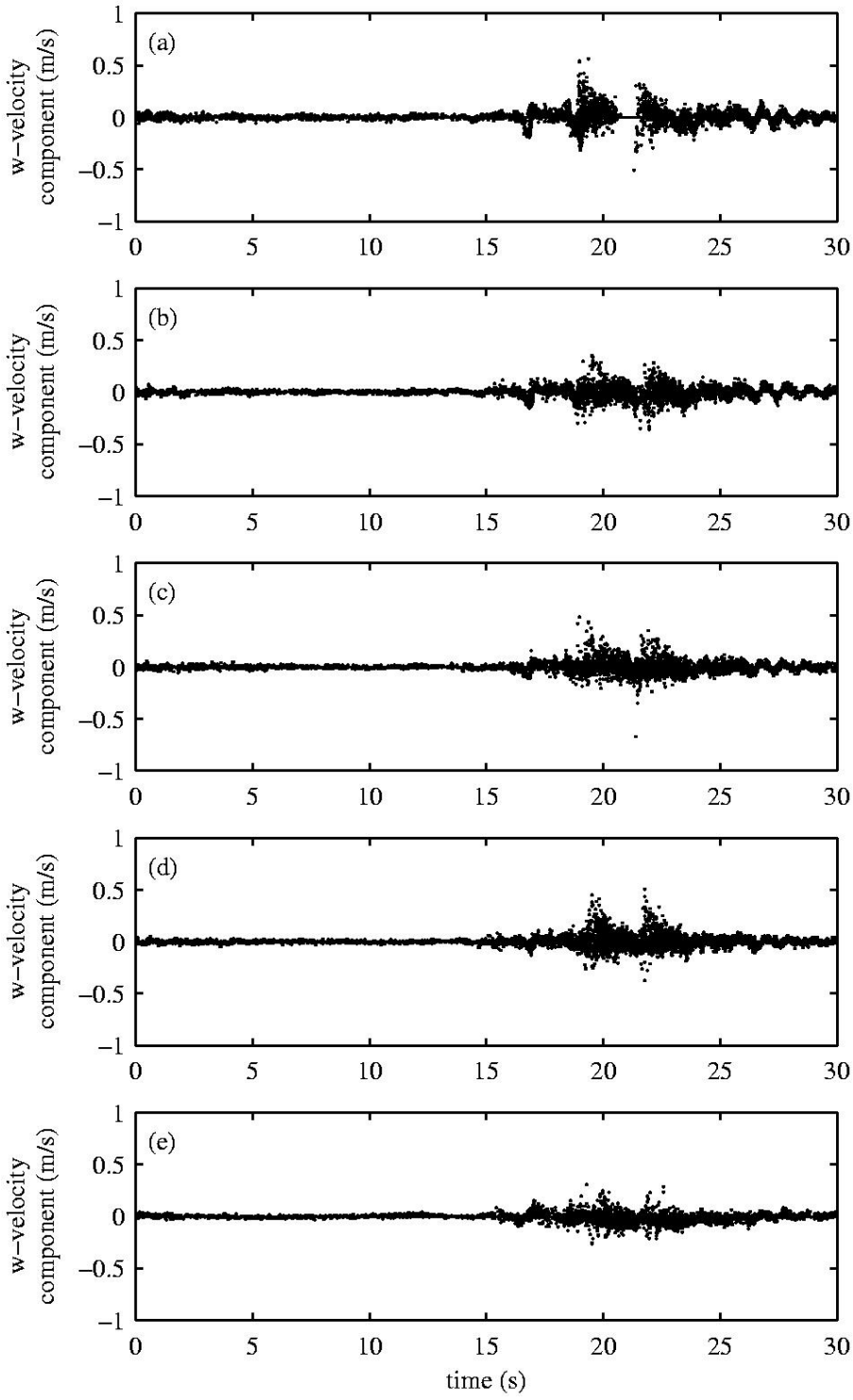

Figure 7.17: Time history of vertical velocity component of normally incident repeating focused wave group, measured with LDA at a still water depth of 120 mm for (a) z = -40 mm (b) z = -60 mm (c) z = -80 mm (d) z = -90 mm and (e) z = -100 mm.

is moved closer to the water surface. These may be due to vibration of the probe. Again, there is evidence of the probe head leaving the water between 20.5 and 21.5 sec in Figure 7.17 (a). At about 20 sec there is a burst following breaking. The scatter in data (particularly in Figure 7.17 (a) closest to the free surface) is due in part to aeration of the water following breaking.

7.5.2 Oblique incidence repeated wave group

Figure 7.18 shows the variation of onshore velocity component time histories with depth, for the oblique wave group. A low frequency wave is evident but the phase of this wave relative to the main group, compared with the case of the normally incident wave of Figure 7.16, is different. This is because, for the oblique case, the distance of travel from the paddles to the beach is further. This means that the long error wave will arrive earlier compared to the main wave group. The structure of the rest of the group is very similar for both angles of incidence, again with the probe leaving the water at the measurement location of -40 mm.

Figure 7.19 shows the vertical velocity component time histories of the repeated oblique wave group. As in the case of the normally incident groups there is no coherent data beyond the background noise, except for high frequency oscillations between 25 and 30 sec, increasing with size, or at least coherence, as the probe is raised. Turbulence due to broken waves is evident in both Figures 7.18 and 7.19.

To investigate the velocities of the oblique wave group in the swash zone further, the ADV was deployed at nine locations up the beach, 2m to the right of the centre-line. Figure 7.20 and Table 7.1 (found towards the end of this Section) provide details of the cross-shore and depth locations for data that are presented in Figures 7.21 to 7.23.

The position of the ADV probe in the water column was kept to a relative depth of around 40% above the bed (where a unidirectional steady current has a value similar to that of the depth-averaged). Positions 1 and 3 are not actually in the surf zone as none of the waves have yet broken, but data are included for comparison purposes. Locations 5 to 9 fall within the region where either one or two of the three waves comprising the group have broken.

Figures 7.21 (a) to (e) show the mean horizontal velocity component at locations progressively closer to the shore. Although the wave group is clearly not focused at a distance away from the toe of the beach, the structure of the group is still evident. The velocities shown in

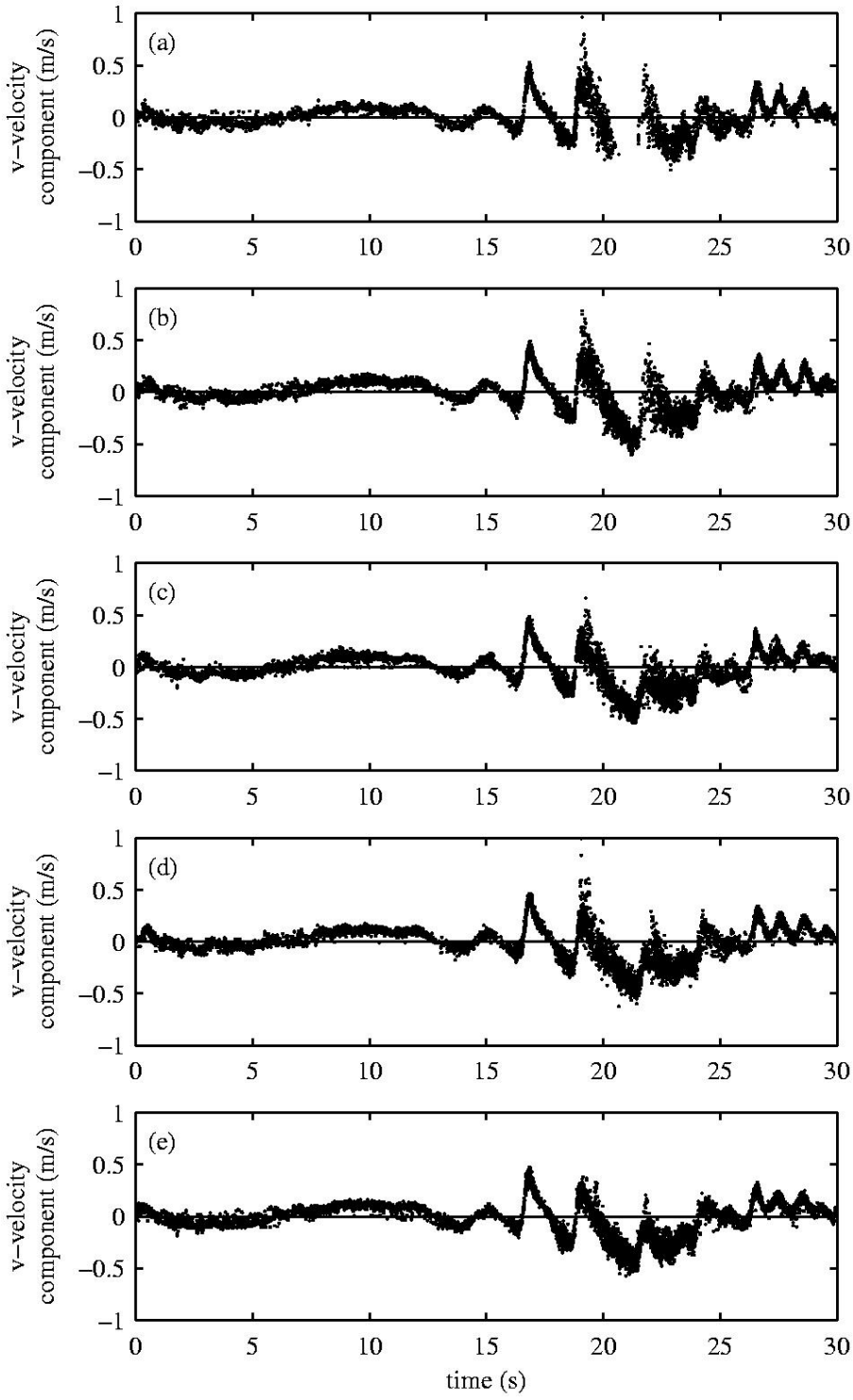

Figure 7.18: Time history of onshore velocity component of oblique incidence repeating focused wave group, measured with LDA at a still water depth of 120 mm for (a) z = -40 mm (b) z = -60 mm (c) z = -80 mm (d) z = -90 mm and (e) z = -100 mm.

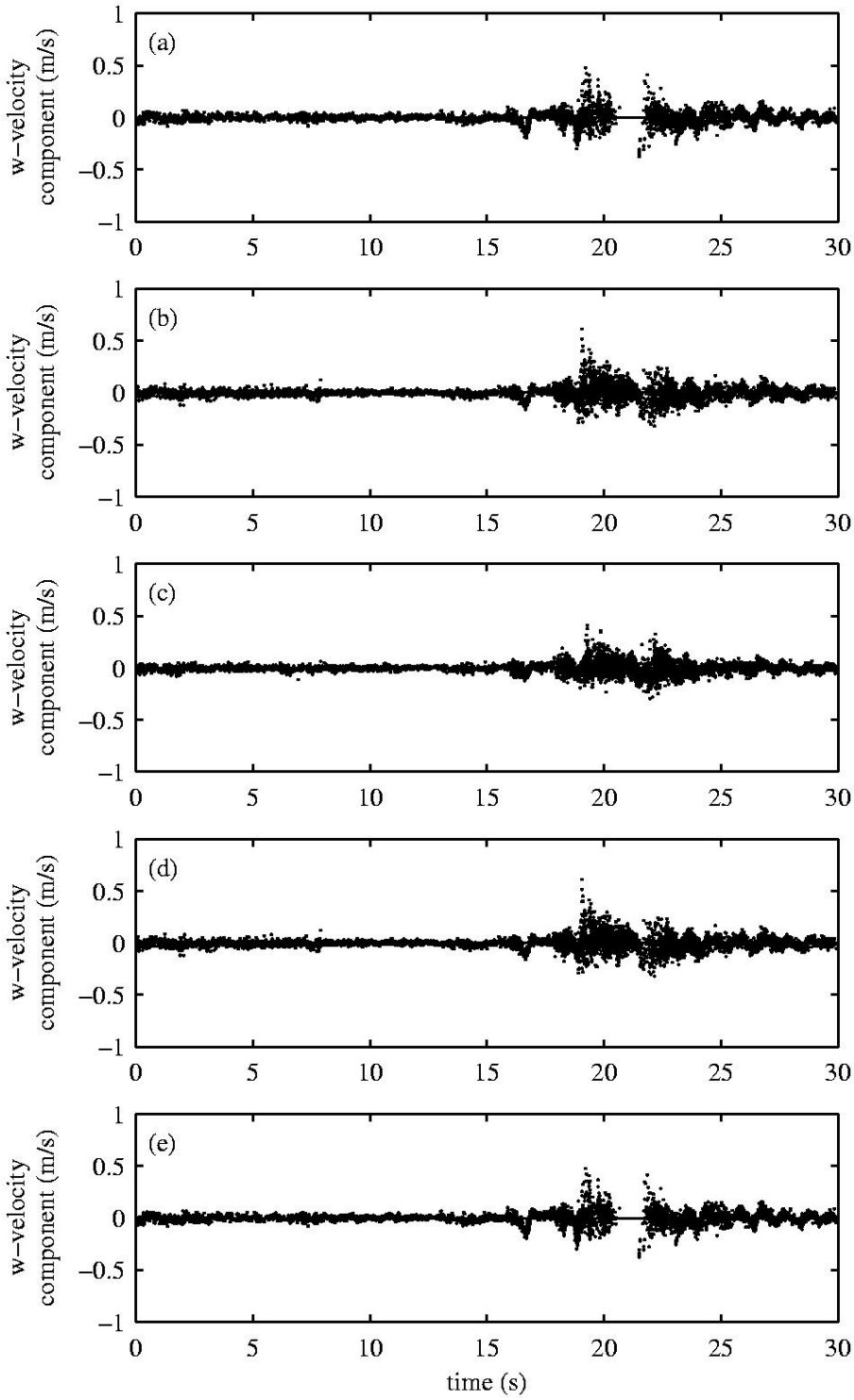

Figure 7.19: Time history of vertical velocity component of oblique incidence repeating focused wave group, measured with LDA at a still water depth of 120 mm for (a) z = -40 mm (b) z =-60 mm (c) z = -80 mm (d) z = -90 mm and (e) z = -100 mm.

Table 7.1: ADV measurement locations of oblique repeated focused wave groups.

location	onshore distance (m) w.r.t. toe	depth (mm)	z (mm) w.r.t. SWL	relative depth (%)
1	4.82	260	-176	32
3	5.32	233	-140	40
5	6.07	195	-111	43
7	6.57	170	-97	43
9	7.32	134	-80	40

Figure 7.21 (c) show a significant departure to those of Figures 7.21 (a) and (b) in that the third main wave appears to be breaking. In Figure 7.21 (d) and (e) the second and third waves have broken and the peak horizontal water velocity components have reduced somewhat. The water particle velocities again exhibit sawtooth behaviour due to corresponding broken waves i.e., there is a rapid rise and slower fall as the bores pass the probe.

The data shown in Figure 7.21 (e) were collected at roughly the same location as for the LDA measurements shown in Figure 7.18. There is good agreement between the data using these two methods. The ADV data may look clearer but it must be borne in mind that the data is ensemble averaged, and it is the LDA which provides the most accurate picture.

Figure 7.22 shows the vertical velocity component at the same positions. It can be seen that the peak vertical velocities reduce as the water depth decreases. The vertical velocity component also becomes subject to greater 'noise' levels.

Figure 7.23 shows the longshore velocities of the oblique repeated wave group. It is clear that there is a background constant velocity that increases in size as the water depth shallows. This is evidence of a longshore current driven by a pulsatile wave group breaking at an oblique angle to the beach. Figure 7.24 shows how the time-averaged longshore velocity varies in the onshore direction. The horizontal axis is the dimensionless onshore distance, where 0 corresponds to the toe of the beach and 1 corresponds to the still water shoreline. It can be seen that the mean longshore velocity is close to zero until around 60% of the way up the beach, after which point it increases sharply with distance, i.e. a longshore current is not generated until the dimensionless onshore distance is about 0.5. This corresponds to the

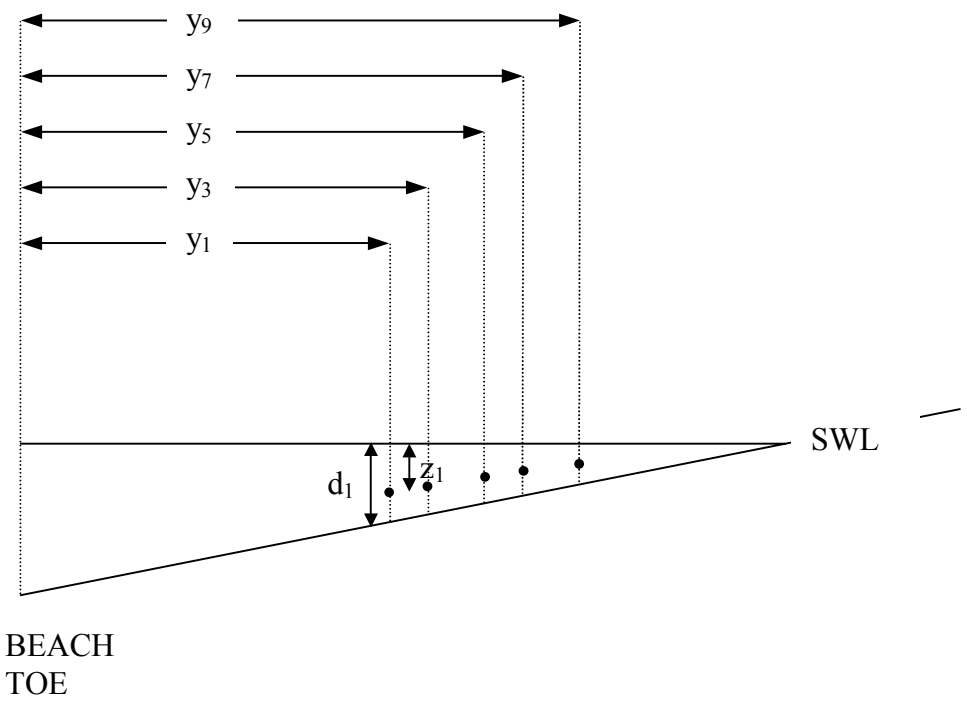

Figure 7.20: ADV surf zone measurement locations of oblique steady-state focused wave groups.

beginning of the surf zone as shown in Figure 6.4 (a).

7.6 Kinematics of repeated focused group in inner surf zone

It is not possible to use the ADV in the shallowest parts of the surf zone as the water depths are too shallow for the relatively large probe head. However, the LDA probe is very compact and it is possible to measure to within 12 mm of the basin floor. LDA measurements were undertaken at a location of 9.04 m onshore of the toe, in just 48 mm of water. This location is beyond the point at which all of the three main waves in both the normal and oblique incident wave groups have broken.

As with the outer surf zone measurements, the depth variation of the velocities was investigated. However, due to depth restrictions it was possible to take measurements at only three positions: -8 mm, -18 mm and -28 mm w.r.t. the SWL. The measurements were made at 2.78 m to the right of the centre-line. Unfortunately all of the onshore velocity data suffered a cut-off of data beyond -0.6 m/s. This was due to an error in setting up the LDA

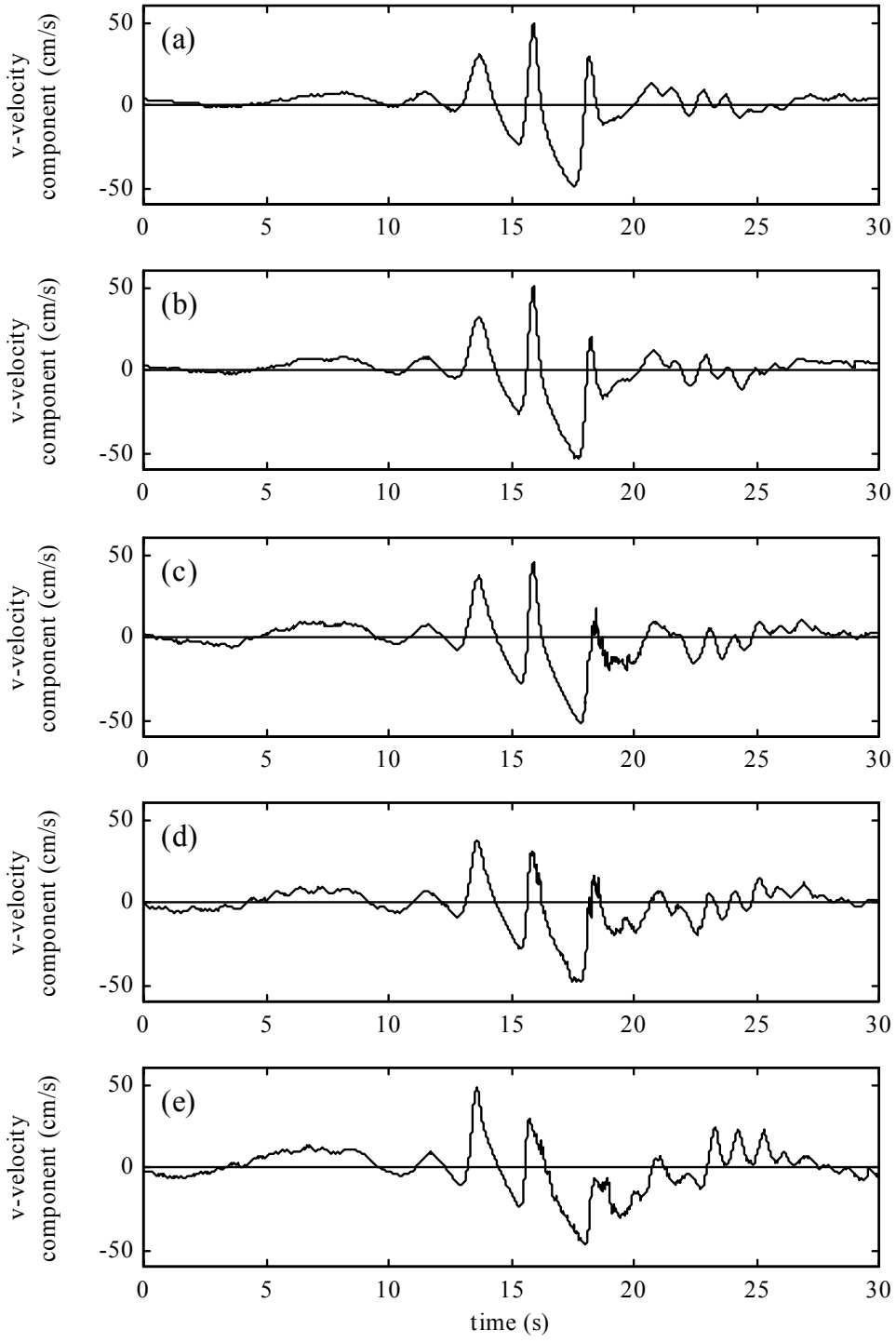

Figure 7.21: ADV measurements of onshore velocity component time histories for oblique repeating focused wave group, at five positions in the surf zone (a) location 1 (b) location 3 (c) location 5 (d) location 7 and (e) location 9 (as described in Table 7.1).

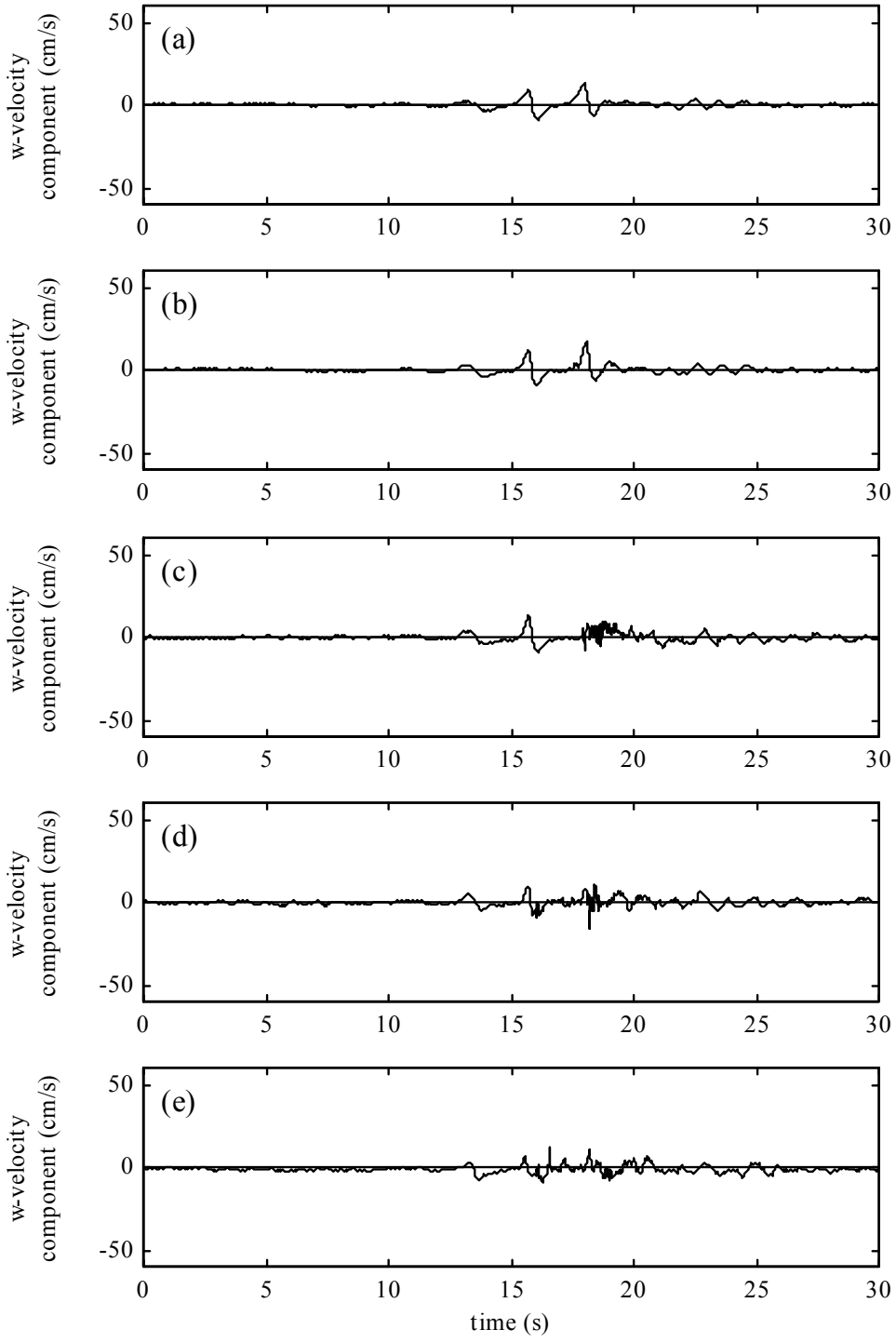

Figure 7.22: ADV measurements of vertical velocity component time histories for oblique repeating focused wave group, at five positions in the surf zone (a) location 1 (b) location 3 (c) location 5 (d) location 7 and (e) location 9 (as described in Table 7.1).

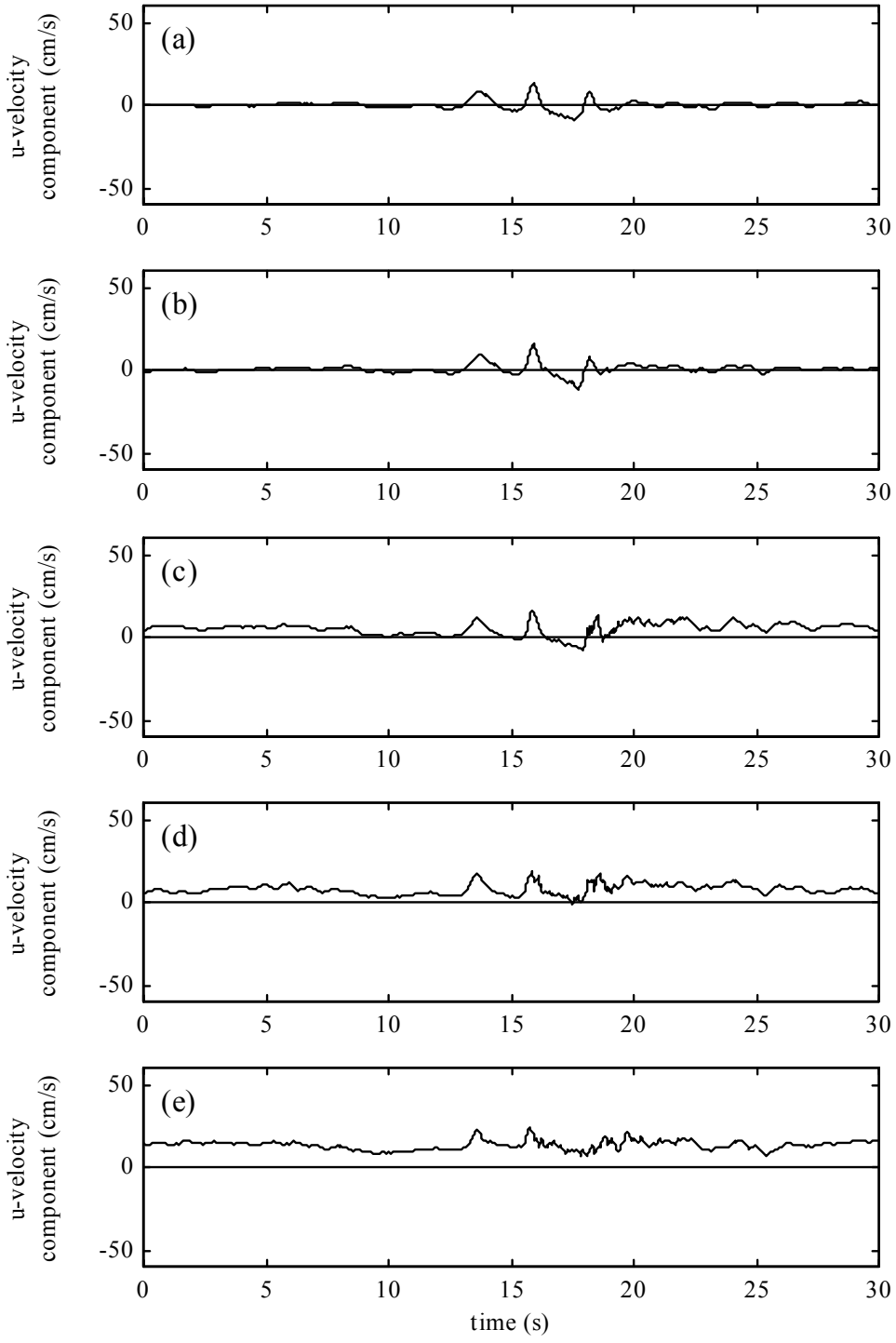

Figure 7.23: ADV measurements of longshore velocity component time histories for oblique repeating focused wave group, at five positions in the surf zone (a) location 1 (b) location 3 (c) location 5 (d) location 7 and (e) location 9 (as described in Table 7.1).

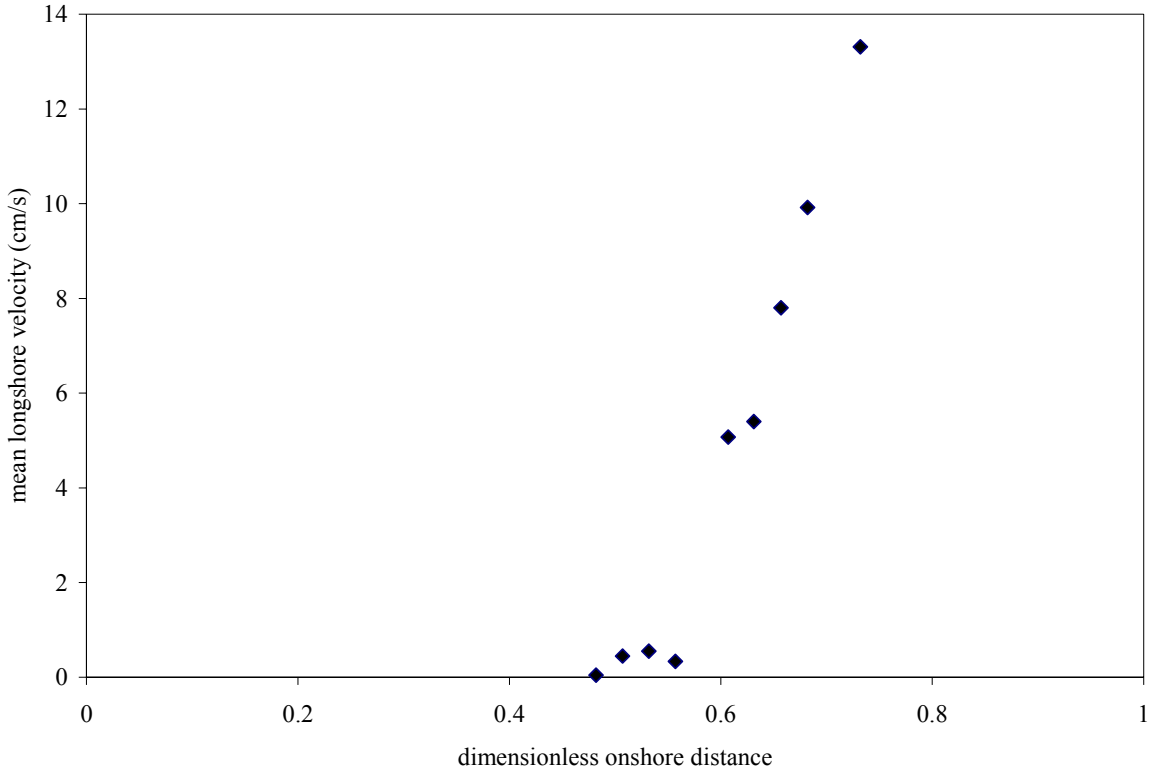

Figure 7.24: Time-averaged longshore velocity measured at nine cross-shore locations.

software. It was not apparent that there was a problem until the data were overlaid, some time later.

7.6.1 Normally incident repeated wave group

Figure 7.25 shows the onshore velocity component time histories at three elevations. There is evidence of the main group between about 15 and 25 sec, a low frequency oscillation between 5 and 15 sec, and a high frequency oscillation beyond 25 sec and from 0 sec until 5 sec. As with the LDA measurements in the surf zone certain data are lost in the location closest to the surface when the trough exposes the probe head, this time at around 25 sec in Figure 7.25 (a). Also, as already mentioned, the data were clipped beyond -0.6 m/s, losing the largest negative velocities. Despite this problem, it should be remarked that the largest negative flow velocity down the beach is clearly larger than the positive onshore velocity.

Figure 7.26 shows the vertical velocities at the same location. These vertical velocities

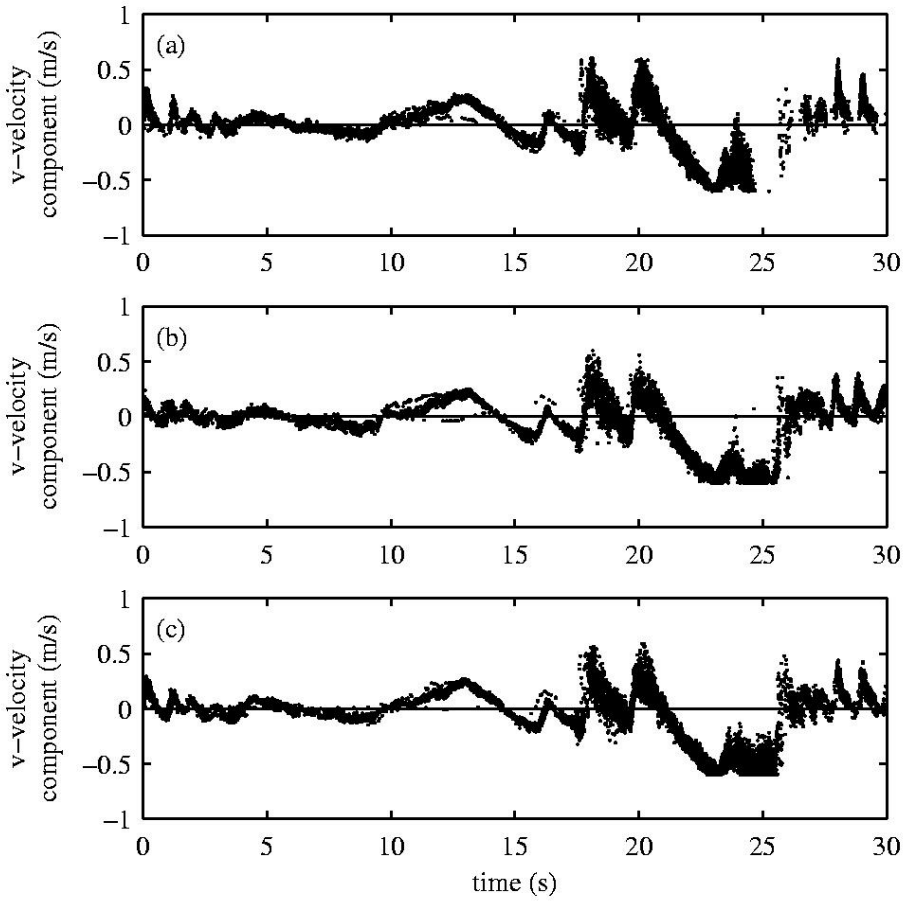

Figure 7.25: Time history of onshore velocity component of normally incident repeating focused wave group, measured with LDA at a still water depth of 48 mm for (a) z = -8 mm (b) z = -18 mm and (c) z = -28 mm.

exceed those measured in the surf zone, though there is no clear structure. This is probably due to churning of water during or following wave breaking, as turbulent bores run up the beach.

7.6.2 Oblique incidence repeated wave group

Figure 7.27 shows the onshore velocity component time histories in the inner surf zone of the oblique repeating group. The greatest difference between these data and the data for the normally incident case is that there are fewer data points. The other difference is that there are more high frequency oscillations. One point of interest is that the largest values of the

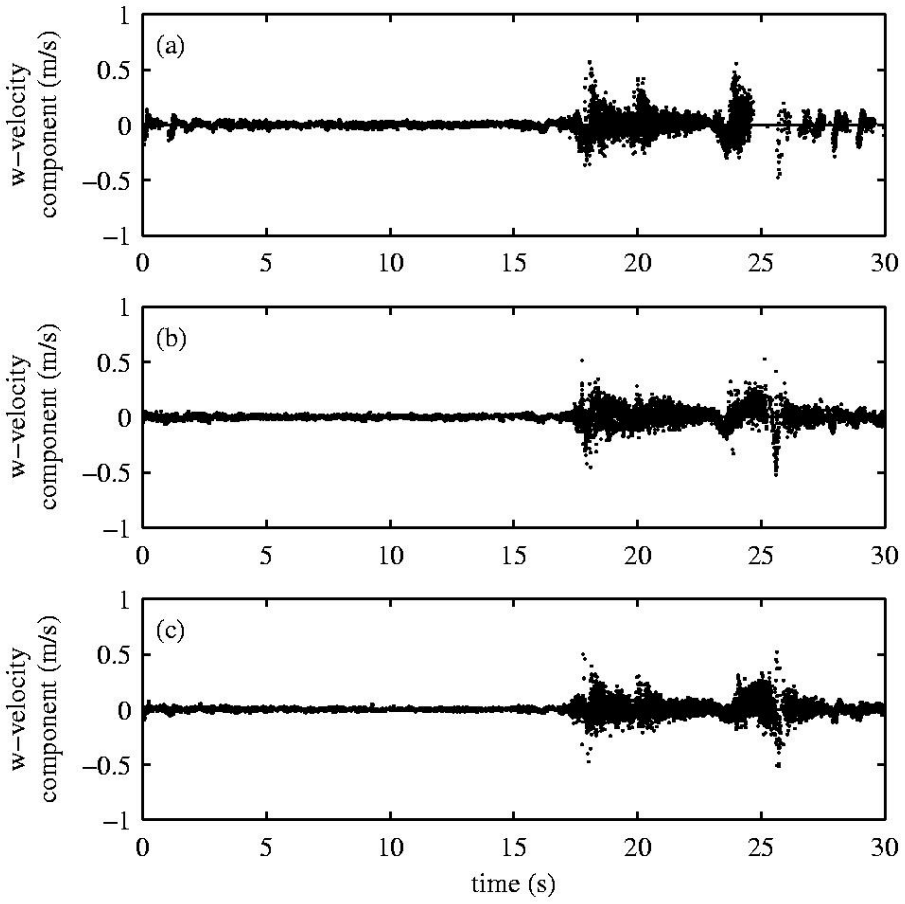

Figure 7.26: Time history of vertical velocity component of normally incident repeating focused wave group, measured with LDA at a still water depth of 48 mm for (a) z = -8 mm (b) z = -18 mm and (c) z = -28 mm.

negative downbeach velocity appear to be larger for the oblique group than for the normally incident one.

Finally, Figure 7.28 shows the vertical velocities. As with Figure 7.26, the velocities are larger than those of the surf zone shown in Figures 7.17 and 7.19. Again this is evidence of active wave breaking and turbulent bores.

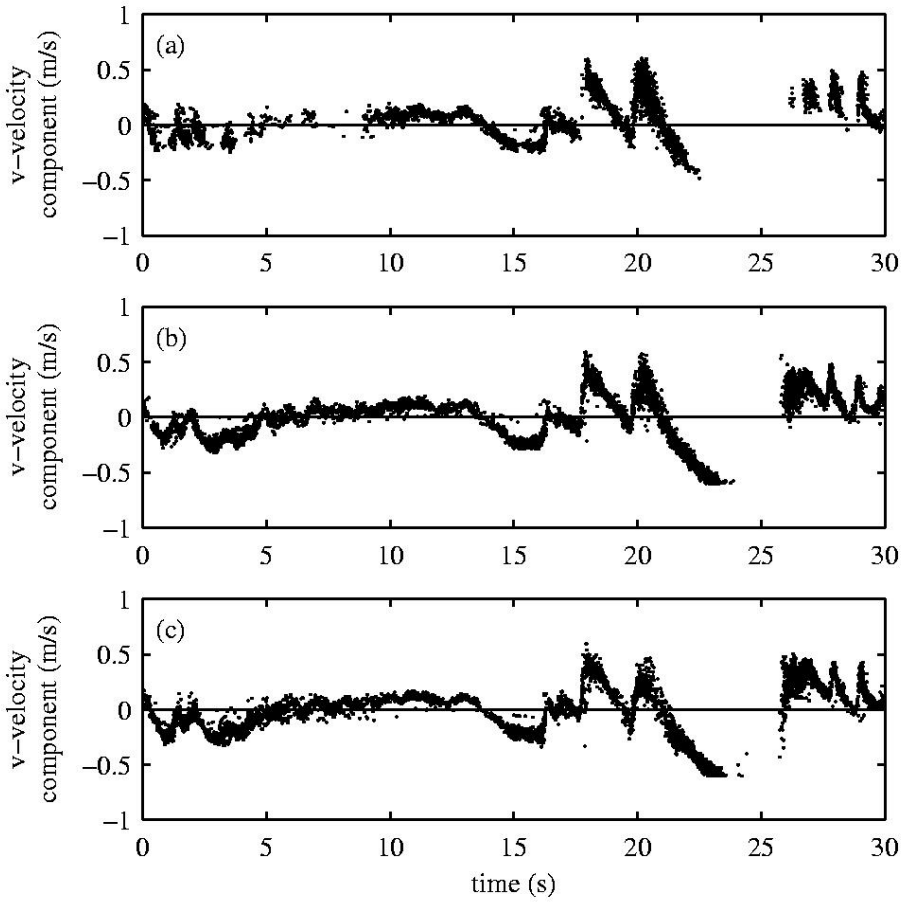

Figure 7.27: Time history of onshore velocity component of oblique incidence repeating focused wave group, measured with LDA at a still water depth of 48 mm for (a) z = -8 mm (b) z = -18 mm and (c) z =-28 mm.

7.7 Conclusions

It has been possible with the use of both an ADV and LDA system to provide insight into the flow kinematics of normal and oblique incidence focused wave groups at the toe of the beach in water of intermediate depth, and also in the surf zone. The agreement between measurements taken by the ADV and LDA was excellent, confirming the accuracy of the experimental set-up.

The method of separating harmonics which was carried out on surface elevation time histories in Chapters 3 and 5 was successfully extended to the onshore velocity component

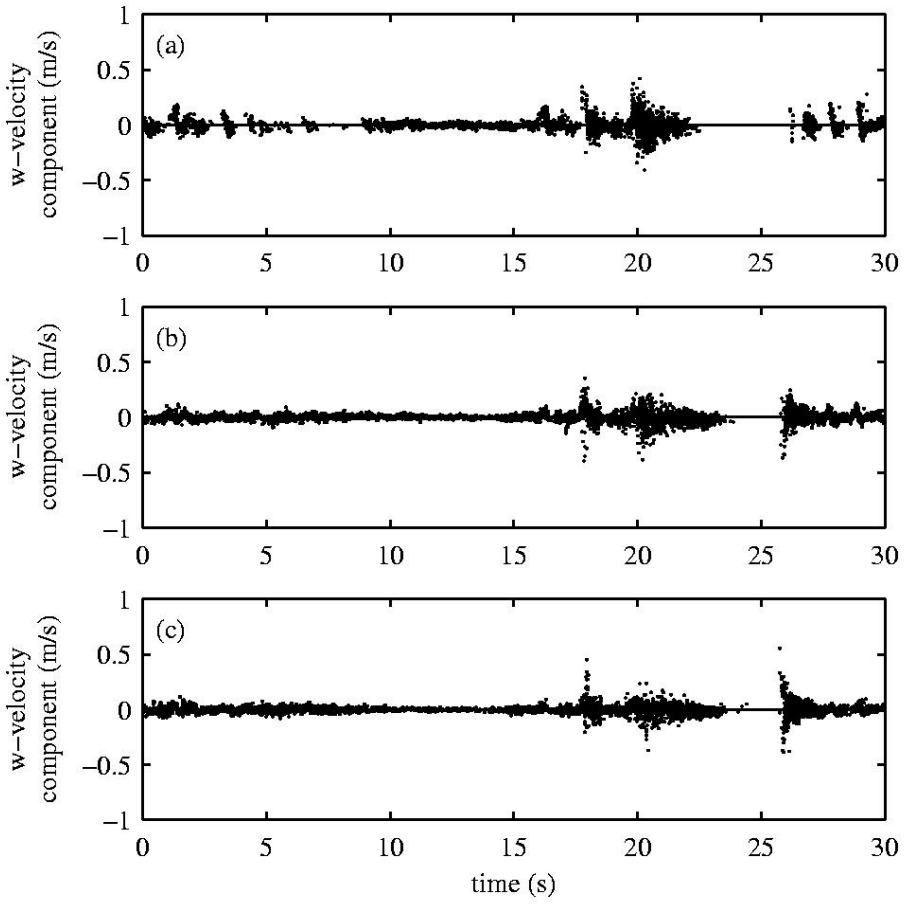

Figure 7.28: Time history of vertical velocity component of oblique incidence repeating focused wave group, measured with LDA at a still water depth of 48 mm for (a) z = -8 mm (b) z = -18 mm and (c) z = -28 mm.

time histories. This process showed harmonic structure analogous to surface elevation time histories such as second order low and high frequency bound and free terms, in addition to a linearised velocity component.

Measurements were carried out through the water column at the toe of the beach and were compared with a simple linear superposition theory. Agreement was satisfactory. Evidence was found that higher order terms make an increasing contribution to the onshore and vertical velocity components close to the water surface. The application of a Stokes-like expansion[8] which would incorporate higher order terms (wave component interactions) is suggested for

[8]The procedure was outlined for surface elevation time histories in Chapter 3.

as future work.

Repeated focused wave groups were generated in a bid to improve data capture rates and importantly, in the case of oblique waves, to build up a large-scale circulating current. This current is strongly localised to the beach region inshore of wave breaking. Measurements were made using both the ADV and LDA in the surf zone. It was possible to see the cross-shore variation of the longshore velocity component using the ADV system. The LDA gave insight into the level of turbulence in the surf zone due to wave breaking. Also with a smaller probe head, the LDA made it possible to make velocity measurements through the water column in just 48 mm of water, where magnitude of the offshore velocities were greatest.

Further analysis will be carried out on these kinematics data. Of particular interest will be the determination of associated accelerations and the relationship between the wave velocity and the free-surface elevation. These are important in the calculation of wave forces, of particular interest for the design and assessment of coastal structures.

Chapter 8

Conclusions and Recommendations

Coastal flooding is a topic of major environmental importance. As the mean sea level rises and storms become more severe, there is growing concern about coastal erosion and the breaching of sea defences of the coast of the U.K. In this thesis, the NewWave concept has been used for the first time to study the behaviour of a realistic extreme storm-induced wave event at a plane beach, with and without a sea wall. Particular emphasis has been placed on the wave transformation, run-up and overtopping.

8.1 Conclusions

The data resulting from experiments carried out in the UKCRF were of exceptional quality particularly when taking into account the difficulties of using a multi-element wave basin. Much effort was taken to calibrate the facility accurately and this led to data of exceptional quality. As a result, it was possible to separate odd and even frequency harmonics, and thus shed light on the behaviour of focused waves interacting with a beach, with and without a seawall present. This was achieved by generating NewWave events and their associated inverted forms. The separation technique depends upon close phase alignment of the NewWave and its inverted form. This phase alignment is seen to work until the onset of wave breaking. The separation of harmonics technique has also successfully been used on kinematics data acquired with a Laser Doppler Anemometer.

Clear evidence of the quality of the data comes from the stacked time history plots. The experiments that were carried out without the wall in place used two different wave gauge

arrangements due to restrictions on the number of gauges that were available. Therefore the stacked plots were a composite from two different experiments. There are no apparent discontinuities between any of the data obtained in the deep water experiment and the shallow water experiment, even though they were obtained on different days.

A significant finding from the visualisation work is that low frequency waves were generated at and reflected off the beach. However, there were no high frequency reflections. This was not the case when the seawall was in place - there are reflected wave components at all frequencies. From the spread sea interactions with the sea wall it was found that the longshore variation in size of the low frequency wave was much more uniform than the amplitude of the linearised group.

Wave breaking, runup and overtopping by focused wave groups and solitary waves were investigated. The single solitary wave runup data point is in perfect agreement with the runup results of Synolakis (1987).

The level of runup of the focused wave groups varied according to whether the wave group was normally incident, or obliquely incident, and also on the degree of spreading for multidirectional groups. It was found that there was good agreement between the runup values of the focused wave groups and the irregular wave predictions of Mase (1989).

Focused wave groups were also embedded into a regular wave background to replicate, to some extent, the effect of other waves being present in a wave train It was found that the level of runup of these embedded focused groups was attenuated when the focused wave group was out of phase with the underlying regular wave train, but was little affected if the two waves were in phase. Therefore, from the limited number of experiments that were undertaken, it could be deduced that a single focused wave group will provide the worst-case scenario for beach runup. The embedding process was also observed to have very little effect on the size of the low frequency wave that was generated.

It was found that there was a strong correlation between the runup of focused wave groups and the maximum individual overtopping volume of the group. The overtopping volumes were measured using two different methods, giving greater confidence in the reliability of the results. However, there is a conceptual difficulty in making comparisons between the UKCRF measured overtopping results with previously published results since overtopping volumes were measured, rather than mean overtopping discharges. It may actually be more useful

to have measurements of overtopping volumes since the overtopping event of an extreme wave is more relevant to impacts on the lee side of a structure rather than mean values. Comparisons of UKCRF overtopping volumes with empirical formulae led to the finding that the Shore Protection Manual (1984) overestimates overtopping of extreme waves by an order of magnitude. The individual overtopping volumes for the focused wave groups were converted into overtopping rates and scaled up to prototype scale. They were then compared with maximum permissible rates that exist in the literature. It was found that the focused waves generated in the UKCRF were of about the same level of severity that would cause danger to people and vehicles.

Kinematics measurements were made with both ADV and LDA. A longshore current due to repeating oblique focused wave groups was detected using the ADV system. The small size of the LDA probe enabled measurements to be made in water depths of only 48 mm shedding light on the behaviour of focused wave groups within the breaker zone.

The presence of paddle error waves in the basin was a potential problem that was ameliorated to some extent by the generation of oblique wave fronts and multidirectional seas. Additionally, the experiments used a transient event rather than a long time series minimising spurious waves generated by reflections.

8.2 Recommendations

For future investigations it would be beneficial to carry out calibration of the second order transfer function for the wave paddles to second order accuracy. This would remove the problem of second order parasitic wave generation. Whilst this error wave does not invalidate the findings of this research (for the reasons noted in the above paragraph) it would certainly be preferable if they were absent.

Also of interest for further work would be the investigation of how the phase of the NewWave affects runup and overtopping volumes. For the UKCRF work the investigation into the effect of phase was limited to the generation of crest focused and trough focused waves. The future research could initially be done in a wave flume using normally incident waves. Numerical studies (Ben Weston 2004) have shown a sinusoidal variation in the level of runup - a maximum value for trough focused waves and a minimum value for crest focused

waves. Whilst the numerical model has shown good agreement with experimental data there is merit in conducting the experiments as the model is not yet fully-validated in the surf and swash zone. The experimental results would be invaluable in validating the numerical model which could then be used more generically.

Finally the use of a Stokes-like expansion for modelling the surface elevation and kinematics has proved successful, but should be developed further to incorporate a low frequency set-down term and also higher (3rd) order terms. This would enable investigations to be made into whether the waves that are reflected off the sea wall are bound or free - shedding light onto the nature of reflection of wave groups.

Appendix A

Experiments undertaken

A.1 Unidirectional wave groups

name	input amplitude (mm)	focus location	angle of incidence (deg)	phase of group (rad)
WG1	114	toe of beach	0	0
WG2	114	$\frac{3}{4}$ depth	0	0
WG3	90	$\frac{1}{2}$ depth	0	0
WG4	57	toe of beach	0	0
WG5	114	toe of beach	0	π
WG6	114	$\frac{3}{4}$ depth	0	π
WG7	90	$\frac{1}{2}$ depth	0	π
WG8	57	toe of beach	0	π
WG9	114	toe of beach	20	0
WG10	114	$\frac{3}{4}$ depth	20	0
WG11	90	$\frac{1}{2}$ depth	20	0
WG12	57	toe of beach	20	0
WG13	114	toe of beach	20	π
WG14	114	$\frac{3}{4}$ depth	20	π
WG15	90	$\frac{1}{2}$ depth	20	π
WG16	57	toe of beach	20	π

A.2 Spread sea wave groups

name	input amplitude (mm)	focus location	spread angle (deg)	phase of group (rad)
WG17	114	toe of beach	±30	0
WG18	114	$\frac{3}{4}$ depth	±30	0
WG19	90	$\frac{1}{2}$ depth	±30	0
WG20	57	toe of beach	±30	0
WG21	114	toe of beach	±30	π
WG22	114	$\frac{3}{4}$ depth	±30	π
WG23	90	$\frac{1}{2}$ depth	±30	π
WG24	57	toe of beach	±30	π
WG25	114	toe of beach	±10	0
WG26	114	$\frac{3}{4}$ depth	±10	0
WG27	90	$\frac{1}{2}$ depth	±10	0
WG28	57	toe of beach	±10	0
WG29	114	toe of beach	±10	π
WG30	114	$\frac{3}{4}$ depth	±10	π
WG31	90	$\frac{1}{2}$ depth	±10	π
WG32	57	toe of beach	±10	π

A.3 Embedded unidirectional focused wave groups

Focused wave input amplitude 114 mm

Regular wave input amplitude 40.3 mm

Focus location: toe of beach

name	phase of focused wave	phase of regular wave
EG1	crest	crest
EG2	trough	crest
EG3	crest	trough
EG4	trough	trough

Appendix B

Second order shallow water coefficients

$$C = \frac{\left[2\omega_1\omega_2\left(\omega_1-\omega_2\right)\left(1+\alpha_1\alpha_2\right)+\omega_1^3\left(\alpha_1^2-1\right)-\omega_2^3\left(\alpha_2^2-1\right)\right]\left(\omega_1-\omega_2\right)\left(\alpha_1\alpha_2-1\right)}{\omega_1^2\left(\alpha_1^2-1\right)-2\omega_1\omega_2\left(\alpha_1\alpha_2-1\right)+\omega_2^2\left(\alpha_2^2-1\right)} + \left(\omega_1^2+\omega_2^2\right)-\omega_1\omega_2(\alpha_1\alpha_2+1) \tag{B.1}$$

$$D = \frac{\left[2\omega_1\omega_2\left(\omega_1+\omega_2\right)\left(\alpha_1\alpha_2-1\right)+\omega_1^3\left(\alpha_1^2-1\right)+\omega_2^3\left(\alpha_2^2-1\right)\right]\left(\omega_1+\omega_2\right)\left(\alpha_1\alpha_2+1\right)}{\omega_1^2\left(\alpha_1^2-1\right)-2\omega_1\omega_2\left(\alpha_1\alpha_2+1\right)+\omega_2^2\left(\alpha_2^2-1\right)} - \left(\omega_1^2+\omega_2^2\right)+\omega_1\omega_2(\alpha_1\alpha_2-1) \tag{B.2}$$

where $\alpha_1 = \coth(k_1 h)$ and $\alpha_2 = \coth(k_2 h)$.

Appendix C

Selected wave gauge locations

Table C.1: Gauge layout C.

index	longshore w.r.t centre-line (mm)	onshore w.r.t. beach toe (mm)
1	0	2500
2	0	2750
3	0	3000
4	0	3250
5	0	3500
6	0	3750
7	0	4000
8	0	4250
9	0	4500
11	0	4750
12	0	5000
13	0	1750
17	0	-1500
18	0	-1250
19	0	-1000
20	0	-750
21	0	-500
22	0	-250
23	0	0
24	0	250
25	0	500
26	0	750
27	0	1000
28	0	1250
29	0	1500
31	0	2000
32	0	2250

Table C.2: Gauge layout L.

index	longshore w.r.t centre-line (mm)	onshore w.r.t. beach toe (mm)
1	0	4740
2	0	5000
3	0	5250
4	0	5500
5	0	5750
6	0	6000
7	0	6250
8	0	6500
9	0	6750
11	0	7000
12	0	7250
13	0	7500
14	0	7750
15	0	8000
16	0	8250
17	0	8500
18	0	8750
19	0	9000
21	0	9500
22	0	9750
23	0	10000
24	0	10250
25	0	9250

Table C.3: Gauge layout H.

index	longshore w.r.t centre-line (mm)	onshore w.r.t. beach toe (mm)
1	0	-1500
2	0	-100
3	0	-500
4	0	0
5	0	500
6	0	1000
7	0	1500
8	0	2000
9	0	2500
10	0	3000
11	0	3500
12	0	4000
13	0	4500
14	0	5000
15	0	5500
16	0	5885
17	0	6500
18	0	6750
19	0	7000
20	0	7250
21	0	7500
22	0	7750
23	0	8000
24	0	8250
25	0	8400
26	0	8590
27	0	8688
28	0	8790
29	0	9005
30	0	9305

Table C.4: Gauge layout P.

index	longshore w.r.t centre-line (mm)	onshore w.r.t. beach toe (mm)
1	-1000	0
2	-500	0
3	0	0
4	500	0
5	1000	0
6	1500	0
7	2000	0
8	2500	0
9	3000	0
11	3500	0
12	4000	0
13	4750	0
14	-1000	5000
15	-500	5000
16	0	5000
17	500	5000
18	1000	5000
19	1500	5000
21	2000	5000
22	2500	5000
23	3000	5000
24	3500	5000
25	4000	5000
27	4500	5000

Bibliography

[1] J. Ahrens. Prediction of irregular wave overtopping. Technical report, Coastal Engineering Research Center, U.S. Army Waterways Experiment Station, Vicksburg, Miss, U.S., 1977.

[2] N.W.H. Allsop. Wave overtopping of seawalls, breakwaters and shoreline structures. *Proc. Instn Civ. Engrs Wat., Marit. and Energy*, 106:355–357, Dec 1994.

[3] R. Archetti, L. Franco, G. Passoni, E. Tautenhain, and C. Zimmermann. Large scale model tests on wave overtopping on rubble-mound breakwaters. *Proc. of International Conference on Coastal and Port Engineering in Developing Countries*, pages 1219–1231, 1995.

[4] T.E. Baldock. *Non-Linear Transient Water Waves*. PhD thesis, Imperial College of Science, Technology and Medicine, UK, 1995.

[5] T.E. Baldock, D.A. Huntley, P.A.D. Bird, T.J. O'Hare, and G.N. Bullock. Breakpoint generated surf beat induced by bichromatic wave groups. *Coastal Engineering*, 39:213–242, 2000.

[6] T.E. Baldock, C. Swan, and P.H. Taylor. A laboratory study of nonlinear surface waves on water. *Phil. Trans. R. Soc. Lond. A*, 354:649–676, 1996.

[7] T. Barnes. *The Generation of Low-Frequency Water Waves on Beaches*. PhD thesis, University of Bristol, U.K., 1996.

[8] J.A. Battjes. Run-up distributions of waves breaking on slopes. *Journal of the Waterways, Harbors and Coastal Engineering Division*, 97(WW1):91–114, 1971.

[9] J.A. Battjes. Surf similarity. *Proceedings of the 14th Coastal Engineering Conference, American Society of Civil Engineers*, pages 466–480, 1974.

[10] C.C. Bird and D.H. Peregrine. Wave groups from deep to shallow water. *Proc. Coastal Dynamics, ASCE*, pages 1013–1022, 1997.

[11] P. Boccotti. Some new results on statistical properties of wind waves. *Appl. Ocean Res.*, 5:134–140, 1983.

[12] A.J. Bowen, D.L. Inman, and V.P. Simmons. Wave 'set-down' and set-up. *Journal of Geophysical Research*, pages 2569–2577, 1968.

[13] Coastal Engineering Manual: Engineer Manual 1110-2-1100. U.S. Army Corps of Engineers. *Washington, D.C.*, 2002.

[14] D. Cotton. Jericho technical report - 32: Factors effecting UK coastal wave climate change. Technical report, Satellite Observing Systems, 1999.

[15] M.A. Davidson, P.A.D. Bird, D.A. Huntley, and G.N. Bullock. Prediction of wave reflection from rock structures: An integration of field and laboratory data. *Proceedings of 25th Coastal Engineering Conference, ASCE*, pages 2077–2086, 1996.

[16] J.P. de Waal and J.W. Van der Meer. Wave runup and overtopping on coastal stuctures. *Proceedings of 23rd Coastal Engineering Conference, ASCE*, pages 1758–1771, 1992.

[17] N. Dodd. Numerical model of wave run-up, overtopping, and regeneration. *Journal of Waterway, Port, Coastal, and Ocean Engineering*, 124(2):73–81, 1998.

[18] S.L. Douglass. Review and comparison of methods for estimating irregular wave overtopping rates. tech. report. Technical Report CERC-85, WES, 1985.

[19] J.D. Fenton. Nonlinear wave theories. *Ocean Engineering Science: The Sea. Chapter 1. Published by Wiley*, 9(A):3–26, 1990.

[20] C. Franco and L. Franco. Overtopping formulas for caisson breakwaters with nonbreaking 3d waves. *Journal of Waterway, Port, Coastal, and Ocean Engineering*, 125(2):98–108, 1999.

[21] L. Franco. Vertical breakwaters: The italian experience. *Coastal Engineering*, 22:31–55, 1994.

[22] N. Fukuda, T. Uno, and I. Irie. Field observations of wave overtopping of wave absorbing revetment. *Coastal Engineering in Japan*, 17:117–128, 1974.

[23] R. Gibbs, 2003. Private communication.

[24] Y. Goda. *Random Seas and Maritime Structures*. University of Tokyo Press, Tokyo, 1985.

[25] N.W. Griffiths, W.J. Easson, and C.A. Greated. Measured internal kinematics for shoaling waves with theoretical comparison. *J. Wtrwy., Port, Coast. and Oc. Engrg., ASCE*, 118(3):280–299, 1992.

[26] The WASA Group. Changing waves and storms in the northeast atlantic? *Bull. Am. Meteor. Soc.*, 79(5):741–760, 1998.

[27] A.R. Gunbak and P.M. Bruun. Wave mechanics principles on the design of rubble-mound breakwaters. *Proceedings of Port and Ocean Engineering Under Arctic Conditions POAC 79, Trondheim, Norway*, pages 1301–1318, 1979.

[28] R.T. Guza and E.B. Thornton. Wave set-up on a natural beach. *Journal of Geophysical Research*, 86(C5):4133–4137, 1981.

[29] R.T. Guza and E.B. Thornton. Swash oscillations on a natural beach. *Journal of Geophysical Research*, 87(C1):483–491, 1982.

[30] T.S. Hedges and M.T. Reis. Random wave overtopping of simple sea walls: A new regression model. *Proc. Instn Civ. Engrs Wat. Marit. and Energy*, 130:1–10, Mar. 1998.

[31] R.A. Holman. Extreme value statistics for wave run-up on a natural beach. *Coastal Engineering*, 9:527–544, 1986.

[32] R.A. Holman and A.J. Bowen. Edge waves on complex beach profiles. *Journal of Geophysical Research*, pages 6339–6346, 1979.

[33] R.A. Holman and A.H. Sallenger. Setup and swash on a natural beach. *Journal of Geophysical Research*, 90(C1):945–953, 1985.

[34] HR Wallingford. *Wave Overtopping of Seawalls Design and Assessment Manual: Technical Report W178*, 1999.

[35] S.-L.J. Hu and J.L. McCauley. Estimation of wave overtopping rates for irregular waves. *Journal of Waterway, Port, Coastal, and Ocean Engineering*, 123(5):266–273, 1997.

[36] S. Hughes. *Physical Models and Laboratory Techniques in Coastal Engineering.*, volume 7 of *Advanced Series in Ocean Engineering*. World Scientific, Singapore, 1993.

[37] M. Hulme, G.J. Jenkins, X. Lu, J.R. Turnpenny, T.D. Mitchell, R.G. Jones, J. Lowe, J.M. Murphy, D. Hassell, P. Boorman, R. McDonald, and S. Hill. Climate change scenarios for the united kingdom: The UKCIP02 scientific report. Technical report, Tyndall Centre for Climate Change Research, School of Environmental Sciences, University of East Anglia, Norwich, UK., 2002.

[38] I.A. Hunt. Design of seawalls and breakwaters. *Journal of the waterways and harbors division*, 85(3):123–152, 1959.

[39] D.A. Huntley. Long-period waves on a natural beach. *Journal of Geophysical Research*, 81(36):6441–6449, 1976.

[40] D.A. Huntley, R.T. Guza, and A.J. Bowen. A universal form for shoreline run-up spectra. *Journal of Geophysical Research*, 82(18):2577–2581, 1977.

[41] O.J. Jensen and J. Juhl. Wave overtopping on breakwaters and sea dikes. *Proceedings 2nd International Conference on Coastal and Port Engineering in Developing Countries, Bejing, China*, pages 716–730, 1987.

[42] M. Jervis and D.H. Peregrine. Overtopping waves at a wall: A theoretical approach. *Proc. 25th Internat. Conf. on Coastal Engng., Orlando, ASCE*, 2:2192–2205, 1996.

[43] T. B. Johannessen and C. Swan. A laboratory study of the focusing of transient and directionally spread surface water waves. *Proc. R. Soc. Lond. A*, 457:971–1006, 2001.

[44] P. Jonathan and P.H. Taylor. Irregular, non-linear waves in a spread sea. *In 14th Int. Conf. on Offshore Mechanics and Arctic Engineering (OMAE), Copenhagen*, 1995.

[45] P. Jonathan, P.H. Taylor, and P.S. Tromans. Storm waves in northern north sea. *In Proc. 7th Int. Conf. on the Behaviour of Offshore Structures, Cambridge, MA, USA*, vol. 2:481–494, 1994.

[46] J. Juhl and P. Sloth. Wave overtopping of breakwaters under oblique waves. *Proceedings of 24th Coastal Engineering Conference, ASCE*, pages 1182–1196, 1994.

[47] N. Kobayashi. *Advances in Coastal and Ocean Engineering*, chapter Wave runup and overtopping on beaches and coastal structures, pages 95–154. World Scientific, 1999.

[48] N. Kobayashi, D.T. Cox, and A. Wurjanto. Irregular wave reflection and run-up on rough impermeable slopes. *Journal of Waterway, Port, Coastal, and Ocean Engineering*, 116(6):708–726, 1990.

[49] N. Kobayashi, G.S. DeSilva, and K.D. Watson. Wave transformation and swash oscillation on gentle and steep slopes. *Journal of Geophysical Research*, 94(C1):951–966, 1989.

[50] N. Kobayashi and E.A. Karjadi. Surf-similarity parameter for breaking solitary-wave runup. *Journal of Waterway, Port, Coastal, and Ocean Engineering*, 120(6):645–650, 1994.

[51] N. Kobayashi and A.W. Raichle. Irregular wave overtopping of revetments in surf zones. *Journal of Waterway, Port, Coastal, and Ocean Engineering*, 120(1):56–73, 1994.

[52] G. Lindgren. Some properties of a normal process near a local maximum. *Ann. Math. Stat.*, pages 1870–1883, 1970.

[53] M.S. Longuet-Higgins. Breaking waves in deep or shallow water. *In Proc. 10th Conf. on Naval Hydrodynamics, Cambridge, MA, USA*, pages 597–605, 1974.

[54] M.S. Longuet-Higgins and R.W. Stewart. Changes in the form of short gravity waves on long waves and tidal currents. *J. Fluid Mech.*, 8:565–583, 1960.

[55] M.S. Longuet-Higgins and R.W. Stewart. Radiation stress and mass transport in gravity waves with application to 'surf beats'. *J. Fluid Mech.*, 13:481–504, 1962.

[56] M.S. Longuet-Higgins and R.W. Stewart. Radiation stresses in water waves; a physical discussion with applications. *Deep-Sea Research*, 11:529–562, 1964.

[57] M.A. Losada and L.A. Gimenez-Curto. Flow characteristics on rough, permeable slopes under wave action. *Coastal Engineering*, 4:187–206, 1981.

[58] H. Mase. Random wave runup height on gentle slope. *Journal of Waterway, Port, Coastal, and Ocean Engineering*, 115(5):649–661, 1989.

[59] H. Mase. Uprush-backrush interaction dominated long wave dominated swash oscillations. *International Symposium: Waves - Physical and Numerical Modelling, Vancouver, Canada*, pages 316–325, August 1994.

[60] H. Mase. Frequency down-shift of swash oscillations compared to incident waves. *Journal of Hydraulic Research*, 33(3):397–411, 1995.

[61] J. McCowan. On the solitary wave. *Philosophical Magazine*, 36(5th Series):430–437, 1891.

[62] R. McIver. *The Transformation of Gravity Waves by a Horizontally Sheared Current.* PhD thesis, University College London, UK, 2001.

[63] W.H. Munk. Surf beats. *Trans. American Geophysical Union*, 30(6):849–854, 1949.

[64] P. Nielsen. Wave setup: A field study. *Journal of Geophysical Research*, 93(C12):15643–15652, 1988.

[65] R.T. Oltman-Shay, J.and Guza. Infragravity edge wave observations on two california beaches. *Journal of Physical Oceanography*, 17:644–663, 1987.

[66] M.W. Owen. Design of seawalls allowing for overtopping, report EX 924. Technical report, HR Wallingford, 1980.

[67] M.W. Owen. Design of seawalls: Model tests to determine overtopping discharges, report EX 923. Technical report, HR Wallingford, 1980.

[68] D.H. Peregrine. Wave jumps and caustics in the propagation of finite-amplitude water waves. *Journal of Fluid Mechanics*, 136:435–452, 1983.

[69] D.H. Peregrine, D. Skyner, M. Stiassnie, and N. Dodd. Nonlinear effects on weakly focussed waves. *Proc. 21st Internat. Conf. Coastal Engng.*, 1:732–742, 1988.

[70] D.H. Peregrine and S.M. Williams. Swash overtopping a truncated plane beach. *Journal of Fluid Mechanics*, 440:391–399, 2001.

[71] Permanent Service for Mean Sea Level. Proudman Oceanography Laboratory. 2003.

[72] R.J. Rapp and W.K. Melville. Laboratory measurements for deep water breaking waves. *Phil. Trans. R. Soc. Lond. A*, 331:735–800, 1990.

[73] R. Saville. Laboratory data on wave runup and overtopping on shore structures. *TM-64, U.S. Army, Corps of Engineers, Beach Erosion Board, Washington, D.C.*, 1955.

[74] T. Saville. Large-scale model tests of wave runup and overtopping, Lake Okeechobee levee sections. *Unpublished manuscript, U.S. Army, Corps of Engineers, Beach Erosion Board, Washington, D.C.*, 1958.

[75] T. Saville. An approximation of the wave run-up frequency distribution. *Proc., 8th Coastal Engineering Conference, ASCE*, pages 48–59, 1962.

[76] T. Saville and J.M. Caldwell. Experimental study of wave overtopping on shore structures. *Proc. Minnesota Int. Hydraulics Convention, Minneapolis, IAHR*, 1953.

[77] A. Seyama and A. Kimura. The measured properties of irregular wave breaking and wave height change after breaking on the slope. *In: Proc. 21st Int. Conf. Coastal Eng. ASCE*, pages 419–432, 1988.

[78] M.C. Shen and R.E. Meyer. Climb of a bore on a beach. part 3. run-up. *J. Fluid Mechanics*, 16:113–125, 1963.

[79] I. Shennan. Holocene crust. *J. Quaternary Science*, 4:77–89, 1989.

[80] Shore Protection Manual. U.S. Army Engineer Waterways Experiment Station. *U.S. Government Printing Office, Washington, D.C.*, 1984.

[81] J.C. Su, C.I. Liu, and C.T. Kuo. Application of weibull distribution for irregular wave overtopping. *Proceedings of the Sixth IAHR International Symposium on Stochastic Hydraulics, Taipei*, pages 267–274, 1992.

[82] J. Sutherland and J. Wolf. The vulnerability of coastal defences to climate change. *Proc. Instn Civ. Engrs Wat., Marit. and Energy*, 2002.

[83] I.A. Svendsen and J. Buhr Hansen. Wave attenuation and setup on a beach. *Proc., 19th Int. Conf. Coast. Engrg.*, pages 54–69, 1984.

[84] I.A. Svendsen and J. Veeramony. Wave breaking in wave groups. *Journal of Waterway, Port, Coastal, and Ocean Engineering*, 127(4):200–212, 2001.

[85] C. E. Synolakis. The runup of solitary waves. *J. Fluid Mech.*, 185:523–545, 1987.

[86] P.H. Taylor, P. Jonathan, and L.A. Harland. Time domain simulation of jack-up dynamics with the extremes of a gaussian process. *Journal of Vibration and Accoustics*, 119:624–628, 1997.

[87] E.B. Thornton and R.T. Guza. Transformation of wave height distribution. *Journal of Geophysical Research*, 88(C10):5925–5938, 1983.

[88] F.C.K. Ting. Laboratory study of wave and turbulence velocities in a broad-banded irregular wave surf zone. *Coastal Engineering*, 43:183–208, 2001.

[89] F.C.K. Ting. Laboratory study of wave and turbulence characteristics in narrow-banded irregular breaking waves. *Coastal Engineering*, 46:291–313, 2002.

[90] P.S. Tromans, A. Anaturk, and P. Hagemeijer. A new model for the kinematics of large ocean waves - application as a design wave. *In Proc. 1st Int. Offshore and Polar Engineering Conf., Edinburgh, UK*, vol. 3:64–71, 1991.

[91] S. Tsuruta and Y. Goda. Expected discharge of irregular wave overtopping. *Proceedings of 11th Coastal Engineering Conference, ASCE*, pages 833–852, 1968.

[92] M.J. Tucker. Surf beats: Sea waves of 1 to 5 min. period. *Proc. R. Soc., London, Ser. A*, 202:565–573, 1950.

[93] J.W. Van der Meer. Stability of breakwater armour layers - design formulae. *Coastal Engineering*, 11:219–239, 1987.

[94] J.W. Van der Meer. Deterministic and probabilistic design of breakwater armor layers. *Journal of Waterway, Port, Coastal, and Ocean Engineering*, 114(1):66–80, 1988.

[95] J.W. Van der Meer. Numerical modelling of wave-structure interaction. *Proc. Instn Civ. Engrs Wat. Marit. and Energy*, 106:359–362, Dec. 1994.

[96] J.W. Van der Meer and J.P.F.M. Janssen. Wave run-up and wave overtopping at dikes. *Wave forces on inclined and vertical wall structures, N. Kobayashi and Z. Demirbilek, eds., ASCE, New York, N.Y.*, pages 1–27, 1995.

[97] J.W. Van der Meer and C.-J.M. Stam. Wave runup on smooth and rock slopes of coastal structures. *Journal of Waterway, Port, Coastal, and Ocean Engineering*, 118(5):534–550, 1992.

[98] J.H. Van Oorschot and K. D'Angremond. The effect of wave energy spectra on wave run-up. *Proc., 11th Coastal Engineering Conference, ASCE*, pages 888–900, 1968.

[99] J.R. Weggel. Maximum breaker height. *Journal of the Waterways, Harbors and Coastal Engineering Division*, 98(WW4):529–548, 1972.

[100] J.R. Weggel. Wave overtopping equation. *Proceedings of 15th Coastal Engineering Conference, ASCE*, pages 2737–2755, 1976.

[101] B. Weston, 2004. Private communication.

[102] B. Weston, P.H. Taylor, A.G.L. Borthwick, and A.C. Hunt. Godunov-type Boussinesq modeling of extreme wave run-up. *Proceedings of the International Symposium on Shallow Flows, Delft, June 16-18*, 2003.